

**Synthesis, Characterization and Kinetic Studies of Porphyrins With  
Thiolated Side Chains for Functionalization of Paramagnetic  
Iron Oxide – Gold, Core – Shell Nanoparticles**

**By**

**ESHILOKUN ADEOLU. O**

**(200818377)**

**BEING A THESIS SUBMITTED IN FULFILMENT OF THE  
REQUIREMENTS FOR THE DGREE OF  
DOCTOR OF PHYLOSOPHY (PhD)**

**IN**

**ORGANIC CHEMISTRY**

**IN THE**

**DEPARTMENT OF CHEMISTRY, SCHOOL OF PATHOLOGY AND PRE-  
CLINICAL SCIENCES, UNIVERSITY OF LIMPOPO, MEDUNSA  
CAMPUS, MEDUNSA, GAUTENG, SOUTH AFRICA**



**SUPERVISOR: PROF. SP SONGCA**  
**CO-SUPERVISOR: DR. M. A. DEBEILA**  
**CO-SUPERVISOR: DR. O. S. OLUWAFEMI**

**AUGUST 2011**

## ABSTRACT

5,10,15,20-Tetrakis[3-(3-thioacetoxypoxy)phenyl]porphyrin, a photosensitizer for photodynamic therapy (PDT) was synthesized from 3-hydroxybenzaldehyde. Acid and alkaline hydrolysis of the thioacetoxypoxyphenyl porphyrin was attempted to afford a free base porphyrin, 5,10,15,20-tetrakis[3-(3-thiolpropoxy)phenyl]porphyrin but not achieved. Spectroscopic data indicates that partial hydrolysis occurred.  $^1\text{H}$ NMR,  $^{13}\text{C}$ NMR, UV-Visible and Infra-red spectrometers were used to characterize all the compounds. The synthesized porphyrin was immobilized on gold coated superparamagnetic iron oxide ( $\text{Fe}_3\text{O}_4@Au$ ) nanoparticles for possible use as a carrier or drug delivery system for the porphyrin to cancer sites.

The use of magnetic nanoparticles for biomedical applications have been proposed to a large extent for several years. In recent years nanotechnology has developed to a stage that makes it possible to produce, characterize and specifically tailor the functional properties of nanoparticles for clinical applications. This has led to various opportunities such as improving the quality of magnetic resonance imaging, hyperthermia treatment for malignant cells, site-specific drug delivery and the manipulation of cell membranes. To this end a variety of iron oxide nanoparticles have been synthesized.

Using co-precipitation method, nanoparticles comprised of gold shell and magnetite/maghemite were synthesized by overgrowing the gold shell onto the magnetic seeds using sodium citrates as a reducing agent. Oxidized magnetites ( $\text{Fe}_3\text{O}_4$ ) fabricated by co-precipitation of  $\text{Fe}^{2+}$  and  $\text{Fe}^{3+}$  in strong alkaline solution were used as magnetic cores. These magnetic nanoparticles were characterized by Transmission Electron Microscopy (TEM), High Resolution Transmission Electron Microscopy (HRTEM), and X-ray diffraction spectroscopy (XRD). The transmission electron microscopy (TEM) image indicated that the particles were well dispersed

and spherical in shape with an average size of 34 – 58 nm with the mean particle diameter of  $42.41 \text{ nm} \pm 12.03 \text{ nm}$  and standard deviation of ( $\sigma$ ) 0.27 nm indicating broad size distribution for the superparamagnetic iron oxide nanoparticles (SPION), the particle diameters for the gold coated SPION are in the range 34-54 nm while the average particle size as determined from the TEM image for the selected fraction is  $44.26 \text{ nm} \pm 6.93 \text{ nm}$ . The relative standard deviation of the sizes of the nanoparticles is 0.16 nm and the TEM for the functionalized gold coated SPION shows monodispersed particles which appear in spherical, cubic, irregular hexagon and oblong shapes with an average diameter of 44.65 nm. The HRTEM image, shows the existence of lattice planes which confirms the crystallinity of the material. The spacing between adjacent lattice planes is about 0.23 nm which corresponds to the (311) interplanar distance of  $\text{Fe}_3\text{O}_4$  nanocrystals. Atomic force microscopy (ATM) was used to confirm the transmission electron microscopy (TEM) and HRTEM findings.

The UV-Visible absorption spectra of the deionised water used in the procedure of preparation of the as-synthesized nanoparticles showed no absorption peak in a wavelength range of 350-750 nm, but after introducing the suspension of the Au-coated magnetic nanoparticles, an absorption peak located at 526 nm appeared which is ascribed to the surface plasmon of nanosized  $\text{Fe}_3\text{O}_4@\text{Au}$  nanoparticles.

The kinetic studies using UV-visible spectrometer and the HRTEM images confirmed the adsorption of the porphyrin macromolecules as a coat on the magnetites particles. At a 5000 revolution per second (rps), aliquot sample of the aqueous phase of the suspension of 0.002 mM  $\text{Fe}_3\text{O}_4@\text{Au}$  in contact with the organic phase solution of the porphyrin taken for absorbance measurement at every 600 s showed a decrease in the concentration of the suspension while a noticeable and appreciable increase was also noted in the concentration of the porphyrin macromolecules measured at a  $\lambda$  max of 420 nm representing the

functionalized sample. A new absorption peak of 535 nm was recorded for the nanoparticle/porphyrin phase.

A clear magnetic behaviour was established from the two different samples (coated and functionalised samples) using superconducting quantum interference device (SQUID) magnetometer. No long-range cooperative behaviour is evident anywhere from room temperature down to 2 K, which attests to a characteristic length of the scale of the Fe-magnetic agglomerations on the nano-scale. Being especially prone to intrinsic ferromagnetic ordering, any impurity form of Fe or macro-scale Fe aggregates would impart a very large and easily identifiable magnetic signal. Such a response was completely absent from these studies and hence testifies to the homogeneity quality of the materials under investigation.

**KEY WORDS:** photodynamic therapy, photosensitizer, porphyrins, magnetites, maghemite, crystallinity, magnetic seeds, nanoparticles,

## DECLARATION

I, **Eshilokun Adeolu. O** declare that the thesis “**Synthesis, Characterization and Kinetic Studies of Porphyrins with thiolated Side Chains for Functionalization of Paramagnetic Iron Oxide-Gold, Core-Shell Nanoparticles**” hereby submitted to the University of Limpopo, Medunsa Campus, Gauteng, South Africa for the degree of PhD, Organic Chemistry has not previously been submitted by me for a degree at this or any other university; that it is my work in design and in execution, and that all materials contained herein has been duly acknowledged.

.....

**A. O. Eshilokun**

.....

**Date**

**Student Number: 200818377**

## **DEDICATION**

To my closely knit family and the Almighty God who made it possible for me to complete the studies with joy in my heart and happiness on my lips.

## **ACKNOWLEDGEMENTS**

It gives me a great pleasure to thank the many people who assisted me in the actualization of this dream. Prof. SP Songca, the Executive Dean, Faculty of Science, Engineering and Technology, Walter Sisulu University, Eastern Cape, South Africa whom God has chosen to give me the opportunity in the first instance of coming to work as a doctoral student under his kind supervision. You have guided me through the long, difficult but interesting journey from office and laboratory discussions, to experimental and final report of the research work. You gave me excellent advice on matters relating to the entire work as well as moral and financial support for my well being. I am indeed very grateful to you, not forgetting the registration of all of us (your students) for any available workshop, symposium and conferences that has relevance to our various research fields which has in no small measure contributed greatly to our knowledge.

I will also count myself lucky for enjoying your kindness to come and take me from the airport to the school on my first landing in South Africa, even when it had become apparent that you have secured another higher position in your present school. You had not left me to wonder in a foreign land which has now become a second home to me. It later became obvious to me how diligent, kind and generous you are by the various comments I heard people made about you after your departure from Medunsa and as a confirmation to this the University itself made a spotlight on you after you had left. I am really lucky and blessed to have you as my supervisor.

Many thanks to my co-supervisor, Dr. M. A. Debeila, a Senior Lecturer in the Chemistry Department who had led me on two occasions to attend competitive symposia at University of Witwatersrand and University of Johannesburg, I may not have won the only price on each occasion but I had not performed poorly as well, and my

participation has not only added to my knowledge and experience but has also increase my confidence as a post graduate organic chemistry student presenting papers at other subsequent conferences and symposia. Prof. N. M. Agyei, a diligent and good listener, and acting head of Chemistry Dept. when I arrived at Medunsa Campus for my studies. You made invaluable contributions to my stay in the school and I am really short of words to describe your tremendous support for me but I need to mention that you ensured that I enjoyed the School Research Fellowship which has in no small measure gave me a stable mind through my stay in the department. I can't but remember the warm welcome you gave me and my wife in your house when she visited South Africa in 2009.

My appreciation also goes to Prof. B. B. Marvey, a youthful and amiable professor of analytical chemistry, and the substantive Head of Chemistry Department. You transformed my stay into a more pleasant one with the role you played when the Human Resource Department was at a cross-road on the renewal of my research fellowship award, though it took a long time to resolve but you ensured it was eventually resolved. Thanks are also due to the followings: Mrs Deborah Moeletsi (Moeletsi my sis) the Chemistry Department secretary for all your assistance and the warm welcome I always received from you, Sebolashi Kolobe, messrs S. Ndlovu, J. Mofokeng, Fred Makhubela (Freddy my brother), and Issac Masilela (Isicco) for your constructive criticisms during the experimental stages. I have learnt a lot from you in terms of techniques and experimental procedures. Thanks to Teboho Taoana, Mrs Christiana Seseng, Mrs. Mogale, Gugu Mphalala of Virology Dept., whom I met at the tail end of my studies and Tebogo Motshwene of Standard Bank who are all good friends to me. Many thanks to Professors F. C. Clarke and P. H. King, and other Biology Department staff especially Mrs van Zyl (Department Secretary) and Dr. J. O. Olowoyo, and Aubrey of the IT Department.



I wish to also express my profound gratitude to the followings for their unprecedented support for me when I was planning my trip to South Africa without hope of how I was going to survive without adequate funding for the trip as well as my for my stay during studies. They are Dr. Akinola Ogunlewe, the Lay President, United African Methodist Church (World-wide), It would be difficult to forget how you made my first departure to South Africa so smooth at short notice and subsequent monetary gifts (sometimes in foreign currencies) each time I was opportune to visit Nigeria during my studies and Sist. (Chief) F. I. Oshodi (the Iya Ewe of UAMC, Ebute-Metta). All members of my church at Ebute-Metta for their unflinching and undying love for me, particularly Mr & Mrs Oshodi, Bros. Kuti, Dosunmu, Dawodu, Adeyinka and Chief Adeolu K. Ojerinde (The local lay president of UAMC, Ebute -Metta). Not to be forgotten are “Emeritus” Amosu and his wife, Sist. Funmi Amosu, who had made it their duties to always check on me by calling to find out how I was fairing in South Africa as well as Mrs. Bailey. How can I forget my Bishop, Right Rev. J. A. Oja-Oba, with your monthly sms prayers for God’s guidance and protection over me.

Prof. O. R. Awofolu, Head of Environmental Science Department, University of South Africa (UNISA). You happen to be a friend and a colleague who is interested in the progress of others. It was at your instance I got the opportunity to meet and study with Prof. Songca, and ever since I came, you have demonstrated to me how a true friendship should be. I thank you and your family very much and particularly for taking keen interest in my studies by checking with me on the progress of my work. I’ll like to remind myself of my first day in Medunsa how you drove me out to get commodities for my immediate needs and comfort. Those areas I saw that very day as a strange land with green plants all around me and royal blue sky above me had now become part of me. I really cherished that day.

Prof. A. A. Adeniyi, whom in all sincerity, I don't know how to describe your role in my life, but suffice to say that you have been a great mentor, a councilor, a pathfinder, an enigma, a brother, a true friend and above all a good and objective critic of whatever situation I presented to you. I have no doubt that the Almighty God has used you to change the course of my life for the best. While some will not care seeing you as a perpetual subordinate, you believe that there is no limit for any human endeavor to achieve the best in life. You have demonstrated to me what Collin Powell (former US Secretary of State) was quoted to have said thus:

*The less you associate with some people, the more your life will improve.*

*Any time you tolerate mediocrity in others, it increases your mediocrity.*

*An important attribute in successful people is their impatience with negative thinking and negative acting people.*

*As you grow, your associates will change.*

*Some of your friends will not want you to go on.*

*They will want you to stay where they are.*

*Friends that don't help you climb will want you to crawl.*

*Your friends will stretch your vision or choke your dream.*

*Those that don't increase you will eventually decrease you.*

*Consider this: Never receive counsel from unproductive people. Never discuss your problems with someone incapable of contributing to the solution, because those who never succeed themselves are always the first to tell you how. Not everyone has a right to speak into your life. You are certain to get the worst of the bargain when you exchange ideas with the wrong person. Don't follow anyone who's not going anywhere. With some people you spend an evening; with others you invest it. Be careful where you stop to inquire for directions along the road of life. Wise is the person who fortifies his life with the right friendships. If you run with wolves, you will learn to howl. But if you associate with eagles, you will learn to soar to great heights. "A mirror reflects a man's face, but what is really like is*

*shown by the kind of friends he chooses.” The simple but true fact of life is that you become like those with whom you closely associate - for the good and the bad.*

*Note: Be not mistaken. This is applicable to family as well as friends. Yes....do love, appreciate and be thankful for your family, for they will always be your family no matter what. Just know that they are human first and though they are family to you, they may be a friend to someone else and will fit somewhere in the criteria above.*

“In prosperity our friends know us in adversity we know our friends.”

**"Never make someone a priority when you are only an option for them."**

*"If you are going to achieve excellence in big things, you develop the habit in little matters. Excellence is not an exception, it is a prevailing attitude."*

Huge thanks and gratitude to the following childhood friends; Leke, Tunji and Saheed. Your prompt intervention in my life is well appreciated, you all realized the consequence of my decision to further my studies without salary to care for myself and my family. Thank you all for believing in me and greater thanks to the Almighty God who has made it possible for me not to lack during my studies in spite of the initial fear and uncertainties ahead and I believe You will still do greater things for me after my studies.

I wish to also express my appreciation to Dr. Baker, Director of Electron Microscope Unit (EMU), UL, Medunsa Campus and Dr. O. S. Oluwafemi, Senior Lecturer, Chemistry Department, Walter Sisulu University, Mthatha, Eastern Cape, South Africa for all my Electron Microscope Analysis and Dr. Oluwafemi for interpretations of the

micrographs, likewise Dr. M. De Jongh and Prof. H. F. Joubert for allowing me to use the Chemical Pathology laboratory for all my optical instrumental analyses. Of equal importance is the assistance from Professor Andre M. Strydom, Professor of Physics in the Faculty of Science and Head of the Physics Department and Scientific Director of the Science Faculty Central Analytical Facility, University of Johannesburg and his research team for the measurement and interpretations of all magnetic properties.

Fellowship award and post graduate merit award from the management of the University of Limpopo, Medunsa Campus and funding from National Research Foundation (NRF) are greatly acknowledged. The contribution of the Lagos State Government under the able leadership of His Excellency, Governor Babatunde Raji Fashola (BRF) and the Special Adviser to the governor on education, Dr Elijah Olu Adewale as well as the efforts of all staff of the Lagos State Scholarship Board starting from Alhaja K. O. Odewale Secretary, Lagos Scholarship Board to the least staff unknown to me who may have contributed to my success in one way or the other unknown to me is well acknowledged and appreciated.

Special thanks to my closely knit immediate and extended families for bearing with me during my studies. There was no doubt that I was unable to cope with my responsibilities to some or all of you, but then you all stood by me not minding my shortcomings. While it was not possible to mention every name, permit me to mention the best half of my life, Fausat Omobolanle, my jewel of inestimable value as well as the best fruits God has given us in the form of Adesola, Adeola and Adekunbi, I am very proud of you guys. My nephews and nieces; Adekanbi (Tosin), Ladi, Abayomi, Seun, Adeniran, and Tope and Princess in United Kingdom to mention just a few. My siblings, Adebola and Obayemi (Sola), thanks to you all for being there for me. How can I forget to mention those who have taken me to be one of their own and have always being there for me, my brothers-in-law,

Bros. Afis, Rasaq and Musiliu as well as Alhaja (my mother-in-law, Alhaja Suwebatu Babajide) and granny (my mother, Elder Felicia Anike Eshilokun). Eternal perfect rest in peace to my father Late Elder (Prince) Lawrence Oresanya Eshilokun and my father-in-law Late Alhaji Junaid Agboola Babajide.

The greatest of the greatest appreciation goes to the Almighty God, the creator of heaven and earth for sparing my life and that of my family all through our journeys on the planet earth. May your name be praised.

<b>Table of Abbreviations &amp; Symbols</b>	
<b>EBR</b>	External beam radiotherapy
<b>HLE</b>	High linear energy transfer
<b>Gy</b>	Gray
<b>DMSO</b>	Dimethylsulfoxide
<b>DDQ</b>	2,3-dichloro-5,6-dicyano-1,4-benzoquinone
<b>THF</b>	Tetrahydrofuran
<b>DCM</b>	Dichloromethane
<b>TFA</b>	Trifluoroacetic acid
<b>BNCT</b>	Boron neutron capture therapy
<b>LDMS</b>	Laser desorption mass spectrometre
<b>BPD</b>	Benzoporphyrin derivative
<b>b.pt</b>	Boiling Point
<b>m.pt</b>	Melting Point
<b>C.P</b>	Chemically Pure
<b>d</b>	Doublet
<b>dd</b>	Double of Doublet
<b>m</b>	Multiplet
<b>t</b>	Triplet
<b>td</b>	Triple of Doublet
<b>HpD</b>	Heamatoporphyrin derivative
<b>Hz</b>	Hertz
<b>NMR</b>	Nuclear Magnetic Resonance
<b><sup>1</sup>H-NMR</b>	Proton Nuclear Magnetic Resonance
<b>IUPAC</b>	International Union of Pure and Applied Chemistry
<b>J</b>	Coupling Constant
<b>MHz</b>	mega-Hertz
<b>p-THPP</b>	5,10,15,20-Tetra(p-hydroxyphenyl)prophyrin
<b>BOPP</b>	Boronated tetraphenylporphyrin
<b>PRT</b>	Photoradiation Therapy
<b>PDT</b>	Photodynamic Therapy
<b>UV</b>	Ultra-violet
<b>IR</b>	Infra-red
<b>MPs</b>	Magnetic Particles
<b>NPs</b>	Nanoparticles
<b>MNPs</b>	Magnetic Nanoparticles
<b>SPION</b>	Super paramagnetic Iron Oxide Nanoparticles
<b>FeO</b>	Iron Oxide
<b>Fe<sub>2</sub>O<sub>3</sub></b>	Maghemite
<b>Fe<sub>3</sub>O<sub>4</sub></b>	Magnetite
<b>DNA</b>	Deoxyribo Nucleic Acid
<b>RNA</b>	Ribo Nucleic Acid
<b>DDS</b>	Drug Delivery System
<b>PEG</b>	Poly Ethylene Glycol
<b>PVA</b>	Poly Vinyl Alcohol
<b>TEM</b>	Transmission Electron Microscope
<b>HRTEM</b>	High Transmission Electron MMicroscope
<b>XANES</b>	X-ray Absorption near Edge Spectroscopy

<b>MRI</b>	Magnetic Resonance Imaging
<b>FFs</b>	Ferro fluids
<b>MFs</b>	Magnetic Fluids
<b>B</b>	Magnetic Field
<b><i>M<sub>s</sub></i></b>	Saturation Magnetization
<b>M</b>	Magnetization
<b>MIH</b>	Magnetic Induction Hyperthermia
<b>MF</b>	Magnetofection
<b>T<sub>c</sub></b>	Curie temperature
<b>M<sub>r</sub></b>	Remanence Magnetization
<b>H<sub>c</sub></b>	Coercive Field
<b>H</b>	Magnetic Field Strength
<b>ZF</b>	Zero Fields
<b>T (K)</b>	Temperature in Kelvin
<b>VSM</b>	Vibrating Sample Magnetometer
<b>SQUID</b>	Superconducting Quantum Interference Device
<b>XRD</b>	X-ray diffraction
<b>μm</b>	Micrometer

	<b>Table of tables</b>	xvi
<b>1</b>	Main features of an efficient photodynamic agent for tumor treatment (Property related structural and biological features) <sup>9</sup>	13
<b>2</b>	Photosensitizers presently used in clinical trials for PDT of tumors	15
<b>3</b>	<i>meso</i> -(R)dipyrromethanes.	99
<b>4</b>	Selected proteins/targeting ligands that could be used for derivatizing Magnetic nanoparticles for various biomedical applications.	114
<b>5</b>	Comparison of different characteristic features of the iron nanoparticles fabricated through different methods.	118
<b>6</b>	General materials used in the experiments	131
<b>7</b>	Standard curve data for nanoparticles	152
<b>8</b>	Concentrations calculated from the absorbance of nanoparticles in the aqueous phase.	153
<b>9</b>	Concentration of nanoparticles calculated from the absorbance of the nanoparticles in the organic phase of the mixture of porphyrin solution and suspension of nanoparticles	154
<b>10</b>	Data for rate order of the reaction	156
<b>11</b>	Band positions and assignments of functional groups	162



<b>Table of Schemes</b>		xvii
<b>1</b>	Synthesis of 5-ALA acid and PBG	45
<b>2</b>	Synthesis of the linear tetrapyrrole	46
<b>3</b>	Synthesis of the linear tetrapyrrole	47
<b>4</b>	Laboratory synthesis of porphyrin	73
<b>5</b>	Metallation of porphyrin	75
<b>6</b>	Statistical synthesis of dimethylporphyrin	83
<b>7</b>	Directed porphyrin synthesis	84
<b>8</b>	Synthesis of ABCD porphyrin	84
<b>9</b>	Synthesis of various <i>trans</i> -porphyrins	88
<b>10</b>	Reduction of the diacyl dipyrromethane to dipyrromethane-dicarbinol	92
<b>11</b>	Dipyrromethane leading to porphyrin synthesis	95
<b>12</b>	Rothmund type reaction leading to porphyrin synthesis	96
<b>13</b>	Use of dipyrromethanes to four types of <i>trans</i> -substituted porphyrins.	97
<b>14</b>	One-flask synthesis of <i>meso</i> -substituted dipyrromethanes.	98
<b>15</b>	One-flask synthesis of a bis-dipyrromethane.	100
<b>16</b>	Synthesis of 3-(3-Formylphenoxy)propyl bromide	135
<b>17</b>	Synthesis of 3-(3-formylphenoxy)propyl thioacetate	135
<b>18</b>	Synthesis of 5,10,15,20-Tetrakis[3-(3-thioacetoxypropoxy)phenyl]porphyrin	136
<b>19</b>	Attempted hydrolysis of Compound 85 to Compound 86	137
<b>20</b>	Proposed reaction mechanism for the acid and alkaline hydrolysis	138

<b>Table of Figures</b>		xviii
-------------------------	--	-------

1	Jablonski diagram to show photosensitization of oxygen <sup>33</sup>	23
2	PDT Photosensitizers	25
3	Meso-tetra(hydroxyphenyl)porphyrin	28
4	How does PDT work?	34
5	Some common light sources for PDT	36
6	Structure of Gadolinium Texaphyrin (Gd- <i>Tex</i> )	39
7	Structure of Lutetium Texaphyrin (Lu- <i>Tex</i> )	40
8	Schematic representation of the biosynthesis of haeme and the influence of uptake of exogenous 5-ALA	43
9	BPD Verteporfin	48
10	Boronated tetraphenylporphyrin (BTPP) and 2,4-( $\alpha,\beta$ -dihydroxyethyl) deuteroporphyrin IX tetrakis(carborane carboxylate ester (BOPP), where open circles o = BH, and asterics * = CH or C.	51
11	<i>Meso</i> -tetra(meta-hydroxyphenyl)chlorin (mTHPC)	60
12	Schematic representation of the cell membrane bilayer	65
13	Structure of porphine, the simplest porphyrin	69
14	<i>Meso</i> steric interactions alone	71
15	<i>Meso</i> , and <i>beta</i> steric interactions	72
16	Naturally occurring porphyrins	73
17	Nomenclature of porphyrins using IUPAC system	74
18	The Frontier Orbitals relevant to the Gouterman Four-Orbital Model <sup>90</sup>	76
19	Orbital diagrams showing possible transitions for porphyrins. <sup>90</sup>	76
20	Rational synthesis of different <i>meso</i> -substituted porphyrins	85
21	Aminomethylpyrroles used to construct porphyrinic macrocycles	86
22	Scheme showing the reaction mechanism of Fe <sub>3</sub> O <sub>4</sub> particle formation from an aqueous mixture of ferrous and ferric chloride by addition of a NH <sub>4</sub> OH.	111
23	Scheme showing different strategies for fabrication and surface modification of Fe <sub>3</sub> O <sub>4</sub> nanoparticles.	113
24	Scheme of derivatization of SPION either with targeting ligands such as lactoferrin (Lf) or ceruloplasmin (Cp) and their targeting to human fibroblasts.	119
25	Internalization of magnetic particles via monoclonal antibodies and transferrin receptors.	120
26	Nanoparticle systems for drug delivery (DD) applications. <sup>218,219</sup>	122
27	Hysteresis loops (M versus applied H) characteristic of ferromagnetic and superparamagnetic nanoparticles	124
28	Schematic diagram for the formation of SPION	139
29	Schematic diagram showing the procedures of coating the Fe <sub>3</sub> O <sub>4</sub> nanoparticles with Au and the formation of magnetic nanoparticles (Fe <sub>3</sub> O <sub>4</sub> @Au NPs).	140
30 (a)	Proton nmr of 3-hydroxybenzaldehyde	143

<b>30 (b)</b>	Spectra showing the aromatic protons of 3-hydroxybenzaldehyde	144
<b>31 (a)</b>	Proton 3-(3-Formylphenoxy)propyl bromide	145
<b>31 (b)</b>	Expanded spectrum of fig.31 (a)	145
<b>31 (c)</b>	Expanded spectrum of fig. 31(a)	146
<b>32 (a)</b>	Proton nmr of 3-(3-Formylphenoxy)propyl thioacetate	147
<b>32 (b)</b>	Expanded spectrum of fig. 32 (a)	147
<b>32 (c)</b>	Expanded spectrum of fig. 32 (b)	148
<b>33 (a)</b>	Proton NMR of 5,10,15,20-Tetrakis(thioacetoxypoxy)phenyl porphyrin	149
<b>33 (b)</b>	Expanded spectrum of fig.33 (a)	149
<b>34</b>	Graph of the standard curve for nanoparticles	152
<b>35</b>	Graph showing the decrease in the concentration of nanoparticles in the aqueous phase of the nanoparticle/porphyrin mixture.	154
<b>36</b>	Graph showing the increase in concentration of nanoparticles in the organic porphyrin phase.	155
<b>37</b>	Graph of transfer of nanoparticles from aqueous phase and concentrations of nanoparticles in the aqueous and organic porphyrin phase.	155
<b>38</b>	UV spectrum of porpyrin solution	157
<b>39</b>	UV spectrum of gold coated SPION	158
<b>40</b>	UV spectrum of functionalized sample	158
<b>41</b>	FT-IR Spectrum Of Compound 82	159
<b>42</b>	FT-IR spectrum of Compound 83	160
<b>43</b>	FT-IR spectrum of Compound 84	160
<b>44</b>	FT-IR spectrum of Compound 85	161
<b>45 (a)</b>	FT-IR spectrum of Compound 86	161
<b>45 (b)</b>	FT-IR spectrum of functionalized gold coated sample	162
<b>46</b>	(a) TEM images and (b) Particle size distribution of super-paramagnetic Iron oxide nanoparticles (SPION).	163
<b>47</b>	(a) TEM images and (b) Particle size distribution of gold coated super paramagnetic Iron oxide nanoparticles.	164
<b>48</b>	(a) TEM and (b) HRTEM images with SAED (inlet) of functionalised gold coated super paramagnetic Iron oxide nanoparticles.	165
<b>49</b>	Atomic force microscopy using the RTESPW tip and a scan rate of 0.803 Hz, and the platinum coated tip, SCM-PIT at a scan rate of 1.00 Hz.	166
<b>50</b>	XRD pattern of the gold coated SPION	167
<b>51</b>	Temperature-dependent magnetic moment of (a) functionalised SPION and (b) gold coated SPION taken in field-cooling (blue) and zero-field cooling (zfc) modes respectively.	168
<b>52</b>	Room-temperature field-dependent measurements of the magnetic moment in (a) sample "2" and (b) sample "F".	168
<b>53</b>	Low-temperature (2 K) field-dependent measurements of the magnetic moment in (a) functionalized SPION and (b) gold	170

	coated SPION.	
--	---------------	--

Table of equations			
$^3\text{S}^* + ^3\text{O}_2$	$\longrightarrow$	$^1\text{S} + ^1\text{O}_2^*$	(1)
$^{10}_5\text{B} + ^1_0\text{Nu}$	$\longrightarrow$	$^{11}_5\text{B} \longrightarrow ^4_2\text{He} + ^7_3\text{Li} + \gamma^{\text{UT}}$	(2)
$\text{H}_2\text{P} + [\text{ML}_n]^{2+}$	$\longrightarrow$	$\text{PML}_{n-4} + 4\text{L}^- + 2\text{H}^+$	(3)
$\text{Fe}^{3+} + x\text{H}_2\text{O}$	$\xrightarrow{\text{Deprotonation}}$	$\text{Fe}(\text{OH})_x^{3-x} + x\text{H}^+$	(4)
$\text{Fe}^{2+} + x\text{H}_2\text{O}$	$\xrightarrow{\text{Deprotonation}}$	$\text{Fe}(\text{OH})_y^{2-y} + y\text{H}^+$	(5)
$\text{Fe}(\text{OH})_x^{3-x} + \text{Fe}(\text{OH})_y^{2-y}$	$\xrightarrow[\text{Dehydration, pH: 9.0, 6.0}]{\text{Deprotonation}}$	$\text{Fe}_3\text{O}_4$	(6)
$\text{Fe}^{2+} + 2\text{Fe}^{3+} + 8\text{OH}^-$	$\longrightarrow$	$\text{Fe}_3\text{O}_4 + 4\text{H}_2\text{O}$ (black colloidal particles)	(7)
$4\text{Fe}_3\text{O}_4 + \text{O}_2 + 18\text{H}_2\text{O}$	$\longrightarrow$	$12\text{Fe}(\text{OH})_3$	(8)
$\text{A} + \text{B}$	$\longrightarrow$	$\text{c}$	(10)
$\text{R} = -\text{d}[\text{A}]/\text{dt} = -\text{d}[\text{B}]/\text{dt} = \text{d}[\text{A}]/\text{dt}$			(11)
$\text{R} = \text{K}[\text{A}]$			(12)

	<b>Table of Contents</b>	xxii
<b>Chapter 1</b>		1
<b>1</b>	Introduction	1
<b>1.1</b>	Chemotherapy	1
<b>1.2</b>	Neo adjuvant chemotherapy (Pre operative treatment)	1
<b>1.3</b>	Adjuvant chemotherapy	1
<b>1.4</b>	Palliative chemotherapy	2
<b>1.5</b>	Radiotherapy	2
<b>1.5.1</b>	Mechanism of Action of Radiation Therapy	4
<b>1.5.2</b>	Dose	5
<b>1.6</b>	Cancer Surgery	6
<b>1.6.1</b>	Cancer Prevention	6
<b>1.6.2</b>	Diagnosis	6
<b>1.6.3</b>	Cancer stage determination	6
<b>1.6.4</b>	Primary Treatment	7
<b>1.6.5</b>	Debulking	7
<b>1.6.6</b>	Relieving Symptoms	7
<b>1.6.7</b>	Combination therapies	7
<b>1.7</b>	Other Techniques Used in Cancer Surgery	7
<b>1.7.1</b>	Cryosurgery	8
<b>1.7.2</b>	Electrosurgery	8
<b>1.7.3</b>	Laser Surgery	8
<b>1.7.4</b>	Mohs' Surgery	8
<b>1.7.5</b>	Laparoscopic Surgery	9
<b>1.7.6</b>	Robotic Surgery	9
<b>1.7.7</b>	Natural Orifice Surgery	9
<b>1.7.8</b>	Stereotactic Surgery	10
<b>1.7.9</b>	Electromagnetic Navigation Bronchoscopy (ENB)	10
<b>1.8</b>	Photodynamic therapy (PDT)	10
<b>1.8.1</b>	What is Photodynamic Therapy?	11
<b>1.8.2</b>	How is PDT used to treat Cancer	12
<b>1.8.2.1</b>	General properties of a photodynamic tumor sensitizer	14
<b>1.8.2.2</b>	Selectivity of PDT Action on The Tumor Tissue	16
<b>1.9</b>	What types of cancer are currently treated with PDT?	17
<b>1.9.1</b>	What are the limitations of PDT?	18
<b>1.9.2</b>	Does PDT have any complications or side effects?	18
<b>1.9.3</b>	What does the future hold for PDT?	19
<b>1.9.4</b>	Identification of Tumor Tissues	21
<b>1.9.5</b>	Summary of Mechanism of Action of a Photosensitizer	24
<b>1.9.6</b>	PDT Photosensitisers	24
<b>1.9.6.1</b>	Development of Photosensitisers	25
<b>1.9.6.2</b>	Porphyrins	26
<b>1.9.6.2.1</b>	Criteria for a good Photosensitiser	27
<b>1.9.6.2.2</b>	Phthalocyanines	28
<b>1.9.6.3</b>	Drug Development in PDT	29

<b>1.10</b>	Improvements for PDT	31
<b>1.10.1</b>	Combination Treatments	31
<b>1.10.2</b>	Improvement of Equipment for Delivery of the Activating Light	31
<b>1.10.3</b>	Interstitial therapies	32
<b>1.10.4</b>	Limitations of PDT	32
<b>1.10.5</b>	Complications and/or Side Effects of PDT	32
<b>1.10.6</b>	Challenges	33
<b>1.10.7</b>	How PDT Works	34
<b>1.11</b>	Light Sources <sup>40c</sup>	34
<b>1.11.1</b>	Argon Laser	35
<b>1.11.2</b>	Prototype	35
<b>1.11.3</b>	Some Laser Systems Used in PDT	36
<b>1.11.3.1</b>	Highly Reflecting Balloon Light Distributors	36
<b>1.11.3.2</b>	Frontal Light Distributors	37
<b>1.11.3.3</b>	Distributor With Cylindrical Light Output	37
<b>1.12</b>	Current Perspectives in Drug Development	37
<b>1.12.1</b>	Texaphyrins	38
<b>1.12.1.1</b>	Gadolinium Texaphyrin (Gd-Tex) <sup>48</sup>	40
<b>1.12.1.2</b>	Lutetium Texaphyrin (Lu-Tex)	41
<b>1.12.2</b>	5-Aminolevulinic acid	42
<b>1.12.2.1</b>	5-ALA Induced Production of Protoporphyrin IX (PPIX)	44
<b>1.12.3</b>	Biosynthesis of Protoporphyrin IX (PPIX)	46
<b>1.12.4</b>	Verteporfin (BPD-Benzoporphyrin Derivatives)	48
<b>1.12.4.1</b>	Mild Sensation	48
<b>1.12.4.2</b>	Sensitivity to light	49
<b>1.13</b>	Boronated neutron therapy	49
<b>1.14</b>	Drugs in Clinical Trials	52
<b>1.14.1</b>	Xcytrin <sup>(R)</sup>	52
<b>1.14.2</b>	Lutrin <sup>(R)</sup>	53
<b>1.14.3</b>	Antrin <sup>(R)</sup>	55
<b>1.14.4</b>	Verteporfin	56
<b>1.14.5</b>	Temopofin	59
<b>1.14.6</b>	Boron Neutron Capture Therapy (BNCT)	60
<b>1.14.7</b>	Third-generation boron delivery agents	61
<b>1.14.8</b>	Amino Levulinic Acid (ALA)	61
<b>1.14.8.1</b>	Pharmacology of ALA	62
<b>1.14.8.2</b>	Adverse Effects of ALA	62
<b>1.15</b>	Estimated New Cancer Cases <sup>78-81</sup>	63
<b>1.16</b>	Photosensitiser Amphilocity in PDT	64
<b>1.16.1</b>	Pharmacokinetics	64
<b>1.16.1.1</b>	Blood and or Plasma Transport	65
<b>1.16.1.2</b>	Excretion and Elimination	65
<b>1.16.2</b>	Activity Determinant	66
<b>1.16.2.1</b>	Tumor Tissue Accumulation	66
<b>1.16.2.2</b>	Singlet Oxygen Quantum Yields	66
<b>1.17</b>	Future Perspectives	66

1.17.1	New Photosensitisers	66
1.17.2	Third Generation Sensitizers	67
1.17.3	Selectivity	67
1.17.4	Photobleaching and General Photosensitivity	68
1.17.5	Mechanisms of Cell Killing	68
1.18	Structure and numbering of the Porphyrin	69
1.18.1	Complexes of porphyrins and related molecules	70
1.18.2	<i>Meso</i> steric interactions	72
1.18.3	<i>Beta</i> steric interactions	72
1.19	Rothemund type Synthesis of porphyrins	72
1.19.1	Nomenclature of porphyrins	73
1.19.2	Properties of porphyrins	74
1.19.2.1	Electronic structure and UV-Visible spectra	76
1.19.2.2	Bathchromic Electronic Spectral Shifts	77
<b>Chapter 2</b>		79
2.1	Problem Statement	79
2.2	Aim And Objectives Of The Research	79
2.2.1	Aim	79
2.2.2	Objectives	80
<b>Chapter 3</b>		82
3.1	Literature Review	82
3.2	Porphyrins	83
3.2.1	Effects of Aldehyde or Dipyrromethane Substituents on the Course of Reactions Leading to <i>meso</i> -substituted Porphyrins	93
3.2.1.1	Reactions of Aldehydes	93
3.2.1.2	Reactions of Dipyrromethanes	94
3.2.2	<i>Meso</i> -substituted Dipyrromethane Formation	98
3.3	Nanoparticles	101
3.3.1	Overview of magnetic nanoparticles (MNPs)	101
3.3.2	Immobilization of special molecules on the surface of nanoparticles	106
3.3.3	Magnetic nanoparticles (MNPs) in biomedical applications	107
3.3.4	Superparamagnetic Iron Oxide Nanoparticles (SPION)	107
3.3.5	Synthesis of magnetic iron oxide nanoparticles	108
3.3.6	Surface modifications of magnetic nanoparticles for biomedical applications and their effect on stability and magnetization	112
3.3.7	Surface modification with non-polymeric organic stabilizers	114
3.3.8	Surface modification with polymeric organic stabilizers	115
3.3.9	Surface modification with inorganic materials	115
3.3.10	Surface modifications with targeting ligands	116



3.3.11	Magnetic properties of iron oxide nanoparticles	117
3.3.12	Biomedical Applications Of Magnetic Nanoparticles	119
3.3.12.1	Cellular labelling/cell separation	119
3.3.12.2	Tissue repair	120
3.3.12.3	Drug delivery	121
3.3.12.4	Magnetic resonance imaging (MRI)	122
3.3.12.5	Hyperthermia	123
3.3.12.6	Magnetofection	124
3.4	Tailoring Magnetic Nanoparticles (MNPs)	125
3.4.1	Essential requisites	126
3.4.2	Coatings on magnetic nanoparticles	127
3.4.3	The fate of nanoparticles after administration into the body	129
3.4.4	The toxicity of Nanoparticles	130
<b>Chapter 4</b>		131
4.1	Methodology And Experimental	131
4.2	Materials	131
4.3	Materials for nanoparticle synthesis	132
4.4	NMR Analysis	132
4.5	Flash column chromatography	132
4.6	Optical Analyses	132
4.6.1	UV Analysis	132
4.6.2	Infra-red analysis	133
4.7	TEM and HRTEM	133
4.8	Magnetization studies	133
4.9	Synthesis of Thiolated Porphyrin	134
4.10	Synthesis of 3-(3-Formylphenoxy)propyl bromide (83)	135
4.11	Synthesis of 3-(3-formylphenoxy)propyl thioacetate (84)	135
4.12	Synthesis of 3-(3-formylphenoxy)propyl thioacetate (85)	136
4.13	Attempted hydrolysis of Compound 85 to Compound 86	137
4.13.1	Attempted Acid Hydrolysis	137
4.13.2	Attempted Base Hydrolysis	138
4.13.3	The mechanism of Hydrolysis of compound 85 to 86	139
4.14	Preparation of Iron Oxide-Gold, Core-Shell nanoparticle	139
4.14.1	Introduction	139
4.14.2	Gold coating	140
4.14.3	Synthesis of the superparamagnetic iron oxide (SPION) <sup>116</sup>	140
4.14.4	The gold coating process was as follows <sup>116</sup> :	141
4.15	Immobilization of the Porphyrin macromolecule onto the Iron Oxide-Gold, Core-Shell Surface.	141
4.15.1	Introduction	141

4.15.2	Procedure	142
<b>Chapter 5</b>		
5.1	Introduction	143
5.1.1	3-Hydroxybenzaldehyde	143
5.1.2	3-(3-Formylphenoxy)propyl bromide	144
5.1.3	3-(3-Formylphenoxy)propyl thioacetate	146
5.1.4	5,10,15,20-Tetrakis[3-(3-thioacetoxypoxy)phenyl]porphyrin	148
5.1.5	Compound 5 NMR	150
5.2	Kinetic Studies of the Immobilization of Porphyrin unto the Magnetic Seeds Using UV-Visible Spectrophotometer to Monitor the Reaction	150
5.2.1	Kinetic Studies	150
5.2.2	Obtaining data for standard curve for nanoparticles.	151
5.2.3	Data for the standard curve for nanoparticles taken at 526nm in the porphyrin/nanoparticle mixture	152
5.2.4	Rate of transfer of nanoparticles from aqueous phase to organic porphyrin phase	153
5.2.5	Rate order of the reaction	156
5.3	Optical Analyses	157
5.3.1	UV-Visible	157
5.3.2	Infra-red Analysis	159
5.4	TEM and HRTEM Micrographs	163
5.5	Atomic force microscopy (ATM), X-ray microscopy (XRD) and SQUID magnetometry	165
5.5.1	Atomic force microscopy	166
5.5.2	X-Ray diffraction measurements	166
5.5.3	Magnetic measurements of the gold coated & functionalised nanoparticles (SQUID magnetometer)	167
<b>Chapter 6</b>		
6.1	Discussion and Conclusion	172
6.2	NMR Results	172
6.3	Optical Analyses	172
6.3.1	UV-Visible	172
6.3.2	Infrared Analysis	173
6.4	Kinetic Studies	173
6.4.1	Discussion on Kinetic Studies	173
6.5	Characterization	174
6.5.1	TEM and HRTEM	174
6.5.2	Magnetic measurements of the gold coated & functionalised nanoparticles	175
6.5.3	Conclusion	175
6.5.4	Recommendations	176

<b>Chapter 7</b>	References	177
<b>Appendix</b>		

## CONTRIBUTIONS TO KNOWLEDGE

### Conferences

1. South African Chemical Institute (SACI) Young Chemist's Symposium 2008 Gauteng Region (sponsored by Royal Society of Chemistry, RSA (Northern Section) and the School of Chemistry, Wits University)

**Date:** Friday 10<sup>th</sup> October 2008

**Paper Presented:** Synthesis and Characterization of Coated and Uncoated Magnetic Nanoparticles.

2. Nanosciences Young Researchers Symposium (NYRS), Gauteng Province

**Date:** Friday 7<sup>th</sup> May 2010

**Venue:** University of Johannesburg, John Orr Building, Room 2212.

**Paper Presented:** Structural Elucidation and Evaluation of Porphyrin Coated Magnetic Iron Oxide-Gold, Core-Shell Nanoparticles.

3. Frank Warreen 2010 Conference, University of Kwazulu-Natal, Pietermaritzburg Campus, UKZN.

**Date:** Sunday 17<sup>th</sup> January – Thursday 21<sup>st</sup> January 2010

**Venue:** Pietermaritzburg Campus Kwazulu-Natal, South Africa

**Poster Presented:** Synthesis, Characterisation and Evaluation of Porphyrin Coated Magnetic Iron Oxide-Gold core Shell Nanoparticles.

4. Walter Sisulu University International Research Conference 2010

**Date:** Wednesday 18<sup>th</sup> – Friday 20<sup>th</sup> August 2010

**Paper Presented:** Synthesis and Characterization of Porphyrins with Thiolated Side chains for Functionalization of Paramagnetic Iron Oxide- Gold, Core-Shell Nanoparticles.

**Research papers in peer reviewed journals.**

4 Journal of Magnetism and Magnetic Materials.

**Paper submitted on the 1st September 2010:** Synthesis and Characterization of Porphyrin Functionalized Iron Oxide-Gold Core-Shell Nanoparticles. Ref. No.: MAGMA-D-11-01048.

**Status:** under review.

## **Chapter 1**

### **1 Introduction**

Existence of cases of cancers abound all over the world and scientists and researchers continue to search for ways to provide remedies for sufferers. Cancer otherwise known as malignant neoplasm is a class of disease in which cells display uncontrolled growth (beyond normal limits). It can be treated in many ways depending on the stage of the disease. Among the various methods employed in the treatment of cancers are:

- Chemotherapy (use of drugs or medications to destroy cancer cells)
- Radiotherapy (use of ionizing radiation to kill cancer cells) and
- Surgery (removal of cancer cells)

#### **1.1 Chemotherapy**

There are three types or modes of chemotherapy treatments. These include: neo adjuvant chemotherapy, adjuvant chemotherapy and palliative chemotherapy.

#### **1.2 Neo adjuvant chemotherapy (Pre operative treatment)**

Neo adjuvant chemotherapy is the initial chemotherapy designed to shrink the primary tumor by rendering local therapy. It is less destructive and more effective than surgery and/or radiotherapy.

#### **1.3 Adjuvant chemotherapy**

Adjuvant chemotherapy is used when there is little evidence of cancer present, but there is risk of recurrence. It can help reduce the chances of developing resistance if the tumor does develop. It is also useful in killing any cancerous cells which have spread to other parts of the body.

## **1.4 Palliative chemotherapy**

Palliative chemotherapy is given without curative intent (intention to cure) but simply to decrease tumor load and increase life expectancy. All chemotherapy regimens (modes of treatment) require that the patient be capable of undergoing the treatment. Performance status is often used as a measure to determine whether a patient can receive chemotherapy or whether dose reduction is required since only a fraction of the cells in a tumor die with each treatment. Repeated doses must be administered to continue to reduce the size of the tumor.

## **1.5 Radiotherapy**

Radiotherapy, also known as radiation therapy, is the treatment of cancer and other diseases with ionizing radiation. Ionizing radiation deposits energy that injures or destroys cells in the area being treated (the “target tissue”) by damaging their genetic material, making it impossible for these cells to continue to grow. Although radiation damages both cancer cells and normal cells, the latter are able to undergo repair and function properly. Radiotherapy may be used to treat localized tumors, such as cancers of the skin, tongue, larynx, breast or uterine cervix. It can also be used to treat leukemia and lymphoma .

The type of radiation therapy commonly used involves photons or “packets” of energy. X-rays were the first form of photon radiation to be used to treat cancer. Depending on the amount of energy they possess, X-rays can be used to destroy cancer cells on the surface of or deeper in the body. The higher the energy of the X-rays beam, the deeper the X-rays can go into the target tissue. Linear accelerators and betatrons are machines that produce X-rays of increasingly greater energy. The use of machines to focus radiation (such as X-rays) on a cancer site is called external beam radiotherapy (EBR).

Gamma rays are another form of photons used in radiotherapy. Gamma rays are produced spontaneously when certain elements (such as radium, uranium and cobalt 60) release radiation as they undergo nuclear decomposition or decay. Each element decays at a specific rate and gives off energy in the form of gamma rays and other particles. X-rays and gamma rays have the same effect on cancer cells.

Another technique of delivering radiation to cancer cells is to place radioactive implants directly in a tumor or body cavity. This is called internal radiotherapy. Brachytherapy, interstitial irradiation, and intracavitary irradiation are types of internal radiotherapy. In this type of treatment, the radiation dose is concentrated in a small area, and the patient stays in the hospital for a few days. Internal radiotherapy is frequently used for cancers of the tongue, uterus and cervix. Several new approaches to radiation therapy are now being evaluated to determine their effectiveness in treating cancer. One such technique is intraoperative irradiation, in which a large dose of external radiation is directed at the tumor and surrounding tissue during surgery.

Another investigational approach is particle beam radiation therapy. This type of therapy differs from photon radiotherapy in that it involves the use of fast-moving subatomic particles to treat localized cancers. A very sophisticated machine is needed to produce and accelerate the particles required for this procedure. Some particles (neutrons, protons and heavy ions) deposit more energy along the path they take through tissue than do X-rays or gamma rays, thus causing more damage to the cells they hit. This type of radiation is often referred to as high linear energy transfer (high LET) radiation.

Scientists are also looking for ways to increase the effectiveness of radiation therapy. Two types of investigational drugs are being studied for their effect on cells undergoing radiation therapy. Radiosensitizers which make the tumor cells more likely to be damaged, and radioprotectors which protect normal tissues from the effect of radiation. Hyperthermia, the use



of heat, is also being studied for its effectiveness in sensitizing tissue to radiation.

Other recent radiotherapy research has focused on the use of radio labeled antibodies to deliver doses of radiation directly to the cancer site (radio immunotherapy). Antibodies are highly specific proteins that are made by the body in response to the presence of antigens (substances recognized as foreign by the immune system). Some tumor cells contain specific antigens that trigger the production of tumor-specific antibodies. Large quantities of these antibodies can be made in the laboratory and attached to radioactive substances (a process known as radio labeling). Once injected into the body, the antibodies actively seek out the cancer cells, which are destroyed by the cell-killing (cytotoxic) action of the radiation. This approach can minimize the risk of radiation damage to healthy cells. The success of this technique will depend on both the identification of appropriate radioactive substances and determination of the safe and effective dose of radiation that can be delivered in this way. Radiation therapy may be used alone or in combination with chemotherapy or surgery. Like other forms of cancer therapy, radiation therapy can have side effects. Possible side effects of treatment with radiation include temporary or permanent loss of hair in the area being treated, skin irritation, temporary change in skin colour in the treated area, and tiredness. Other side effects are largely dependent on the area of the body that is treated.

### **1.5.1 Mechanism of Action of Radiation Therapy**

Radiation therapy works by damaging the deoxyribonucleic acid (DNA) in the cells.<sup>1</sup> The damage is caused by a photon, electron, neutron, or ion beam directly or indirectly ionizing the atoms which make up the DNA chain. Indirect ionization happens as a result of the ionization of water, forming free radicals, notably, hydroxyl radicals, which then damage the DNA. In the most common forms of radiation therapy, most of the radiation effect is through free radicals. Because cells have mechanisms for repairing DNA damage, breaking the DNA on both strands proves to be the

most significant technique in modifying cell characteristics. Because cancer cells generally are undifferentiated and stem cell-like, they reproduce more, and have a diminished ability to repair sub-lethal damage compared to most healthy differentiated cells. The DNA damage is inherited through cell division, accumulating damage to the cancer cells, causing them to die or reproduce more slowly.

One of the major limitations of the radiotherapy is that the cells of solid tumors become deficient in oxygen. Solid tumors can outgrow their blood supply, causing a low-oxygen state known as hypoxia. Oxygen is a potent radio-sensitizer. It increases the effectiveness of a given dose of radiation by forming DNA-damaging free radicals. Tumor cells in a hypoxic environment may be as much as 2 to 3 times more resistant to radiation damage than those in a normal oxygen environment.<sup>2</sup> Much research has been devoted to overcome this problem. This includes the use of high pressure oxygen tanks, blood substitutes that carry increased oxygen, hypoxic cell radio-sensitizers such as misonidazole and metronidazole, and hypoxic cytotoxins, such as tirapazamine.<sup>2</sup>

### **1.5.2 Dose**

The amount of radiation used in radiation therapy is measured in grays (Gy), and varies depending on the type and stage of cancer being treated.<sup>2</sup> One gray (Gy) is the international system of units (SI) equivalent of 100 rads, which is equal to an absorbed dose of 1 Joule / kilogram. An absorbed dose of 0.01 Gy means that 1 gram of material absorbed 100 ergs of energy (a small but measurable amount) as a result of exposure to radiation. For curative purposes, the typical dose for a solid epithelial tumor ranges from 60 to 80 Gy, while lymphomas are treated with 20 to 40 Gy.<sup>2</sup>

Delivery parameters of a prescribed dose are determined during treatment planning. Treatment planning is generally performed on dedicated computers using specialized treatment planning software. Depending on

the radiation delivery method, several angles or sources may be used to sum up the total necessary dose.<sup>2</sup>

## **1.6 Cancer Surgery**

Cancer Surgery is an operation to repair or remove part of the body in order to diagnose or treat cancer so that the symptoms it causes are relieved. Cancer surgery may be used to achieve one or more goals<sup>3</sup> including cancer prevention, diagnosis, cancer stage determination, primary treatment, debulking, relieving symptoms, combination therapy and others.

### **1.6.1 Cancer Prevention**

If there is reason to believe that a patient will develop cancer in certain tissues or organs, a doctor may recommend removing the tissues or organs before the cancer develops. For example if a patient presents with a genetic condition called familial polyposis, a doctor may recommend cancer surgery to remove the colon and rectum because the patient has a high risk of developing colon cancer.<sup>3</sup>

### **1.6.2 Diagnosis**

A doctor may use a form of cancer surgery to remove all or part of a tumor – allowing the tumor to be studied under a microscope – to determine whether the growth is cancerous (malignant) or noncancerous (benign).

### **1.6.3 Cancer stage determination**

Cancer surgery helps the doctor to define how advanced a cancer is - (its stage). It also allows the doctor to evaluate the size of tumor and determine whether it has spread to the lymph nodes.

#### **1.6.4 Primary Treatment**

For many tumors, cancer surgery is the best chance for a cure, especially if the cancer is localized and hasn't spread. If there is evidence that the cancer has not spread, the oncologist may recommend surgery to remove the cancerous tumor as a primary treatment.

#### **1.6.5 Debulking**

When it is not possible to remove all of a cancerous tumor – for example, because doing so may severely harm an organ – the surgeon may remove as much as possible (debulking) in order to make chemotherapy or radiation therapy more effective.

#### **1.6.6 Relieving Symptoms**

Sometimes surgery is used to improve quality of life rather than to treat the cancer itself – for example, to relieve pain caused by a tumor that is pressing on a nerve or bone or to remove a tumor that is obstructing the intestine.

#### **1.6.7 Combination therapies**

Surgery is often combined with other cancer techniques, such as chemotherapy and radiation.

### **1.7 Other Techniques Used in Cancer Surgery**

Many other types of surgical methods for treating cancer and precancerous conditions exist, and investigators continue to research new methods. Other common types of cancer surgery include cryosurgery, electrosurgery, laser surgery, Mohr's surgery, laparoscopic surgery, robotic surgery, natural orifice surgery, stereostatic surgery, electromagnetic and navigation bronchoscopy<sup>4</sup>

### **1.7.1 Cryosurgery**

During this type of surgery, the doctor uses very cold material, such as liquid nitrogen spray or a cold probe to freeze and destroy cancer cells or cells that may become cancerous, such as irregular cells in a woman's cervix that could become cervical cancer.<sup>5</sup>

### **1.7.2 Electrosurgery**

By applying high-frequency electrical currents, a doctor can kill cancer cells for example in the mouth or on the skin.

### **1.7.3 Laser Surgery**

Laser Surgery is used to treat many types of cancers. It uses beams of high intensity light to shrink or vaporize cancer cells. In some cases, the heat of the laser accomplishes this. Laser surgery may be used to excise all or some of the cancerous tumor. In other cases, the laser is used to activate a previously administered chemical that cancer cells absorb. When such a chemical is stimulated by light, the chemical kills the cancer cells. This technique is known as photodynamic therapy (PDT).<sup>5</sup>

### **1.7.4 Mohs' Surgery**

Mohs' Surgery is useful for removing cancer from sensitive areas of the skin, such as near the eye, and for assessing how deep a cancer is. This method of surgery involves carefully removing cancer layer by layer with a scalpel. After removing a layer, the doctor evaluates the cancer under a microscope. This process will be repeated until all the abnormal cells have been removed and the surrounding tissue shows no evidence of cancer.<sup>5</sup>

### **1.7.5 Laparoscopic Surgery**

A surgeon uses a laparoscope to see inside a body without making large incisions. Instead, several small incisions are made and a tiny camera and surgical tools are inserted into the body. The surgeon watches a monitor that projects what the camera sees inside the body. The smaller incisions mean faster recovery and a reduced risk of complications. Laparoscopic surgery is used in cancer diagnosis, staging, treatment and symptom relief.

### **1.7.6 Robotic Surgery**

In robotic surgery, the surgeon sits away from the operating table and watches a screen that projects a 3-D image of the area being operated on. The surgeon uses hand controls that tell a robot how to maneuver surgical tools to perform the operation. Robotic surgery helps the surgeon operate in hard-to reach areas. But robotic surgical systems are expensive and require specialized training, so robotic surgery is usually available only in specialized medical centers.<sup>5</sup>

### **1.7.7 Natural Orifice Surgery**

Natural orifice surgery is currently being studied as a way to operate on organs in the abdomen without cutting through the skin. Instead, the surgeon passes the surgical tools through a natural orifice, such as the mouth, rectum or vagina. As an example, a surgeon might pass surgical tools down the throat into the stomach during natural orifice surgery. A small incision is made in the wall of the stomach and surgical tools pass into the abdominal cavity in order to take a sample of liver tissue or remove the gallbladder. Natural orifice surgery is experimental, and few operations have been performed this way. Doctors hope it can reduce the risk of infection, pain and other complications.<sup>5</sup>

### **1.7.8 Stereotactic Surgery**

The procedure allows surgeon to locate, map and remove tumors that are otherwise difficult to reach using computer-assisted surgical tools and magnetic resonance imaging (MRI) or computerized tomography (CT) imaging technology. The technique can also be used in radiation to deliver high dosages to very precise location of cancer cells.<sup>6</sup>

### **1.7.9 Electromagnetic Navigation Bronchoscopy (ENB)**

In traditional bronchoscopy, doctors insert a bronchoscope, or long thin, fiber optic camera, through the nose or mouth into the deepest tissue of the lungs for diagnosis. However ENB uses imaging to guide the bronchoscope and creates a 3D image of lesions in the areas of the lungs that are otherwise inaccessible. This allows a much higher rate of accuracy in diagnosing cancer without the risk of complications common to other kinds of tests.<sup>6</sup>

As with any surgery, cancer surgery carries risks which include: pain, infections as the site of surgery may become infected, loss of organ function. In order to remove a cancer the surgeon may need to remove an entire organ, bleeding; all operations carry a risk of bleeding, blood clots; while recovering from surgery, the patient may be at an increased risk of developing a blood clot, and altered functioning of internal organs.

## **1.8 Photodynamic therapy (PDT)**

All of the above mentioned methods or procedures suffer one disadvantage or the other in that they are not only complex but costly. The development of photodynamic therapy (PDT) in which porphyrins, phthalocyanines and related macrocyclic compounds, play a major role as photosensitizer agents has arguably ameliorated a large number of these risks.

Porphyrins are among the most widely used PDT drugs<sup>5</sup> and this is the area in which this research focuses. Our aim is to produce a potential PDT drug and immobilize it on iron oxide-gold, core-shell nanoparticles. The iron oxide-gold core-shell nanoparticles will serve as the carrier and delivery system to transmit the drug to the cancer sites.

In literature,<sup>7,8</sup> photodynamic therapy was commended as the most suitable method for cancer therapy in the developing world. PDT has been described to have the advantages of being:

- Cost effective and simple to use
- No special training is required for nurses
- No post treatment course in the intensive care unit is needed
- No engineer or computerized dosimetry computations is required
- No additional costs for isotope re-treatment as in radiotherapy and
- No blood transfusions, or sophisticated operating theaters is needed as in surgery.

### **1.8.1 What is Photodynamic Therapy?**

Photodynamic therapy is defined as the combined effect of a photosensitizing agent and suitable light to produce biological damage of a therapeutic value under conditions where either the drug or the light operating alone have no effect<sup>9</sup>. It is a treatment that uses a drug, called photosensitiser or photosensitizing agent, and a particular type of light to treat cancers. When the photosensitisers are exposed to a specific wavelength of light, they produce a form of oxygen radicals that kills nearby cells.<sup>7-9</sup> The photosensitiser is activated by light of a specific wavelength.<sup>7,8</sup> This wavelength determines how far the light can travel into the body<sup>7,9</sup> thus, doctors use specific photosensitisers and wavelengths of light to treat different areas of the body with PDT.



Photodynamic therapy (PDT), matured as a feasible medical technology in the 1980s at several institutions throughout the world. It is a third-level treatment for cancer involving three key components: a photosensitizer, light, and tissue oxygen. It is also being investigated for treatment of psoriasis and acne, and is an approved treatment for wet macular degeneration. The German physician Friedrich Meyer-Betz performed the first study with what was first called photoradiation therapy (PRT) with porphyrins in humans in 1913. Meyer- Betz tested the effects of haematoporphyrin-PRT on his own skin.<sup>7</sup>

Thomas Dougherty of Roswell Park Cancer-Center, among others, became a highly visible advocate and educator on PDT. Early patients were treated at Roswell, Los Angeles Children's Hospital, Los Angeles County Hospital, and other clinics and Hospitals in the USA and overseas.<sup>8</sup> It was John Toth, in early 1980s, as product manager for Cooper Medical Devices Corp/Cooper Lasersonics, who acknowledged the "photodynamic chemical effect" of the therapy with early clinical argon dye laser and wrote the first "white paper" renaming the therapy as "Photodynamic Therapy" (PDT).<sup>8</sup>

### **1.8.2 How is PDT used to treat Cancer**

In the first step, a photosensitizing agent is injected into the blood stream. The agent is absorbed by cells all over the body, but stays in cancer cells longer than it does in normal cells. Approximately 24 to 72 hours after injection,<sup>9</sup> when most of the agent has left the normal cells but still remained in cancer cells, the tumor is exposed to suitable light. The photosensitizer in the tumor absorbs the light and produces an active form of oxygen radicals that destroys nearby cancer cells.<sup>7-9</sup> In addition to directly killing the cancer cells, PDT appears to shrink or destroy tumor in two other ways by damaging the blood vessels in the tumor thereby preventing the cancer cells from receiving necessary nutrients and may also activate the immune system to attack the tumor cells.

The light used for PDT can come from a laser or other sources of light.<sup>8-10</sup> Laser light can be directed through fibre optic cables (thin fibres that transmit light) to deliver light to areas inside the body.<sup>5</sup> For example, a fibre optic cable can be inserted through an endoscope (a thin, lighted tube used to look at tissues inside the body) into the lungs or oesophagus to treat cancer in these organs. Other light sources include light-emitting diodes (LEDs), which may be used for surface tumors, such as skin cancer.<sup>9</sup> PDT is usually performed as an out-patient procedure. It may be repeated and or may be used together with other therapies, such as surgery, radiation, or chemotherapy depending on the type and nature of the cancer.<sup>10</sup>

<b>Table 1:</b>	<b>Main features of an efficient photodynamic agent for tumor treatment (Property related structural and biological features)<sup>9</sup></b>
Physicochemical	High chemical purity purification may be especially labourious in the presence of two or more peripheral substituents and/or chiral centers. Large molar extinction in the red. Extensive conjugation of $\pi$ electrons along the region macrocycle. Low tendency to aggregation in the presence of electrically charged peripheral aqueous milieu substituents or bulky axial ligands to the central metal ion.
Photophysical	Long triplet lifetime Extensive monomerization (favoured by distribution in polar regions of membranous systems). High yield of $^1\text{O}_2$ generation and/ Easy accessibility by molecular oxygen or close or electron transfer to substrate proximity to substrates with suitable redox potential.
Pharmacological	Efficient and selective targeting Hydrophobic or amphiphilic properties; association with suitable delivery systems of the tumor tissue. Fast clearance from serum and High affinity for serum proteins responsible for healthy tissues transport of dyes from peripheral tissues to liver. Low systemic toxicity Lethal dose (LD-50) higher than $\sim 300\text{mg Kg}^{-1}$ body weight.
Phototherapeutic	Efficient and preferential killing of malignant cells peritumoural tissues and/or fast healing of any large concentration difference between tumor/photodamaged healthy tissue. Lack of side effects, minimal accumulation in skin to avoid cutaneous photosensitivity. Lack of mutagenic potential, no photoeffect on DNA

### **1.8.2.1 General properties of a photodynamic tumor sensitizer**

Some properties which have been identified as typical of an efficient photodynamic tumor sensitizer are listed in Table 1.<sup>11</sup> Such properties can be operationally subdivided into physico – chemical, photophysical, pharmacological and phototherapeutic. It is obvious from Table 1 that the success of a PDT treatment requires an optimal interplay among a number of several different parameters and none of the presently available tumor photosensitizers meets all requirements to a satisfactory extent. However, porphyrins and their analogs (chlorins, phthalocyanines, naphthalocyanines, porphycenes) are endowed with two favourable features.

The first is the possibility to modify the chemical structure at different positions and with various levels of complexity, including the size of the macrocycle and the extension of the aromatic electron cloud, the coordination of metal ions with four central nitrogen atoms, and the nature of the peripheral substituents and/or axial ligands. This allows a remarkable flexibility in the design of the photosensitizing agent, so that different levels of hydro-lipophilicity, tendency to undergo aggregation, subtissular or subcellular distribution, spectroscopic and photophysical properties can be imparted to the photosensitizer molecule.

The insertion of two polar substituents (e.g. carboxylate, sulphonate or hydroxyl groups) on two adjacent rings of the macrocycle and the consequent presence of a hydrophobic matrix on the opposite side of the molecule (two unsubstituted rings) makes the photosensitizer an amphiphilic species; in this way, the porphyrin achieves sufficient water-solubility, to allow its systemic injection in vivo, while it retains a high tendency to cross the lipid barrier of the cytoplasmic membrane of tumor cells and localize at endocellular sites. In the case of deeply hydrophobic porphyrins, such as those having one or no polar substituents, systemic injection into the bloodstream is possible, provided the photosensitizers are pre-incorporated into suitable delivery systems. At the same time, the

presence of electrically charged functional groups protruding from the pyrrole rings or bulky axial ligands perpendicular to the plane of the porphyrin molecule generates electrostatic repulsion and steric hindrance. This prevents the formation of aggregates, which would drastically inhibit the photosensitizing activity of the porphyrin macrocycle.<sup>11</sup>

The second is the presence of absorption bands in the 600-850 nm wavelength region, which corresponds with maximal light penetration into mammalian tissues. For lightly pigmented tumors the transmission of incident light increases up to about 700 nm, while in the presence of an extensive pigmentation (such as in melanotic melanoma) some tissue transparency is observed only at wavelengths longer than 700 nm. As a consequence, pigmented melanoma is insensitive to PDT with a photosensitizing agent like photofrin and undergoes an important photodamage only in the presence of naphthalocyanines which display an intense absorbance (molar absorptivity about  $500\,000\text{ M}^{-1}\text{cm}^{-1}$ ) at 780 nm.<sup>11</sup>

In general, the use of photosensitizers with a high extinction coefficient offers the possibility to inject smaller drug doses. This gives further advantage over a photosensitizer like photofrin and other haematoporphyrin-related porphyrins which exhibit a weak absorbance above 600 nm as shown in Table 2.

Table 2: Photosensitizers presently used in clinical trials for PDT of tumors		$\lambda_{\text{max}}$ (nm)	$\epsilon(\text{M}^{-1}\text{s}^{-1})^{\text{a}}$ $\text{cm}^{-1}$ <sup>a</sup>
Photosensitizer	Remarks		
Photofrin	<i>contains mainly covalent Hp, Pp and HpD</i>	630	3 2000 <sup>b</sup>
Benzoporphyrin derivative	requires lipid-based delivery systems	690	43,000
Monoaspartyl-chlorin e <sub>6</sub>	fast clearance from tumor/skin	675	47 000
m-Tetrahydroxyphenyl-chlorin	in alkaline solution or water/DMSO mixtures	652	35 000
Sn(IV)-etioporphyrin	requires lipid-based delivery system	660	28 000
Zn(II)-phthalocyanine	requires lipid-based delivery system	675	243 000

Hp = haematoporphyrin; Pp = protoporphyrin; HVD = hydroxyethyl-vinyl-deuteroporphyrin. <sup>a</sup>Data for monomeric compounds, with the exception of Photofrin. <sup>b</sup>Approximate value due to inhomogeneity of the preparation and scarce reproducibility of monomer-oligomer equilibria.

### **1.8.2.2 Selectivity of PDT Action on The Tumor Tissue**

The essential goal of PDT is to induce an efficient photosensitized necrosis of the tumor mass while minimizing the damage of the peritumoural tissues.<sup>11</sup> The first criterion to assess the potential selectivity of PDT treatment is the ratio between the photosensitizer concentration in the tumor and the tissue from which the tumor originates or into which the tumor grows. The ratio is hardly predictable since the determinants of porphyrin uptake and clearance by tumors are poorly understood and it is likely that the overall process is the resultant of various properties typical of most neoplastic tissues, including the leaky vasculature, high cell proliferation rate, lower pH value, and inefficient lymphatic drainage.<sup>11</sup>

For a photosensitizing agent like Photofrin, reported ratios vary from 1-1.5 (skin tumors) to above 10 (brain tumors, as one would expect owing to the inability of porphyrin derivatives to cross the intact blood-brain barrier).<sup>11</sup> In general, the selectivity of tumor targeting is enhanced upon increasing the degree of hydrophobicity of the photosensitizer or by imparting amphiphilic properties to its molecule. In order to induce a more specific localization of the injected photosensitizer in the tumor tissue, one can take advantage of the intrinsic features of the malignant cells. While the potential of these approaches has not been fully exploited, encouraging results have been obtained in several cells and animal studies.<sup>11</sup> Hence further investigations along these directions are certainly warranted.

For relatively low-tumor/healthy tissue ratios of photosensitizer concentration, the selectivity of PDT action can still be achieved provided the peritumoural compartments are less responsive to red light-irradiation or heal more rapidly from photodamage as compared with tumor tissues. However no general prediction is possible at this stage of research in this field, since the photochemical behavior of a tissue is strictly dependent on its biochemical composition and physiological properties. For example, since photodynamic action occurs via photooxidative steps, the local

concentration of antioxidants plays a major role. However it must be emphasized that the main cellular constituents, such as proteins, saturated or unsaturated lipids, nucleic acids and carbohydrates display a very different susceptibility to photosensitized oxidation. A very interesting start in this direction was performed by Bown and coworkers who undertook a systematic study on the responsiveness of normal tissues, such as liver, pancreas or colon, to PDT.<sup>12,13</sup>

### **1.9 What types of cancer are currently treated with PDT?**

To date, the U.S. Food and Drug Administration (FDA) has approved the photosensitizing agent called Porfimer sodium, or Photofrin for use in PDT to treat or relieve the symptoms of bladder, oesophageal cancer and non-small cell lung cancer.<sup>14</sup> Porfimer sodium is approved to relieve symptoms of oesophageal cancer when the cancer obstructs the esophagus or when the cancer cannot be satisfactorily treated with laser therapy alone. Porfimer sodium is used to treat non-small cell lung cancer in patients for whom the usual treatments are not appropriate, and to relieve symptoms in patients with non-small cell lung cancer that obstructs the airways. In 2003, the FDA approved Porfimer sodium for the treatment of precancerous lesions in patients with Barrett's esophagus (a condition that can lead to esophageal adenocarcinoma).<sup>15</sup> The approval opens new challenge to both clinicians and basic investigators since time now seems ripe for a qualitative improvement of the technique along different guidelines, such as:

- Definition of PDT protocols which yield optimal results with specific tumor types (e.g. tumors at different anatomical sites, or having different thickness, histological features, degree of vascularization, etc.) and assessment of the potential of PDT to compete with existing therapies for the same tumors;

- Enhancement of the efficacy of PDT (e.g. increased selectivity of tumor targeting possibly through conjugation of the photosensitizer to tumor-specific delivery systems; intra-operatorial application of PDT for the sterilization of the tumor bed after surgical section); and
- Expansion of the scope of PDT to treat conditions other than malignancies, including atheromas, restenosis of arteries after angioplasty, psoriasis and sexually transmitted diseases, viral or microbial infections and blood banking.

### **1.9.1 What are the limitations of PDT?**

The light needed to activate most photosensitizers cannot pass through more than about one-third of an inch of tissue (1 centimeter). For this reason, PDT is usually used to treat tumors on or just under the skin or on the lining of internal organs or cavities<sup>7</sup>. As a consequence PDT is less effective in treating large tumours.<sup>7,10</sup> PDT is a local treatment and generally cannot be used to treat cancer that has spread (metastasized).<sup>10</sup>

### **1.9.2 Does PDT have any complications or side effects?**

Porfimer sodium makes the skin and the eyes sensitive to light for as long as 6 weeks after treatment.<sup>7,10</sup> Thus, patients are advised to avoid direct sunlight and bright indoor light for at least 6 weeks. Photosensitisers tend to build up in tumors and the activating light is focused on the tumor. As a result, damage to healthy tissue is minimal. However, PDT can cause burns, swelling, pain, and scarring in nearby healthy tissue.<sup>7</sup> Other side effects of PDT are related to the area that is treated. They can include coughing, trouble swallowing, stomach pain, painful breathing, or shortness of breath; these side effects are usually temporary.

### 1.9.3 What does the future hold for PDT?

Photodynamic therapy (PDT) has been defined as the combined effect of a photosensitizing drug and light to produce biological damage of therapeutic value, under conditions where either the light or the drug alone have no effect.<sup>16</sup> The approach has aroused considerable interest in scientific, medical and commercial circles in recent years, partly because it is not only conceptually very exciting, but also because there is no doubt that it works in destroying malignant or otherwise problematic tissue. The basis for PDT lies with two remarkable properties of the photosensitizing drugs that are used in the approach – their preferential accumulation in cancer tissue and the subsequent light triggered toxicity of the drugs.<sup>17</sup>

Cancer tissue destruction is achieved because the drug (photosensitizer) absorbs the energy of light and transfers it to molecular oxygen, generating singlet oxygen, a highly reactive species, which causes biological damage.<sup>18</sup> The extremely short lifetime of singlet oxygen within the biological environment means that the treatment is highly localized, without systemic side effects.<sup>19</sup> For this reason, PDT can be especially effective in disease sites close to vital organs, such as in cancers of the head, neck, and the brain.<sup>20</sup> PDT drugs belong to the unique family of macrocyclic porphyrin, and phthalocyanine type of compounds.<sup>21</sup>

Researchers continue to study ways to improve the effectiveness of PDT and expand it to other cancers. Clinical trials are under way to evaluate the use of PDT for cancers of the brain, skin, prostate, cervix, and peritoneal cavity. Other research is focused on the development of photosensitisers that are more powerful<sup>7</sup>, more specifically target cancer cells<sup>7,9</sup> and are activated by light that can penetrate tissue and treat deep or large tumours.<sup>7</sup> Researchers are also investigating ways to improve the equipment<sup>7</sup> used for the delivery of the activating light<sup>9</sup>.

What is PDT today used to be known as photoradiation which is the use of visible light or ultraviolet light in clinical medicine. The process may be



either direct, when light is used alone, or indirect, when light is used in conjunction with other substances such as a photosensitizer. Because it has been widely studied, various names for it have emerged: to some, it is known as photoradiation therapy (PRT)<sup>22-25</sup>. In this approach visible light is used in combination with light sensitive agents in an oxygen-rich environment. The source of the photons may be an ordinary tungsten lamp, an argon lamp or a laser. A tunable dye laser has the advantage that monochromatic light of a predetermined wavelength can be effectively channeled by way of a fibre optic device into a deeply located tumour.<sup>25</sup>

Photodynamic therapy involves selective uptake of the photosensitizer in a much higher concentration in tumor tissues than in normal tissue. It is worth noting that unlike X-rays, in the absence of a photosensitizer, the visible light is essentially harmless. Basic photochemical properties of porphyrins which have to do with detecting the tumor cells by fluorescence and destroying them by the photodynamic effect, have been reported.<sup>25</sup>

Photochemotherapy was first reported by a Dane, Niels Finsen, in the 1880s when he showed that a tubercular condition of the skin called *lupus vulgaris* could be treated by direct photochemotherapy.<sup>25</sup> It was also observed in the early years of this century that certain substances called photodynamic agents could photosensitize mammals. Subsequent research showed that when photosensitizers like porphyrins are injected under the skin, sunburns occur due to photodynamic reactions. Visible light, oxygen and a photosensitizer were found to be necessary for the photodynamic reaction, which destroys living cells. Of the substances which acted as photodynamic agents, porphyrins were among the first group of compounds to be used as photodynamic agents.<sup>25</sup>

The first chemical substance to show selective retention by tumor tissue while normal surrounding tissues had a low comparable content after intravenous injection was haematoporphyrin derivative (HpD).<sup>26</sup> As early as 1936, it was suggested that haematoporphyrin when combined with ultra violet light could be effective in the treatment of skin diseases such as

psoriasis.<sup>27</sup> The results of experiments which followed led to the treatment of a wide variety of infectious diseases<sup>28,29</sup> including skin diseases.<sup>30,31</sup> Several reports have been published in which haematoporphyrin derivative in combination with ultraviolet light has been used to treat psoriasis.<sup>31</sup>

Haematoporphyrin derivative had the remarkable property of concentrating, with some degree of selectivity in tumor tissue. Due to its selectivity for tumor tissue, it was then used as a photosensitizer for the treatment of cancer. However, there were some reasons why HpD was not the most ideal photosensitizer. First, it is a complex mixture of compounds some of which are not PDT active, and may cause side effects on patients. Another reason is that, it is cleared quite slowly from the body and patients need to stay a long time in the dark. HpD is also inefficient at light absorption and therefore produces only a relatively small and shallow photodynamic effect. Subsequently porfimer sodium (Photofrin) was formulated as a product of the purification of HpD by removal of monomeric porphyrins, although it is still a mixture of porphyrin dimers and higher oligomers derived from HpD, linked primarily by ether bonds and some ester bonds.<sup>25,32</sup> Porfimer sodium was found to be useful in the treatment of psoriasis when irradiated with light of a suitable wavelength.

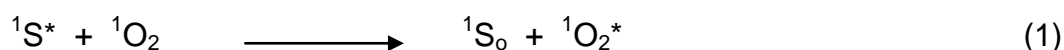
#### **1.9.4 Identification of Tumor Tissues**

Metal-free or free base porphyrins emit a bright red fluorescence when irradiated with ultraviolet light. This observation provided a means of detecting small amounts of porphyrins in a bed of normal tissue. They show a strong absorption band at a wavelength of about 400 nm, called the Soret band and four weaker bands in the region of 500-630 nm; and because of this, porphyrins have a reddish purple colour.

When electronically excited by the absorption of light, they may show two sorts of emissions. The emission in the red region, used for the detection of tumor tissue results from the first excited singlet state ( $^1S^*$ ) which in turn results from the excitation of the electronic ground state ( $S_0$ ) of the

porphyrin when it absorbs light of suitable wavelength, ( $S_0$  to  $^1S^*$ ). The singlet excited state porphyrin can decay back to the ground state with the release of energy in the form of fluorescence and enable identification of tumor tissue ( $^1S^*$  to  $S^0$ ).

The singlet excited state is short lived and under suitable conditions it undergoes conversion to a longer-lived triplet excited state ( $^3S^*$ ). This process is known as intersystem crossing, which involves the unpairing of paired electrons in the excited state. Another emission is observed, usually in the near-infra-red region, coming from the longer lived excited triplet state of the porphyrin. In fluid solution this emission is usually not observed in organic molecules because the triplet excited state is de-activated in other ways. In the presence of oxygen ( $^3O_2$ ) which is found in most cells, one of these ways involves the transfer of excitation energy from the porphyrin triplet species to the dioxygen. The dioxygen molecule is excited from its triplet ground state to the singlet excited state, provided the energy of the triplet excited state of the porphyrin is higher than that of the singlet excited state dioxygen<sup>25</sup> which is equal to  $94\text{kJ}\cdot\text{mole}^{-1}$ .



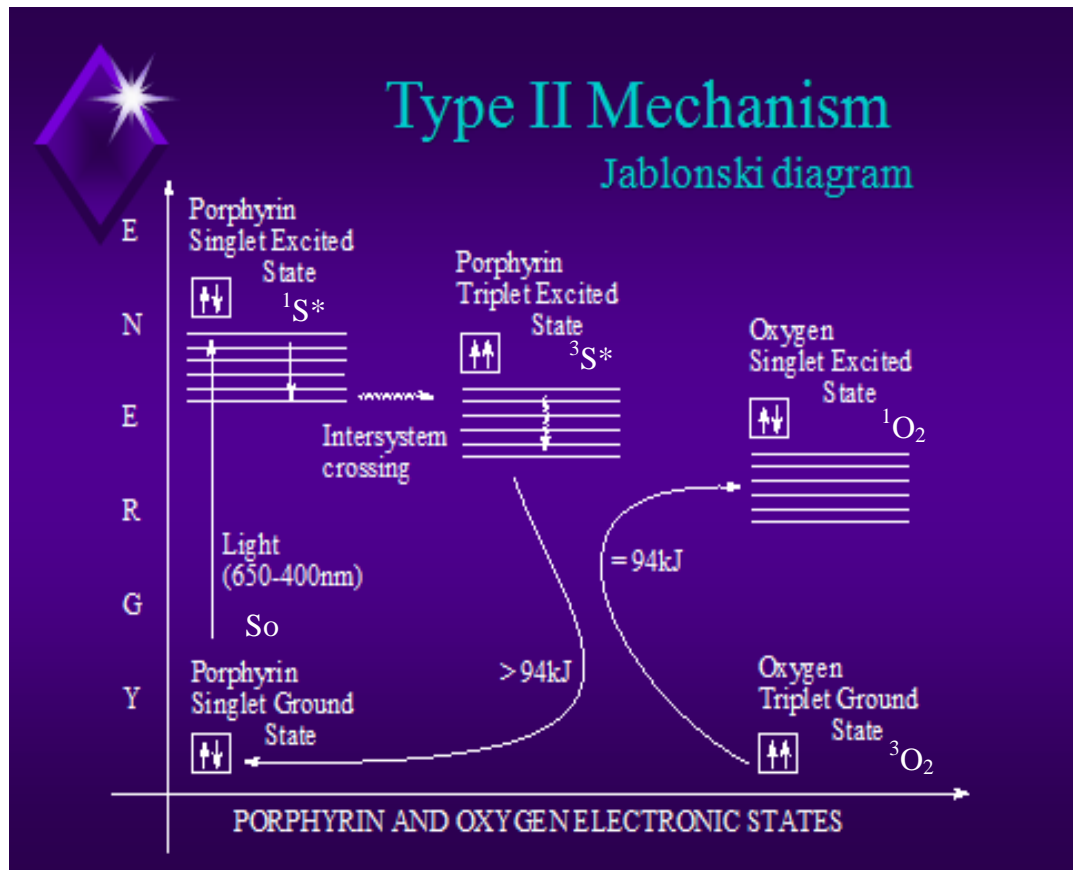


**Figure 1:** Jablonski diagram to show photosensitization of oxygen<sup>33</sup>

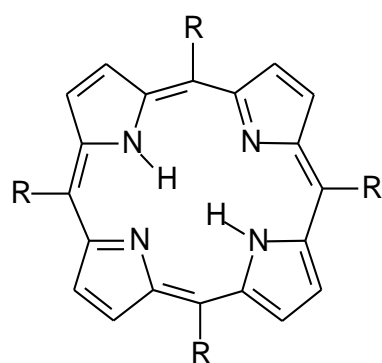
The singlet excited state dioxygen is much more toxic and reactive than the triplet ground state oxygen, and is known to react with membrane components such as unsaturated lipids, cholesterol and proteins. Therefore just like the chlorophyll in plants that utilizes energy from the sunlight to produce sugars, porphyrins utilize energy from light to produce toxic oxygen species. In photosensitized tissue such a reaction would be expected to lead to membrane damage and eventually to cell death. It is most important to note that when the excited triplet state porphyrin transfers electronic energy to ground state  $^3\text{O}_2$ , it returns back to its singlet ground state.<sup>34,35</sup> Singlet oxygen formed in this way is generally accepted to be the main pathway leading to photo necrosis in sensitized tissue.

### 1.9.5 Summary of Mechanism of Action of a Photosensitizer

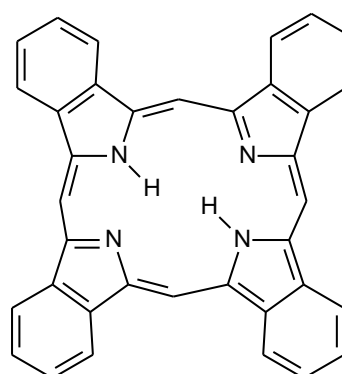
A **photosensitizer** is a chemical compound that can be excited by light of a specific wavelength, followed by transfer of the excitation energy to another species. This excitation uses visible or near-infrared light. In photodynamic therapy, either a photosensitizer or the metabolic precursor of one is administered to the patient. The tissue to be treated is exposed to light suitable for exciting the photosensitizer. Usually, the photosensitizer is excited from a ground singlet state to an excited singlet state. It then undergoes intersystem crossing to a longer-lived excited triplet state. One of the few chemical species present in tissue with a ground triplet state is molecular oxygen. When the photosensitizer and an oxygen molecule collide, an energy transfer can take place that allows the photosensitizer to relax to its ground singlet state, and create an excited singlet state oxygen molecule. Singlet oxygen is a very aggressive chemical species and will very rapidly react with any nearby biomolecules. The specific targets depend heavily on the photosensitizer chosen. Ultimately, these destructive reactions will kill cells through apoptosis or necrosis.

### 1.9.6 PDT Photosensitisers

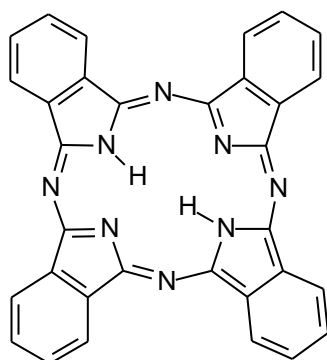
The most widely studied photosensitisers are porphyrins, phthalocyanines and their derivatives.<sup>36</sup> Figure 2 shows the basic structures of a porphyrin, a benzoporphyrin, a phthalocyanine and a naphthalocyanine.



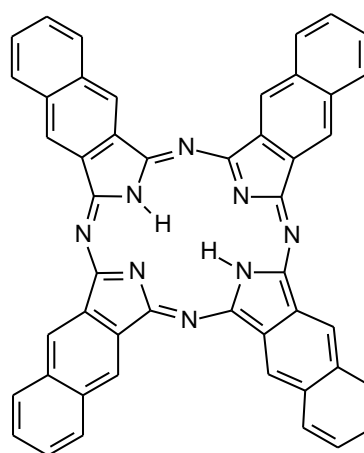
**1** Porphyrin



**2** Benzoporphyrin



**3** Phthalocyanine



**4** Naphthalocyanine

**Figure 2:** PDT Photosensitizers

### 1.9.6.1 Development of Photosensitisers

As a complex mixture of compounds, with photosensitization properties, haematoporphyrin derivative represents the first-generation of photosensitisers. First generation photosensitisers are complex mixtures of compounds that contain compounds that are responsible for the photosensitization properties of the mixture. Photofrin therefore is also a first-generation photosensitiser since it is a mixture of porphyrin dimmers and oligomers. Second-generation photosensitisers on the other hand are

pure single compounds that exhibit photosensitization properties and they include a number of porphyrins and phthalocyanines derivatives.

### 1.9.6.2 Porphyrins

Porphyrins are a group of organic compounds many of which occur in nature. One of the best known is heme, the pigment in red blood cells. Heme is a cofactor of the protein hemoglobin. They are aromatic heterocyclic macrocycles composed of four modified pyrrole subunits interconnected at their  $\alpha$  carbon atoms via methine bridges ( $=\text{CH}-$ ). Porphyrins are aromatic. That is, they obey Hückel's rule for aromaticity, possessing  $4n+2$   $\pi$ -electrons ( $n=4$  for the shortest cyclic path around the macrocycle) that are delocalized over the macrocycle. The macrocycles, therefore, are highly-conjugated systems. Consequently, they typically have very intense absorption bands in the visible region and may be deeply colored. The name porphyrin comes from a Greek word for *purple*. The macrocycle has 26 pi electrons in total. The parent porphyrin is porphine, and substituted porphines are called porphyrins.

One of the more common synthetic routes for porphyrins is based on work by Paul Rothmund.<sup>37a</sup> His techniques underpin more modern syntheses such as those described by Adler and Longo.<sup>37b</sup> The synthesis of simple porphyrins such as *meso*-tetraphenylporphyrin ( $\text{H}_2\text{TPP}$ ) is also commonly carried out in university teaching labs.<sup>37c</sup> It can be done by heating an equimolar mixture of pyrrole and benzaldehyde in refluxing propionic acid for about an hour.

Using this method, porphyrins are assembled from pyrrole and substituted aldehydes. Acidic conditions are essential for porphyrin formation; formic acid, acetic acid, and propionic acid are typical reaction solvents, or *p*-toluenesulfonic acid can be used with a non-acidic solvent. Lewis acids such as boron trifluoride etherate and ytterbium triflate have also been

known to catalyse porphyrin formation. A large amount of side-product, polypyromethene oligomers is formed, and is removed usually by recrystallization or chromatography.

#### **1.9.6.2.1 Criteria for a good Photosensitiser**

During the early years in the development of photosensitisers for PDT, certain design criteria for a good photosensitiser became apparent. These can be summarized as follows.<sup>25,37d</sup>

- Lack of toxicity in the dark
- Selective uptake by tumor tissue
- Short term retention to avoid the persistence of photosensitivity
- Triplet energy greater than 94KJ/mol
- Intermediate lipid water partition coefficient
- Single substance
- Light absorption in the red or far red range in the visible spectrum

Substances that meet these criteria include suitably modified porphyrins, chlorines and phthalocyanides. So far, more than 150 photosensitisers have been synthesized and tested. Many of them show little or no activity in photo necrosis. But these efforts have not been wasted, for they have provided the basis for the above design criteria and will continue to do so. Some of them however have shown significant photodynamic activity. Among these, three porphyrins which contain hydroxyphenyl constituents have shown great promise.<sup>25,37e</sup>



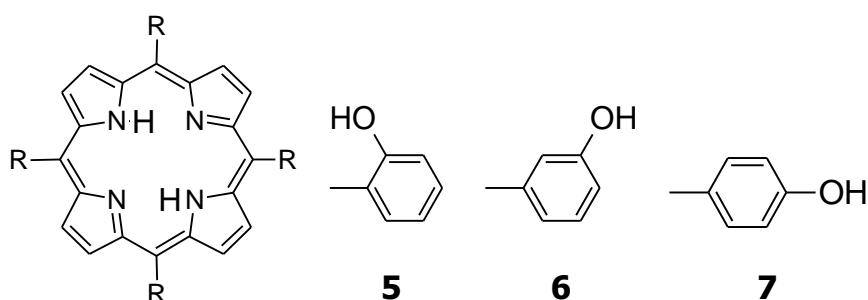


**Figure 3:** Meso-tetra(hydroxyphenyl)porphyrin

These compounds are the isomers 5,10,15,20-tetra(*o*-hydroxyphenyl)porphyrin (**5**), 5,10,15,20-tetra(*m*-hydroxyphenyl)porphyrin (**6**), and 5,10,15,20-tetra(*p*-hydroxyphenyl)porphyrin (**7**), shown in figure 3, which can be prepared from simple precursors. All these are excellent sensitizers leading to tumour photo necrosis, but the *ortho*- isomer (**5**) is not sufficiently selective and causes skin photosensitization. The other two (**6**) and (**7**) show good selectivity for experimental tumours.<sup>25,37e</sup>

#### 1.9.6.2.2 Phthalocyanines

Phthalocyanine is an intensely coloured symmetrical 18  $\pi$ -electron aromatic macrocycle closely related to the naturally occurring porphyrins (Figure 2, **3**). Like the porphyrins, phthalocyanine macrocycle plays host to over seventy different metal ions in its central cavity. Since its discovery over seventy years ago, phthalocyanine and its derivatives have been extensively used as colourants. More recently, they have been employed in several “hi-tech” applications such as photoconducting material in laser printers and the light absorbing layer in recordable compact discs. They are also used as photosensitizers in laser cancer therapy, as nonlinear optical materials and industrial catalysts.

Phthalocyanines and their derivatives have shown great promise in PDT<sup>38</sup>. They are porphyrin-like second-generation sensitizers for photodynamic

therapy.<sup>37e,38</sup> The most important attribute that makes phthalocyanines suitable for PDT is the intense absorption in the far red and long-lived excited triplet state.

### **1.9.6.3 Drug Development in PDT**

Drug development in PDT is a much more difficult process than is the case with conventional chemotherapy. This is because PDT actually requires both a drug and a device, the device being a light source. This two-part procedure makes it possible to avoid the toxicity associated with drug based therapy, since only light-activated sensitizer will yield a cytotoxic result. However, it becomes necessary to consider several new variables, the time between sensitizer administration and irradiation, avoidance of skin and eye photodamage, long-term dark toxicity, and appropriate wavelength of irradiation.<sup>36</sup>

During the past few years, a large number of new sensitizers have been suggested for clinical use, on the basis of experimental studies in animal or in cell cultures. There are several uncertainties and considerable expenses related to bringing new agents to the clinic, and these account for the slowness in the incorporation of new sensitizers into medical practice. While adverse reactions are often considered to be of less than major importance in conventional drug therapy of life-threatening disease, PDT will be applied generally to early lesions with curative intent. The occurrence of unexpected toxicity could seriously impair future trials.<sup>36</sup> PDT is advantageous over standard therapy because, since it is not painful, so there is no need for anesthesia. PDT also has the ability to treat multiple lesions at one sitting, good patient acceptance, excellent cosmetic results and apparent lack of major side effects. Acute effects caused by singlet oxygen include damage to various cell membranes including plasma, mitochondria, liposomal, endoplasmic reticulum, and nuclear membranes; inhibition of enzymes; and inactivation of membrane transport systems. The diseased tissue in which the photosensitizer is localized

should be destroyed with either little or no damage to surrounding normal tissue.<sup>39a</sup>

The major stumbling block to the use of PDT in the removal of tumor cells is the lack of suitable photosensitisers that can accumulate selectively to the tumor cells and destroy them leaving normal cells undestroyed or unaffected after illumination with light.<sup>28</sup> Although photosensitisers that can accumulate selectively to the tumor cells have been discovered, their major limitation is that, they are activated with wavelengths of light that are not capable of penetrating deeply through tissues or blood.<sup>37e</sup>

Other important limitations of current photosensitisers include the difficulty in the functionalisation and purification of the functionalized compounds. Photosensitisers are generally water insoluble, but they can be made to be water-soluble by functionalisation with hydrophylic groups.<sup>37e</sup>

Clearance from the body is also one of the important limitations in the use of photosensitisers. Most of the as-synthesized photosensitizers are cleared very slowly from the body and therefore cause skin toxicity when the patient comes into contact with light. In addition, delayed clearance results in the patient being forced to stay in the dark for a long period of time before exposing the diseased tissue to light. This is intended to give enough time for the photosensitiser to clear from the normal tissue, while not too long for it to clear also from tumor tissue.

The most common cancers originate and spread within the chest, abdomen, or pelvis. These sites are difficult to treat because of the close positioning of many overlapping organs. Continued cell division leads to the formation of tumors that invade normal tissues and organs. In many cases, the cancer cells become dislodged and spread to other locations within the body where they then take up residence and grow forming secondary tumors. In these situations, the cancer is frequently advanced and not curable by current approaches.<sup>39a</sup>

PDT has been used experimentally to treat many types of cancers, such as cutaneous viral infections, psoriasis and certain diseases of the retina. The selectivity of certain compounds for hyperproliferative tissue,<sup>39</sup> added to the observation that photodynamic therapy can lead to blood vessel stasis suggest that PDT might be effective in non-tumor diseases. Some of the diseases characterized by tissue hyper proliferation and/or neovascularisation, which are being considered for PDT, are choroidal neovascularisation (ophthalmology), menorrhagia (gynecology), cutaneous hemangiomas (dermatology), benign prostatic hyperplasia (urology) and rheumatoid arthritis (rheumatology). These applications of non-tumor PDT, as well as the treatment of various bacterial and fungal conditions, blood sterilization (PDT kills bacteria and viruses) prior to transfusion, certain viral included pathologies, immune modulation and bone marrow purging are under investigation.<sup>39a</sup>

## **1.10 Improvements for PDT**

### **1.10.1 Combination Treatments**

Photodynamic therapy is often used in combination with other therapeutic techniques. For example PDT has been used to help keep cancer from coming back on large surface of the body, such as the pleura and peritoneum, which are common sites of spread for some types of cancer. Photodynamic therapy in combination with magnetic hyperthermia is an approach which is being investigated due to the advent of magnetic nanoparticle based drug delivery systems which can be made to preferentially accumulate in tumor tissue.<sup>39b</sup>

### **1.10.2 Improvement of Equipment for Delivery of the Activating Light**

Different types of lasers and other light sources are being researched, some newer agents may respond to small doses of radiation. This could allow doctors to use smaller amounts of radiation than doses used in standard radiation therapy, which could lead to fewer side effects. In

addition, several light delivery systems are being investigated in order to develop systems that are suitable for various types and locations of the tumors.

### **1.10.3 Interstitial therapies**

To treat larger solid tumors, a technique known as interstitial therapy involves using imaging tests such as computer tomography (CT) scans to guide fibre optics directly into tumors using needles. This may be specially useful in areas that would require major surgery.

### **1.10.4 Limitations of PDT**

There are important limitations associated with PDT. Some of the more prominent limitations include

- Light is needed to activate most photosensitizers, and this light cannot pass or penetrate through more than one centimeter of tissue, at best. For this reason photodynamic therapy using normal light delivery is usually used to treat tumors on or just under the skin, or on the lining of internal organs or cavities. For deeper seated tumors, optic fibre light delivery systems are required.
- Photodynamic therapy is less effective in treating large tumors, because light cannot pass far into these tumors. To effectively treat such tumors, they must be penetrated with several light delivery systems to cover the entire tumor.
- Photodynamic therapy is a local treatment and generally cannot be used to treat cancer that has spread (metastasized). Some photosensitisers are being investigated for metastasized tumors.

### **1.10.5 Complications and/or Side Effects of PDT**

PDT is not without complications and/or side effects. Some of the complications include

- Light triggered photosensitivity reactions – redness, tingling or burning.
- Swelling in the treated areas.
- Pain, trouble breathing or swallowing which can be caused by swelling in surrounding tissues.
- Coughing.

### **1.10.6 Challenges**

There are several challenges facing facing scientists and these include designing new drugs that

- are able to treat tumors deeper under the skin or in body tissues
- are selective for cancer cells as opposed to normal cells.
- will go into cancer cells more quickly, reducing the time needed between administering the drug and doing the light treatment.
- may be removed from the body more quickly, reducing the time people need to worry about photosensitivity reactions, and therefore time spent in the dark.

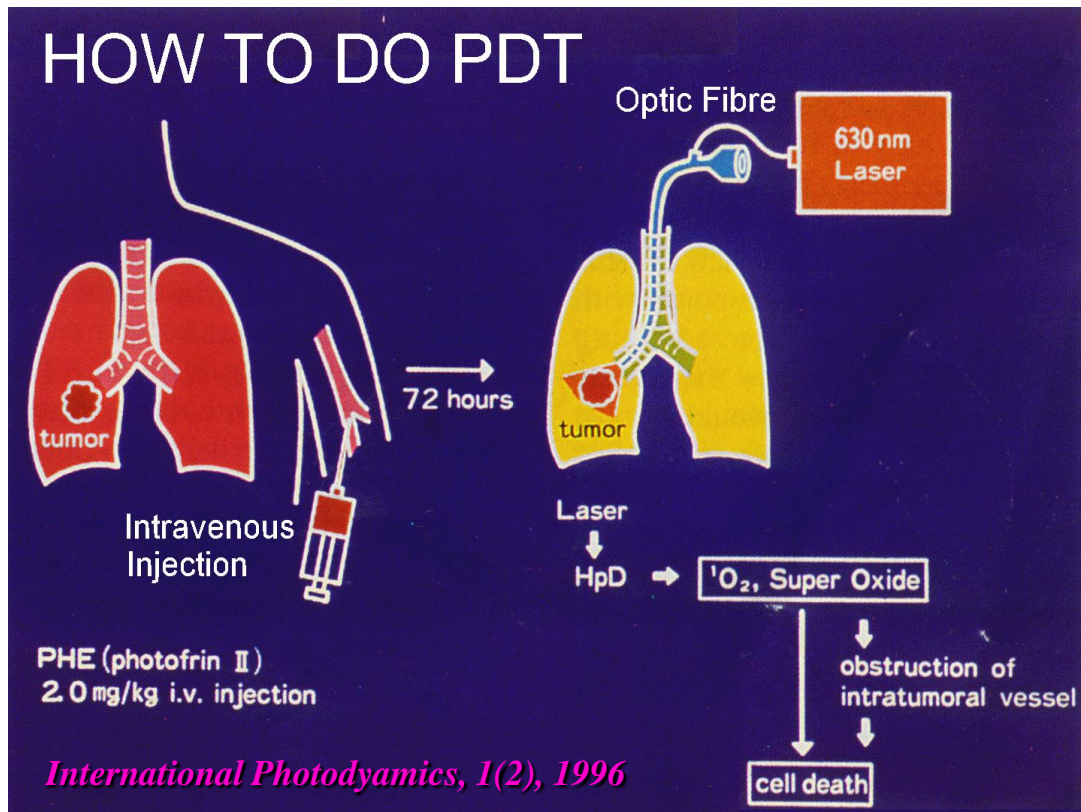


**Figure 4:** How does PDT work?

### 1.10.7 How PDT Works

In a typical treatment of tumourous cancer with PDT, the photosensitiser is dissolved in ethanol, polyethylene glycol, and water (2:3:5 v/v).<sup>36</sup> The patient is then injected intravenously with a dose of the photosensitiser and confined to the dark. After a period of equilibration (24-72 hrs), during which most of the photosensitiser accumulates preferentially in the tumor tissue, the patient is anaesthetized, and a dose of light is administered using an appropriate light delivery technique, such as an optic fibre from a laser source. Tumor cell destruction begins immediately and a period of time is allowed for the photosensitiser and its metabolites to be eliminated from the body, before the patient is allowed back into the light.<sup>40a,b</sup>

### 1.11 Light Sources<sup>40c</sup>

There is currently a wide variety of light sources used in PDT. The argon laser and the prototype are among the more prominent light sources. There

is also a wide variety of laser light delivery systems. Among the more prominent ones are the

### **1.11.1 Argon Laser**

Argon laser treatments were done mostly in 1988-1990 on vascular lesions in elderly patients. Since 1994, a second generation of a pulsed dye laser system, such as Cyosure, Photogenica V emitting at 585nm have been used. These are faster lasers with a larger spot diameter. Recently, new light sources have been designed and tested for their efficacy because the older laser systems are limited by their uniqueness. Older systems are commonly limited to one medical application and this can be inhibiting. High power laser light source systems consisting of visible diode arrays operating at wavelengths of 670nm, coupled to multimode fibres have recently become available. These have great promise for monochromatic delivery and wavelength selection.

### **1.11.2 Prototype**

Previous attempts at phototherapy using non-laser light sources have resulted in machines prone to heat damage and long exposure times. Non-laser sources which have been used previously used exposed delivery beams and suitable shielding was necessary to protect patient and operator alike. The Prototype light source was the first light with properties resembling those that are suitable for PDT; that is, brightness, high photoactivation efficiency and fibre deliverable, while at the same time avoiding high costs and complexity. It measures 30cm x 15cm x 15cm and incorporates a short arc discharge producing a continuous wave broad band flat spectral out-put. Custom filters select the appropriate wavelength and bandwidth before the out-put is focused into a light guide via a programmed shutter. The Prototype delivers over 3W of photoactivating light directly or 1W via a light guide bandwidth of 30 nm which can be tuned to any wavelength from 300-1200 nm and is currently in worldwide use.





## *PDT Laser Light Delivery Systems*

*International Photodyamics, 1(4), 1996*

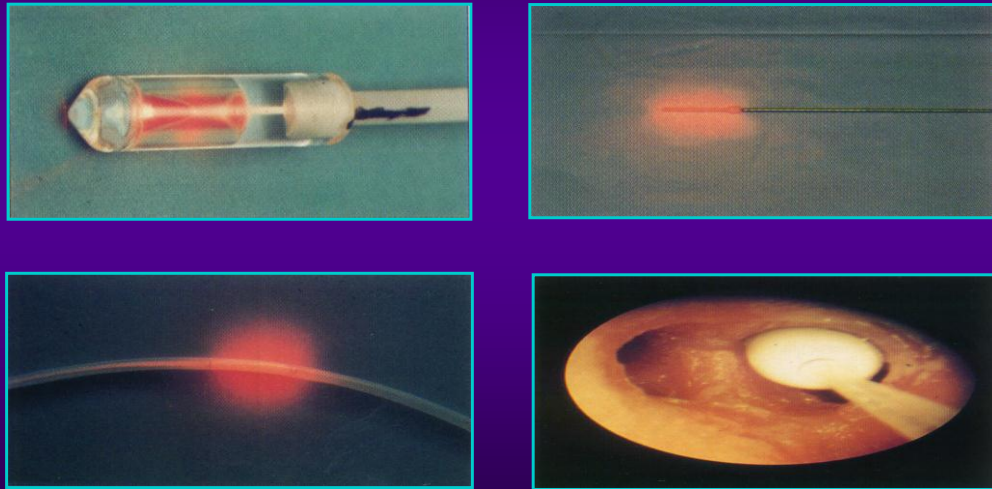


**Figure 5:** Some common light sources for PDT

### **1.11.3 Some Laser Systems Used in PDT**

There are a number of laser light systems used in PDT. Some of them are suitable for research while others are suitable for medical use. The shape and design of the laser and intensity of the light are key features that determine the utility of the laser light system of choice for each purpose.

#### **1.11.3.1 Highly Reflecting Balloon Light Distributors**

For geometrical shapes which are more complex than a flat surface or a cylindrical tube, one way of attaining an approximately homogeneous light intensity as part of the surface of a hollow organ is to use a balloon. The balloon is either made of an elastomer, so that it adjusts under pressure to the shape of the organ, or it is made of a flexible none-elastic material which inflates under pressure to give the desired shape. Such light distributors are used for PDT in the bronchi, cervix and esophagus.<sup>41</sup>

### **1.11.3.2 Frontal Light Distributors**

A frontal light distributor is used to create a circular spot of homogenous light intensity distribution at a small distance from the fibre tip. This particular one is based on the fact that a long multimode fibre “scrambles” the injected light so that the distal end of the fibre core is homogeneously illuminated. A self micro lens is then used to project an enlarged image of the surface at some distance. Such a frontal light distributor can be used, for instance, in conjunction with a flexible bronchoscope where it fits through a 2.2 mm diameter biopsy channel, for irradiating cancers on bronchial spurs, or simply for irradiation of skin cancers, buccal cancers, and cell structures etc.<sup>41</sup>

### **1.11.3.3 Distributor With Cylindrical Light Output**

This device provides a cylindrical light that can be used in interstitial PDT, or in PDT of narrow hollow organs like bronchi, the ureter or the urethra. The fibre core is roughened over the length that will become optically emitting. The roughened fibre is covered with an approximately 10µm thick layer of clear silicon. A highly flexible polymer core optical fibre in the range of 400-600 µm core diameter is used. Hence, the fibre tip can be both quite long and homogeneous in light intensity; essentially independent of wavelength over a large range of wavelengths: very flexible and quite small outside diameter of the order of 1 mm.<sup>41</sup>

## **1.12 Current Perspectives in Drug Development**

Several new drugs, with a number of promising features for PDT have come under scrutiny as pharmaceutical companies enter the race for the development and synthesis of PDT photosensitisers.

### 1.12.1 Texaphyrins

Texaphyrins are a sub-class of heterocyclic macrocycle porphyrin type of molecules. The molecule was invented by Jonathan Sessler, a professor at the University of Texas, Austin, USA.<sup>42a</sup> The name texaphyrin arose because some of the molecules have a shape that can superimpose onto the points of the star featured on the state flag of Texas.<sup>42a</sup> Sessler described possible medicinal uses of these compounds in the *Proceedings of the National Academy of Sciences* and in other scientific journals.<sup>42a</sup>

The texaphyrins are penta aza Schiff-base derived expanded porhyrins that are known to form stable 1:1 complexes with many metal cations, including those of the trivalent lanthanide series. The gadolinium(III) complex of one particular texaphyrin derivative, motexafin gadolinium (MGd; Xcytrin) was extensively studied as a potential magnetic resonance imaging (MRI) detectable enhancer of X-ray cancer therapy and clinical studies have confirmed that this agent is taken up into and retained in tumors with high specificity.<sup>42a</sup> Magda et al<sup>42b</sup> also established that this agent could be administered safely to cancer patients at the 5 mg/kg dose level over the course of a two-week regimen and various supporting studies revealed a clearance pathway that was predominantly hepatic and provided support for a very novel mechanism of action.<sup>42b</sup> This later, manifested in terms of increased apoptosis which is believed to involve redox modulation processes that take place outside of the nucleus. The fact that this particular texaphyrin-type species was known to localise in tumors, with the fact that it was believed to act via a mechanism that was “orthogonal” to those of standard cancer chemotherapeutics, led to the consideration that motexafin gadolinium (MGd) could provide the tumor localising, biocompatible core needed to generate cancer-seeking conjugates.<sup>42c</sup>

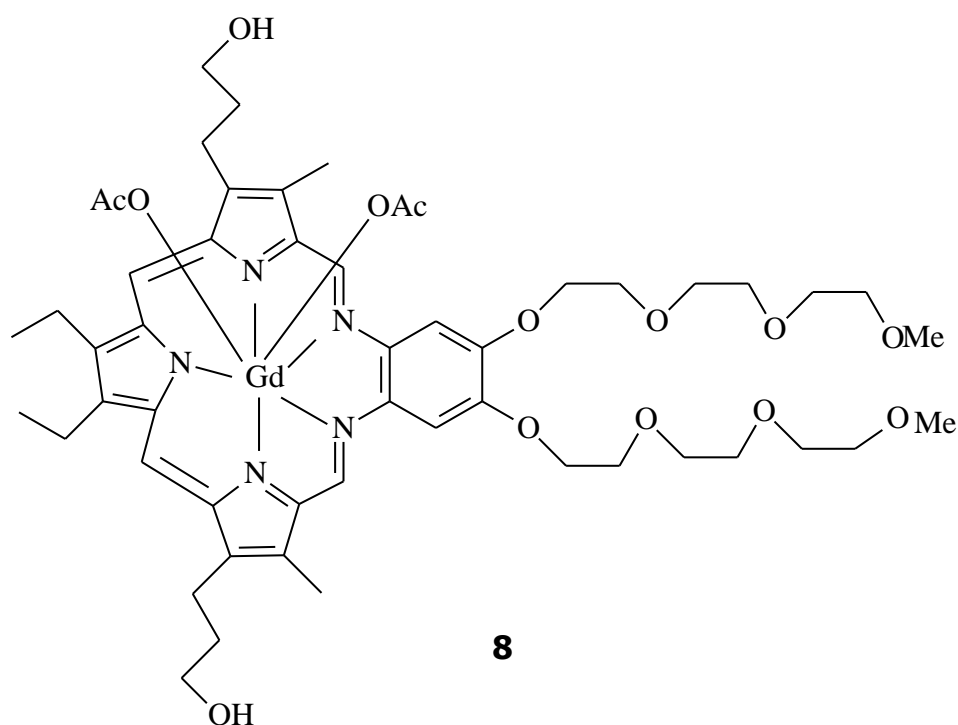


**Figure 6:** Structure of Gadolinium Texaphyrin (Gd-Tex)

Texaphyrins are manufactured by Pharmacyclics Inc. and its academic collaborators. Texaphyrins are ring shaped, planar, expanded porphyrin type of molecules with large metal cations such as the lanthanides<sup>42-44</sup> (figs. 6 & 7). They have been synthesized with the hope that they can perform specific functions in a number of medical applications. Like other porphyrins, texaphyrins accumulate in those parts of the body where energy usage or metabolism occurs such as in cancer cells. Thus they are useful in the treatment of cancer and other atherosclerotic cardiovascular diseases.<sup>43,45</sup> Texaphyrins have the ability to bind large metal ions, which allows the metal to interact freely with adjacent molecules while still being retained within the texaphyrin structure.

In the case of porphyrins, this capability is limited only to few smaller metals and in any case once metalated, porphyrins lose the electronic capabilities required in PDT. Because of their binding effect with metals, texaphyrins can be engineered to mediate a number of biomedical reactions. Pre-clinical testing has shown that the ratio of texaphyrins in cancerous lesions relative to the surrounding normal tissue ranges from 5:1

to 15:1. Texaphyrins are soluble in water, which makes it safer for them to be used in PDT and simple to be administered to patients. Two of the texaphyrin derivatives for which the first phase of clinical trials have been done are Lu-Tex and Gd-Tex. Since they act like porphyrins in selectively targeting tumor cells, they have the potential to enhance the effects of radiation in the tumor cells and not the surrounding normal tissues.<sup>46,47</sup>

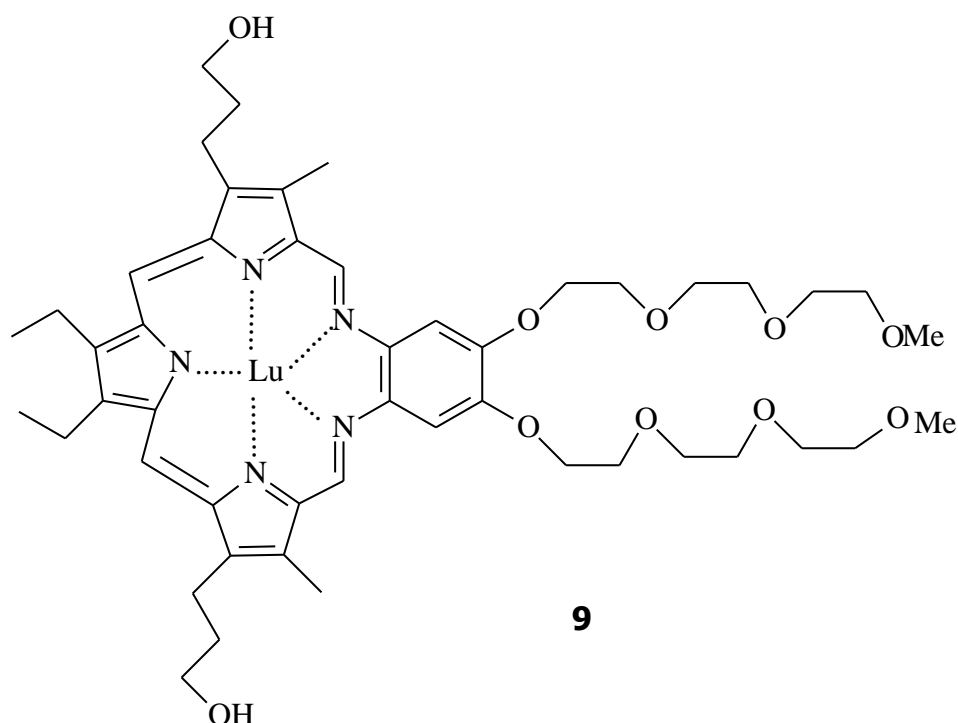


**Figure 7:** Structure of Lutetium Texaphyrin (Lu-Tex)

#### 1.12.1.1 Gadolinium Texaphyrin (Gd-Tex)<sup>48</sup>

This is a texaphyrin with gadolinium metal also bonded at its center and is developed by Pharmacyclics with its collaborators with potential use as a radiation sensitizer. The Gd-Texaphyrin (Fig. 6) is a pentadentate aromatic metalloporphyrin, that was developed as a sensitizer for radiation and chemotherapy.<sup>49</sup> It has selective biolocalisation in tumor tissue, and has unique advantages over previous radiation sensitizers in that it functions independently of oxygen. Thus it has the potential to destroy both poxic and radiation-resistant hypoxic tumor cells.<sup>50</sup> Animal studies using Gd-Tex injected into tumor-bearing animals demonstrated rapid clearance of the

drug from blood and normal tissue, with delayed clearance from tumors, which resulted in up to 8-fold greater concentrations in tumours compared with surrounding tissues.<sup>50</sup>

### **1.12.1.2 Lutetium Texaphyrin (Lu-Tex)**

Lutetium texaphyrin ( Figure 7 ) carries an ion of lutetium, a metal that allows the texaphyrin to be activated by a wavelength of light that can penetrate deeply through tissues, blood and pigments such as melanin. It is water soluble which makes it to be easily administered and rapidly cleared from the body reducing potential toxicity. A challenge discovered in its test was due to high drug dosage which had to be administered in some patients.

Patients experienced pain at the treatment site during light illumination and burning in areas exposed to light such as finger tips and tips of the nose and ears.<sup>45-47,51,52</sup> This drug has the potential to combine the features of selective localization, water solubility, ability to be activated by deeply penetrating far red light and has a low incidence of skin photosensitization.<sup>53-55</sup> Recent investigations using this drug have indicated low incidence of toxicity or skin photosensitization to ambient light. The rapid clearance from the normal tissue enables light therapy to begin within 3 hrs following administration of the drug which shows some improvements when compared with other photosensitisers. It has shown improvement in tumor tissue penetration compared to PDT using other photosensitisers, by penetrating bulky tumors of up to 3-7 mm in thickness.

Lu-tex has also been investigated for suitability as a fluorescence imaging agent in the delineation of retina vascular and choroidal vascular diseases. The results showed that lutetium texaphyrin angiography is a potentially valuable method for retina and choroidal evaluation. It has advantages over some other methods of evaluation like fluorescein and indocyanine green (ICG) and could also be used conceivably for both the identification of abnormal vasculature and subsequent photodynamic therapy.<sup>55</sup> The brand name for lutetium texaphyrin is Antrin™ Photosensitiser.<sup>56-58</sup> The

photosensitizer Lu-TeX was synthesized by Pharmacyclics for potential use in the photoangioplasty for atherosclerosis.<sup>59</sup> It has the following advantages over other sensitizers:

- It possesses a strong broad absorption band centered at 732nm.
- At this wavelength excitation photons are able to penetrate through blood and tissues.
- On absorption of light, it becomes activated to a long-lived triplet state complex that efficiently reacts with oxygen molecules to generate cytotoxic singlet oxygen,
- Antrin™ is a synthetic, well characterized and chemically stable compound.
- It is soluble in aqueous media which allows aqueous formulation and ease of intravenous administration.
- Importantly, Antrin™ has been designed to be selectively taken up in diseased tissue which potentially allows the diseased cells in which the drug is retained to be damaged when exposed to light while the surrounding normal cells remain undamaged.

#### **1.12.2 5-Aminolevulinic acid**

5-Aminolevulinic acid (ALA) is the first compound in the porphyrin synthesis pathway, the pathway that leads to heme in mammals and chlorophyll in plants. In plants, production of  $\delta$ -ALA is the step upon which the speed of synthesis chlorophyll is regulated. Plants that are fed with external  $\delta$ -ALA accumulate toxic amounts of chlorophyll precursor, protochlorophyllide, indicating that the synthesis of this intermediate is not suppressed anywhere downwards in the chain of reactions. In mammals it elicits synthesis and accumulation of fluorescent protoporphyrin IX (PPIX) in epithelia and neoplastic tissues, among them malignant gliomas. It is used to visualise tumorous tissue in neurosurgical procedures. Studies have shown that the intraoperative use of this guiding method may reduce the

tumour residual volume and prolong progression-free survival in patients suffering from this disease.<sup>51</sup>

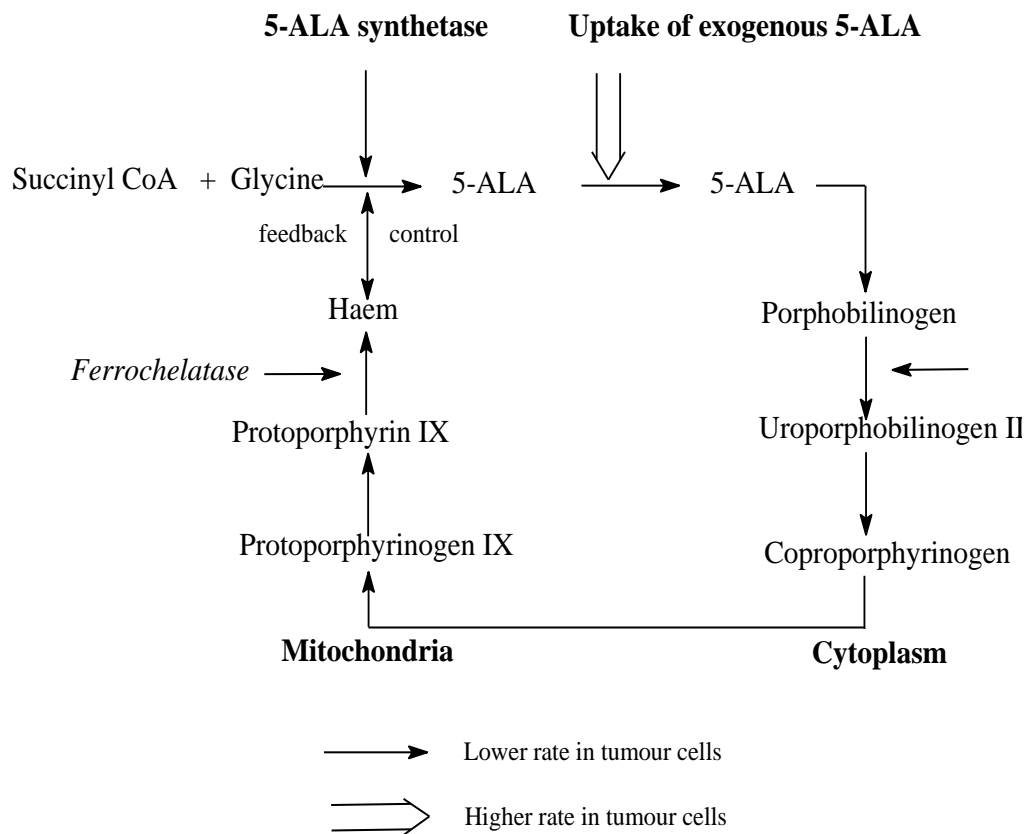


**Figure 8:** Schematic representation of the biosynthesis of haeme and the influence of uptake of exogenous 5-ALA

5-Aminolaevulinic acid has been shown to be capable of producing reliable photosensitization when administered orally.<sup>60a</sup> 5-ALA is not a photosensitizer but on clinical trials it has shown a promising effect in PDT because upon application, it leads to the biochemical formation and preferential accumulation of PPIX in tumor tissue. The advantage of 5-ALA compared to other photosensitizers is that it is present in human cells and is a metabolic precursor of the endogenously formed photosensitizer, ALA-derived PPIX which is capable of tumor cell destruction.<sup>60b</sup>

Its synthesis is normally tightly controlled by feedback inhibition of 5-ALA synthetase, presumably by intracellular heme levels. Since it can be synthesized inside cells, little or no undesirable effects are expected in its



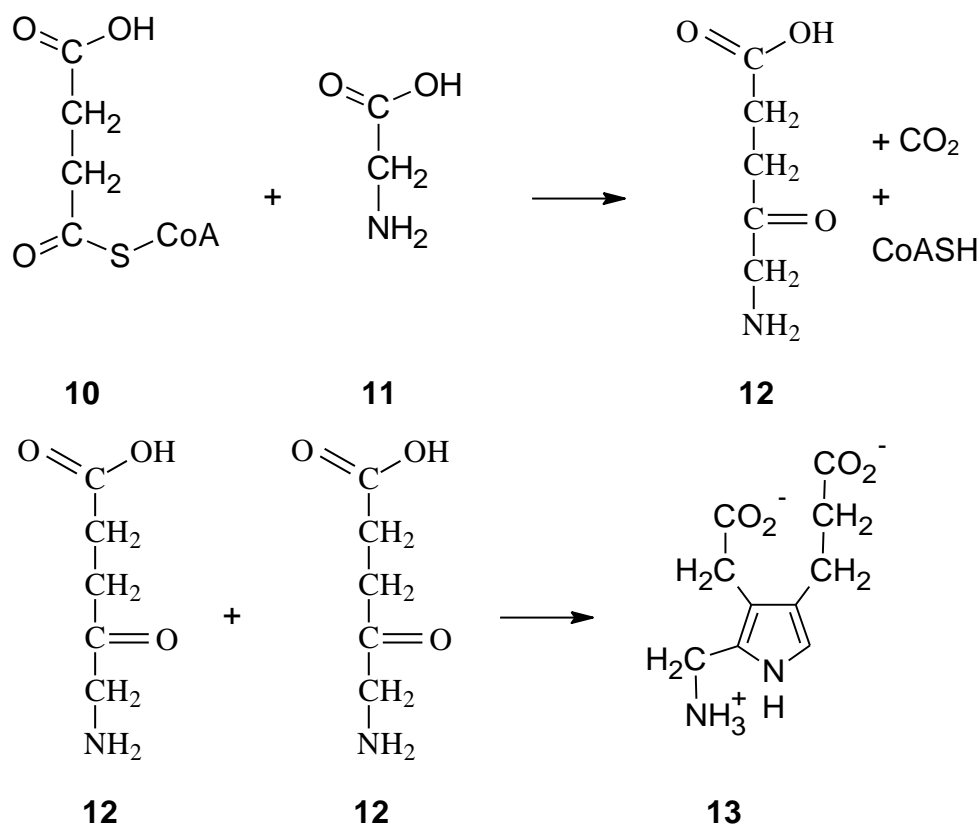
use as a photosensitiser. The first step in its synthesis, the condensation of succinyl coenzyme A with glycine, which is the rate limiting step, occurs in the mitochondria. The other reactions occur in the cytoplasm.

#### **1.12.2.1 5-ALA Induced Production of Protoporphyrin IX (PPIX)**

5-ALA induced protoporphyrin IX production has been extensively investigated as a modality in photodynamic therapy and fluorescence photodetection (PD) of cancerous and precancerous lesions which has led to a phase III clinical trial for treatment of actinic keratosis.<sup>61,62</sup> Even though there are some promising results obtained with ALA modulated photodetection and photodynamic therapy, some significant limitations of its application have been observed, and further improvements are essential. It has been suggested that ALA-modulated photodetection and photodynamic therapy procedures can be improved by:<sup>63</sup>

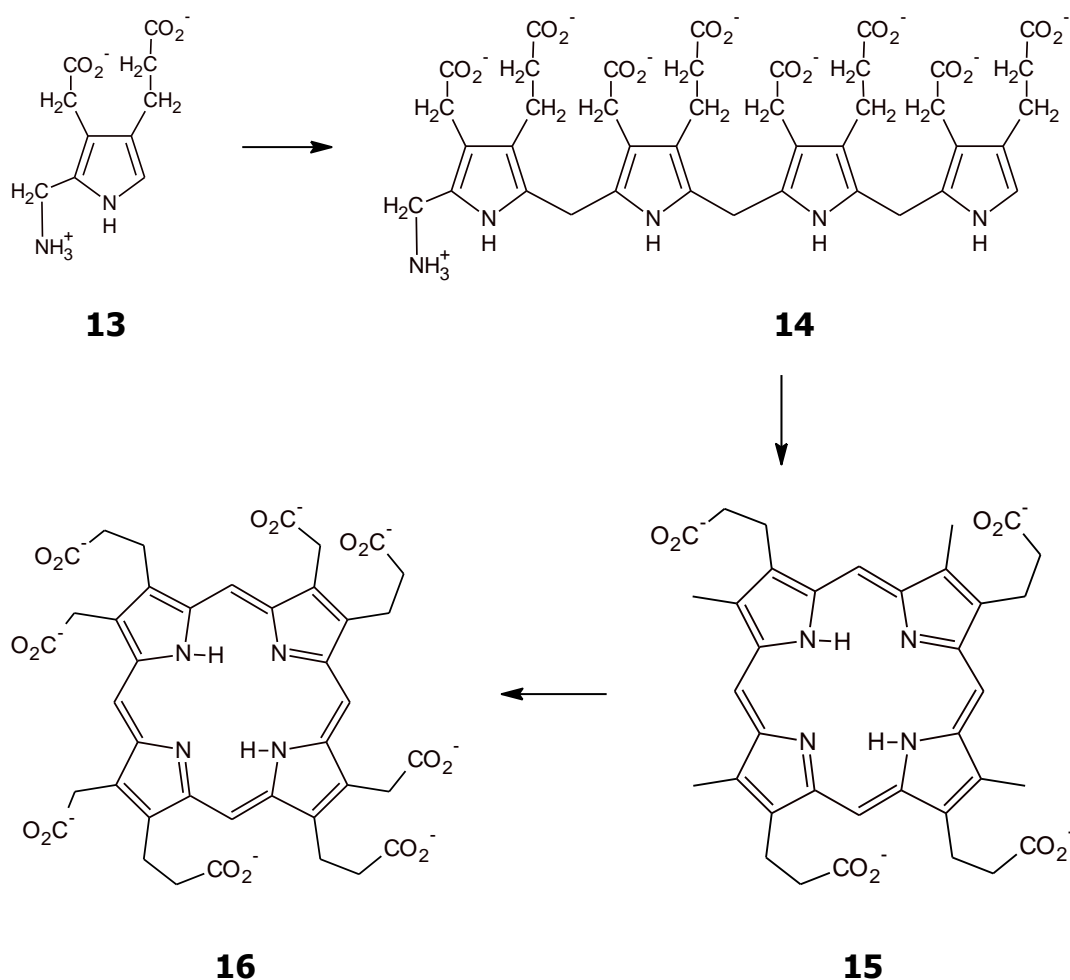
- Changing the drug formulation by adding a transport promoter like dimethylsulfoxide (DMSO), or packaging in liposomes. This is expected to accelerate the delivery of the drug to the affected tissue.
- Modulation of the biosynthetic pathway by addition of iron chelators, will remove the iron that complexes with PPIX to form haem, and repress the synthesis of  $\delta$ -aminolevulinic synthetase.
- Iontophoretic transport through skin. It is hoped that drug administration by electric field-induced molecular transport through the human skin can accelerate drug transport.
- Applying more lipophilic ALA derivatives. This possibility can be explored by using ALA-esters. This would lead, after hydrolysis, to the formation of PPIX derivatives which are more lipophilic than PPIX.<sup>63</sup> The advantages of using esters include the improvement of the penetration depth and a more homogenous tissue distribution. This results in shorter application times, lower drug dose and cost, reduced side effects and improved drug stability. Therefore ester ALA

derivatives can lead to significantly improved photodynamic therapy and photo detection.



**Scheme 1:** Synthesis of 5-ALA acid (**12**) and PBG (**13**)

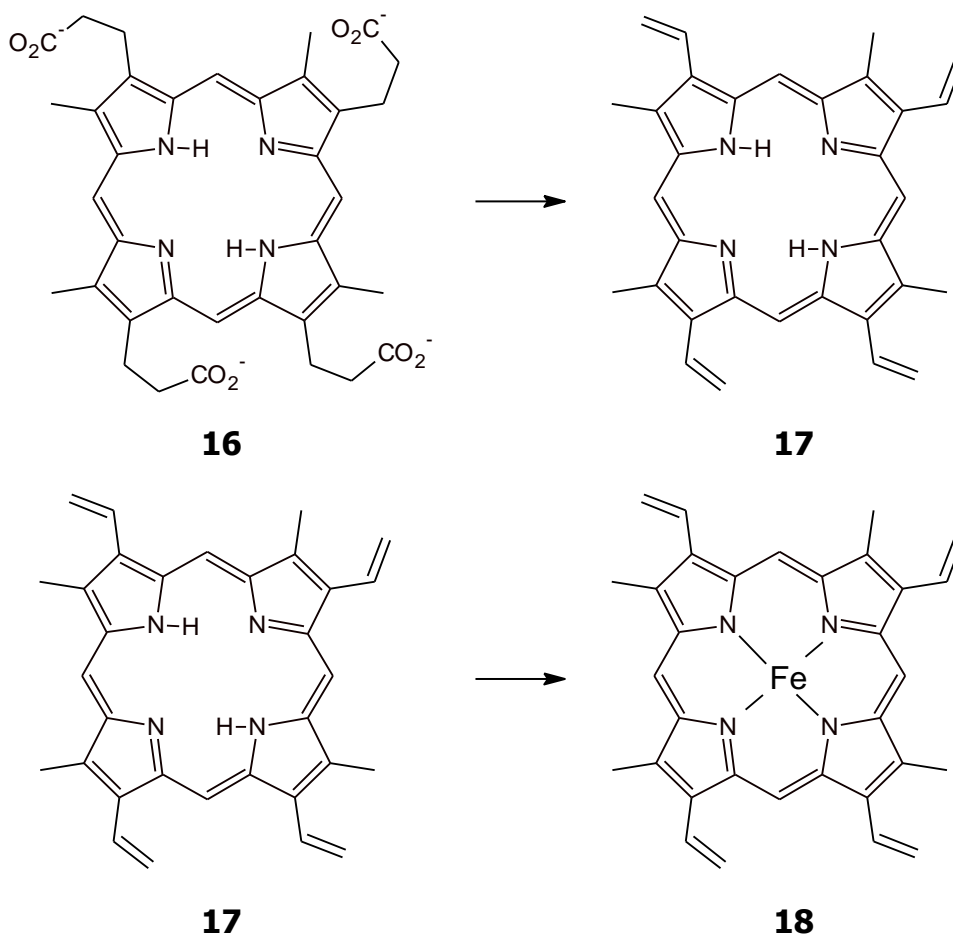
The low molecular weight and polar properties of 5-ALA allow it to be a useful PDT agent for a variety of dermatologic clinical indications other than cancer, like the treatment of actinic keratoses, and the exploration of topical 5-ALA PDT as a treatment of acne and for permanent hair removal. The poor cancer tissue localization of protoporphyrin IX (PPIX) is overcome when it is made *in situ* using 5-ALA. Peak protoporphyrin IX (PPIX) levels are usually reached several hours after 5-ALA is administered, compared with up to 96 hours for tumor localization of a sensitizer after intravenous administration and it is cleared from the body within 24 hours which reduces the risk of continued photosensitivity.



**Scheme 2:** Synthesis of the linear tetrapyrrole

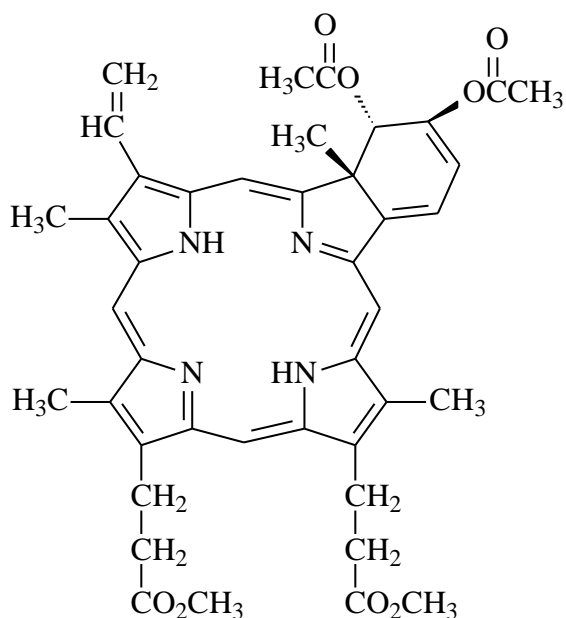
### 1.12.3 Biosynthesis of Protoporphyrin IX (PPIX)

The biosynthetic pathway of 5-ALA induced PPIX is shown below.<sup>64,65</sup> The first step is the decarboxylation of glycine **11** followed by condensation with succinyl CoA **10** to form ALA **12**. The reaction is catalyzed by  $\delta$ -ALA synthetase, an enzyme found in the mitochondria. Two molecules of  $\delta$ -ALA condense to form porphobilinogen (PBG) **13**. The dehydration reaction is catalyzed by  $\delta$ -ALA dehydrase.<sup>62</sup> Four PBG molecules condense head-to-tail to form the linear tetrapyrrole **14** which remains bound to the enzyme known as uroporphyrinogen synthetase that, by itself is inactive. The remaining conversions involve decarboxylations and oxidations that are not completely understood but that result in PPIX, which can react spontaneously but at a low rate with iron, to form haem.



**Scheme 3:** Synthesis of the linear tetrapyrrole

The linear tetrapyrrole in the presence of synthetase and cosynthetase cyclises by losing  $\text{NH}_4^+$  to form the asymmetric uroporphyrinogen III **15**. Decarboxylation of the acetate side chains into methyl group yields coproporphyrinogen III **16**. Unsaturation of the propionate side chains into vinyl groups yields protoporphyrin IX **17**, which is then followed by chelation of iron to give haem **18**. The insertion of the ferrous iron is catalyzed by ferrochelatase and the iron is transported in the plasma by transferrin, a protein that binds two ferric irons. Iron is stored in tissues as  $\text{Fe}^{2+}$  inside molecules of ferritin. All the enzymes required for the bio-synthesis of haemoglobin are contained in the reticulocyte, the immature red blood cell.



**19**

**Figure 9:** BPD Verteporfin

#### 1.12.4 Verteporfin (BPD-Benzoporphyrin Derivatives)

Verteporfin (figure 9) is a photosensitizing agent that accumulates preferentially in neovasculature, including that in the choroid, such as occurs in age-related macular degeneration, ocular histio-plasmosis, or pathologic myopia. It is then activated by light of a specific wavelength (693 nm), in the presence of oxygen. It produces highly reactive short-lived singlet oxygen and other reactive oxygen radicals and causes local damage to the neovascular endothelium followed by vessel occlusion. It is administered intravenously 15 minutes before irradiation of tumor with light from a compatible laser. Verteporfin is derived from animal hemoglobin and its test has shown promising results when used for PDT. However, some side effects occur during the treatment and the most common include mild sensations and sensitivity to light.<sup>66</sup>

##### 1.12.4.1 Mild Sensation

Shortly after the patient is exposed to light, some patients feel warmth, stinging or burning. With cancer patients the effect may gradually develop

into a dull ache that may last for a few days. For psoriasis patients, discomfort is not so much since they are treated with lower doses of BPD Verteporfin or light. However any discomfort like burning or warmth, when present, may be relieved by acetaminophen.

#### **1.12.4.2 Sensitivity to light**

Patients become sensitive to bright light sources (blurred vision). Bright sources of light such as light from the sun, tungsten lamp in the bulbs, photocopy machines, sitting under a dentist's examining light, and etc., may cause sunburn if care is not taken. Hence it is good to avoid bright sources of light for 2-3 days after each treatment because BPD Verteporfin will still be present in normal skin.

#### **1.13 Boronated neutron therapy**

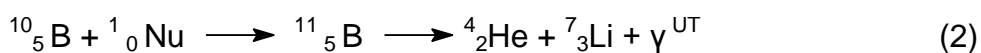
The treatment of cancer with boron containing drugs is based on the high probability of the reaction of the stable  $^{10}\text{B}$  isotope with slow neutrons, which produces an alpha-particle and a recoil lithium particle.<sup>67</sup> The system used is a binary system since it involves tumor localization of the compound with the stable  $^{10}\text{B}$  followed by activation by epithermal neutrons, resulting in the production of the high linear energy particles,  $^4\text{He}$  and  $^7\text{Li}$  which can cause extremely localized tumor cell death and is referred to as boron neutron capture therapy (BNCT).<sup>68a</sup> Boron neutron capture therapy has the potential to control local recurrence of tumor. BNCT is useful in the treatment of primary and metastatic tumors. It is a bimodal cancer treatment based on the selective accumulation of a  $^{10}\text{B}$  carrier compounds in tumors, and subsequent irradiation with thermalised neutrons.<sup>68b</sup>

The selective tumor uptake of a boronated porphyrins had been studied in mice bearing an implanted intracerebral glioma. Biopsy samples of tumor, normal brain, and blood were analysed by a fluorometric assay following intraperitoneal and intravenous administration of a boronated porphyrin

(BOPP). The compound was selectively localized to tumor at ratios 400:1 relative to normal brain. This discrete selective localization suggests this compound as a good BNCT sensitizer.<sup>68c</sup>

When boron neutron capture therapy (BNCT) is used in patients with malignant brain tumors, the patient is injected with a boron carrier compound that is highly enriched in  $^{10}\text{B}$ . The boronated compound used is one chosen that has the property of concentrating preferentially in the brain tumor within a radiation volume. For some BNCT compounds, the action of the blood-brain barrier slows or prevents the entry of the BNCT compounds into healthy, normal, surrounding central nervous system tissues. The patient's head is then irradiated in the general area of the brain tumor with an incident beam or field of epithermal (0.5 eV-10 eV) neutrons. These neutrons become progressively thermalized (average energy, approx. eq. 0.04 eV) as they penetrate deeper into the head. As they become thermalized, they can be more readily captured by the boron-10 concentrating in the tumor cells and /or tumor supporting tissues. A small portion of the boron-10 nuclei in and around a tumor undergo a nuclear reaction immediately after capturing a neutron which produces a high linear-energy-transfer (LET)  $\alpha^4\text{He}$  and  $^7\text{Li}$  particles. The tumor in which the boron-10 is concentrated is thus irradiated by these short range particles, which, on average travel a distance comparable to or slightly less than the diameter of a typical tumor cell. Therefore, a very localized, specific reaction takes place whereby the tumor receives a large dose of radiation compared with that received by surrounding non-neoplastic tissues, with relatively low boron-10 concentrations. An example of a boron enriched compound is p-boronophenylalanine (BPA).<sup>68c</sup>

Summarily, the first step in the treatment is the tumor localization by an appropriate chemical compound tagged with  $^{10}\text{B}$ . The second step is the irradiation of the local tumor site by neutrons, the  $^{10}\text{B}$  absorbs low energy neutrons and ejects an energetic short-range alpha particle. The alpha particle deposits most of its energy within the cell containing the original  $^{10}\text{B}$  atom.<sup>69-73</sup> The reaction is given in equation 1.



The heavy, charged particles,  $^4\text{He}$  and  $^7\text{Li}$ , have ranges in tissue of only 9 and  $5\mu\text{m}$  respectively and thus ionizing radiation is deposited preferentially in and around the tumor. Few of the BNCT sensitizers exhibit highly selective tumor uptake. The boron neutron capture therapy (BNCT) is dependent on the absolute amount and location of boron in the tumor as well as the tumor/normal tissue ratio of the boron concentration ratios.<sup>74</sup>

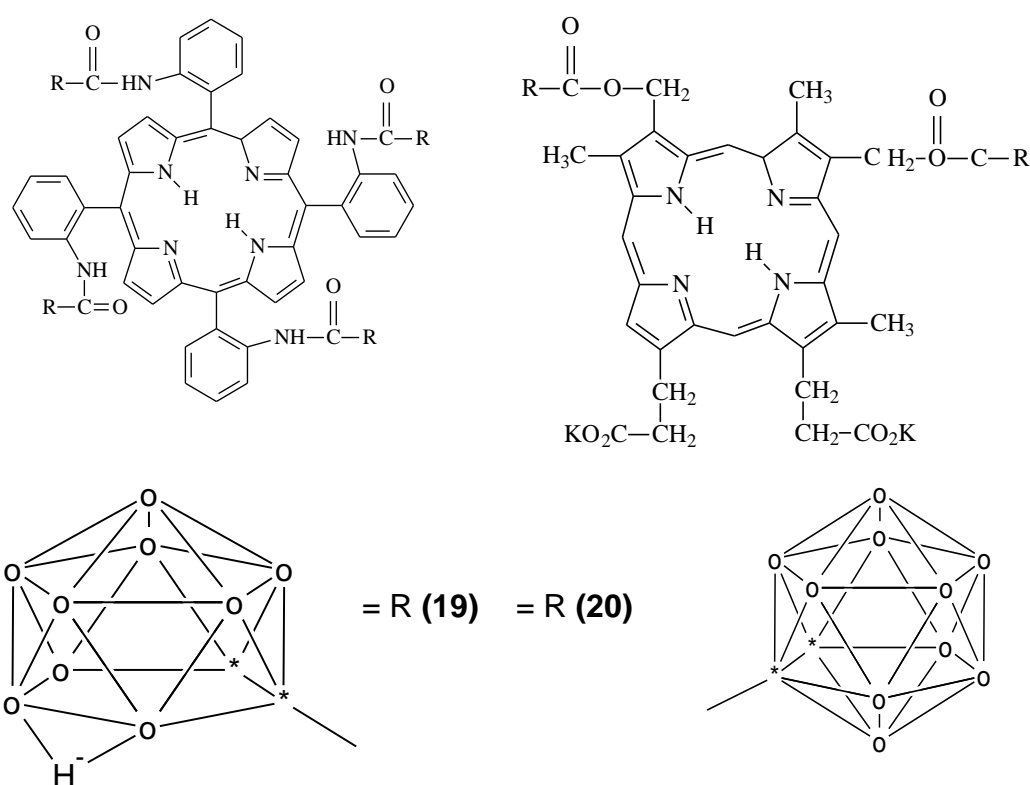


**Figure 10:** Boronated tetraphenylporphyrin (BTPP) and 2,4-( $\alpha,\beta$ -dihydroxyethyl) deuteroporphyrin IX tetrakis(carborane) carboxylate ester (BOPP), where open circles o = BH, and asterics \* = CH or C.

The boronated porphyrin, 2,4-( $\alpha,\beta$ -dihydroxyethyl)deuteroporphyrin IX tetrakis(carborane) carboxylate ester (BOPP) is said to be more selective for tumor cells than other drugs used for PDT, which have been used previously.<sup>65</sup> BOPP represents the second generation of photosensitisers. Its concentration in tumor cells is estimated to be about 200 to 400 times



compared to healthy brain.<sup>57</sup> This is much greater than the ratios which were found to be between 10-50 times compared to healthy brain for heamatoporphyrin derivative (HpD) in the same animal model used in the *in vivo* test experiments.<sup>75a-j</sup>

Other advantages offered by BOPP are high water solubility, stability, intracellular localization in mitochondria, efficient tumor cell killing and low phototoxicity effects. Studies show that BOPP requires less light for activation resulting in greater tumor destruction in less time compared with other PDT agents and is useful in the treatment of tumors outside the brain and treatment of other non-cancer indications.

## **1.14 Drugs in Clinical Trials**

Most of the drugs in use presently for photodynamic therapy are those developed by Pharamacyclics Inc. which is a pharmaceutical company developing products to improve upon current therapeutic approaches to cancer, atherosclerosis and retinal disease. The company's products are rationally designed, ring-shaped small molecules called texaphyrins (figure 5) which disrupt the biogenetic processes of diseased cells, such as cancer and atherosclerotic plaque.

### **1.14.1 Xcytrin<sup>(R)</sup>**

Xcytrin (8 in figure 6) is the first of an investigational class of drugs under texaphyrins. It is a small molecule that has a unique way of working inside diseased cells. It targets tumors in a new way. Xcytrin<sup>(R)</sup> was developed as an anti-cancer agent with a novel mechanism of action that is designed to selectively concentrate inside cancer cells, where it disrupts cellular metabolism, interferes with the flow of energy and ultimately induce apoptosis (programmed cell death), leading to the selective destruction of the cancer cells. It is a redox-active drug that has been shown to disrupt redox-dependent pathways in cells and inhibit oxidative stress related proteins. Its multifunctional mode of action provides the opportunity for

Xcytrin to be used in a broad range of cancers. It completed Phase 1 clinical testing in August 1996 to evaluate its safety in cancer patients receiving radiation therapy.<sup>76</sup> In March 1998, Phase 2 clinical trials to evaluate the safety and efficacy of Xcytrin<sup>(R)</sup> radiation sensitizer in patients with brain metastases was completed.<sup>76</sup> In the Phase 3 studies, an integrated analysis of 805 lung cancer patients demonstrated a statistically significant 6.5 month improvement in time to neurologic progression for patients receiving Xcytrin<sup>(R)</sup> plus whole brain radiation therapy compared to those receiving radiation alone. Xcytrin inhibits the enzyme thioredoxin reductase, which is a tumor growth promoter. It is paramagnetic, therefore it is detectable by magnetic resonance imaging (MRI),<sup>74</sup> thereby allowing the visualization of the drug in tumors. Preclinical studies showed that Xcytrin enhances the efficacy of radiation therapy and that of several commonly used chemotherapy agents. Currently, it is being investigated as a potential therapeutic agent in combination with radiation therapy and/or chemotherapy and as a single agent for various types of cancers.

#### **1.14.2 Lutrin<sup>(R)</sup>**

Lutrin (Lu-Tex, 9 in figure 7) was developed for the treatment of recurrent breast cancer to the chest wall and it has been found to be safe and effective. With Lutrin<sup>(R)</sup>, Phase 1 testing was completed in December 1996 for the treatment of cancer cells and its purpose was to determine the maximum tolerated dose and the pharmacokinetic profile for a single dose in the treatment for advanced cancer that is accessible to externally applied light. Phase 2 trial of Lutrin was initiated in July 1997 to evaluate safety, tolerability and efficacy of Lutrin photosensitizer in photodynamic treatment of recurrent breast cancer to the chest wall in patients who have failed previous chemotherapy and radiation therapy and by May 1999 it was found to be safe and effective in drug and light dose trials.<sup>77a</sup>

Fifty-seven (57) treatment courses were given to 52 patients with advanced refractory disease. Eighty-two percent of these patients had failed three or

more chemotherapy regimens and all the patients had recurrence or persistence of tumor following radiation therapy to the chest wall.

The study evaluated the administration of different doses of Lutrin, followed by illumination of the chest wall with light delivered at either three hours, six hours, twenty four hours, forty-eight hours, seventy-two hours or ninety-six hours after intravenous injection of the drug. Each patient, in the 11 cohorts tested, received illumination with light to large areas of the chest wall (up to 240 cm<sup>2</sup>) encompassing both the tumor and adjacent uninvolved skin. The purpose of the study was to identify treatment regimens that demonstrated anti-tumor activity with an acceptable level of treatment-related adverse events.

Tumor response was determined using an investigator's global assessment, which was based on physical examinations and photographs of the chest wall disease. All lesions within the treatment field were evaluated and an overall assessment of efficacy was made for each patient. Tumor responses were seen in 64 % of patients. In 42 % of patients, the global assessment following treatment indicated that tumors were either not detectable (20 %) or had obvious significant decrease evident on physical examination or photographs (22 %).

Safety and tolerability appeared to be dependent on both drug dose and the time interval between Lutrin administration and illumination of the chest wall with light. Patients receiving chest wall illumination 24 hours or more, following intravenous administration of Lutrin, experienced pain that was manageable with standard analgesics. Pain was more severe in patients treated with light given at shorter intervals, sometimes requiring conscious sedation. Cutaneous toxicity, including eschar formation or necrosis, was seen in the skin overlying the tumors in 11 of 39 patients treated with light at time intervals less than 24 hours.

Only two out of 18 patients receiving light illumination 24 hours or more after receiving Lutrin experienced this toxicity. Cutaneous toxicity was

limited to the tumor-involved areas of skin except in patients receiving the highest doses of Lutrin followed by photoillumination given at the shortest intervals in this group of patients.

Lutrin is a lutetium-texaphyrin molecule that is activated by a wavelength of light that is capable of penetrating deeply through tissues and blood. Lutrin is cleared relatively quickly from the blood and normal tissues but accumulates in tumors providing the potential to selectively treat large tumors with reduced damage to adjacent normal tissues. In previous studies, significant pain and skin reactions in the illuminated field were seen in patients with recurrent breast cancer receiving photoillumination of large areas of the chest wall within three hours of administration of Lutrin.

#### **1.14.3 Antrin<sup>(R)</sup>**

Antrin<sup>(R)</sup> (Lu-Tex, 9 in figure 7) phase 1 clinical trials were conducted at Stanford University Medical Centre and Mid-America Heart Institute in Kansas city for the photoangioplasty of peripheral disease in January 1998. In 2002, Pharmacyclics announced that researchers had presented preclinical and Phase 1 data showing the potential utility of photoangioplasty (PA) with antrin injection in helping to eliminate some of the underlying causes of atherosclerosis. The presentations by Dr. Moyota Hayase of Stanford University and Dr. Krishnankutty Surhir of Pharmacyclics showed that Antrin photoangioplasty caused elimination of macrophages through apoptosis, that is, cell death and atheroma burden in an *in vivo* animal model, and apoptosis of macrophages and coronary smooth muscle cells *in vitro* in human coronary artery cells respectively. Antrin<sup>®</sup> Injection is a water-soluble photoactive agent that accumulates selectively in vascular plaque and is cleared readily from the rest of the body. In photoangioplasty, Antrin is injected into the bloodstream, where it accumulates in blood vessel plaque. These targeted areas are then exposed to far-red light, which is delivered by an optical fiber inserted into the vessel using standard techniques. When activated by the light, Antrin generates a chemical reaction that may reduce or destroy the plaque by

eliminating macrophages and smooth muscle cells that are involved in atherosclerosis and restenosis.<sup>77b</sup>

#### **1.14.4 Verteporfin**

Verteporfin, (Visudyne<sup>®</sup>, 19 in figure 9) is a light-activated drug used in photodynamic therapy (PDT). Once Verteporfin is activated by light in the presence of oxygen, highly reactive, short-lived reactive oxygen radicals are generated. Light activation of Verteporfin results in local damage to neovascular endothelium, resulting in vessel occlusion.

BPD Verteporfin is in Phase 2 clinical trials for cutaneous lesions which were planned from 1995 having completed Phase 1 and Phase 2 and has achieved 100% complete response rates. Clinical trials of BPD Verteporfin were conducted at the Skin Care Centre in Vancouver Hospital, Canada.<sup>75a</sup> Photodynamic therapy with Visudyne<sup>®</sup> (Verteporfin) has been shown in two randomized controlled studies involving 609 patients to be effective for patients with choroidal neovascularization (CNV) secondary to age-related macular degeneration (so-called "wet form of AMD"), the type of late age-related macular degeneration that is the most frequent cause of visual loss to the level of legal blindness or worse. In clinical studies, patients with predominantly classic choroidal neovascularization (CNV with distinct, subretinal neovascular membranes) showed clinically significant results; in comparison, among patients demonstrating less than 50% classic choroidal neovascularization at the initial visit, there was no improvement in outcome compared to placebo treatment. After 12 months, 67 % of patients treated with Verteporfin lost less than 3 lines of visual acuity, compared to 40 % of patients treated with placebo (sham treatment). Patients with predominantly classic (as opposed to occult) CNV lesions exhibited the greatest benefit, with 77 % of Verteporfin -treated patients versus 27 % of placebo-treated patients losing less than 3 lines of visual acuity at 12 months. A series of evaluation and studies spanning over 15 years by different scientists and researchers have confirmed Verteporfin to be effective compare to classic treatments.<sup>75b</sup>

Augustin and Schmidt-Erfurth<sup>75c</sup> reported that pilot studies as well as large case studies suggested that a combination of photodynamic therapy (PDT) and intra-vitreous triamcinolone acetonide has the potential to improve visual outcomes and reduce the need for additional PDT treatments. They noted that randomized, prospective clinical trials are underway to confirm the safety and effectiveness of this novel treatment modality.

Cruess et al.<sup>75d</sup> noted that PDT has been performed in several other ocular pathologies with some remarkable results. These extended applications include choroidal neovascularisation (CNV) secondary to choroiditis and retino-choroiditis, angioid streaks, central serous chorioretinopathy, retinal angiomatous proliferation, parafoveal telangiectasia or CNV associated with macular dystrophy and idiopathic CNV, as well as diseases without CNV, such as choroidal hemangioma, retinal hamartoma, choroidal melanoma, chronic central serous chorioretinopathy, angiomatous lesions secondary to systemic diseases, rubeosis iridis or neovascular glaucoma. With the introduction of anti-vascular endothelial growth factor (VEGF) therapy, the role of PDT will certainly change.<sup>75e</sup>

Brown et al.<sup>75f</sup> discussed the rationale for combining anti-angiogenic treatment with Visudyne PDT in the management of choroidal neovascularization (CNV) due to age-related macular degeneration (AMD) and evaluated available evidence for the therapeutic benefits of such approaches. Treatments for CNV due to AMD can be directed at either the vascular component of CNV or the angiogenic component that leads to the development of the condition. Verteporfin targets the vascular component, whereas anti-angiogenic agents (such as pegaptanib and ranibizumab) target key mediators of the angiogenic cascade. The different mechanisms of action of these approaches offer the potential for additive or synergistic effects with combination therapy. In addition, anti-angiogenic agents might counteract up-regulation of angiogenic factors (including VEGF) that occur after Verteporfin PDT. Results from pre-clinical and clinical studies of the

combination of ranibizumab or pegaptanib with Verteporfin warrant continued investigation. The author concluded that the use of anti-angiogenic agents in combination with Verteporfin may have the potential to improve visual outcomes and reduce the number of treatments in eyes with CNV due to AMD, and requires further evaluation in randomized, controlled clinical trials.

In a recent review on Verteporfin combination regimens in the treatment of neovascular age-related macular degeneration, Shah et al.<sup>75g</sup> concluded that a rationale exists for investigating combination approaches to target different processes in CNV pathogenesis, which may optimize treatment benefits in neovascular AMD.

Cruess et al.<sup>75d</sup> noted that PDT with Verteporfin has been used less comprehensively in the treatment of age-related macular degeneration (AMD), and specifically of choroidal neovascularisation (CNV), since the advent of anti-angiogenic therapies. Recently, there has been a renewed interest in PDT as an adjunct to these and other agents in the treatment of neovascular AMD. In light of this new development and the European Medicines Evaluation Agency's (EMA) recent labelling decision to rescind approval for the use of PDT in occult CNV lesions, these investigators reviewed the evidence supporting its clinical application. Photodynamic therapy provided the first pharmacological treatment for patients suffering from subfoveal CNV, the major cause of severe vision loss in AMD. Key clinical trials evaluating the safety and effectiveness of PDT have examined patients with all lesion subtypes, with the primary labelled indication (i.e., lesions containing a classic component of greater than or equal to 50 %) deriving from the results of the treatment of Age-related Macular Degeneration with Photodynamic Therapy (TAP) study.<sup>75h-j</sup> The subsequent TAP Study Group post-hoc categorization of lesions as predominantly classic is open to question, however, as it appears that the overall effectiveness in this group only may have reflected the especially strong response in 100 % classic lesions. Based on a subgroup analysis of the Verteporfin in Photodynamic Therapy Study, the indication for PDT

subsequently was expanded in some jurisdictions, including that of the EMEA, to include occult lesions with no classic component. However, the subsequent Visudyne in Occult Study found no benefit in 100% occult lesions, resulting in the EMEA rescinding its approval for this indication.<sup>75j</sup>

#### 1.14.5 Temopofin

Temopofin (**21** in figure 11), trade name Foscan, [*meso*-tetra(*meta*-hydroxyphenyl)chlorin] (mTHPC) represents a very potent second-generation synthetic photosensitizer. It was shown to be effective in the photodynamic therapy of early or recurrent oral carcinomas, in the palliative treatment of refractory oral carcinomas and in the treatment of primary non-melanomatous tumors of the skin of the head and neck.<sup>67</sup> Until now for all positive findings an intravenous application of the photosensitizer was mandatory.<sup>78a</sup> In the case of cutaneous malignant or non-malignant diseases a topical application of the drug onto the site of the disease followed by illumination is advantageous. Unfortunately, mTHPC is a highly hydrophobic drug with a low percutaneous absorption.

It is marketed in the European Union (EU) under the brand name Foscan. The United States Food and Drug Administration (FDA) deemed Foscan non-approvable in 2000. The EU approved its use in June 2001 while in Germany good results were obtained in 21 out of 35 patients treated with the drug.<sup>78b</sup> The disadvantage of the drug is that, due to the fact that it is highly hydrophobic and therefore takes a long time to clear from the body, patients can remain photosensitive for several weeks after treatment.<sup>78c</sup>

Temoporfin (Foscan) is a single pure chlorin derivative which is photoactivated at 625 nm and has a molar extinction coefficient of  $3 \times 10^4 \text{ M}^{-1} \text{ cm}^{-1}$  and it has been shown to have a plasma half-life in humans of ~45-65 hrs. Due to the potency of Foscan, a smaller drug dose (as low as 0.1 mg  $\text{Kg}^{-1}$  of body weight) and light intensity (as low as  $10 \text{ J cm}^{-2}$ ) are required for obtaining a very robust response. Moreover, drug doses and light intensity required to obtain a similar response to Photofrin are up to



100 times lower due to the superior photophysical properties and higher singlet oxygen yield of Foscan. The biological mechanism of action of Foscan is via direct tumor cell toxicity as well as vascular damage.<sup>78d-g</sup>

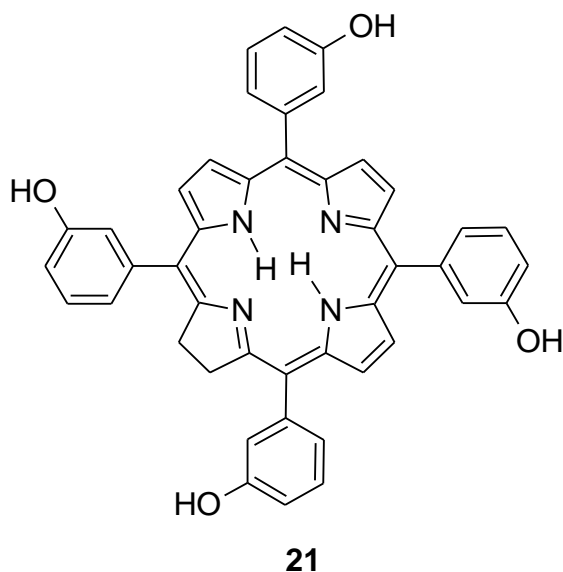


**Figure 11:** *Meso-tetra(meta-hydroxyphenyl)chlorin (mTHPC)*

#### 1.14.6 Boron Neutron Capture Therapy (BNCT)

The clinical trials of boron containing compounds as boron neutron capture therapy (BNCT) started in the 1950s and early 1960s. These compounds used boric acid and some of its derivatives as delivery agents, but these simple chemical compounds were nonselective, with poor tumor retention, and attained low tumor/brain ratios.<sup>79a</sup> In the 1960s, two other boron compounds emerged from investigations of hundreds of low molecular weight boron-containing chemicals. The first was [(L)-4-dihydroxyborylphenylalanine] called boronophenylalanine, (BPA) which was based on arylboronic acids. The second was sodium mercaptoundecahydro-*closo*-dodecaborate called BSH based on a newly discovered borane anion. The major challenge in the development of boron delivery agents has been the requirement for selective tumor targeting to achieve boron concentrations (~20 µg/g tumor) sufficient to deliver therapeutic doses of radiation to the tumor with minimal normal tissue toxicity.<sup>79b</sup> These second-generation compounds had low toxicity, persisted longer in animal tumors

compared with related molecules, and had tumor/brain and tumor/blood boron ratios of  $> 1$ .<sup>79b</sup>

#### **1.14.7 Third-generation boron delivery agents**

So-called third-generation compounds mainly consist of a boron group or cluster attached via a hydrolytically stable linkage to a tumor-targeting moiety, such as low molecular weight biomolecules or monoclonal antibodies (mAb).<sup>79b</sup> For example, the targeting of the epidermal growth factor (EGF) receptor (EGFR) and its mutant isoform EGFRvIII, which are over expressed in gliomas as well as in squamous cell carcinomas of the head and neck, also has been one such approach. Usually, the low molecular weight bio-molecules have been shown to have selective targeting properties and many are at various stages of development for cancer chemotherapy, photodynamic therapy and antiviral therapy.<sup>79b</sup>

Currently boronated porphyrin (BOPP) is in clinical trials in Japan, Europe and the United States. The vast majority of patients treated have had high-grade gliomas. Treatment consist first of “debulking” surgery to remove as much of the tumor as possible, followed by boron neutron capture therapy (BNCT) at varying times after surgery. Sodium borocaptate and boronophenylalanine administered intravenously have been used as the boron delivery agents.<sup>57,65,68</sup> The best survival data from these studies are at least comparable with those obtained by current standard therapy for glioblastoma multiforme, and the safety of the procedure has been established.

#### **1.14.8 Amino Levulinic Acid (ALA)**

Amino levulinic acid (ALA) has demonstrated highest efficacy in topical photodynamic therapy (PDT), and has become the most clinically useful agent for topical PDT. For actinic (solar) keratosis, topical ALA-PDT using Levulan<sup>R</sup> (20 % topical solution, DUSA Pharmaceuticals) is already postulated to be the treatment of choice.<sup>78g</sup> In December 1999, the United

States Food and Drug Administration (FDA) approved this topical product for the treatment of actinic keratosis.<sup>78g</sup> Levulan<sup>R</sup> is well tolerated and leads to excellent cosmetic results with only minor side effects.

$\delta$ -ALA is an endogenous precursor of photosensitizing porphyrin metabolites. Normally, the synthesis of ALA is tightly controlled by feedback inhibition of the enzyme ALA-S, presumably by intracellular heme levels.<sup>78g</sup> Therefore, when exogenous ALA is provided to the cell through topical application, PPIX (a metabolite of ALA) accumulates by bypassing the rate limiting enzyme ALA-S (Schemes 1-5).

In PDT, light absorption by 5-ALA metabolites, e.g., PPIX, results in an excited state of the molecule and subsequent generation of reactive oxygen species, which can react further to form superoxide and hydroxyl radicals. The tissue-specific phototoxic effects resulting from local application of ALA and light irradiation are the basis of photodynamic therapy for actinic keratosis (AKs) and other in situ neoplasias.<sup>78g</sup>

#### **1.14.8.1 Pharmacology of ALA**

The standard procedure of topical ALA-PDT for skin tumors involves the application of 10-20% ALA in an oil-in-water emulsion, which is then covered by an occlusive dressing to enhance the tissue penetration of the drug and to prevent undesired photobleaching of porphyrins by visible light.<sup>78g</sup> Removal of the dressing is followed by irradiation of the PPIX that is produced in situ, and this leads directly to tissue photodamage.

#### **1.14.8.2 Adverse Effects of ALA**

Contraindications for ALA-PDT include cutaneous photosensitivity, porphyria, and allergies to ALA or to any of its components. Patients who have concomitant disorders that are provoked or aggravated by light are evaluated cautiously, and it is still not known whether ALA or its metabolites are excreted in breast milk, therefore, caution is advised when treating women who are breast feeding.<sup>78g</sup>

Following topical applications of ALA, the treated site becomes photosensitive, and patients are warned to avoid sunlight or bright indoor light (e.g., examination lamps, theater lamps, tanning beds, or lights at close proximity), because exposure may result in a stinging and burning sensation and cause erythema and/or edema of the lesions. As a result of light exposure during PDT treatments, patients may experience burning, stinging, or itching, which is restricted to the illuminated area. The discomfort will peak within the first minutes of irradiation and it may continue for several hours, though in a decreasing manner. Local anesthesia or intensive cooling can help control the pain, especially when disseminated, large, ulcerative, or inflamed areas are treated.<sup>78g</sup> The normal course of clinical response to PDT is usually distinguished by crusting, scaling, pruritus, and healing within 1-4 weeks. Urea preparations can be used to resolve dry crusts and accelerate re-epithelialization. ALA produces very good cosmetic results, often superior to the outcome achieved by cryosurgery, surgery, or topical chemotherapy. Generally, scar formation is minimal or absent and rarely, residual hyperpigmentation or hypopigmentation of the treated area can occur.<sup>78g</sup>

### **1.15 Estimated New Cancer Cases<sup>78-81</sup>**

Cancer is the second leading cause of death and the number of deaths increases annually. The most recent estimates in 1990 suggest a total of 8.1 million new cases which is an increase of about 37% from 1975 suggesting an increase of 2.1% per year which is faster than that of the world population (1.7% per year). The main cancer in the world today is the lung cancer (1.04 million cases and 921,000 deaths), followed by the stomach cancer (789,000 cases and 628,000 deaths). Breast cancer is the third most common cancer (796,000 cases) in the world but is the fifth cause of deaths in women. Cancers of the colon and rectum (783,000 cases and 437,000 deaths) and liver (437,000 cases 427,000 deaths) rank more highly than female breast cancer as cause of death.

The estimated results of 1995 showed that by 1999 after 4 years, the increase in cancer cases may be very high (1,221,800 new cases which are expected to be diagnosed in United States only) with an increase in cancer death excluding basal and squamous cell skin cancers, breast carcinoma *in situ* melanoma and carcinoma. Among men, the most common cancers in 1999 were expected to be cancers of the prostate, lung and bronchus, and colon and rectum. Among women, the three cancers expected to be the most highly diagnosed were breast, lung and bronchus, and colon and rectum. It was estimated that there will be more than 12 million new cancer cases in 2007 worldwide, of which 5.4 million would occur in economically developed countries and 6.7 million in economically developing countries. The corresponding estimates for total cancer deaths in 2007 were 7.6 million (about 20,000 cancer deaths a day), 2.9 million in economically developed countries and 4.7 million in economically developing countries. By 2050, the global burden is expected to grow to 27 million new cancer cases and 17.5 million cancer deaths simply due to the growth and aging population.<sup>81a</sup> In economically developed countries, the three most commonly diagnosed cancers are prostate, lung, bronchus, colorectal among men breast, colorectal and lung and bronchus among women. In economically developing countries, the three most common diagnosed cancers are lung and bronchus, stomach and liver in men, and breast, cervix uteri, and stomach in women. In both economically developed and developing countries, the three most common cancer sites are also the three leading causes of cancer deaths.<sup>81b</sup>

## **1.16 Photosensitiser Amphiphilicity in PDT**

### **1.16.1 Pharmacokinetics**

Fig.12 shows a schematic representation of the membrane bi-layer showing the two layers. The aliphatic portion of the membrane is hydrophobic while the ionic portion is hydrophilic. All cellular organelles such as the nucleus, mitochondria, and cytoplasmic reticulum are surrounded by such a membrane. Entry of extracellular substances into

the cell and into all intracellular organelles is controlled by such membranes. The dissolved photosensitiser is transported by the blood or plasma fluid to the tumor cells. Before reaching the target cells, it passes through the different cell environments, a hydrophobic environment in the cell membrane and a hydrophilic environment in the cytoplasm. Most of the blood is composed of water, so for the photosensitiser to be transported by the blood it must be hydrophilic. However for the photosensitiser to reach the affected cells, it must also be hydrophobic enough to pass easily through the various cell membranes. Hence, a good photosensitiser must possess enough hydrophilicity to be transported easily through the blood and enough hydrophobicity to cross the various membranes.

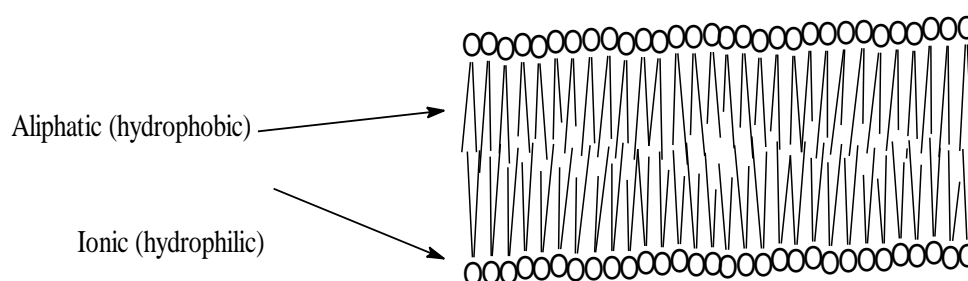


**Figure 12:** Schematic representation of the cell membrane bilayer

#### **1.16.1.1 Blood and or Plasma Transport**

#### **1.16.1.2 Excretion and Elimination**

If the photosensitiser is too hydrophobic, it won't get out of the body and will persist in the tissues. For excretion and elimination, it must be hydrophilic. Experimental studies have shown that hydrophobic photosensitisers take a long time to be excreted out of the body. So there is a high risk for the patient since a long period of time is needed for the patient to be in the dark so as to prevent general photosensitivity, while the drug is being cleared from the body. Ideally, the photosensitiser needs to

possess equal hydrophilicity and hydrophobicity since it needs to pass through both hydrophilic and hydrophobic environments before and after reaching the target cells.

### **1.16.2 Activity Determinant**

After several years in the development of PDT photosensitisers, tumor tissue accumulation and singlet oxygen quantum yields have emerged among the many criteria required for a good PDT photosensitiser.

#### **1.16.2.1 Tumor Tissue Accumulation**

If the porphyrin is too hydrophilic, much of it will not reach the tumor cells leaving many affected cells having low photosensitiser concentration. This leads to incomplete death of tumor cells since most of the photosensitiser passes out of the body before reaching the target cells, resulting in a small amount of the porphyrin that accumulates in tumor tissue. Much more of the photosensitiser will accumulate in tumor tissue if it is hydrophobic.

#### **1.16.2.2 Singlet Oxygen Quantum Yields**

Since singlet oxygen is important in cell destruction by PDT, it is needed in large quantities to maximize tumor destruction. Simply put, the more singlet oxygen produced, the more tumor cells will be destroyed.

### **1.17 Future Perspectives**

#### **1.17.1 New Photosensitisers**

Several new second generation photosensitisers are now on clinical trials and are promising good results because their treatment times, typical light and drug doses are marginally smaller than for haematoporphyrin derivative (HpD). One of these photosensitisers is the aluminum

phthalocyanine which shows good activity against brain, colon, bladder and pancreatic cancers in experimental studies and is effective against large and deeply penetrating tumours.<sup>81</sup> Another one is 5,10,15,20-tetra(3-hydroxyphenyl)chlorin (Foscan) which is useful in treating mouth, head and neck cancers, being superior to Photofrin, and 5-ALA. It is possible that the PDT properties of this sensitizer are so promising because of its amphiphilic properties and tumor selectivity, although it is significantly hydrophobic. Viewed against Photofrin, which was approved in the U.S in January 1998 for treating esophageal cancers, early stage lung cancer, and other malignancies, the second-generation sensitizers including ALA-PDT are beginning to prove their worth.

### **1.17.2 Third Generation Sensitizers**

After the second generation sensitizers, third-generation photosensitizer are now expected. Investigations are looking for sensitizers that can have two-photon absorption. Such sensitizer molecules could have two parts; one part rapidly picks up two photons at say 840 nm or higher and converts them into a single photon at 420 nm which is then absorbed by the sensitizer's second porphyrinic part. Such a sensitizer would be able to generate singlet oxygen from its triplet state even though infrared exciting light was being used. With the emergence of the second-generation and third-generation sensitizers, it should not be long before PDT takes its place in the diagnosis and treatment of many different cancers.

### **1.17.3 Selectivity**

Tumor selectivity is the destruction of tumor relative to non-tumour tissue and is related to the ratio of the concentration of the photosensitizer in tumor tissue over the concentration of the photosensitizer in non-tumor tissue. The higher this ratio the better the selectivity, provided the destruction of tumor is directly proportional to the concentration ratio. An important factor with new sensitizers is the ability to enhance selectivity of tumor damage by using low doses of the sensitizer. Whether



photosensitivity is an important issue depends on the treatment. In treatment of lethal tumors, it doesn't matter how photosensitive patients become; the priority is to ensure maximum tumor kill.

#### **1.17.4 Photobleaching and General Photosensitivity**

At low concentration, the photo excited photosensitiser may undergo photobleaching (light induced self-destruction). This can occur by a variety of mechanisms. Photofrin II, which has got its clinical approval, undergoes photobleaching under clinical conditions but this is not so disadvantageous, but in fact adds another dimension to photodynamic therapy. If there is a drug that is several times concentrated in tumors than in normal tissues, it will be possible to cure a tumor at depth, if a high enough light dose is available to it. A low dose of drug can be chosen which because of bleaching will not kill the normal cells. However, much light will be used, and if the tumors contain more drug in it, it will be destroyed before the drug is bleached. If a drug has greater penetration to the skin, it is likely for that drug to have more side effects than the one that penetrates the skin only slightly. It may be that clinical applications need to be looked upon so as to avoid general skin photosensitivity.

#### **1.17.5 Mechanisms of Cell Killing**

It has been suggested that the singlet oxygen produced from the excited state of the photosensitiser is not involved in producing cytotoxic species because it is too short-lived. Scientists have also failed to detect singlet oxygen in cells because it is so short-lived. Thus there is uncertainty in what is happening. The photosensitiser singlet state may be short-lived because it is very reactive, which may lead to difficulty in detection. While it is agreed that the photosensitiser triplet states and singlet oxygen are probably important agents in cytotoxicity, the role for the sensitizer excited singlet state cannot be ruled out.

In order to clarify the *in vivo* photodynamic mechanism, additional evidence of the interaction of oxygen with sensitizer triplet state is necessary. Direct observation of effective quenching of sensitizer triplet state by oxygen and the absence of quenching of triplet states without oxygen with simultaneous cessation or weakening of the photodynamic effects as proof of *in vivo* formation of singlet oxygen and predominant involvement of this mechanism in photodynamics was accomplished using sensitizer phosphorescence at room temperature by Losev.<sup>82a,b</sup> Subsequently, Knyukshto *et al*<sup>83</sup> found new bands in the absorption spectra of Pt(II) and Pd(II) complexes of octaethylporphyrin and tetraphenylporphyrin that differ in the nature, number, and position of their side substituents. The bands were attributed to spin-forbidden transitions from the ground  $S^0$  state to the excited  $T^1$  and  $T^2$  triplet states, suggesting intersystem crossing.

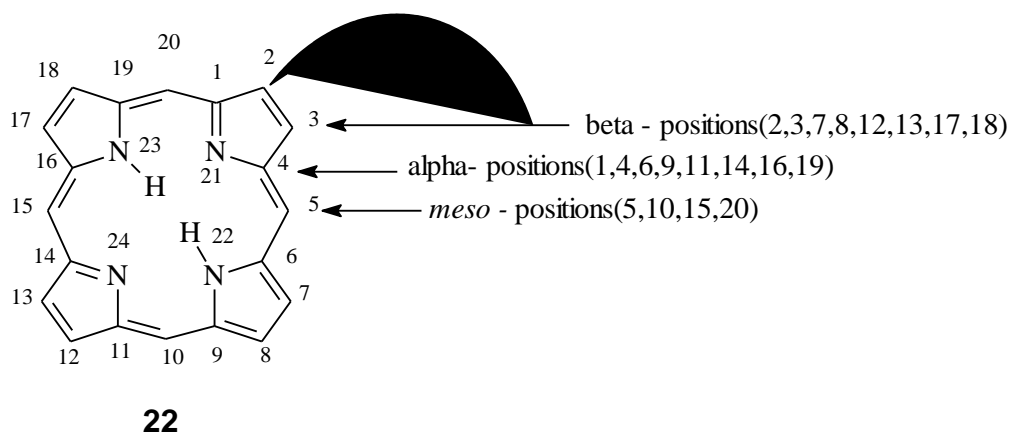


**Figure 13:** Structure of porphine, the simplest porphyrin

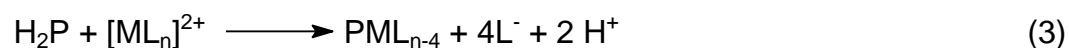
### 1.18 Structure and numbering of the Porphyrin

A porphyrin is a heterocyclic macrocycle derived from four pyrroline subunits interconnected at their  $\alpha$ -carbon atoms via methine bridges ( $=CH-$ ). Many porphyrins occur in nature, such as in green leaves and red blood cells, and in bio-inspired synthetic catalysts and devices. They are

most famous as components of hemoglobin, which is a component of red blood cells and chlorophyll, which is a component of green leaves in plants. Hemoglobin is responsible for carrying oxygen in the blood and chlorophyll is responsible for the production of carbohydrates in plants.

### 1.18.1 Complexes of porphyrins and related molecules

Porphyrins bind metals to form complexes. The metal ion, usually with a charge of +2 or +3, is in the central  $N_4$  cavity formed by the loss of two protons, in which most metals can be inserted. A schematic equation for these syntheses is shown:



Where M = metal ion and P = porphyrin, L = counter anion (ligand).

A porphyrin in which no metal is inserted in its cavity is sometimes called a *free base porphyrin*. Some iron containing porphyrins include hemes and heme-containing proteins or hemoproteins. They are found extensively in nature. Hemoglobin and myoglobin are two oxygen binding proteins that contain iron porphyrins.

Related to porphyrins are several other heterocycles, including corrins, phthalocyanines, chlorins, bacteriochlorins, and corphins. Chlorins (2,3-dihydroporphyrin) are reduced porphyrins that contain two more hydrogens than porphyrins in one of the four pyrrole subunits.<sup>84a,b</sup> This structure occurs in chlorophyll. Replacement of two of the four pyrrole subunits with reduced pyrrole subunits that contain two more hydrogens results in either a bacteriochlorin (where the reduced subunits are across) or an isobacteriochlorin (where the reduced subunits are adjacent), depending on the relative positions of the reduced pyrrole subunits.

Porphyrins occur widely in nature with many important biological representatives, including hemes, chlorophylls, and several others.

Porphyrins are present in the urine, excreta, bile, bone marrow and blood. In the blood most of the porphyrins are in the red cells, in very small quantities as protoporphyrin and coproporphyrin. The analysis of these porphyrinic products in the urine and excreta forms the basis for the diagnosis of many liver diseases.<sup>85</sup>

Porphyrins also occur in minerals, and they survive many years in carboniferous fossils. They make blood red and grass green. They were originally studied for their importance in oxygen transport, photosynthesis, energy production, metabolism and the disease porphyria.<sup>86</sup> There are a number of synthetic porphyrins prepared for purposes ranging from basic research to functional applications in society. All the different kinds of porphyrins share in common the porphyrin macrocyclic substructure and the basic substructure of all porphyrins consists of four pyrrolic subunits linked by four methine bridges as shown in Fig. 13 above.

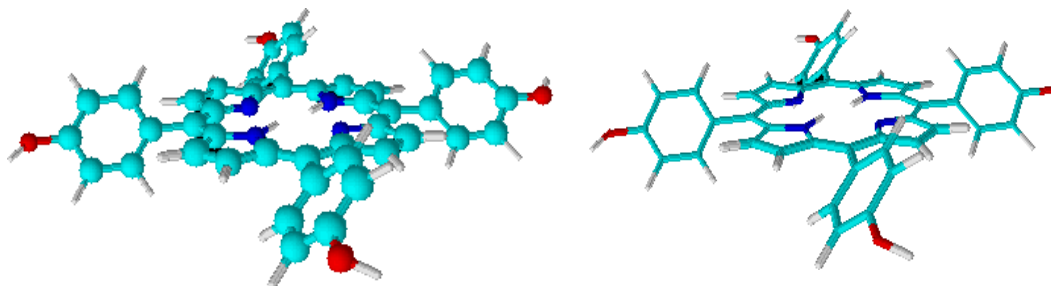


**Figure 14:** *Meso* steric interactions alone

Many porphyrins have been reported to have been synthesized bearing numerous and bulky substituents. A porphyrin has twelve positions available for substitution including eight beta-positions (2,3,7,8,12,13,17,18) and four *meso* positions (5,10,15,20) Fig. 13. The basic porphyrin macrocycle is flat or planar. Among the porphyrins with numerous or bulky substituents in the *meso* positions, it has been suggested that non-planarity is predominantly imparted by steric interactions. This is illustrated in figure 14.

### 1.18.2 *Meso* steric interactions

When a porphyrin is substituted with a large group on one or more of the *meso* carbons, there are steric interactions between the *meso* substituents and the adjacent *beta*- substituents.

### 1.18.3 *Beta* steric interactions

When porphyrin is substituted with a large group on adjacent *beta* carbons, there is additional steric strain between substituents. It has been observed that the more highly substituted the porphyrin periphery and, the greater the substituents the less planar the porphyrin will be. This is illustrated in figure 15.

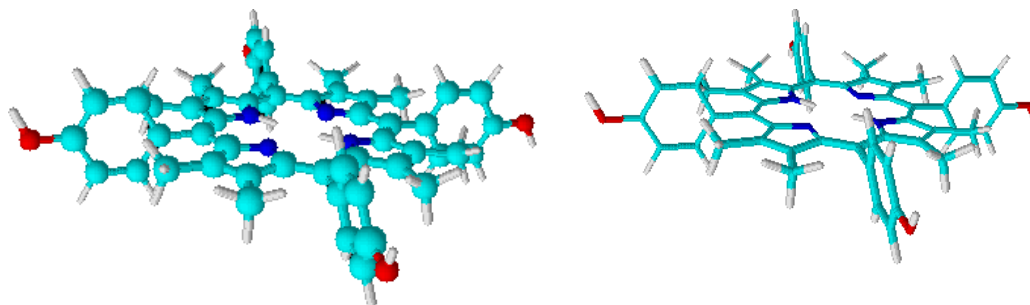
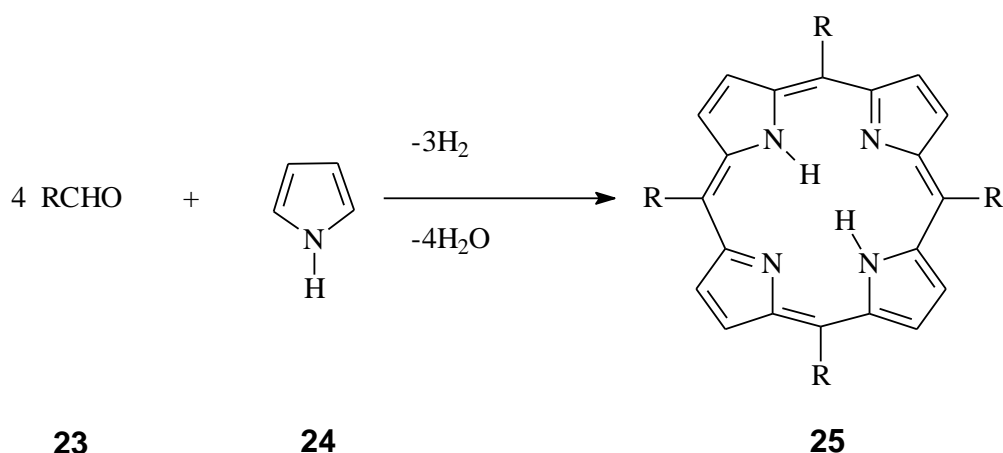


**Figure 15:** *Meso*, and *beta* steric interactions

## 1.19 Rothmund type Synthesis of porphyrins

One of the more common syntheses for porphyrins is based on work by Paul Rothmund. His techniques underpin subsequent syntheses such as those described by Adler et al.<sup>87-89</sup> These syntheses of simple porphyrins such as *meso*-tetraphenylporphyrin are also commonly carried out in university teaching laboratories.<sup>88</sup> In this method, porphyrins are assembled from pyrrole and substituted aldehydes. Acidic conditions are essential. Formic acid, acetic acid and propionic acid are typical reaction solvents, or the use of *p*-toluenesulphonic acid with a non-acidic solvent. Lewis acids such as boron trifluoride etherate and ytterbium triflate have

also been known to catalyse porphyrin formation. A large amount of side product is formed and is usually removed by chromatography.



**Scheme 4:** Laboratory synthesis of porphyrin (based on Rothemund<sup>88,89</sup>)

### 1.19.1 Nomenclature of porphyrins

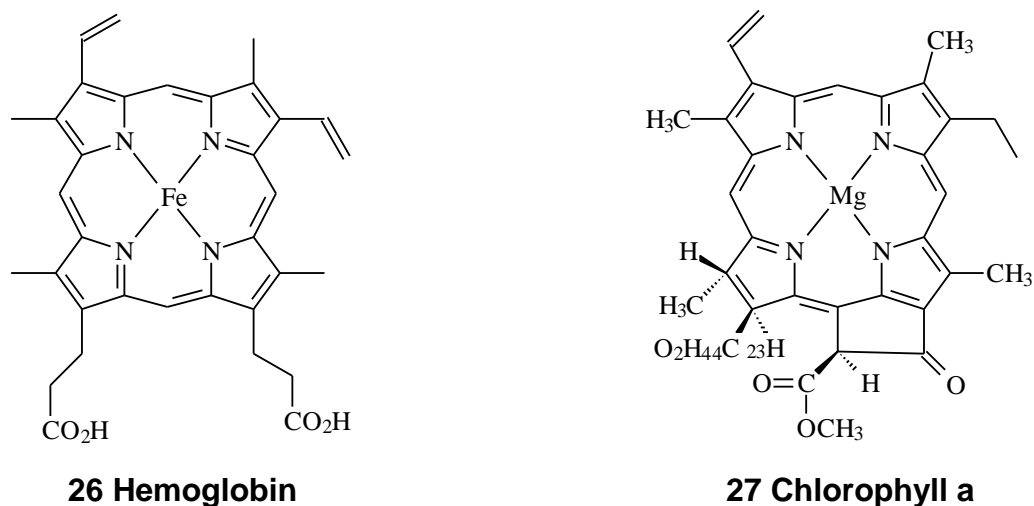
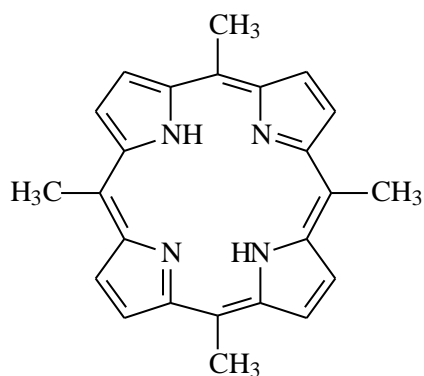


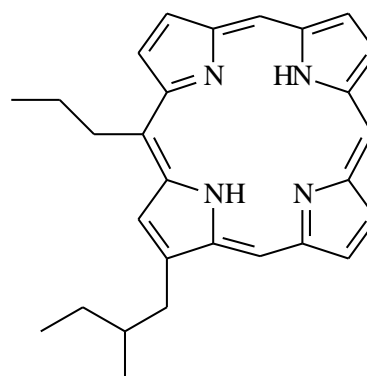
**Figure 16:** Naturally occurring porphyrins

Natural as well as synthetic porphyrins are named using their common names, but they can also be named using the IUPAC system. Most naturally occurring porphyrins are named using their common names. Examples are hemoglobin **26** and chlorophyll a **27**. The IUPAC nomenclature of porphyrins uses the numbering system shown in figure 13 on page 69. Examples of porphyrin naming using the IUPAC system are

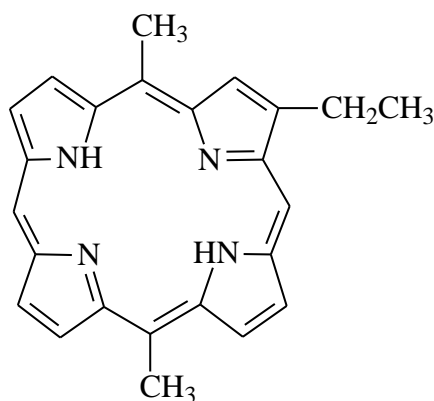
5,10,15,20-tetramethylporphyrin **28**, 3-(2-methylbutyl)-10-propylporphyrin **29**, and 8-ethyl-5,15-dimethylporphyrin **30** as shown in figure 17. The pyrrole rings of a porphyrin are usually numbered with Roman numerals I through IV (not shown), starting at the top left hand ring and proceeding clockwise. Positions at which substituents could be attached are numbered 1-20 starting from the alpha positions and proceeding clockwise.



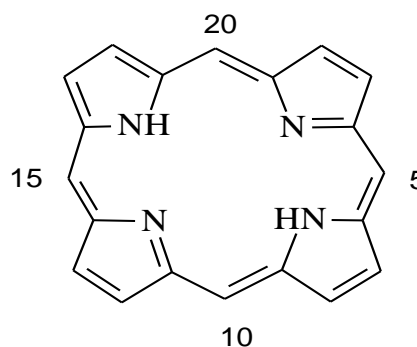
**28: 5,10,15,20-tetramethylporphyrin**



**29: 3-(2-methylbutyl)-10-propylporphyrin**



**30: 8-ethyl-5,15-dimethylporphyrin**



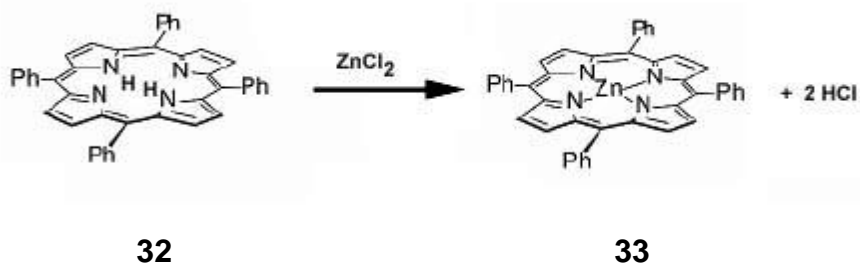
**31: Porphyrin Numbering**

**Figure 17: Nomenclature of porphyrins using IUPAC system**

### 1.19.2 Properties of porphyrins

Porphyrins comprise an important class of molecules that serve nature in variety of ways. The Metalloporphyrin ring is found in a variety of important biological systems where it is the active component of the system or in some ways intimately connected with the activity of the system. Many of these porphyrins synthesized are the basic structure of biological

porphyrins which are the active sites of numerous proteins, whose functions range from oxygen transfer and storage (haemoglobin and myoglobin) to electron transfer (cytochrome c, cytochrome oxidase) to energy conversion (chlorophyll). They also have been proven to be efficient sensitizers and catalyst in a number of chemical and photochemical processes notably photodynamic therapy (PDT). The diversity of their functions is due in part to the variety of metals that bind in the interior of the porphyrin ring system.<sup>90</sup> Upon metalation the interior of the porphyrin ring system deprotonates, forming a dianionic ligand.<sup>91</sup> The metal ions behave as Lewis acids, accepting lone pairs of electrons from the dianionic porphyrin ligand. Unlike most transition metal complexes, their color is due to absorptions within the porphyrin ligand involving the excitation of electrons from the  $\pi$  to the  $\pi^*$  molecular orbitals of the porphyrin ring.<sup>91</sup>



**Scheme 5:** Metallation of porphyrin

### 1.19.2.1 Electronic structure and UV-Visible spectra

The electronic absorption spectrum of a typical porphyrin consists of a strong transition to the second excited state ( $S^0$  to  $S^2$ ) at about 400 nm (the Soret or B band) and a weak transition to the first excited state ( $S^0$  to  $S^1$ ) at about 550 nm (the Q band). Internal conversion from  $S^2$  to  $S^1$  is rapid so fluorescence is only detected from  $S^1$ .<sup>90-92</sup>

It was Martin Gouterman who first proposed the four-orbital model in the 1960s to explain the absorption spectra of porphyrins<sup>92</sup>. According to this theory, the absorption bands in porphyrin systems arise from transitions between two highest occupied molecular orbitals (HOMOs) and two lowest



unoccupied molecular orbitals (LUMOs), and it is the identities of the metal center and the substituents on the ring that affect the relative energies of these transitions (Figures 18 and 19). Mixing splits these two states in energy, creating a higher energy 1 eu state with greater oscillator strength, giving rise to the Soret band, and a lower energy 1 eu state with less oscillator strength, giving rise to the Q-bands. The molecular orbital diagrams implicated in Gouterman's electronic transitions are illustrated in figures 18 and 19.

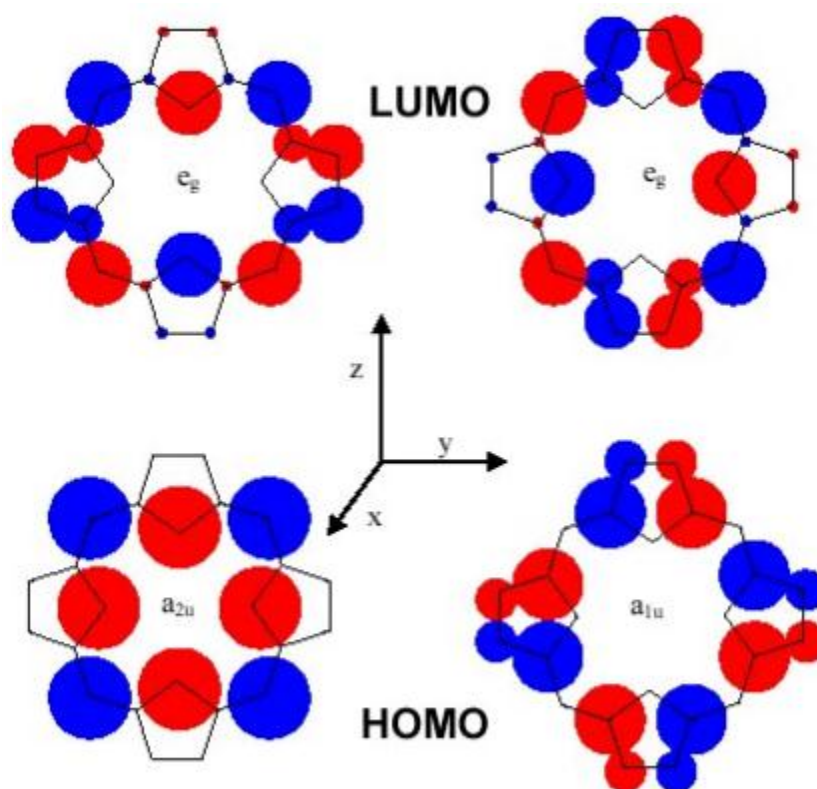


**Figure 18:** The Frontier Orbitals relevant to the Gouterman Four-Orbital Model<sup>90</sup>

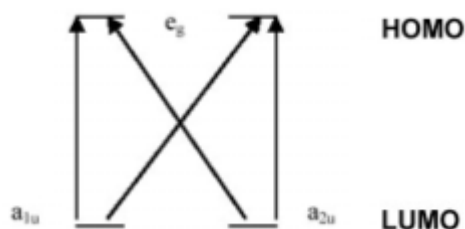


**Figure 19:** Orbital diagrams showing possible transitions for porphyrins.<sup>90</sup>

In the visible absorption spectra of porphyrins, the highly conjugated aromatic macrocycle shows an intense absorption in the region of about

400 nm; this absorption maximum is referred to as the Soret Band. Visible spectra of porphyrins also show four weaker bands, the Q bands, at longer wavelengths from about 450-700 nm.

Porphyrins contain a 22  $\pi$  electron system, although only 18 electrons can be involved in any particular delocalization; a feature that is critical for effecting a wide range of extra ordinary properties such as the ability to absorb visible light, to mediate the conversion of absorbed light to other forms of chemical and physical energy, and to enhance thermodynamic and kinetic stability. This conjugated system assumes so many resonance forms and can accept substituents at a number of positions. Porphyrins obey Huckel's rule for aromaticity in that they possess  $4n+2$   $\pi$ -electrons which are delocalized over the macrocycle. The extent of conjugation in the porphyrin system lowers the energy necessary for inner sphere electron transfer to occur due to the availability of  $\pi$ -orbitals and their ability to participate in the transfer of electrons.

#### **1.19.2.2 Bathchromic Electronic Spectral Shifts**

This is the guiding principle that provide chemists with the most difficult problem since they need to ensure that the porphyrin chromophore has the desired long-wavelength of absorption. Red shift or bathochromic effect is a shift of an absorption maximum towards longer wavelength. It may be produced by the change in the medium or by a substituent in the chromophore which leads to the red shift.<sup>90</sup>

Red shift or bathochromic effect has been achieved either by expanding the macrocycle to produce phthalocyanines, texaphyrins, porphyrin vinylogues etc; or by reducing one or more of the porphyrin's pyrrole rings to give chlorines. Another way of red-shifting and intensifying the long wavelength absorption band of the porphyrin is to extend the macrocycle conjugation, e.g. with ethynyl groups. The net effect is to give these compounds a green colour, compared to the usual porphyrinic purple/red colour. Hydrophilic environments also tend to cause red shifts.

These strategies caused a red shift and an increase in the intensity of the long wavelength absorption of the chromophore. Chlorins and phthalocyanines typically absorb more strongly in the 650-700 nm region (red region). In the red region there is the deepest tissue penetration of light. For the light to reach even the deepest cells, the wavelength must be in the red region. Since the tumor can be quite deep, red absorption of the photosensitizer is therefore needed for the light to effect damage at greater tissue depth. Hydrophilic groups in the porphyrin also tend to cause red shifts.

## **Chapter 2**

### **2.1 Problem Statement**

In an article, photodynamic therapy (PDT) was recommended as the most suitable method for cancer therapy in the developing world.<sup>78</sup> PDT is cost effective and simple to use. Unlike chemotherapy, no special training is required for nurses, or any post treatment course in intensive care unit. No engineer, computerised dosimetry computations, or additional costs for isotope re-treatment are required, as in radiotherapy. There are no blood transfusions, or sophisticated operating theatres, as in surgery. Ironically it is in the developing world that there appears to be very little awareness of and access to PDT. Cancer sufferers are thus limited to chemotherapy, radiotherapy, and surgery, procedures that are relatively complex and costly, without distinctive advantage in cure or palliation. It is possible that the low level of clinical practice in PDT in developing world is related to the low level of articulation of what is admittedly a relatively new modality. However, this slow emergence of clinical practice in PDT when compared to advances in its developmental research was also observed in the developed world in the last century. While photosensitizers (porphyrins) are administered in various ways, there is no record of it being administered intravenously on iron oxide-gold nanoparticles. The purpose of this study therefore is to prepare a porphyrin photosensitizer that has thiol-terminated side chains and deposit it on the electro-active gold surface of iron oxide – gold core – shell nanoparticles for delivery unto cancer sites thus contributing to knowledge about PDT.

### **2.2 Aim And Objectives Of The Research**

#### **2.2.1 Aim**

The aim of this research is to prepare and characterize a porphyrin drug delivery system for photodynamic therapy based on magnetic nanoparticles with an inert outer layer on which the porphyrin drug is deposited for

delivery. Magnetic core – shell type nanoparticles, with a core of superparamagnetic iron oxide and a shell of gold will therefore be prepared and characterized. A porphyrin drug will be prepared and characterized.

The drug will then be deposited onto the inert surface of the nanoparticles and this deposition will be characterized using kinetic studies as well as comparative spectroscopic studies of the nanoparticles before and after deposition of the porphyrin drug. The kinetic studies of the deposition will be used to show that the envisaged deposition reaction does take place and the spectroscopic studies will confirm that the porphyrin drug is on the surface of the inert outer gold layer of the nanoparticles. Experiments will also be conducted to show that the porphyrin drug is not stripped by merely dissolving the nanoparticles in organic solvents.

### **2.2.2 Objectives**

The objectives of this study are:

- To synthesize a porphyrin photosensitizer to be deposited on the gold surface of the iron oxide – gold, core – shell nanoparticles.
- To prepare iron oxide nanoparticles to be used as core in subsequent preparation of iron oxide–gold, core–shell nanoparticles.
- To grow a gold shell onto the iron oxide magnetic seeds leading to the formation iron oxide – gold, core – shell nanoparticles.
- To immobilize the porphyrin photosensitizer on the outer gold surface of the iron oxide–gold, core-shell nanoparticles using the thiol terminated side chains as anchors.
- To undertake the kinetic studies of the deposition of porphyrin photosensitizer on the nanoparticles.
- To conduct serial dissolution and decanting experiments with intervening spectroscopic studies to show that the porphyrin drug is not stripped by dissolving the nanoparticles in organic solvents.

- To characterize the porphyrin photosensitizer, the iron oxide–gold, core-shell nanoparticles and the porphyrin functionalized iron oxide–gold, core-shell nanoparticles using Nuclear Magnetic Resonance (NMR), UV-Visible and Fourier Transformer Infra-red (IR) spectroscopies and electron microscope studies using Transmission Electron Microscope (TEM), High Resolution Transmission Electron Microscope (HRTEM), Atomic Force Microscopy (AFM), X-ray Diffraction spectroscopy (XRD).
- To measure the magnetic response of the porphyrin functionalized iron oxide – gold, core – shell nanoparticles using the Superconducting Quantum Interference Device (SQUID).

## Chapter 3

### 3.1 Literature Review

In this chapter an extensive review of the literature is presented in order to outline the current state of research and understanding of PDT, synthesis of porphyrins for PDT, the design and synthesis of magnetic nanoparticles, notably the core – shell type and their applications, particularly for PDT. The literature survey covers a range of topics related to, and with potential impact in the design and synthesis of iron oxide – gold, core - shell nanoparticles for use as drug delivery systems for PDT. The review starts with porphyrins in general, followed by the reactions used for porphyrin synthesis. These reactions include the reactions of aldehydes leading to meso-substituted porphyrins, the synthesis of porphyrins via reactions of dipyrromethanes and the meso-substituted dipyrromethane as directed synthesis of porphyrins explored extensively by Lindsey and his group.<sup>102-</sup>

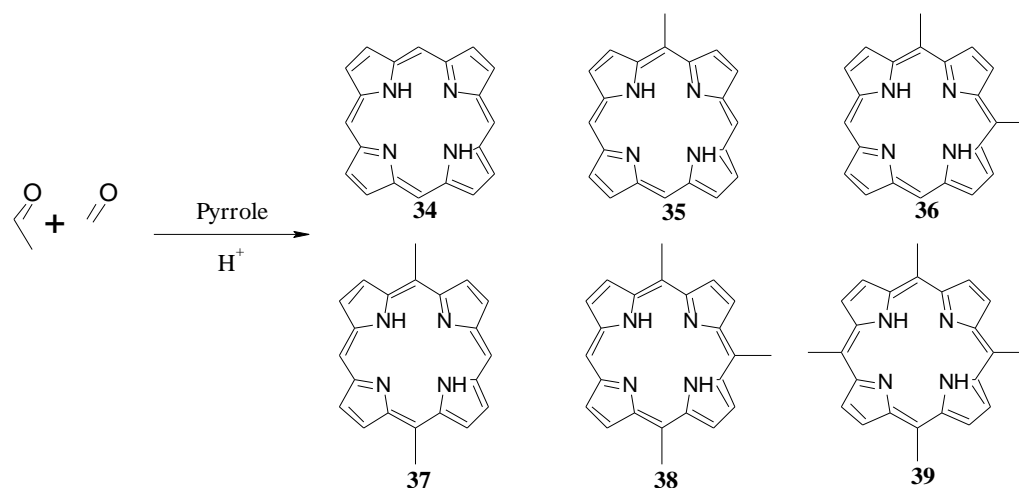
106

This is followed by a survey of nanoparticle science in general and magnetic nanoparticles as drug delivery systems. The topics covered in this part of the survey include an overview of magnetic nanoparticles, and magnetic nanoparticles in biomedical applications, the immobilization of special molecules on the surface of nanoparticles. The synthesis of magnetic superparamagnetic iron oxide nanoparticles and surface modifications of magnetic nanoparticles for biomedical applications and their effect on stability and magnetization are dealt with next. Magnetic properties of iron oxide nanoparticles, cellular labelling/cell separation and biomedical applications of magnetic nanoparticles are followed by a discussion of tailoring magnetic nanoparticles, essential requisites and coatings on magnetic nanoparticles. The toxicity and fate of nanoparticles after administration into the body are considered last.

## 3.2 Porphyrins

A substantial body of knowledge on the reactions that mediate the synthesis of macro-cyclic compounds such as porphyrins and phthalocyanines have been developed over the years.<sup>40, 87-89,93-103</sup> Some of these reactions have become established and common routes to these macrocycles, while others are at developmental stages, being explored by a variety of research groups all over the world.

Synthetic porphyrins bearing one-carbon substituents on the meso positions are known. Synthetic routes for these porphyrins however rely on statistical conversions when two such substituents are required in the various meso positions. The most common procedure at present to access such porphyrins is to react two different aldehydes with pyrrole followed by conversion to the desired group after chromatographic separation.<sup>89</sup>

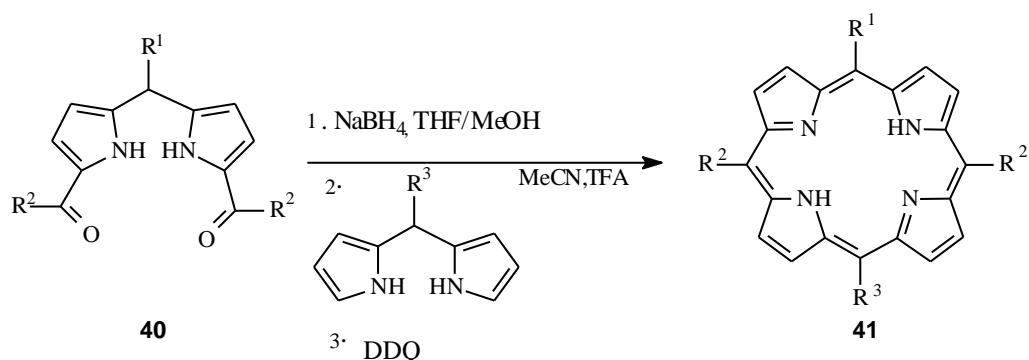


**Scheme 6:** Statistical synthesis of dimethylporphyrin

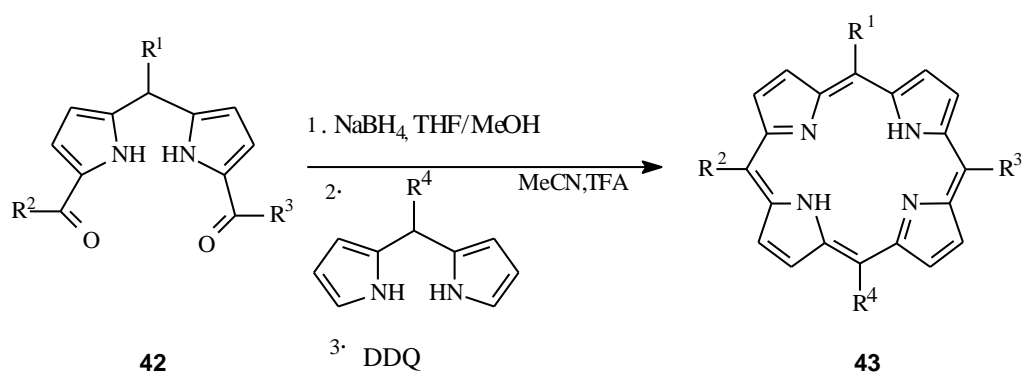
In practice the statistical synthesis of dimethyl porphyrin would involve Rothemund reaction of a mixture of formaldehyde and acetaldehyde with pyrrole using an acid catalyst to give a mixture of six porphyrins: porphine, methylporphyrin, 5,10-dimethylporphyrin, 5,15-dimethylporphyrin, 5,10,15-trimethylporphyrin and 5,10,15,20-tetramethyl-porphyrin. These would be separated by chromatography and then reacted to the desired porphyrins.



Recently a methodology was developed for the synthesis of porphyrins bearing from one to four hydroxymethyl groups attached directly to the *meso*-positions.<sup>89,93</sup> This methodology allowed introduction of hydroxymethyl group(s) and conversion to other oxygenic substituents such as ethoxycarbonyl or formyl. However the synthesis of porphyrins bearing distinct one-carbon oxygenic substituents simultaneously at the *meso*- and *beta*- positions remains a challenge.



**Scheme 7:** Directed porphyrin synthesis



**Scheme 8:** Synthesis of ABCD porphyrin

The current methodologies for preparing porphyrins with one-beta substituents include (1) the condensation of an aldehyde and a mixture of pyrrole and a beta-substituted pyrrole, and (2) the derivatisation at one beta-position following porphyrin formation. Both methods rely on statistical reactions, in turn requiring the desired product to be isolated from a mixture of porphyrins. Although high yields have been reported for

introduction of a single deactivating substituent,  $\beta$ -derivatisation is typically limited to porphyrins that bear the same substituent at all four *meso*-positions because a statistical reaction will afford regioisomers when a porphyrin carries different *meso*-substituents, moreover,  $\beta$ -derivatisation typically is not applicable for porphyrins with free *meso*-positions due to possible *meso*-substitution.

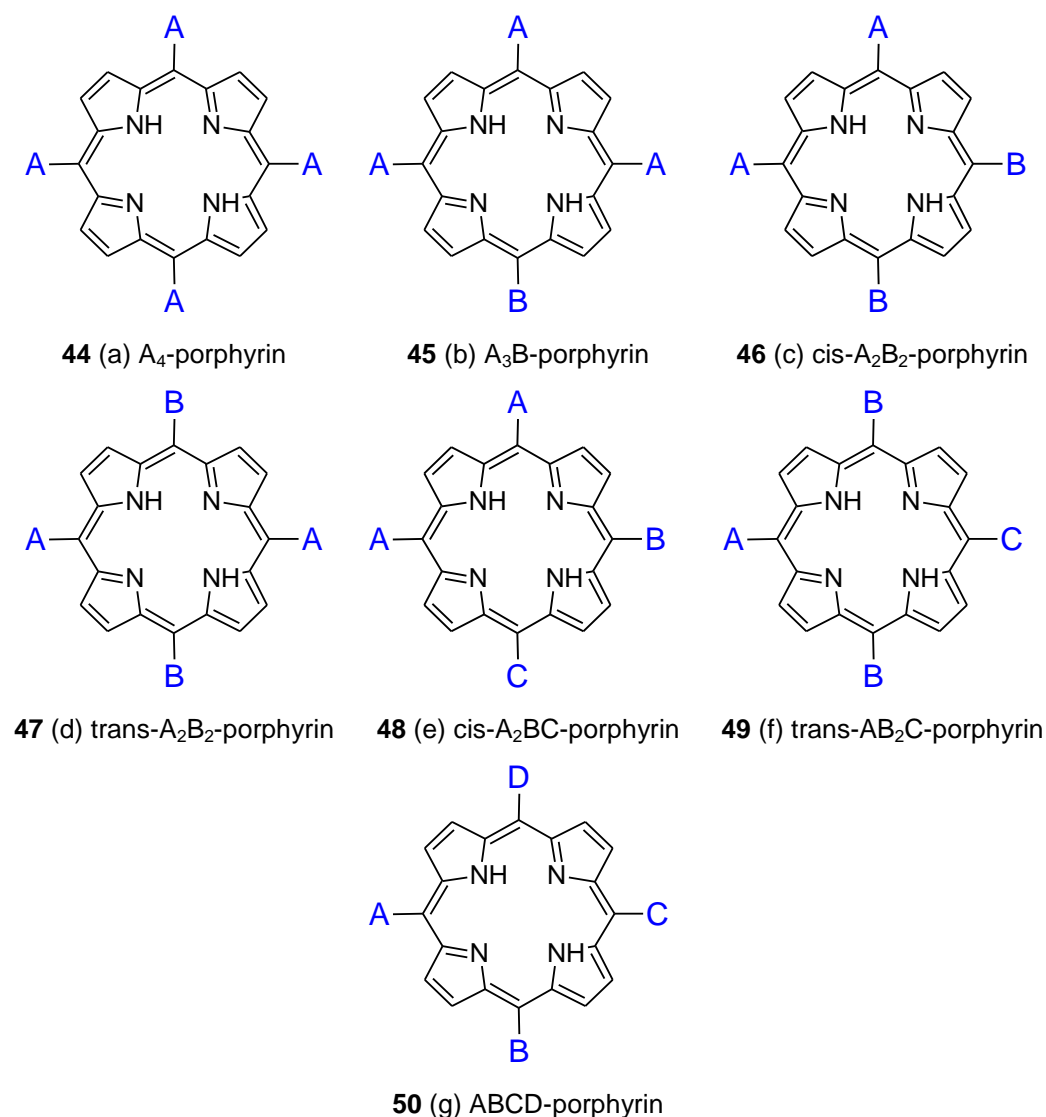


**Figure 20:** Rational synthesis of different *meso*-substituted porphyrins

The opinion of Dazhong et al.<sup>102</sup> is that porphyrins bearing only one or two substituents present a compact architecture suitable for a wide variety of applications (chemical studies, biological investigations and materials chemistry) or further synthetic elaboration in the synthesis of porphyrins

bearing one or two *meso* substituents. For substituents at the *meso* – positions, the methodology established for preparing porphyrins bearing four distinct *meso*-substituents also appears to be applicable.

The route to different *meso*-substituted porphyrins (tetrasubstituted porphyrins, where (a)  $R_1=R_2=R_3=R_4$ , (b)  $R_1\neq R_2=R_3=R_4$ , (c)  $R_1=R_2\neq R_3=R_4$ , (d)  $R_1=R_3\neq R_2=R_4$ , (e)  $R_1=R_2\neq R_3\neq R_4$ , (e)  $R_1=R_3\neq R_2\neq R_4$ , (e)  $R_1\neq R_2\neq R_3\neq R_4$ ) (figure 18) entails condensation of dipyrromethanes with dipyrromethane-1,9-dicarbinoles, where the four substituents are introduced via the *meso*-positions of both the dipyrromethane species and the carbinol units at the 1 and the 9 positions. The corresponding synthesis of *trans*-tetrasubstituted porphyrins (a), (b), (d) and (f) all employ *meso*-substituted dipyrromethanes with the same substituents at the carbinol sites.

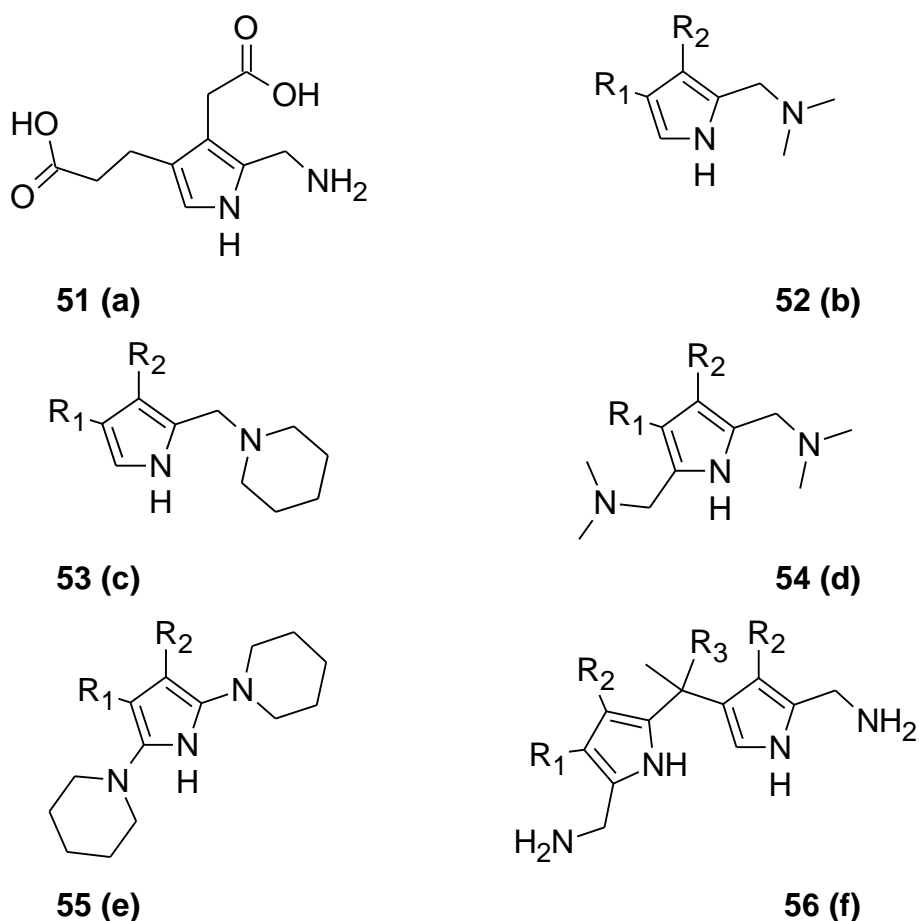


**Figure 21:** Aminomethylpyrroles used to construct porphyrinic macrocycles

A wide variety of synthons have been employed in porphyrin chemistry, either as functional groups (aldehyde, hydroxymethyl) attached to a pyrrolic species or as added reagents (formic acid, trimethyl orthoformate, formaldehyde and imines). A key consideration in the use of dipyrromethanes is the possibility of acidolysis followed by undesired recombination of dipyrromethane-derived fragments, affording undesired porphyrin species (i.e., scrambling of the meso substituents). The possibility of scrambling constrains the nature of the reactive groups employed as position 5 synthons (e.g., aldehyde or hydroxymethyl) and reaction conditions that can be employed.

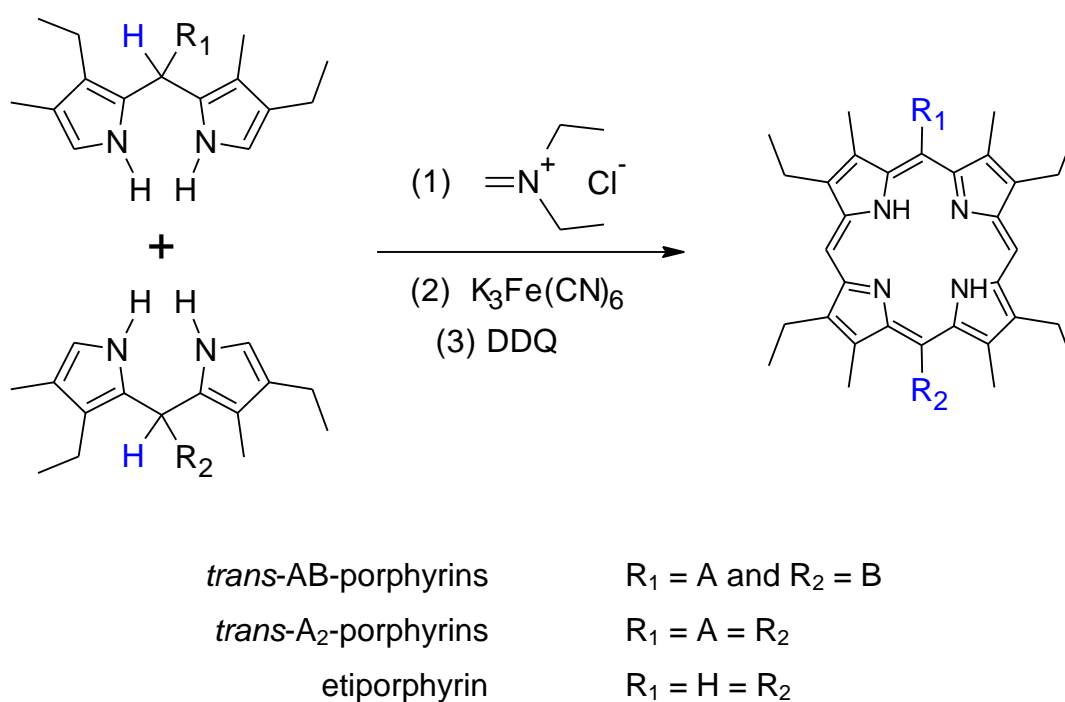
The aminomethyl group has been found to be an attractive candidate for position 5 synthons leading to porphyrinic macrocycles because of the ease of introduction and the possibility that the reaction can be carried out without added acid catalysts. Indeed the porphobilinogen A is the biosynthetic precursor formed before the ring closure leading to porphyrinic macrocycles (figure 21 **51 a**).<sup>103</sup>

Synthetically aminomethylpyrroles are prepared by the condensation of pyrrole derivatives with aldehydes and amines. To construct porphyrinic macrocycles from aminomethylpyrroles, three different approaches have been investigated<sup>102</sup>

- self condensation of an aminomethylpyrrole, e.g., (**52 b**) or (**53 c**);
- condensation of a bis(aminomethylpyrrole), e.g., (**54 d**) or (**55 e**) with a pyrrole derivative; and
- 3+1 condensation of a bis(aminomethyl)pyrrole (**54 d**) with a tripyrrane.

These approaches may appear attractive in their simplicity but have the potential limitation of forming a mixture of porphyrin regioisomers depending on the beta-substitution pattern of the aminomethylpyrrole substrates and in all of these reactions the yields have been very poor.<sup>103</sup>

Although aminomethyl-dipyrromethanes can be attractive precursors for porphyrinic macrocycles, aminomethyl-dipyrromethane derivatives (f) have been mainly used for the synthesis of expanded porphyrins, such as porphocyanine. The only previous example of amino-methyl-dipyrromethane derivatives in porphyrin chemistry is Hombrecher's synthesis of meso-substituted etioporphyrins:<sup>103</sup> treatment of a dipyrromethane with a Mannich reagent ( $\text{CH}_2=\text{N}(\text{Et})_2\text{Cl}$ ) gave the 1,9-bis(N,N-diethylaminoaminomethyl)dipyrromethane (not isolated), which upon condensation with a dipyrromethane *in situ* afforded a mixture including a *trans*-substituted porphyrins (figure 20 (d)), *meso*-substituted porphyrins (figure 20 (a)), and etioporphyrin.<sup>103</sup>



**Scheme 9:** Synthesis of various *trans*-porphyrins

*Meso*-substituted porphyrins bearing specific patterns of functional groups are valuable components in the synthesis of porphyrin based biomimetic systems and other molecular materials.<sup>102</sup> Indeed, the level of architectural sophistication that can be achieved in such systems is closely tied to the availability of suitable porphyrin building blocks, as a result considerable

efforts have been considerably devoted to the development of methodologies for the synthesis of diverse porphyrin building blocks.<sup>101,103</sup>

There are seven types of *meso*-substituted porphyrins as shown in figure 20. Goals for developing syntheses for these classes of porphyrins include the achievement of a broad scope, minimal use of chromatography, and to obtain up to 1-g quantities of porphyrin in terms of yield. The objective of broad scope has motivated the use of mild reaction conditions, while the desire to avoid chromatography and to work on a reasonable scale has prompted the development of rational approaches that do not require the separation of a mixture of porphyrins.

The strategy for the synthesis of *meso*-substituted porphyrins depends on the pattern of different substituents. The routes employed generally become more elaborate as the number of different substituents increases. Methods on how to prepare each of the seven classes of *meso*-substituted porphyrins lacking  $\beta$ -substituents are summarized below:

- $A_4$ -porphyrins [44 (a) in figure 20] are readily synthesized under mild conditions and at high concentration in a one-flask reaction of pyrrole and the corresponding aldehyde.
- $A_3B$ -porphyrins [45 (b) in figure 20] can be prepared by reaction of pyrrole and two aldehydes, affording a statistical mixture of all six substituted products, which are then separated by chromatography. The chromatographic separation is generally lengthy and will only afford small quantities of (typically <100 mg) of the desired porphyrin.
- *Trans*- $A_2B_2$ -porphyrins [47 (d) in figure 20] can be prepared by reaction of an aldehyde and a dipyrromethane. In any acid-catalysed reaction involving polypyrromethanes, acid-catalysed fragmentation followed by an alternate recombination is an ever-present possibility resulting in a mixture of porphyrins. However, conditions have been identified that afford *trans*- $A_2B_2$ -porphyrins without scrambling, from the condensation of a dipyrromethane bearing a sterically hindered substituent, such as a mesityl group, at the 5-position with an aldehyde. On the other hand a

high level of scrambling is observed under the same conditions with a dipyrromethane bearing a sterically unhindered substituent. Though extensive study has identified conditions that minimized scrambling for sterically unhindered dipyrromethanes the porphyrin yield has been generally poor.<sup>104</sup> An example of *trans*-A<sub>2</sub>B<sub>2</sub>-porphyrins is the self-condensation of a dipyrromethane-monocarbinol (derived from a monoacyl dipyrromethane); the method provides a general method for the rational synthesis of *trans*-A<sub>2</sub>B<sub>2</sub>-porphyrins in good yield without scrambling.

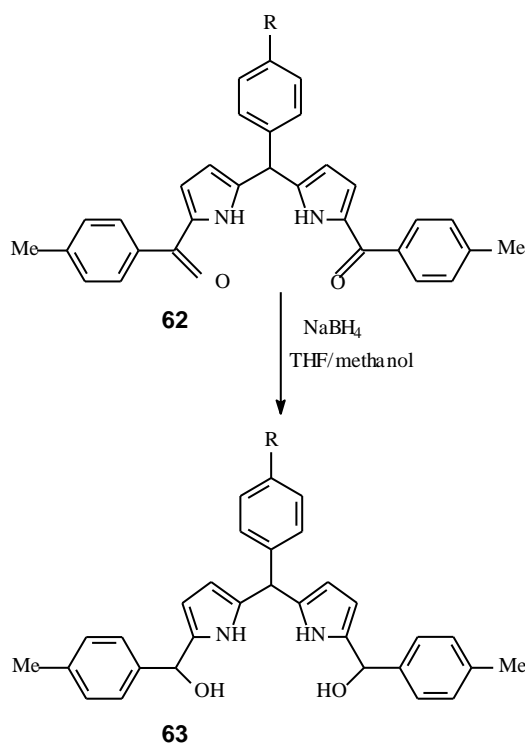
- *Cis*-A<sub>2</sub>B<sub>2</sub>-porphyrins [**46** (c) in figure 20] have been prepared rationally in milligram quantities by reaction of a tripyrrane with a pyrrole-dicarbinol. Statistical syntheses requiring extensive subsequent chromatographic separation have involved mixed condensations of two aldehydes and pyrrole, or a linked dialdehyde, an aldehyde and pyrrole.
- *Trans*-AB<sub>2</sub>C-porphyrins [**49** (f) in figure 20] are prepared statistically by reaction of a dipyrromethane and two aldehydes, or of two dipyrromethanes and one aldehyde. In each case the resulting three porphyrins (assuming no acidolytic scrambling) are separated chromatographically. In pursuit of rational routes to *trans*-AB<sub>2</sub>C-porphyrins, methods have been reported for diacylation of dipyrromethanes and reduction of the resulting diacyl dipyrromethanes to the corresponding dipyrromethane-dicarbinol. However, lack of suitable conditions for performing the reaction of dipyrromethane-dicarbinol with dipyrromethane hindered the implementation of this rational route. An alternative route to this class of porphyrins involves treating a 5,15-disubstituted porphyrin with an organolithium reagent, quenching with water, and then treating with an alkyl iodide followed by oxidation.
- *cis*-A<sub>2</sub>BC-porphyrins [**48** (e) in figure 20] have not been prepared via rational routes.
- ABCD-porphyrins [**50** (g) in figure 20] can be prepared in small quantities by a rational approach involving sequential introduction of acyl groups (or their equivalent) onto the dipyrromethane nucleus,

followed by reduction to the dipyrromethane-dicarbinol, and then condensation of the dipyrromethane-dicarbinol with a dipyrromethane. The methods for monoacylation or diacylation are only partially selective, in each case affording a mixture of unreacted, monoacylated, and diacylated species which are separated by chromatography. The condensation conditions for the reaction of dipyrromethane-dicarbinol with dipyrromethane afforded a regioisomerically pure porphyrin in low yield (<10%). These limitations in dipyrromethane chemistry and the low yield of porphyrin formation have limited the scale to milligram quantities. All acid catalysis conditions that have been examined gave higher yields of porphyrins although they also resulted in scrambling.<sup>104</sup> Scrambling needs to be avoided altogether in the synthesis of porphyrins bearing three or four different substituents because of a large number of possible products and the problem of separations. The route to ABCD-porphyrins in principle encompasses the synthesis of porphyrins bearing two or three different substituents; however, low yields, small scale, and prohibitive levels of chromatography have effectively limited the applications of this approach. Also other routes to ABCD-porphyrins have been plagued by one or more of these problems.<sup>104</sup>

There has been keen interest in the synthesis of monomeric and oligomeric porphyrin macrocycles that could overcome the above problems. Rao et al<sup>104</sup> indicated that porphyrins bearing specific patterns of substituents are crucial building blocks in biomimetic systems and materials chemistry and have therefore developed a methodology that avoids statistical reactions, employs minimal chromatography, that afford up to gram quantities of regioisometrically pure porphyrins bearing predesignated patterns of up to four different *meso* substituents. The methodology is based upon the availability of multigram quantities of dipyrromethanes while the procedures for the diacylation of dipyrromethanes using ethylmagnesium bromide (EtMgBr) and an acid chloride were refined.



A new procedure for the preparation of unsymmetrical diacyl dipyrromethanes was also developed that involved monoacylation with EtMgBr and a pyridyl benzothioate followed by introduction of the second acyl unit upon reaction with EtMgBr and an acid chloride. The scope of these acylation methods was examined by preparing multigram quantities of diacyl dipyrromethanes bearing a variety of substituents. Reduction of the diacyl dipyrromethane to the corresponding dipyrromethane-dicarbiniol was achieved with sodium borohydride (NaBH<sub>4</sub>) in methanolic tetrahydrofuran (THF). Porphyrin formation however, involved the acid-catalysed condensation of a dipyrromethane-dicarbiniol and a dipyrromethane, followed by oxidation with 2,3-dichloro-5,6-dicyano-1,4-benzoquinone (DDQ). Optimal conditions for the condensation were identified after examining various reaction parameters like solvent, temperature, acid, concentration and time.<sup>105</sup>



**Scheme 10:** Reduction of the diacyl dipyrromethane to dipyrromethane-dicarbiniol

### 3.2.1 Effects of Aldehyde or Dipyrromethane Substituents on the Course of Reactions Leading to *meso*-substituted Porphyrins

Geier et al<sup>105</sup> examined the effects of diverse substituents on the condensations reactions of pyrroles and aldehydes and related reactions of dipyrromethanes leading to porphyrins. The course of condensation reactions of pyrroles and aldehydes was investigated by monitoring the yield of the porphyrins using UV-Vis spectroscopy, the reactions of aldehydes was monitored by thin layer chromatography (TLC) while changes in oligomers were monitored by laser desorption mass spectrometry (LDMS). Reaction reversibility was examined via exchange experiments and reversibility reactions leading to porphyrin formation were further probed with studies of the formation of dipyrromethanes.

The course of the reaction was found to depend on the nature of the substituent and the acid catalyst. Alkyl or electron-donating substituents were found to display levels of reversibility (exchange/scrambling) on par or greater than that of the phenyl substituent, whereas electron-withdrawing or sterically bulky substituents exhibited little or no reversibility. The results obtained provided insight into the electronic and steric effects of different substituents and this facilitates the design of synthetic plans for successful preparation of porphyrinic macrocycles.<sup>107</sup>

#### 3.2.1.1 Reactions of Aldehydes<sup>105-107</sup>

Two specific groups of aldehydes of a given type were selected for comparison to benzaldehyde in reactions leading to *meso*-substituted porphyrins. In each case, the two aldehydes used for comparison have similar structures but different molecular weights in anticipation of the exchange experiments. The selected aldehydes were benzaldehyde and *p*-tolualdehyde as bench mark case, *p*-anisaldehyde and 4-ethoxybenzaldehyde (electron donating), pentafluorobenzaldehyde and 2,3,5,6-tetrafluorobenzaldehyde (electro withdrawing), mesitaldehyde and

2,6-dimethylbenzaldehyde (sterically bulky), and hexanal and heptanal (alkyl).

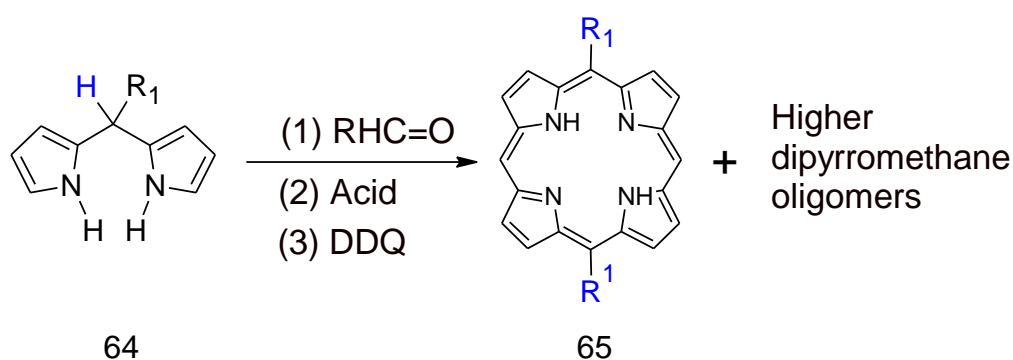
The catalytic requirements for each aldehyde were investigated by reacting an aldehyde and a pyrrole (10 mM each) at room temperature in dichloromethane ( $\text{CH}_2\text{Cl}_2$ ) over a range of concentrations of trifluoroacetic acid (TFA) or  $\text{BF}_3$ -etherate. After condensation for 15 min, 1 hr, and 4 hrs, an aliquot of the reaction mixture was oxidized with DDQ and the yield of porphyrin was determined. For example, for *p*-anisaldehyde, the reaction time with 46 mM TFA afforded a yield of 26 % at 15 min, 5 % after 1 hr, and 0 % after 4 hrs. However, the reaction with 22 mM TFA provided a yield of 29 % after 1 h and approximately 17 % after 4 hrs. For the reaction at 10 mM TFA, the reaction at 4 h afforded the highest yield (24 %), with less than a 10 % yield obtained at the earlier time points.

### 3.2.1.2 Reactions of Dipyrromethanes<sup>106,107</sup>

5-Substituted dipyrromethanes possessing substituents analogous to those employed in the reactions of aldehydes were selected for the investigation: phenyl (benchmark case), 4-methoxyphenyl (electron donating), pentafluorophenyl (electron withdrawing), mesityl (sterically hindered), and pentyl (alkyl). Two general types of experiments were performed: acidolysis and oligomerization of the dipyrromethanes in the absence of added aldehyde, and reactions of a dipyrromethanes and aldehydes. Each dipyrromethane (10 mM) was treated with acid catalysis conditions in the presence of added aldehyde (Scheme 13).

The acid catalysis conditions were those identified for porphyrin formation in the corresponding reaction of pyrrole with an aldehyde, the standard condition of TFA (20 mM), the standard condition of  $\text{BF}_3$ -etherate (1.0 M) and the “low scrambling” conditions used in earlier studies for the condensation of sterically unhindered dipyrromethanes and an aldehyde leading to *trans*- $\text{A}_2\text{B}_2$ -porphyrins (1.0 mM  $\text{BF}_3$ -etherate, 100 mM  $\text{NH}_4\text{Cl}$ , in MeCN at 0°C). The reactions were monitored from 4 min to 4 hrs for the

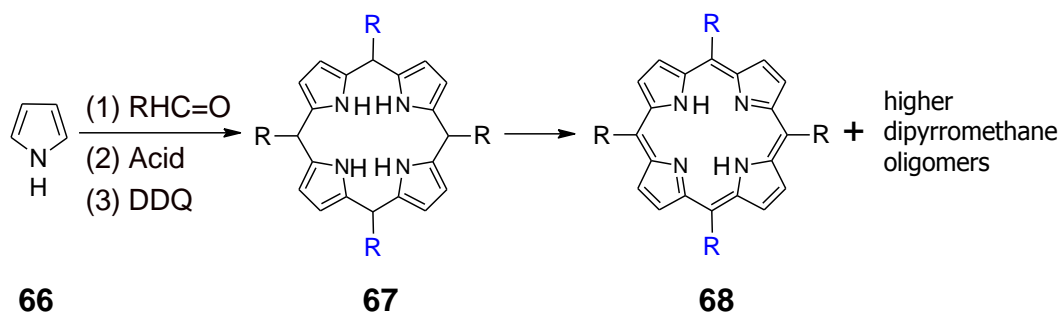
yield of porphyrin (UV-Vis) and oligomer composition (LD-MS). The results showed that 5-mesityldipyrromethane was stable towards all conditions investigated, and that only 5-pentafluorophenyldipyrromethane underwent significant, although slow reaction under  $\text{BF}_3$ -etherate catalysis to produce porphyrin. The other dipyrromethanes generally underwent rapid reaction (except under the low scrambling conditions), but 5-(4-methoxyphenyl)dipyrromethane underwent significant reaction in the presence of 1.0 mM  $\text{BF}_3$ -etherate while the same condition fails to cause the reaction of pyrrole with *p*-anisaldehyde to produce detectable porphyrin.



**Scheme 11:** Dipyrromethane leading to porphyrin synthesis

The level of scrambling observed with various 5-substituted dipyrromethanes is somewhat dependent on the reaction conditions. Nevertheless, dipyrromethanes bearing phenyl, alkyl and electron-donating aryl groups are generally prone to scrambling, while 5-pentafluorophenyldipyrromethanes are very insensitive, and 5-mesityldipyrromethane is essentially inert toward scrambling.

The synthesis of *meso*-substituted porphyrins via a one-flask reaction involve condensation of pyrrole and an aldehyde in one-to-one ratio, however the reaction is performed in two stages: (1) acid catalysed condensation of pyrrole and an aldehyde forming predominantly polypyrromethane oligomers and the cyclic porphyrinogen; (2) addition of an oxidant (e.g., DDQ or *p*-chloranil) to give the corresponding polypyrromethanes and porphyrin (Scheme 11).



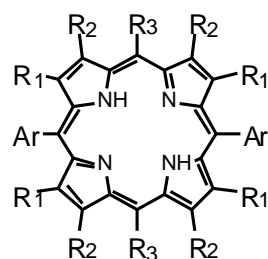
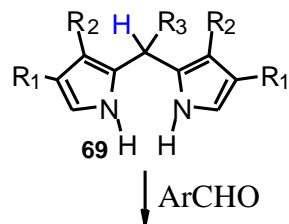
**Scheme 12:** Rothemund type reaction leading to porphyrin synthesis

Obtaining a maximal yield of porphyrin requires careful monitoring of the reaction “trajectory” so that oxidation, the second step of the porphyrin-forming process (which terminates all condensation processes) can be initiated at the appropriate time. The decline in porphyrinogen yield that occurs under some conditions is accompanied by a shift of the oligomer composition to shorter species (“oligomer truncation”).

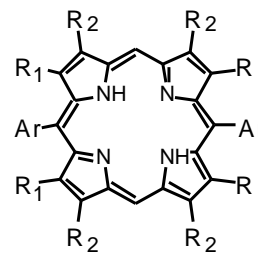
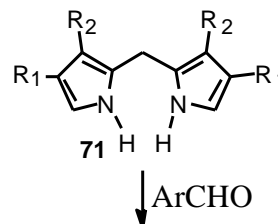
Examination of the catalytic requirements of the condensations of pyrroles with aldehydes revealed that quite a broad range of acid concentrations can be employed as long as the differing reaction trajectories resulting from the various aldehydes are taken into account. Application of one or both of the standard catalysis conditions [TFA (20 mM) or  $\text{BF}_3$ -etherate (1.0 mM)] usually results in reasonable yields of porphyrin for most aldehydes (except sterically bulky aldehydes such as mesitaldehyde) provided that the condensation is monitored so that the oxidant is added at the time of maximum yield of porphyrinogen.

The reaction course of the condensations of pyrroles with aldehydes showed dependence on reaction conditions and aldehyde substituent. The reactions of the phenyl, *p*-tolyl, and alkyl aldehydes using  $\text{BF}_3$ -etherate generally afforded little turnover in porphyrinogen, little oligomer truncation and a medium to high level of reversibility but the same aldehydes with TFA catalysis will generate a higher turnover of porphyrinogen with a commensurate increase in level of oligomer truncation. However turnover in porphyrinogen level and extent of oligomer truncation are not always correlated.

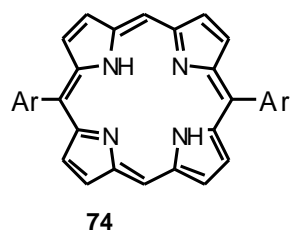
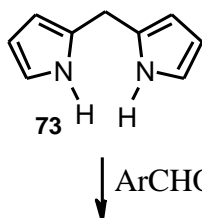
**Route 1: Meso and beta substituted dipyrromethane**



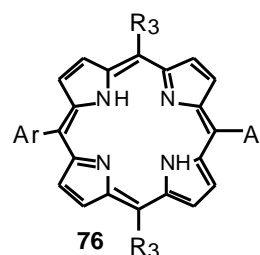
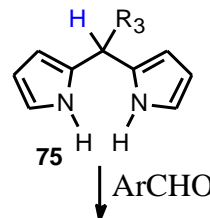
**Route 2: Beta substituted dipyrromethane**



**Route 3: Unsubstituted dipyrromethane**



**Route 4: Meso substituted dipyrromethane**



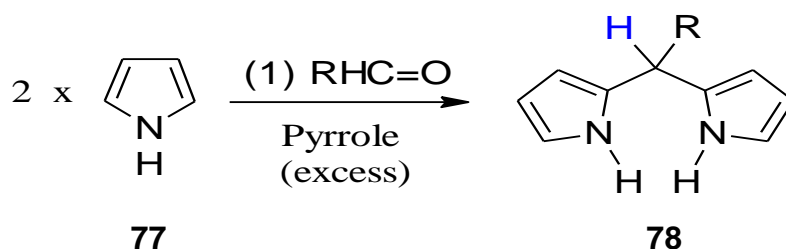
**Scheme 13:** Use of dipyrromethanes to four types of *trans*-substituted porphyrins.

For example, the reaction of *p*-anisaldehyde under the reaction conditions being considered gives high turnover (~35 % yield of porphyrin at 1 hr; <4 % at 24 hrs) with both TFA and BF<sub>3</sub>-etherate catalysis. However, the oligomer truncation is pronounced in the former yet low in the latter. In addition the condensations with mesitaldehyde and pentafluorobenzaldehyde are generally irreversible as evidenced by the lack of porphyrinogen and oligomer exchange. This illustrates that

reversibility is not a prerequisite for achieving a good yield of the porphyrin.<sup>104</sup>

### 3.2.2 *Meso*-substituted Dipyrromethane Formation

The chemistry of *meso*-substituted dipyrromethanes has been rather undeveloped. With the exception of the work by Nagarkatti and Ashley,<sup>108</sup> who showed that condensation of 4-pyridine carboxyaldehyde with pyrrole in acidified methanol afforded crystals of the hydrochloride salt of *meso*-(4-pyridyl)dipyrromethane.

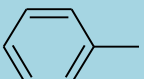
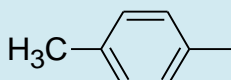


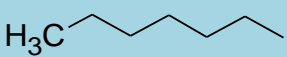
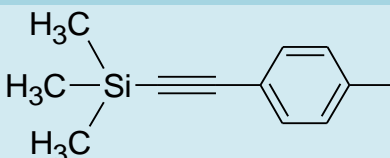
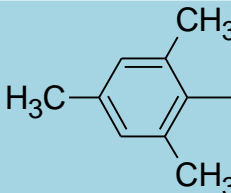
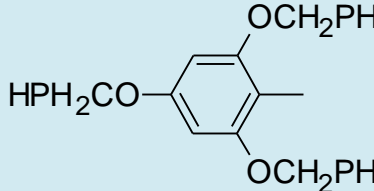
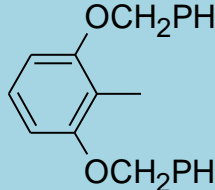


**Scheme 14:** One-flask synthesis of *meso*-substituted dipyrromethanes.

Direct syntheses of *meso*-substituted dipyrromethanes started emerging in 1992. Casiraghi *et al*<sup>109</sup> prepared dipyrromethanes by reaction of aliphatic aldehydes with the Grignard reagent of pyrrole in the presence of TiCl<sub>4</sub> and in 1994. Vigmond *et al*<sup>110</sup> published the direct synthesis of *meso*-substituted dipyrromethanes involving reaction of pyrrole and aryl aldehyde in tetrahydrofuran/acetic acid. A similar synthesis employing reaction in acidified methanol was described by Mizutani *et al*.<sup>111</sup> In addition to these direct syntheses, two stepwise syntheses of *meso*-substituted,  $\beta$ -unsubstituted dipyrromethanes have been developed.<sup>112,113</sup>

Lee and Lindsey<sup>114</sup> also developed a one-flask synthesis of *meso*-substituted dipyrromethanes, the approach appears to offer advantages for application in porphyrin chemistry and in dipyrromethanes synthesis without continued oligomerization. The reaction involves condensation of pyrrole and an aldehyde in the presence of large excess of pyrrole

(Scheme 14). Pyrrole serves as the reactant in excess and as the solvent for the reaction, giving direct formation of the dipyrromethane. This method has been applied to the synthesis of a variety of meso-substituted dipyrromethanes as shown in table 3. The reactions were catalysed by acidified methanol.

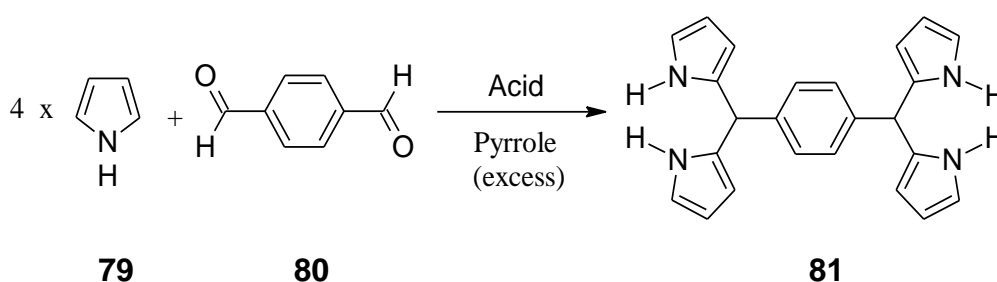
Table 3: <i>meso</i> -(R)dipyrromethanes		Yield
1		49%
2		76%
3		55%
4		57%
5		60%
6		47%
7		55%
8		56%
9		86%

The reactions were catalysed with trifluoroacetic acid. In this typical analysis, the reaction with mesitaldehyde afforded a dark red solution which did not clarify upon washing with base. The mesityldipyrromethane



**(6)** is isolated in 60 % yield following chromatography. The same condensation with  $\text{BF}_3 \cdot \text{O}(\text{Et})_2$  catalysis gives a light-brown oil and the product is obtained in 55 % yield by direct crystallization from the reaction mixture, thereby avoiding chromatography. When excess pyrrole is removed by vacuum distillation at room temperature, TLC analysis of each reaction mixture shows the dipyrromethane, a tiny amount (<5%) of a tailing component, and some material at the origin of the TLC plate. Upon exposure to  $\text{Br}_2$  vapour the dipyrromethane appears red and the tailing material appears violet-brown. In the synthesis of **(4)**, the tailing component was isolated and proton NMR spectroscopy showed the compound to be corresponding tripyrromethane which is less stable than the dipyrromethanes and turned from a white solid to a black material over one day at room temperature.

This one flask reaction can also be employed with dialdehydes (Scheme 15). For example reaction of terephthalaldehyde with pyrrole afforded the bis-dipyrromethane. Similar syntheses have been performed with  $\beta$ -substituted pyrroles, yielding  $\beta$ -substituted, meso-substituted dipyrromethanes.<sup>110</sup>



**Scheme 15:** One-flask synthesis of a bis-dipyrromethane.

The chemistry of dipyrromethanes is such that slightly different methods and conditions can yield significantly different results. For example, the procedure of Vigmond et al<sup>110</sup> begins with a solution of pyrrole (~3 M) in acetic acid to which a stoichiometric amount of the aldehyde in THF/acetic acid is added, but the procedure of Lee and Lindsey<sup>114</sup> employs pyrrole

(~10 M) in excess relative to the aldehyde, no solvent, and a catalytic amount of an acid.

The results of these procedures differ in the following manner. First, the yields from the solventless method were reported to be 1.5 – 3 times higher and the products are cleaner. Looking at Scheme 11 page 99, dipyrromethanes in Routes **1** and **2** provided a direct comparison of the two methods. Lee and Lindsey<sup>114a-i</sup> obtained *meso*-phenyl dipyrromethane (**1**) as a white solid with melting point 100-101<sup>0</sup>C rather than a liquid as reported by Vigmond *et al.*<sup>110</sup> and *meso*-(*p*-tolyl)dipyrromethane (**2**) has melting point 110-111<sup>0</sup>C rather than 75<sup>0</sup>C as reported by Hombrecher and Hoorter.<sup>106</sup> Second, the chromatography of the *meso*-dipyrromethanes on silica was found to be best performed using mildly basic eluants as the use of neutral organic solvents leads to decomposition of the dipyrromethane on silica. Lee and Lindsey<sup>114a</sup> explained that the differing chromatography conditions may partially explain the higher yields and cleaner products that were obtained. Third, Vigmond *et al.*<sup>110</sup> reported that using 4 equivalents of pyrrole causes a decline in yield of the dipyrromethane, while Lee and Lindsey<sup>114a</sup> found that in the absence of a solvent, the amount of excess pyrrole can be varied from 40-70 fold with only slight effect on the dipyrromethane yield.

### **3.3 Nanoparticles**

#### **3.3.1 Overview of magnetic nanoparticles (MNPs)**

Since the mid-1970s, magnetic particles (MPs) from nanometer (nm) to micrometer ( $\mu\text{m}$ ) size have been widely used in biological and medical fields. The unique feature of magnetic nanoparticles is their response to magnetic force. For biomedical applications, magnetic nanoparticles exhibiting superparamagnetic behavior at room temperature are preferred because they do not retain any magnetism after removal of the magnetic field. Furthermore, the particles must have combined properties of high magnetic saturation, biocompatibility and interactive functions at the

surfaces. Among magnetic nanoparticles, iron oxide (FeO) such as magnetite (Fe<sub>3</sub>O<sub>4</sub>) or its oxidized form maghemite (Fe<sub>2</sub>O<sub>3</sub>) are by far the most commonly employed in biomedical applications since their biocompatibility has already been proven.<sup>115</sup> Highly magnetic materials such as cobalt (Co) and nickel (Ni) are toxic, susceptible to oxidation and hence are of little interest. Fe<sub>3</sub>O<sub>4</sub> or Fe<sub>2</sub>O<sub>3</sub> nanoparticles are usually modified through the formation of few atomic layers of polymer/surfactant or inorganic metallic (such as gold) or oxide surfaces (such as silica or alumina), which are suitable for further functionalization by the attachment of various biomolecules.<sup>116</sup> Magnetic nanoparticles are either well dispersed in a liquid, i.e., for medical application, or form composites with polymer or inorganic matrices, the so-called magnetic microspheres or beads.

Over the past twenty years the computer and semiconductor industry has been fuelling an explosive growth in material research to reach the lofty goals required by the market. This explosion has pushed research for new materials into the nanometer size regime. Nanoparticles have been synthesized in a variety of methods ranging from sputtering to chemical vapor deposition. Currently, one of the most versatile methods explored are wet chemical methods such as the microemulsion technique.<sup>117</sup>

Microemulsion techniques rely on the self assembly nature of surfactants to push aqueous reactants into a micelle. Due to the dynamic nature of micelles, aqueous components can come together and react to form particles that are constrained to the size of the micelle. By changing the reaction conditions the methods can even be applied sequentially to form core-shell structures.<sup>117</sup>

Magnetic nanoparticles with suitable surface characteristics have potential applications both *in vitro* and *in vivo*. In almost all applications, the preparation and surface modification of magnetic nanoparticles present significant challenges in determining the particle size and shape, the size distribution, the surface chemistry and consequently the magnetic

properties of the particles, which are very important for biomedical applications.<sup>118,119</sup>

In recent years, magnetic nanoparticles have been studied for their potential applications as magnetic carriers for various biomedical uses such as cell and Deoxyribonucleic acid (DNA) separation, drug delivery system (DDS), magnetic resonance contrast enhancement and gene cloning. In particular, magnetic beads with a few micrometer in diameter are already commercialized and used for cell separation, DNA isolation and protein isolation. For these applications, their surfaces are coated with a layer to combine with functional biomolecule for each purpose and avoid nonspecific adsorption. However, the commercially available magnetic beads cannot be used as a general purpose carrier. For each biomolecule it is necessary to coat the particles with an appropriate layer. On the other hand, gold nanoparticles (Au NPs) are also widely studied in the field of biotechnology.<sup>120</sup>

Gold combines firmly with biomolecules possessing mercapto groups and exhibits a characteristic reddish color due to surface plasmon resonance. The color changes when gold nanoparticles aggregate with the molecules attached on their surface.<sup>121</sup> Thus colorimetric detection of specific biomolecules is possible. The magnetic nanoparticles with 'shell/core' structure have attracted great interests as potential candidates for applications in magnetic recording media, catalysis, Ferro fluids (FFs), diagnosis, drug delivery (DD) and microwave absorbents. The outer shell can protect metallic magnetic nanoparticles against environmental degradation, and effectively increase the distance of neighboring magnetic nanoparticles, which result in weak magnetic coupling between individual nanoparticles.<sup>122</sup>

Magnetic nanoparticles have potential applications in many biological and medical fields such as drug delivery, hyperthermia treatment, magnetic resonance contrast enhancement and cell separation. Even though biocompatible iron oxide nanoparticles are currently the material of choice,

there is significant interest in developing alternative high magnetic moment Co (and related alloys) for specific biomedical applications.<sup>123</sup> While the majority of magnetic nanoparticles prepared at present for biomedical applications are bead-like or spheres, other anisotropic shapes with larger dipole moment per unit volume have been considered for cell manipulation applications. Irrespective of their shape, the challenge here is to prepare uniform, un-agglomerated particles with controlled size, shape and narrow size distribution.<sup>124</sup>

However, since metallic cobalt nanoparticles (Co NPs) are highly sensitive to oxidation and are toxic for biological application, it would be highly desirable to coat them with an inert shell for biocompatibility and stability. Further, if the shell could provide additional functionality, such as sensitivity to optical probes and other biomolecules, it would be highly desirable for a number of applications. Gold coating of the magnetic nanocrystals would be a natural choice to accomplish both of these goals.<sup>124</sup>

Magnetic nanoparticles have been attractive materials in biology and biomedicine. They have size ranges from a few nanometers (nm) to tens of nanometer (nm) that are comparable to those of a protein; antibody, DNA or Ribonucleic acid (RNA), and can interact with or bind to such biomolecules.<sup>125</sup> Magnetic iron-oxide nanoparticles are intensively studied as a promising candidate material for these uses because of their high chemical stability and non-toxicity. For these applications, the surface of the particles is modified by a biocompatible compound such as polyethylene glycol (PEG), polyvinyl alcohol (PVA), dextran, gold (Au) or silica (Si). These surface modifications act to shield the magnetic nanoparticles from the surrounding environment.<sup>125</sup> To bind the biomolecules onto their surface often requires chemical reactions. On the other hand, gold nanoparticles (AuNPs) are also widely studied for biological applications. In general, gold (Au) combines firmly with biomolecules possessing thiol (-SH) or mercapto groups, via Au-S bonds. Gold nanoparticles exhibit a reddish colour in a colloidal solution due to the surface plasmon absorption. Aggregation of the gold nanoparticles caused

by cross-linking, such as during DNA hybridization, may change the colour of the colloidal solution to purple, thus making a colorimetric DNA detection possible.<sup>125</sup>

During the past years, the preparation and characterization of nanoscale materials have become an important branch of materials research and attracted considerable attention from both fundamental and applied research due to their unique, electrical and other properties. To date, a variety of preparative approaches have been investigated and many reviews are now available.<sup>126</sup> Solution-phase syntheses may represent the most promising route to nanoparticles in terms of cost, throughput, and the potential for high-volume production. Unfortunately, unprotected metal colloids are susceptible to irreversible aggregation in solution due to small size. One of the effective strategies is to protect colloids with protective agents, which can spontaneously absorb on the particle surface leading to colloids in which individual particle is separated from each other, preventing them from agglomeration.<sup>126</sup>

As an emerging active area of contemporary materials science, nanocomposites containing two or more different nanoscale functionalities attract much attention. Interests in this kind of nanomaterials originate not only from the curiosity of scientists who are exploring the mesoscopic world, but also from the ever-increasing demands placed on materials synthesis and performance by nanotechnology. The magnetic core/shell nanoparticles with a shell of gold, for example, is one of such nanocomposites.<sup>127</sup>

Nanocomposite materials containing a magnetic phase and another functional phase have been attracting much interest from materials scientists because of many interesting and important scientific and technological aspects.<sup>128</sup> In particular, the nanoparticles in which both the phases i.e that is magnetic phase and other functional phase, are included is one of the most challenging targets of materials science because of its vast versatility. For example application to the drug delivery and bio

detection technologies. However, it is not an easy task to characterize such a complex nanoparticle from the view point of the internal structure and the phase that gives rise to magnetism. Carpenter *et al.*<sup>129</sup> have reported synthesis of core-shell structured iron Fe-Au nanoparticles with an average diameter of 12 nm by the reverse micelle method and proposed many applications. They postulated that their particle is composed of a core of metallic Fe and a shell of metallic Au, on the basis of much circumstantial evidence. This group has synthesized superparamagnetic nanocomposite materials composed of magnetic nanograins of iron oxide or nitride dispersed in a silica matrix by the inert gas condensation method<sup>130,131</sup>. They also studied the phase of the Fe-containing nanograins giving rise to the magnetism of the particles. The average magnetic moment size and its standard deviation were examined by analyzing the magnetization (M) behavior<sup>132,133</sup> and the phase containing iron was identified by X-ray absorption near edge spectroscopy (XANES).<sup>134,135</sup>

### **3.3.2 Immobilization of special molecules on the surface of nanoparticles**

There has been extensive investigation of the applications of the immobilization of special molecules on the surface of the nanoparticles.<sup>136,137</sup> For example the immobilization of substrate specific ligands on the surface of nanoparticles can be used for the specific removal or recycling of the substrates.<sup>138-140</sup> Furthermore, because the surface reactions of nanoparticles and those of ligands immobilized on the surface of nanoparticles have dramatic effects on a number of physical, chemical and electronic properties of the nanoparticles, the immobilization of substrate specific ligands on the surface of nanoparticles can also be used for the detection of substrates in mixtures.<sup>115</sup> The immobilization of antibodies on the surface of nanoparticles can be used for the detection of specific antigens.<sup>141,142</sup> The description of core-shell nanoparticles with a superparamagnetic core materials and relatively inert shell materials has introduced several interesting possibilities.<sup>143,144</sup> The magnetic core allows

for exclusion and/or removal of the nanoparticles by application of a magnetic field.<sup>138-140</sup> This can provide a powerful tool for the detection, purification and recycling of substrates, particularly bio-molecules such as DNA and protein.<sup>141,142</sup>

### **3.3.3 Magnetic nanoparticles (MNPs) in biomedical applications**

The use of magnetic nanoparticles in biomedical applications requires a non-toxic core material and bio-compatible or bio-inert shell. This can be achieved with a core of super- paramagnetic material and a shell of inert material. In addition the shell of inert material may be coated with bio-compatible molecules or molecules with specific bio-responses or bio-activities. In this way, in addition to enhancing this bio-compatibility, the immobilization of bio-compatible ligands on the inert shell can also introduce generic or specific bio-sensitivity.<sup>145</sup>

For example the functionalization of magnetic nanoparticles with antibodies in magnetic immunoassays and binding experiments to confirm the bonding capacity and demonstrate the bio-medical applications have been reported.<sup>141,142</sup> Some of the commonly used core materials include superparamagnetic iron oxide,<sup>146</sup> ferromagnetic cobalt<sup>147</sup> and ferromagnetic cobalt platinum.<sup>148</sup> Probably due to the wide range of available synthetic procedures and magnetic properties, silica has been the coating material of choice<sup>138-140,143-146,148,149</sup> although the use of inert metals, notable gold (Au)<sup>127,150,151</sup> and silver (Ag),<sup>138</sup> have proved to be quite competitive in recent studies.

### **3.3.4 Superparamagnetic Iron Oxide Nanoparticles (SPION)**

Super paramagnetic iron oxide nanoparticles (SPION) are small  $\gamma$ -Fe<sub>2</sub>O<sub>3</sub> or Fe<sub>3</sub>O<sub>4</sub> particles with a size of <10 nm in diameter. The term “superparamagnetism” is used to infer an analogy between the behavior of the small magnetic moment of a single paramagnetic atom and that of the much larger magnetic moment of a nanosized magnetic nanoparticles



which arises from the coupling of many atomic spins. After eliminating the magnetic field strength, the particles no longer show magnetic interaction; a feature that is important for their usability.<sup>152</sup> Superparamagnetic iron oxide nanoparticles with appropriate surface chemistry have been widely used experimentally for numerous *in vivo* applications such as magnetic resonance imaging (MRI) contrast enhancement, tissue repair, immunoassays, detoxification of biological fluids, hyperthermia, drug delivery and in cell separation, etc. All these biomedical and bioengineering applications require that these nanoparticles have high magnetization values and size smaller than 100 nm with overall narrow particle size distribution, so that the particles have uniform physical and chemical properties.

In addition these applications need special surface coating of the magnetic nanoparticles, which must not only be non-toxic and biocompatible, but also allow a targetable delivery with particle localization in a specific area. Most work in this field has been done in improving the biocompatibility of the materials, but only a few scientific investigations and developments have been carried out in improving the quality of magnetic nanoparticles, their size distribution, their shape and surface in addition to characterizing them to get a protocol for the quality of these particles.<sup>153</sup>

Iron oxide (usually  $\text{Fe}_3\text{O}_4$  and  $\text{Fe}_2\text{O}_3$ ) nanoparticles are mostly used as magnetic nanoparticles in ferro fluids due to their high saturation magnetization ( $M_s$ ) and high magnetic susceptibility.  $\text{Fe}_3\text{O}_4$  particles are preferred because of their greater saturation magnetization. The nanoparticles need to be stabilized in the carrier liquid because they tend to agglomerate due to van der waals forces.<sup>154</sup>

### **3.3.5 Synthesis of magnetic iron oxide nanoparticles**

The preparation and synthesis of  $\text{Fe}_3\text{O}_4$  nanoparticles can be divided into physical methods such as gas phase deposition, electron beam lithography, wet chemical methods and biological methods.<sup>118,119</sup> Among

these methods, wet chemical methods are widely used due to their straightforward nature and ease of control over size, composition and even the shape of the nanoparticles. Co-precipitation is by far the most commonly used method for the preparation of  $\text{Fe}_3\text{O}_4$  nanoparticles for biotechnology. There are two main methods for the synthesis of both  $\text{Fe}_3\text{O}_4$  and  $\gamma\text{-Fe}_2\text{O}_3$  nanoparticles in solution. In the first, ferrous hydroxide  $\text{Fe}(\text{OH})_2$  suspensions are partially oxidized with different oxidizing agents, such as nitrate ions,<sup>155</sup> aqueous hydrogen peroxide ( $\text{H}_2\text{O}_2$ ) solution,<sup>156</sup> “spontaneously” in an open atmosphere or else in an inert atmosphere.<sup>157</sup> The other involves co-precipitation of  $\text{Fe}^{2+}$  to  $\text{Fe}^{3+}$  aqueous salt solutions by addition of a base.<sup>158</sup> The control of size, shape and compositions of nanoparticles depends on the type of salts used,  $\text{Fe}^{2+}$  and  $\text{Fe}^{3+}$  ratio, pH and ionic strength of the precipitation medium.<sup>159-161</sup> The disadvantage of these bulk solution syntheses is that the pH of the reaction mixture needs to be adjusted during synthesis. The production of large quantities of magnetic nanoparticles with narrow size distribution remains a significant challenge for these methods.

Some new methods with better control over size distribution of magnetic nanoparticles have recently been developed. These include the micro emulsion method and high-temperature decomposition of organic precursors.<sup>162</sup> A micro emulsion is a transparent, isotropic, and thermodynamically stable liquid medium. In water-in-oil (W/O) micro emulsion, the fine micro droplets of the aqueous phase are trapped within assemblies of surfactant molecules dispersed in a continuous hydrocarbon phase. The surfactant-stabilized micro cavities provide a confinement effect that limit particle nucleation, growth, and agglomeration. Micro emulsions have been successfully used as nanoreactors for the synthesis of magnetic nanoparticles. Lopez-Quintela and Rivas<sup>162</sup> and Gupta and Wells<sup>163</sup> prepared magnetic nanoparticles of 4 nm and 15nm with narrow size ranges and uniform chemical and physical properties using aqueous core of aerosol-[OT](AOT)/n-hexane reverse micelles (W/O micro emulsions), respectively. The nanoparticles exhibit superparamagnetic behavior with high magnetization values reaching 40-50 emu/g. The

principal advantage of the micro emulsion system is that the size of nanoparticles can be controlled by varying the concentrations of aqueous aerosol emulsions composition and by modulating the size of the aqueous micellar core. However, there are several disadvantages of using micro emulsion for the synthesis of magnetic nanoparticles. First, extensively agglomerated nanoparticles are often generated. Second, the nanoparticles are poorly crystalline for the procedure is usually performed at a relatively low temperature. Third, the yield of the nanoparticles is often very low. To overcome these, Lee *et al.*<sup>164</sup> developed novel micro emulsion methods performed at high temperature (90°C) for the synthesis of large amounts of magnetic nanoparticles ranging from 2 to 10 nm. A uniform size distribution can be achieved by adjusting the concentration of the iron (II) salt or the surfactant. The decomposition of iron precursors in the presence of hot organic solvents has yielded nanoparticles with narrow size distribution, good crystallinity and dispersibility. For example, Rockenberger *et al.*<sup>165</sup> synthesized  $\gamma$ -Fe<sub>2</sub>O<sub>3</sub> nanoparticles ranging from 4-10 nm in diameter from the direct decomposition of Fe(Cup)<sub>3</sub> (where Cup: N-nitrosophenylhydroxylamine) in octylamine at 250-300°C. Sun and Zeng<sup>166</sup> prepared mono-dispersed Fe<sub>3</sub>O<sub>4</sub> nanoparticles with size from 3 to 20 nm by the high-temperature reaction of Fe (III) acetyl acetone, (Fe (C<sub>5</sub>H<sub>7</sub>O<sub>2</sub>)<sub>3</sub>). Although they produced highly crystalline and uniform magnetic nanoparticles, this method cannot be applied to large scale and economic production, because they usually use expensive and toxic reagents, complicated synthetic steps, and high reaction temperatures.

There are various chemical methods aimed at synthesizing magnetic nanoparticles for a wide range of applications. LaConte *et al.*<sup>167</sup> focused on synthetic methods that have been adapted from the analysis of magnetic nanoparticles used for medical imaging applications. The most commonly used methods to form iron oxide nanoparticles use a precipitation-based synthesis approach, which are done by co-precipitation on reverse micelle synthesis. Although the co-precipitation method can vary the average size of nanoparticles by adjusting pH and the temperature of aqueous media, it has only limited control over the size distribution of the particles. On the

other hand, reverse micelle synthesis, can produce very uniform particles (<10% variability). Since the magnetic nanoparticles produced using reverse micelle method are soluble only in organic solvents, this technique has not been commonly used for biomedical applications. To overcome this difficulty, in a recent study by Nitin *et al.*,<sup>168</sup> a coating procedure was developed to render these uniformly sized nanoparticles water-soluble. A new development in magnetic nanoparticle synthesis is the ability to produce a large amount (~ 40g) of mono-disperse magnetic nanoparticles using metal salts as reactants. This method allows precise control of nanoparticle size (with size variation < 5%) simply by varying the experimental conditions such as temperature and concentration, which is a distinct improvement over other methods.<sup>168</sup>

It has long been of scientific and technological challenge to synthesize the magnetic nanoparticles of customized size and shape. Iron oxide (either Fe<sub>3</sub>O<sub>4</sub> or Fe<sub>2</sub>O<sub>3</sub>) can be synthesized through the co-precipitation of Fe<sup>2+</sup> and Fe<sup>3+</sup> aqueous salt solutions by addition of a base.<sup>169</sup> The control over the size, shape and composition of nanoparticles depends on the type of salts used (e.g. chlorides, sulphites, nitrates, perchlorates, etc), Fe<sup>2+</sup> and Fe<sup>3+</sup> ratio, pH and ionic strength of the media.<sup>170</sup> Conventionally, Fe<sub>3</sub>O<sub>4</sub> is prepared by adding a base to an aqueous mixture of Fe<sup>2+</sup> and Fe<sup>3+</sup> chloride at a 1:2 molar ratio. The precipitated Fe<sub>3</sub>O<sub>4</sub> is black in color. The chemical reaction of Fe<sub>3</sub>O<sub>4</sub> precipitation is given as follows:

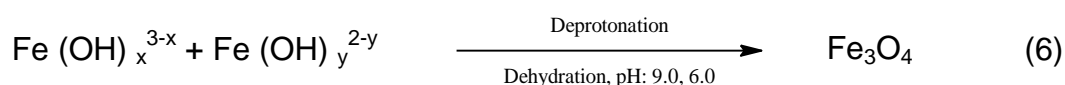
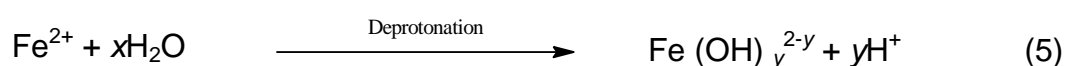
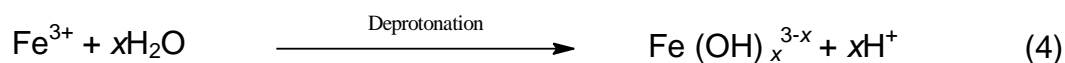
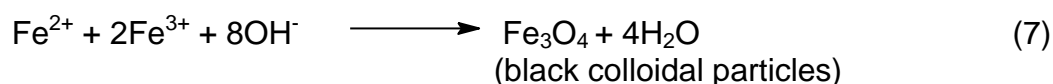
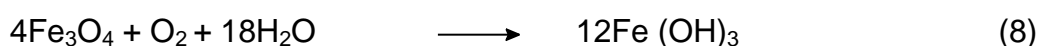


**Figure 22:** Scheme showing the reaction mechanism of Fe<sub>3</sub>O<sub>4</sub> particle formation from an aqueous mixture of ferrous and ferric chloride by addition of a NH<sub>4</sub>OH.

The overall reaction may be written as follows:



According to the thermodynamics of this reaction, a complete precipitation of  $\text{Fe}_3\text{O}_4$  should be expected between pH 9 and 14, while maintaining a molar ratio of  $\text{Fe}^{3+}:\text{Fe}^{2+}$  of 2:1 under non-oxidizing, oxygen ( $\text{O}_2$ ) free environment, i.e inert environment. Otherwise,  $\text{Fe}_3\text{O}_4$  might also be oxidized as:



This would critically affect the physical and chemical properties of the nanosized magnetic nanoparticles. In order to prevent them from possible oxidation in air as well as from agglomeration,  $\text{Fe}_3\text{O}_4$  nanoparticles produced by equation (1) are usually coated with organic or inorganic molecules during the precipitation process. To control the reaction kinetics, and therefore the oxidation speed of iron species, the synthesis of particles must be done in an oxygen free environment by passing nitrogen gas. Bubbling nitrogen gas through the solution not only removes critical oxygen from the  $\text{Fe}_3\text{O}_4$  but also reduces the particle size when compared with methods without removing the  $\text{O}_2$ .<sup>171,172</sup>

### **3.3.6 Surface modifications of magnetic nanoparticles for biomedical applications and their effect on stability and magnetization**

In the preparation and storage of nanoparticles in colloidal form, the stability of the colloid is of utmost importance. Ferro fluids are colloidal suspensions of magnetic nanoparticles ( $\text{Fe}_3\text{O}_4$  or  $\text{Fe}_2\text{O}_3$ ), forming magnetisable fluids that remain liquid in the most intense magnetic field strength. As a result of their composition, the magnetic fluids (MFs) possess a unique combination of fluidity and the capability to interact with the magnetic fields.<sup>158,173,174</sup> In the absence of any surface coating,  $\text{Fe}_3\text{O}_4$

particles have hydrophobic surfaces with a large surface area to volume ratio. Due to electrostatic interactions between the particles, these particles agglomerate and form large clusters resulting in increased particle size. These clusters, then, exhibit strong magnetic dipole-dipole attractions between them and show ferromagnetic behaviour.<sup>175</sup> When two large particle clusters approach one another, each of them comes into the magnetic field strength of the neighbour. Besides the induction of attractive forces between the particles, each particle is in the magnetic field of the other and gets further magnetized.<sup>176</sup>

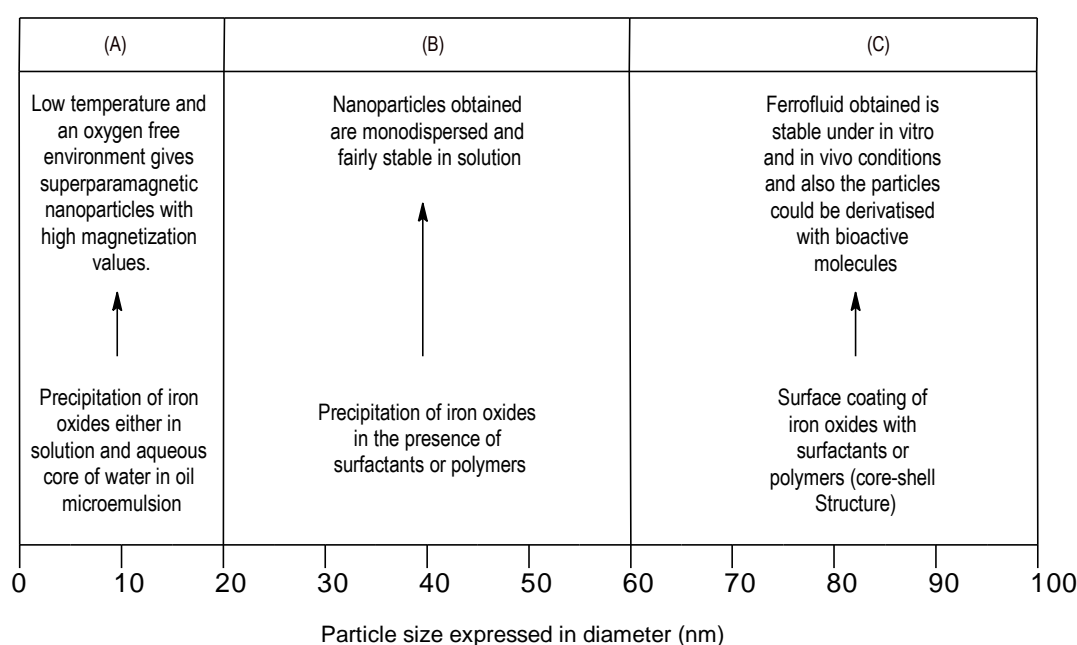


**Figure 23:** Scheme showing different strategies for fabrication and surface modification of  $\text{Fe}_3\text{O}_4$  nanoparticles.

The adherence of remnant magnetic nanoparticles causes a mutual magnetization, resulting in increased aggregation properties. Since particles are attracted magnetically, in addition to the usual flocculation due to van der Waals forces, surface modification is often indispensable. For effective stabilization of iron oxide nanoparticles, often coating is desirable. Some stabilizer such as a surfactant or a polymer is usually added at the time of preparation to prevent aggregation of the nanoscale particulate materials. Most of these polymers adhere to surfaces in a substrate

specific manner.<sup>177</sup> A scheme showing different strategies for fabrication and surface modification of Fe<sub>3</sub>O<sub>4</sub> nanoparticles is shown in figure 23.

### 3.3.7 Surface modification with non-polymeric organic stabilizers

In order to stabilize the colloidal dispersion, Yee *et al.*<sup>178</sup> studied the adsorption of alkanesulphonic and alkanephosphonic acids on the surfaces of amorphous Fe<sub>3</sub>O<sub>4</sub> nanoparticles and proposed two possible bonding schemes for phosphonate ions on Fe<sup>3+</sup>, i.e., one or two O<sub>2</sub> atoms of the phosphonate groups binding onto the surface. Sahoo *et al.*<sup>179</sup> and Tadmor *et al.*<sup>180</sup> have reported the surface derivatization of Fe<sub>3</sub>O<sub>4</sub> by oleic acid, lauric acid.etc, to stabilize the nanoparticles in organic solvents. They (Sahoo *et al.*<sup>179</sup> and Tadmor *et al.*<sup>180</sup>) found that alkyl phosphonates and phosphates could be used for obtaining thermodynamically stable dispersions of magnetic nanoparticles. The authors suggested on the basis of the results obtained from the temperature and enthalpy desorption studies that these ligands form a quasi-bilayer structure with the primary layer strongly bonded to the surface of the nanoparticles.<sup>180</sup>

Table 4: Selected proteins/targeting ligands that could be used for derivatizing Magnetic nanoparticles for various biomedical applications.	
Protein/ligand	Functionality activity
Insulin	A hormone that regulates blood glucose levels, is a small protein
Nervegrowth factor (NGF)	Promotes neurite outgrowth and neural cell survival
Ceruloplasm	Principal carrier of copper in plasma, which plays an important role in iron homeostasis and is also an effective anti-oxidant for variety of free radicals
Pullulan	High water soluble, no toxicity, usefulness as a plasma expander, non-immunogenic, non-antigenic properties. Also, evidences for receptor-mediated hepatic uptake of pullulan in rats
Elastin	A cross-linked protein in the extra cellular matrix that provides elasticity for many tissues
Albumin	The major serum protein, binds a wide variety of lipophilic compounds including steroids etc
Tat-peptide	Membrane-permeating peptide, enhances intracellular delivery
RCD peptide	Increases cell spreading, differentiation, and enhances DNA synthesis
Folic acid	Preferentially target cancer cells, poorly immunogenic, folate receptor facilitates internalization of particles

### 3.3.8 Surface modification with polymeric organic stabilizers

Various biological molecules such as antibodies, proteins, targeting ligands, etc., may also be bound to polymer surfaces on the nanoparticles by chemically coupling via amide ( $R_1$  (CO)  $NR_2R_3$ ) or ester ( $R$ -COOR') bonds to make the particles target specific. Polymeric coatings on magnetic nanoparticles offer a high potential in several areas of applications. Precipitation of inorganic particles in a cross-linked polymer matrix or network of gel often prevents coagulation of particles, giving rise to monodisperse particles.<sup>181,182</sup>

The pioneering work of Ugelstad *et al.*<sup>183</sup> based on the preparation of hydrophobic monosized polystyrene magnetic nanoparticles, has stimulated the research in this domain. Lee *et al.*<sup>184</sup> have modified nanoparticles's surface with poly vinyl alcohol (PVA) by precipitation of Fe salts in PVA aqueous solution to form stable dispersion. They found that the crystallinity of the particles decreased with increasing PVA concentration, while the morphology and particle size remained unchanged.<sup>185</sup>

### 3.3.9 Surface modification with inorganic materials

Metallic core-shell types of iron oxide nanoparticles have been investigated by several researchers. These nanoparticles have inner iron oxide core with an outer metallic shell. The iron oxide nanoparticles have been coated with silica (Si), gold (Au) or gadolinium (Gd) etc. This coating provides not only the stability to the nanoparticles in solution but also helps in binding the various biological ligands on the nanoparticles surface for various biomedical applications. Chen *et al.*<sup>186</sup> synthesized two kinds of Au-coated Fe based particles: a circular and spherical, and studied the effect of heat treatment in acid on the coercivity and saturation magnetization ( $M_s$ ) of the particles. The Au-coated circular particles had initial coercivities very close to those of the uncoated sample, and the changes after heating in acid were small. The relative saturation magnetization ( $M_s$ ) after treatment was



higher than for the uncoated particles, indicating at least partial passivation of the Fe. The uncoated spherical Fe-based particles were superparamagnetic at room temperature, but the Au-coated spherical particles had a very small coercivity due to slight oxidation during the coating process. While the relative magnetization decreased, the particle moment was still greater than would be expected for pure FeO. The Au also provides a good surface for subsequent functionalization with chemical or biological agents. Magnetic nanoparticles designed for drug delivery must also be completely biocompatible. Iron oxide nanoparticles are known to be non-toxic, and are eventually broken down to form blood haemoglobin<sup>187</sup>. Carpenter *et al.*<sup>151</sup> prepared metallic iron particles covered by a thin layer of Au via a micro emulsion. The Au shell protects the Fe core against oxidation and also provides functionality, making these composites applicable in biomedicine. Several authors have reported the Fe<sub>3</sub>O<sub>4</sub> nanoparticles coated with silica.<sup>188-192</sup> An advantage of having a surface enriched in silica is the presence of silanol groups that can easily react with hydroxyl (OH) and silane (SiH<sub>4</sub>) coupling agents<sup>188</sup> to produce dispersions that are not only stable in non-aqueous solvents but also provide the ideal anchorage for covalent bonding of specific ligands.<sup>189</sup>

### **3.3.10 Surface modifications with targeting ligands**

Various biological molecules such as antibodies, proteins, targeting ligands, etc., may also be bound to the polymer surfaces of the nanoparticles by chemical coupling via amide ester bonds to make the particles target specific. The possibilities of targeting protein coatings are numerous. Some interesting ligands with regard to targeting cell surface receptors are provided in the table 4 above. Linker molecules such as 1-ethyl-3-(3-dimethylaminopropyl) carbodiimide hydrochloride (EDCI), N-succinimidyl-3-(2-pyridyldithio) proprionate (SPDP), N-hydroxysuccinimide or N,N'methylene bis-acrylamide (MBA) are usually used to attach the initial hydrophilic coated molecules to a protein coating aimed at cell surface attachment.<sup>193</sup>

### 3.3.11 Magnetic properties of iron oxide nanoparticles

Sato *et al.*<sup>194</sup> suggested that the loss of magnetization as the particle size decrease depends largely on the crystalline magnetic anisotropy energy constant,  $K$ . Smaller  $K$  constants display lower relative magnetization ( $M$ ) values.<sup>194</sup> Experimental analyses including microscopy, X-ray diffraction (XRD) and magnetometry studies suggest that the reduced magnetization is due to surface characteristics of nanoparticles. Specifically, the loss of magnetization may be due to the existence of a magnetically dead layer, approximately 1 nm thick, caused by an asymmetric environmental effect of the surface atoms.<sup>183</sup>

Particles made from iron oxide usually behave differently in magnetic fluids depending on their size. It was reported previously by several researchers<sup>195,196</sup> that abrupt changes in magnetic properties take place when the sizes of the particles are reduced from  $\mu\text{m}$  to nm size range. For example, particles have super- paramagnetic behaviour when the size are sufficiently small (i.e. 6–15 nm) and they behave as ferromagnetic when the grain size is in  $\mu\text{m}$  range.

It was shown by Chatterjee *et al.*<sup>197</sup> that the magnetic behaviour is dependent on the blocking temperature ( $T_B$ ) of the particles ( $T_B$  is the transition temperature between the ferromagnetic and super paramagnetic state and it is directly proportional to the size of the particles), which in turn is dependent on the size of the particles. Particles with lower  $T_B$  exhibited super-paramagnetic properties, whereas the higher  $T_B$  of the particles showed the ferromagnetic behaviour of the particles.

Despite the increase in super-paramagnetic behaviour of the particles with decrease in particle size, several authors have reported a decline in the absolute saturation magnetization ( $M_s$ ) values when the size of the particle is reduced to less than 10 nm.<sup>198,199</sup>

Characteristics of the iron oxide	Preparation Method: Synthesis of iron oxide nano-particles prepared through				
	Aerosol/ vapour pyrolysis method	Gas deposition method	Bulk solution method	Sol-gel method	Micro emulsion method
Size and size distribution	About 5-60 nm with broad distribution	About 5-50 nm with narrow size distribution	About 10-50 nm with broad size distribution	About 20-200 nm with broad size distribution	About 4-15 nm with very narrow size distribution
Morphology	Spherical	Spherical	Spherical (large aggregates)	Spherical with high porosity	Cubic or spherical (no aggregation)
Magnetization values	10-50 emu/g with desired magnetic property	> 20 emu/g	20-50 emu/g with super paramagnetic behavior	10-40 emu/g with paramagnetic behavior	>30 emu/g with super paramagnetic behavior
Advantages	High production rate	Useful for protective coatings and thin film deposition	Large quantities can be synthesized	Particles of desired shape and length can be synthesized, useful for making hybrid nanoparticles	Uniform properties and also size of the nanoparticles can be modulated
Disadvantages	large aggregates formed	Require very high temperatures	Uncontrolled oxidation of magnetite maghemite, diamagnetic contribution	Product usually contains sol-gel matrix components at their surfaces	Surfactants are difficult to remove, only a small quantities of iron oxide can be synthesized

Surface modification of the iron oxide nanoparticles usually leads to the formation of a non-magnetic shell due to the formation of particle outer layer and the thickness of such a layer could be in the order of 1–20 nm.<sup>200</sup> The coating of particles with non-magnetic materials may result in decrease in saturation magnetization ( $M_s$ ) values. Gomez-Lopera *et al.*<sup>201</sup> found that surface coverage with poly(lactide-co-glycolide) polymer on the iron oxide nanoparticles decreased the saturation magnetization ( $M_s$ ) of particles to about one-half of that of the pure iron oxide nanoparticles and the initial magnetization–magnetic field strength dependence is steeper in the case of the polymer covered nanoparticles.

Voit *et al.*<sup>202</sup> also observed similar results. They studied the magnetic behaviour of super-paramagnetic nanoparticles in ferro fluids (FFs) coated with different polymers such as sodium oleate, PVA or starch. They found that surface coverage of the iron oxide with either of these polymers resulted in decreased saturation magnetization values of the particles. They also observed that the values of particle sizes calculated from the magnetization data are found to be lower than the values calculated by

XRD and Transmission Electron Microscopy measurements, which may be attributed to a magnetically ineffective layer on the particle surface.<sup>203-209</sup>

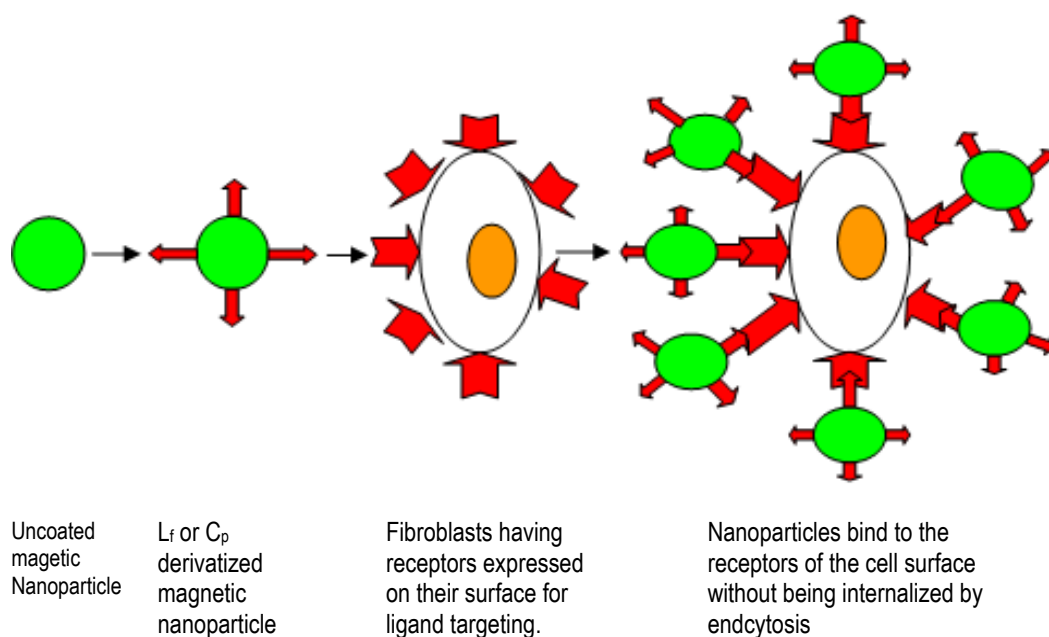


**Figure 24:** Scheme of derivatization of SPION either with targeting ligands such as lactoferrin (Lf) or ceruloplasmin (Cp) and their targeting to human fibroblasts. The derivatized NPs act as cellular markers that are targeted at the surface receptors expressed on human fibroblasts surface without being internalized (Gupta and Curtis, 2003; Gupta and Curtis, 2004)<sup>203,210</sup>.

### 3.3.12 Biomedical Applications Of Magnetic Nanoparticles

#### 3.3.12.1 Cellular labelling/cell separation

Cell labelling with ferro paramagnetic substances is an increasingly common method for *in vivo* cell separation<sup>210</sup> as the labelled cells can be detected by magnetic resonance imaging.<sup>211</sup> Most current labelling techniques utilize either of two approaches: (a) attaching magnetic nanoparticles to the cell surface<sup>212</sup> (Fig. 24) or by internalizing biocompatible magnetic nanoparticles by fluid phase endocytosis,<sup>213</sup> or phagocytosis (engulfing or ingesting of foreign particles by phagocytes).<sup>214</sup> A variety of potential ligands have been conjugated to nanoparticle surfaces to facilitate receptor-mediated endocytosis of the particles, including monoclonal antibodies (Mabs),<sup>214</sup> (Fig. 25).

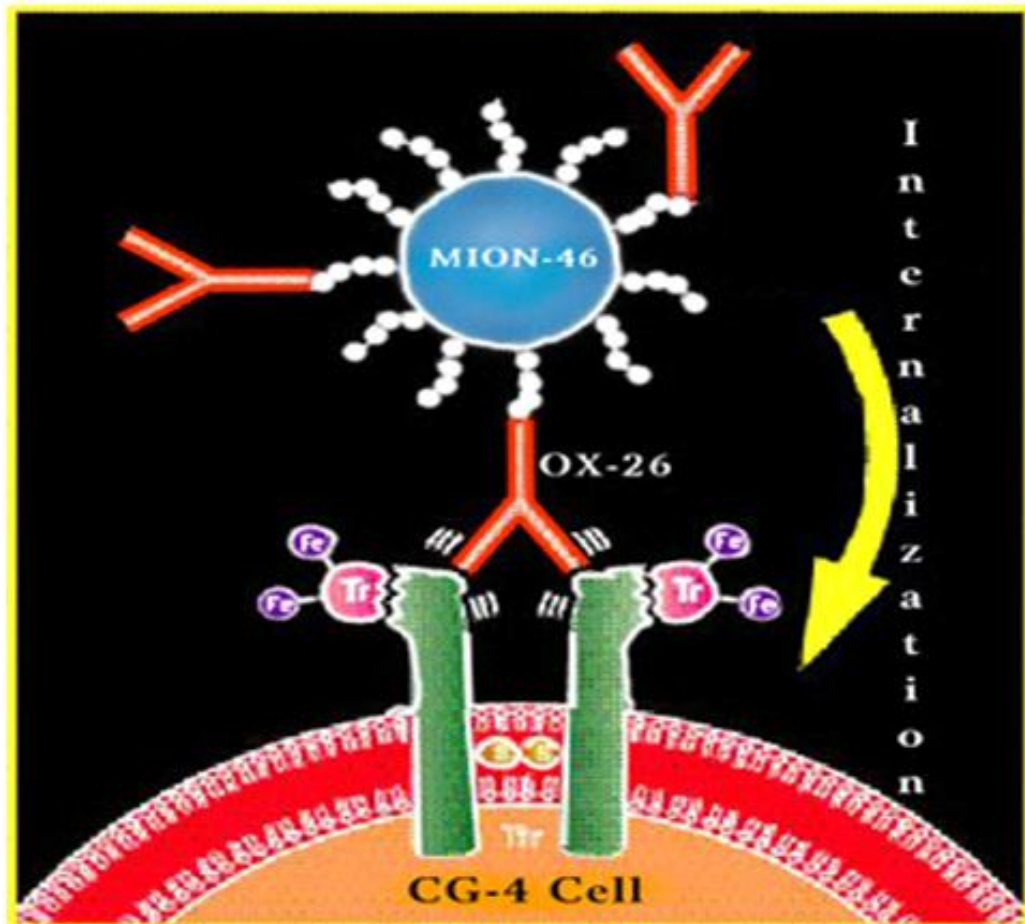


**Figure 25:** Internalisation of magnetic particles via monoclonal antibodies and transferrin receptors. Original magnetic tagging system developed by the Laboratory of Diagnostic Radiology Research (LDRR) team and their colleague's shuttles nanoparticles of FeO (MION-46L) into cells via monoclonal antibody (OX-26) to the cell's transferrin receptors.<sup>215</sup>

### 3.3.12.2 Tissue repair

Tissue repair using iron oxide nanoparticles is accomplished either through welding opposing two tissue surfaces then heating the tissues sufficiently to join them, or through soldering, where protein or synthetic polymer-coated nanoparticles are placed between two tissue surfaces to enhance joining of the tissues.<sup>211</sup> Nanoparticles that strongly absorb light corresponding to the output of a laser are also useful for tissue-repairing procedures. Specifically, gold or silicon coated iron oxide nanoparticles have been designed to strongly absorb light.<sup>212,213</sup>

The nanoparticles could be coupled to specific cells and used to target these cells towards a desired site in the body. In addition, various proteins, growth factors, etc., could be bound to these nanoparticles and delivered at the damaged tissue, where they would play a role in tissue development. While there is no doubt that the use of stem cells in the form of cell based therapies offers tremendous potential for diseases including diabetes, cancer, heart disease, Alzheimer's and Parkinson's disease, central to this process would be the ability to target and activate these stem cells at the sites of injury and/or repair using magnetic particle targeting technology.<sup>212,213</sup>

### **3.3.12.3 Drug delivery**

Another possible and most promising application of these colloidal magnetic nanoparticles is in drug delivery, as carriers of drug for site-specific delivery of drugs. Ideally, they could bear either on or in their bulk a pharmaceutical drug that could be delivered to the target organ and released there. For these applications, the size, charge and surface chemistry of the magnetic particles are particularly important as they strongly affect both the blood circulation time as well as bioavailability of the particles within the body.<sup>216</sup>

In addition, magnetic properties and internalization of particles depend strongly on the size of the magnetic particles.<sup>197</sup> A number of authors have described the preparation of particles or liposome's containing a certain amount of  $\text{Fe}_3\text{O}_4$  or other ferrites. Some of them have focused on the field of drug transport and release: thus, the use of albumin with entrapped  $\text{Fe}_3\text{O}_4$  has been studied for the release of anti-cancer drugs like mitomycin and adriamicin.<sup>216,217</sup> The attachment of drugs to magnetic nanoparticles can be used to reduce drug doses and potential side effects to healthy tissues and the costs associated with drug treatment.

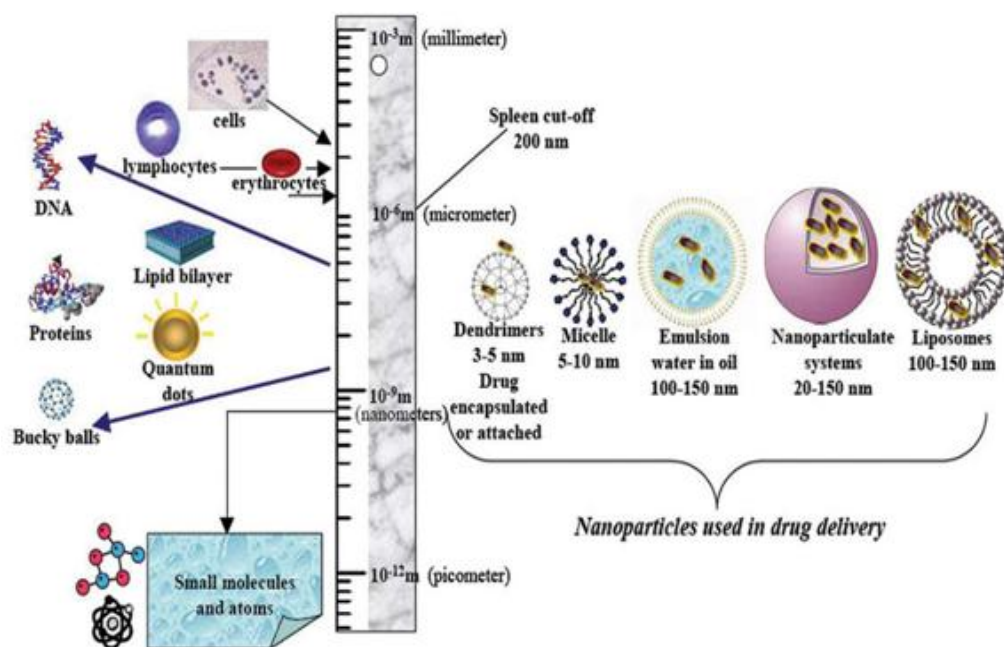


**Figure 26:** Nanoparticle systems for drug delivery (DD) applications.<sup>218,219</sup>

### 3.3.12.4 Magnetic resonance imaging (MRI)

Superparamagnetic iron oxide nanoparticles play an important role as contrast agents in magnetic resonance imaging (MRI), to better differentiate healthy and pathological tissues. Recent developments in magnetic resonance imaging have enabled *in vivo* imaging at near microscopic resolution.<sup>220</sup> Clinical diagnostics with MRI has become a popular non-invasive method for diagnosing mainly soft tissue or recent cartilage pathologies, because of the different relaxation times of hydrogen atoms.<sup>221,222</sup> SPION were developed as contrast agents for MRI and increase the diagnostic sensitivity and specificity due to modifications of the relaxation time of the protons.<sup>117,221,223</sup> The first dextran coated SPION were already 10 years ago officially registered as contrast agents for MRI of the liver in Europe.<sup>224</sup> The efficacy of the SPION as contrast agents in various tissues depends on their physicochemical properties, such as size, charge and coating,<sup>225</sup> and can be increased through surface modifications by biologically active substances such as antibodies, receptor ligands, polysaccharides, proteins., etc.<sup>221,223,226</sup>

The hydrodynamic diameter of the SPION used with MRI varies between 20 and 3500 nm, although intravenously applied particles are relatively small and range between 20 and 150 nm with, or 5-15 nm without coating.<sup>179,227</sup> SPION are predestined for use as combined carrier systems for drug delivery while at the same time serving as contrast agent.<sup>223</sup> In this way, the kinetics of the pharmaceutical agent could be followed by means of MRI. In addition, distribution of particles can be influenced through the application of an external magnet.<sup>197</sup> Most iron oxide nanoparticles have a relatively short half-life and their primary application is for imaging of liver, spleen and gastrointestinal (GI) tract. Surface-modified iron oxide nanoparticles having long blood circulation times, however, may prove very useful for imaging of the vascular compartment (magnetic resonance angiography), imaging of lymph nodes, perfusion imaging, receptor imaging and target specific imaging.<sup>228</sup>

### **3.3.12.5 Hyperthermia**

Through the oscillation of the magnetic moment inside the particles the magnetic field strength energy is liberated in the form of heat and conducted to the tissue environment.<sup>221</sup> The use of hyperthermia (heat) in the treatment of malignant tumors is as old as medicine itself. For example, Hippocrates, the father of medicine, proposed that surface tumors should be cauterized by application of hot iron.<sup>229,230</sup> In modern times, more advanced methods (hot water bath, pyrogens such as mixed bacterial toxins, perfusion heating, high-frequency radiation, magnetic fluid hyperthermia) were employed to heat, and hopefully destroy, tumors.<sup>231</sup> Magnetic induction hyperthermia (MIH), one of the approaches for cancer treatment, is the exposure of cancer tissues to an alternating magnetic field. The energy of the alternating magnetic field strength is not absorbed by the living tissues, but is absorbed by the magnetic nanoparticles, and can be applied to deep seated tumors in the living body. When magnetic particles are subjected to the alternating magnetic field strength, some heat is generated due to magnetic hysteresis loss. The amount of heat generated depends on the nature of magnetic material and or magnetic



field strength parameters. Magnetic particles embedded in a tumor site and placed within an oscillating magnetic field strength will heat up to a temperature dependant on the magnetic properties of the material, the strength of the magnetic field strength, the frequency of oscillation and the cooling capacity of the blood flow in the tumor site.

Cancer cells are destroyed at temperature higher than 43°C; where as the normal cells can survive at higher temperatures. Heat could be generated applying an appropriate magnetic field strength. The size of the iron oxide nanoparticles is sub micrometric, so the powders or bulk of these biomaterials have comparable properties. These materials are not only biocompatible but also bioactive and could be useful for bone tumors.<sup>232</sup> Much work using magnetic particles for hyperthermia has been done in order to manifest a therapeutic effect on several types of tumors by performing experiments with animals<sup>233</sup> or using cancerous cell cultures.<sup>234</sup>

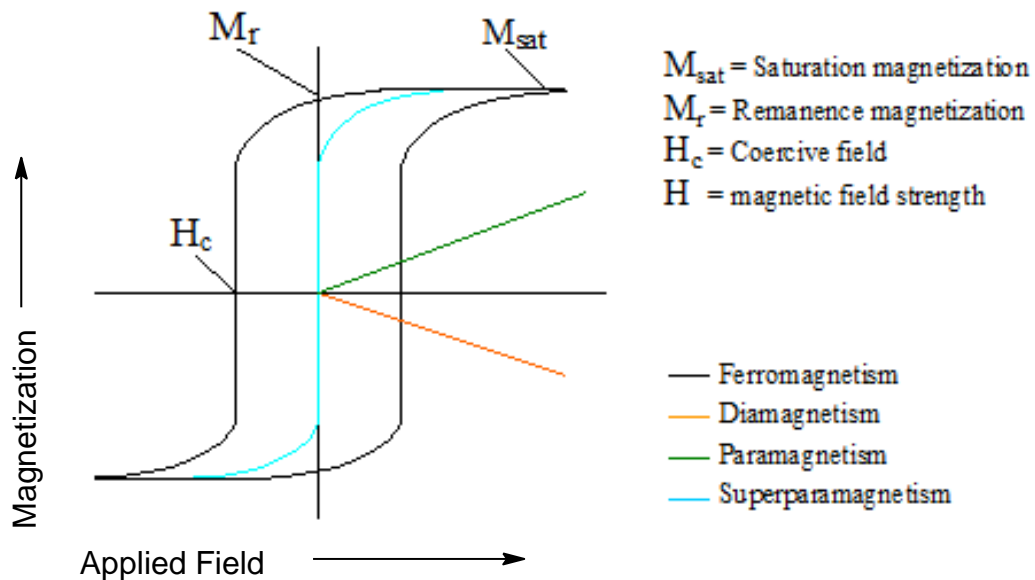


**Figure 27:** Hysteresis loops (M versus applied H) characteristic of ferromagnetic and superparamagnetic nanoparticles

### 3.3.12.6 Magnetofection

Magnetofection (MF) is a method in which magnetic nanoparticles associated with vector DNA are transfected into cells by the influence of an

external magnetic field (B). For this purpose, magnetic particles might be coated with the polycation polyethylenimine (PEI).<sup>235</sup> These complexes readily associate with negatively charged DNA since the magnetic nanoparticles are positively charged due to the PEI.

Whether viral or nonviral vectors, magnetofection has been shown to enhance the efficiency of the vectors up to several thousand times.<sup>235</sup> For magnetically enhanced nucleic acid delivery, magnetofection is universally applicable to viral and nonviral vectors; because it is extraordinarily rapid, simple and yields saturation level transfection at low dose *in vitro*.<sup>236</sup> Furthermore, since these magnetic particles do not rely on receptors or other cell membrane-bound proteins for cell uptake, it is possible to transfect into cells that normally are transfection non-permissive.<sup>235</sup>

### **3.4 Tailoring Magnetic Nanoparticles (MNPs)**

Recently, synthesis of magnetic materials on the nanoscale has been a field of intense study, due to the novel mesoscopic properties shown by particles of quantum dimensions located in the transition region between atoms and bulk solids. Nanosized particles have physical and chemical properties that are characteristic of neither the atom nor the bulk counterparts<sup>161</sup>. Quantum size effects and the large surface area of magnetic nanoparticles dramatically change some of the magnetic properties. They exhibit superparamagnetic phenomena and quantum tunneling of magnetization, because each particle can be considered as a single magnetic domain. Based on their unique mesoscopic physical, tribological, thermal, and mechanical properties, superparamagnetic nanoparticles offer a high potential for several applications in different areas such as ferrofluids, color imaging, magnetic refrigeration, detoxification of biological fluids, magnetically controlled transport of anti-cancer drugs, magnetic resonance imaging contrast enhancement and magnetic cell separation.<sup>161</sup> A difficulty related to the nature of ferrofluids is that the nanoparticles, which have a large ratio of surface-area to volume, tend to agglomerate in order to reduce their surface energy ( $> 100$  dyn/cm)

by strong magnetic dipole-dipole attractions between particles. Therefore, one of the main problems in producing stable magnetic fluid is to prevent agglomeration during the synthesis and coating process.<sup>161</sup>

Ferrofluids or magnetic fluids are stable colloidal homogeneous suspensions of magnetic nanoparticles (around 10 nm in diameter) in an appropriate carrier (aqueous or non-aqueous) liquid.<sup>143</sup> They are said to be superparamagnetic (SPM), meaning that they are attracted by a magnetic field but retain no residual magnetism after the field is removed<sup>143</sup>. Due to their small size and superparamagnetic behavior, ferrofluids have been extensively used in several technological and biomedical applications.<sup>143</sup> Iron oxide (usually magnetite and maghemite) nanoparticles are mostly used as magnetic particles in ferrofluids due to their high saturation magnetization and high magnetic susceptibility, the magnetite ( $\text{Fe}_3\text{O}_4$ ) particles are preferred because of their greater saturation magnetization. The nanoparticles need to be stabilized in a carrier liquid because they tend to agglomerate due to Van der Waals forces. In addition the magnetite nanoparticles are very much susceptible to air oxidation. In order to prevent the possible air oxidation as well as agglomeration, the  $\text{Fe}_3\text{O}_4$  nanoparticles are coated with a surfactant for example fatty acids or a polymer for example dextran.<sup>143</sup> Also once the dispersing agent is adsorbed on the iron oxide particles, the number of accessible sites for further crystal growth is reduced to keep the particle size small.<sup>143</sup>

### **3.4.1 Essential requisites**

Magnetic nanoparticles for biological applications must be endowed with the specific and required characteristics. The first requirement is quite often super-paramagnetism. Super-paramagnetism occurs in magnetic materials composed of very small crystallites. Threshold sizes depend on the nature of the material, for instance, iron-based nanoparticles become superparamagnetic at sizes less than 25 nm.<sup>184</sup> In a paramagnetic material, the thermal energy overcomes the coupling forces between neighboring atoms above the Curie temperature ( $T_c$ ) causing random fluctuations in the

magnetization direction that result in a null overall magnetic moment. However in super paramagnetic materials, the fluctuations affect the direction of magnetization of entire crystallites. When the external magnetic field strength is applied, instead of each individual atom being independently influenced by an external magnetic field strength, the magnetic moment of entire crystallites aligns with the magnetic field strength. In large nanoparticles, energetic considerations favor the formation of domain walls. However, when the particle size decreases below a certain value, the formation of domain walls becomes unfavorable and each particle comprises a single domain. This is the case for super-paramagnetic nanoparticles. Super-paramagnetism in drug delivery is necessary because once the external magnetic field strength is removed, magnetization of the magnetic particles must disappear, so that agglomeration is avoided. Another key requirement is the biodegradability or intact excretion of the magnetic particles. Thus, SPION are considered to be biodegradable with iron being reused/recycled by cells using normal biochemical pathways for iron metabolism.<sup>237</sup>

### **3.4.2 Coatings on magnetic nanoparticles**

Surface coatings of nanoparticles with various materials to form core-shell morphologies results in the formation of materials that can be used for the development of catalysts and optic-electronic devices.<sup>238-240</sup> Studies on protective layer-coated ferromagnetic nanoparticles are of great interest for both fundamental magnetic investigations and practical engineering applications. In fundamental studies the coating on nanoparticles is of interest as it can prevent the nanoparticles from coarsening, surface oxidation, and agglomeration; in clinical applications, the coating protects the nanoparticles from leaching in an acidic environment; in soft magnetic applications, the coating not only works as an insulative phase to achieve high electric resistivity, but also behaves as a binder to ease the consolidation of the nanoparticles.<sup>241,242</sup>

The coatings on magnetic nanoparticles often serve multiple purposes. Their role in reducing leaching of the cores has already been mentioned. Often coating also facilitates the stabilization of nanoparticles in an environment with a slightly alkaline pH or a significant salt concentration. For instance, the isoelectrical point of silicon dioxide (SiO<sub>2</sub>) is reached at pH 2-3, meaning that Si-coated nanoparticles are negatively charged at the pH of blood, inducing electrostatic repulsion that helps avoid aggregate formation. Si coatings also have additional advantages. The external surface of Si coatings can be functionalized to allow the binding of biomolecules. This is mainly related to the presence of hydroxyl surface groups in significant concentrations that provide intrinsic hydrophilicity and allow surface attachment by covalent linkage of specific biomolecules.<sup>243</sup>

A variety of approaches have been developed to coat magnetic nanoparticles including *in situ* coatings and post synthesis coatings. In the *in situ* coating approach, the magnetic nanoparticles are coated during the synthesis process. For example, Sunderland *et al*<sup>244</sup>, and Neuberger *et al*<sup>245</sup> have developed a co-precipitation process in the presence of the polysaccharide dextran. The coating is further cross linked chemically to increase the stability. This particular coating approach has been very successful in producing dextran superparamagnetic iron oxide nanoparticle which are biocompatible and water-soluble, and can be used for a range of preclinical and clinical imaging studies. Other coatings in this class include a starch-based coating<sup>246</sup> and dendrimer coating.<sup>247,248</sup>

The post-synthesis coating methods used for magnetic nanoparticles use a variety of materials, including monolayer ligands<sup>249,250</sup> and polymer<sup>250,251</sup> and combinations of polymers and biomolecules such as phospholipids and carbohydrates,<sup>252,253</sup> and silicon (Si) coatings.<sup>184,254</sup> Most monolayer coatings have low colloidal stability and because of toxicity of the capping ligands, limited application in medical imaging. The polymer and Si based coating process are difficult to control, often resulting in multilayered coatings and multiple nanoparticles in the same encapsulation.<sup>254</sup>

### 3.4.3 The fate of nanoparticles after administration into the body

The distribution of nanoparticles and their loads throughout the body depends on numerous physicochemical factors: size of particles, toxicity, surface charge, capacity for protein adsorption, surface hydrophobicity, drug loading and release kinetics, stability, degeneration of carrier system, hydration behavior, electrophoretic mobility, porosity, specific characteristics, density, crystallinity, contact angle, and molecular weight.<sup>245</sup> Nevertheless, the fate and consequently the possible toxicity of magnetic nanoparticles also depends strongly on the dose and administration route.

After particles are injected into the blood stream, they are conditioned or coated by elements like plasma proteins and glycoproteins available in the circulatory system. This process is called opsonization. The process makes the nanoparticles recognizable by the major defense system of the body like the macrophages (mainly kupffer cells in the liver) and other macrophages remove these opsonized particles. Particles having hydrophobic surface are more efficiently coated, but those having hydrophilic surface resist coating and are therefore cleared more slowly from the body. The macrophages take the particles to the endosomes and lysosomes where they are degraded, so that the drug the particle is carrying is released and diffused to the circulatory system. The particles are later excreted from the body or processed further by the body for other possible metabolic activities.

Where uptake of particles by macrophages may be a hinderance in drug delivery to target area, the particles may be disguised, so that they are not recognized by the kupffer cells and therefore escape capture by the cells. The nanoparticles may be disguised partly by making them hydrophilic (depending on the type of treatment) and by stabilizing them using absorbed polymers which did not allow recognition of liposome by macrophages and thus prevent opsonization.<sup>255</sup>

### 3.4.4 The toxicity of Nanoparticles

When discussing the toxicity of nanoparticles, generalization becomes difficult because their toxicity depends on numerous factors including the dose, chemical composition, method of administration, size, biodistribution, surface chemistry, shape, and structure, to name but a few. With nanoparticles, as with any new biomedical discovery, the risk – benefit trade-off must be considered to assess whether the risks can be justified. In general, the size, surface area, composition, and coating of a nanoparticle is the most important characteristic regarding cytotoxicity<sup>256</sup> and modifications of the nanoparticle surfaces are a key tool to minimize toxicological effects.<sup>257</sup>

It is well documented that the large surface-to-volume ratio of all nanosized particles can potentially lead to unfavorable biological responses if they are inhaled and subsequently absorbed via the lung or swallowed and then absorbed across the gastro-intestinal tract.<sup>258</sup> Interestingly, it has also been reported that in 20-100 mg/ml concentration, large magnetic nanoparticles show higher cytotoxicity than smaller ones even after normalizing for surface area despite the lower surface-to-volume ratio.<sup>259</sup> Although it is difficult to perform comparable experiments with differently sized particles. In any case, toxicity studies should consider not only acute toxicity but also that of degradation products, the possible stimulation of cells with subsequent release of inflammatory mediators and long-term toxicity.<sup>245</sup>

## Chapter 4

### 4.1 Methodology And Experimental

### 4.2 Materials

All materials were purchased from the commercial supplier Sigma Aldrich (Pty) Ltd and used without any further purification. However solvents like dichloromethane (DCM:  $\text{CH}_2\text{Cl}_2$ ), triethylamine [ $\text{CH}_3\text{CH}_2$ ] $_3\text{N}$ ], pyrrole ( $\text{C}_4\text{H}_5\text{N}$ ) and *N,N*-dimethylformamide [DMF:  $(\text{CH}_3)_2\text{CONH}_2$ ] were distilled from anhydrous calcium hydride ( $\text{CaH}_2$ ), prior to use. Tetrahydrofuran (THF:  $\text{C}_4\text{H}_8\text{O}$ ) was dried on sodium metal and benzophenone until the solution turns blue then distilled under vacuum prior to use.

1. 3-Hydroxybenzaldehyde	2. 1,3-Dibromopropane
3. Potassium thioacetate	4. Pyrrole
5. p-Choranil	6. Trichloroacetic acid
7. Trichloroacetic acid	8. Calcium chloride
9. Dry <i>N,N</i> -Dimethyl formamide (DMF)	10. Dichloromethane (DCM)
11. Tetrahydrofuran (THF)	12. Calcium hydride
13. Sodium hydroxide	14. Hydrochloric acid
15. Triethylamine	16. Sodium metal
17. Benzophenone	18. Hexane
19. Diethyl ether	20. Pentane
21. Ethyl acetate	22. Agron gas
23. Nitrogen gas	24. Pyrrole
25. Silica gel	26. Distilled deionised water
27. All glass vacuum apparatus	28. Sodium chloride
29. TLC plates	30. Filter papers
31. Chromatographic columns	32. Hot plates
33. Needles and syringes	34. Dark room
35. Ferric chloride hexahydrate	36. Ferrous chloride tetrahydrate
37. Deoxygenated ammonium hydroxide	38. Deoxygenated water
39. Sodium citrate	40. Gold chloride



### 4.3 Materials for nanoparticle synthesis

Ferric (III) chloride hexahydrate ( $\text{FeCl}_3 \cdot 6\text{H}_2\text{O}$ , >99%), Ferrous (II) chloride tetrahydrate ( $\text{FeCl}_2 \cdot 4\text{H}_2\text{O}$ , >99%), hydrogen tetrachloroaurate (III) hydrate ( $\text{HAuCl}_4$ ), sodium citrate dihydrate ( $\text{Na}_3\text{C}_6\text{H}_5\text{O}_7 \cdot 2\text{H}_2\text{O}$ , >99%), ammonium hydroxide ( $\text{NH}_4\text{OH}$ ) were obtained from Sigma-Aldrich. The other chemicals were of analytical grade from other local suppliers and used without further purifications. All aqueous solutions were prepared using Millipore purified water ( $18.2 \text{ M}\cdot\Omega\text{cm}^{-1}$ ). All the water used in experiments was deionized water ( $18.2 \text{ M}\Omega \text{ cm}^{-1}$ , Millipore Synergy 185).

### 4.4 NMR Analysis

$^1\text{H}$ -NMR and  $^{13}\text{C}$ -NMR spectra were measured on a Varian Mercury (300 MHz and at 75 MHz) in  $\text{CDCl}_3$  as solvent. Chemical shifts ( $\delta$  values) are reported in ppm, using the residual solvent peak in  $\text{CDCl}_3$  ( $\delta_{\text{H}} = 7.26$  and  $\delta_{\text{C}} = 77.0$ ) and tetramethylsilane ( $(\text{CH}_3)_4\text{Si}$  ( $\delta_{\text{H}} = 0.00$ )) as internal standards, coupling constants ( $J$ ) are given in Hz without signs.

### 4.5 Flash column chromatography

Flash column chromatography was performed using  $60 \text{ \AA}$  (35-70 $\mu\text{m}$ ) silica gel in a 50 cm x 3 cm glass chromatographic column.

### 4.6 Optical Analyses

#### 4.6.1 UV Analysis

UV-Visible measurement was carried out on UV-Visible (Varian Cary 100) at scan mode to obtain the wavelength of maximum ( $\lambda$ -max) absorption for the solution of porphyrin and suspension of gold coated nanoparticles. The  $\lambda$ -max of the porphyrin coated, with gold coated SPION was similarly obtained.

#### 4.6.2 Infra-red analysis

Infra-red analysis was carried out on all the compounds using Perkin Elmer Spectrum 100, FT-IR Spectrometer with universal ATR sampling accessory from the starting material 3-hydroxybenzaldehyde (Scheme 18, **82**) to the precursor, (5,10,15,20-Tetrakis[3-(3-thioacetoxypropoxy)phenyl]porphyrin) (**85**) then (5,10,15,20-Tetrakis[3-(3-thiolpropoxy)phenyl]porphyrin) (**86**) the desired target porphyrin, to confirm the presence of some functional groups on the respective molecules. The FT-IR of the porphyrin alone was compared with that of the immobilized porphyrin on nanoparticles to show some of the features of the FT-IR spectrum that are indicative of immobilization of the porphyrin on the gold surface of the nanoparticle.

#### 4.7 TEM and HRTEM

Other spectroscopic and microscopic analyses for characterization of the nanoparticles and the functionalized gold coated nanoparticles was done on Transmission Electron Microscope (**TEM**) JEN -1010 (JEOL, JAPAN) and High Resolution Transmission Electron Microscope (**HRTEM**) was carried out on JEOL 2100 operating at 200 KV. An x-ray diffraction (**XRD**) (D8 FOCUS 2.2 kW, Bruker, Germany) was used to characterize iron oxide nanoparticles and gold coated nanoparticles.

#### 4.8 Magnetization studies

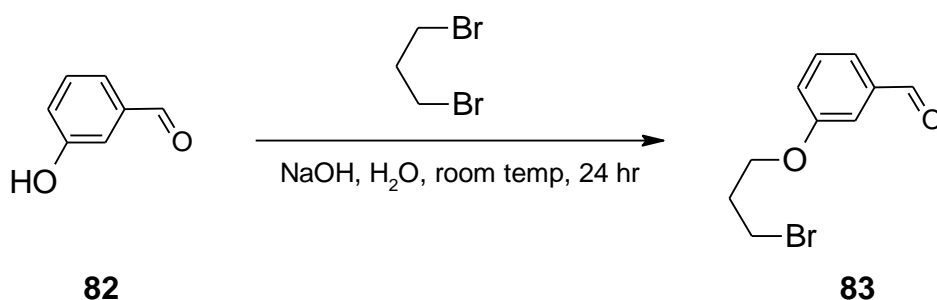
Vibrating sample magnetometer (**VSM**, EG & G Princeton Applied Research Vibration Sample Magnetometer, Model 155) was used to investigate the magnetic properties of nanocomposites by measuring the magnetization as a function of magnetic field strength intensity. The temperature dependence of the magnetization of nanocomposites were investigated on superconducting quantum interference device (**SQUID**) magnetometer (MPMS5, Quantum Design) at a temperature ranging from 2 to 300 K under different applied magnetic field strength (H).

## 4.9 Synthesis of Thiolated Porphyrin

The prevalent synthetic routes to porphyrin thioacetates comprise the derivatization of the substituted porphyrins with a suitable reagent to form the thioacetate.<sup>103</sup> Alternatively, there are routes present in the literature where *S*-acetylated thio-benzaldehydes were converted into the corresponding porphyrins which upon alkaline or acid hydrolysis afforded the free thiols.<sup>103-105</sup> Representative examples include the reaction of a porphyrin-amine with an *S*-protected alkanethiol bearing an acid chloride reaction of a porphyrin-amine with the disulphide of an  $\omega$ -mercaptoalkanoic acid, reaction of a porphyrin-bromide with thioacetate or thio-urea, or conversion of a phthalocyanine-alcohol to the thiol via a treatment of the mesylate with thiourea.<sup>105</sup> In this manner, porphyrins bearing one to four thiols have been prepared. Most of these compounds have structures with long flexible hydrocarbon chains intervening between the thiol and the porphyrin. A complementary but rarely used route involves introducing the thiol unit into the aldehyde precursor of the porphyrin.

One example of this strategy involves the conversion of *p*-(thiomethyl)benzaldehyde to the *meso-tetrakis-p*-(thiomethyl)phenyl-substituted porphyrin, which upon Pummerer rearrangement and cleavage afforded the free thiol. The only other examples using this route involves the conversion of *S*-acetylated thiolbenzaldehydes to the corresponding porphyrins, which upon alkaline hydrolysis afforded the free thiols.

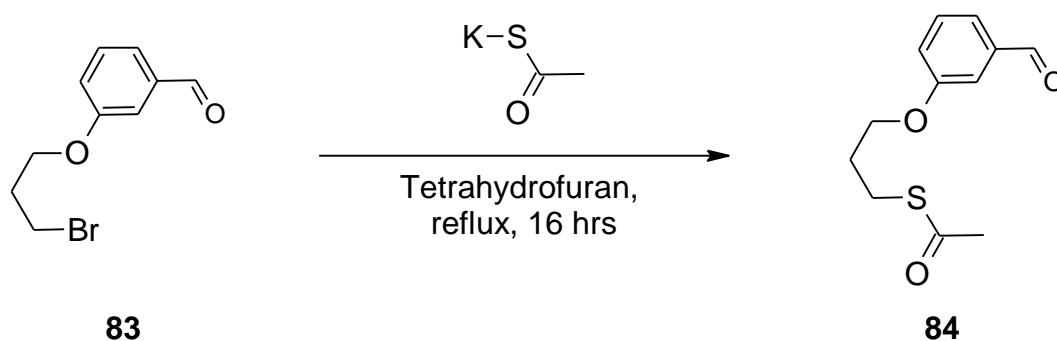
Although undeveloped, this latter route affords the opportunity to prepare porphyrins bearing protected thiols without performing extensive manipulations on the porphyrin. In this work, the method according to Schweizer *et al*<sup>114b</sup> and Backvall *et al*<sup>114j</sup> was adopted for the synthesis of the thiolated porphyrin. However, nuclear magnetic resonance data from the material obtained after the attempted acid and alkaline hydrolysis of the *S*-acetylated porphyrin indicated that the hydrolysis did not take place.



**Scheme 16:** Synthesis of 3-(3-Formylphenoxy)propyl bromide

#### 4.10 Synthesis of 3-(3-Formylphenoxy)propyl bromide (83)

3-Hydroxybenzaldehyde (**82**) (9.15 g, 0.075 M) was dissolved in NaOH (37 ml of 2 M). After flushing with argon, 1,3-dibromopropane (18.1 g, 0.09 M) was added and the reaction mixture stirred vigorously over a 24-h period under reflux. The mixture was cooled, the layers were separated and the aqueous phase extracted twice with dichloromethane (20 ml). The non-aqueous phase were combined and washed with four 25 ml portions of 2 M NaOH and once with 25ml 2 M HCl and finally with two 25 ml portions of water. The organic layer was dried over CaCl<sub>2</sub> and concentrated to give a dark brown solution. The product was purified using column chromatography (Hexane 3: Ethyl acetate 2), to give a clear yellow pure sample of 3-(3-bromopropoxy)benzaldehyde **83**. Yield: 10.4g, 57.10%

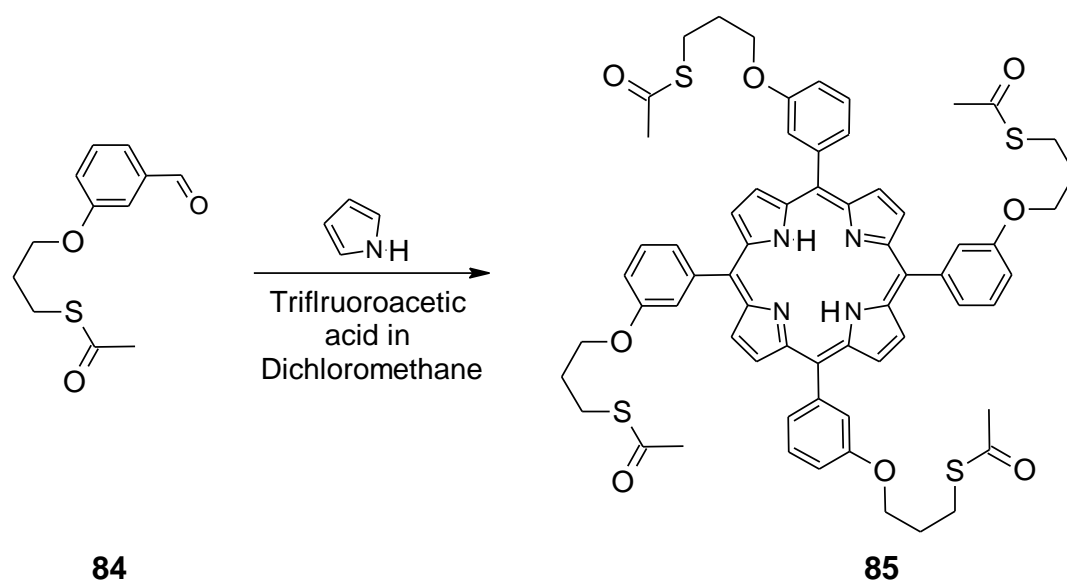


**Scheme 17:** Synthesis of 3-(3-formylphenoxy)propyl thioacetate

#### 4.11 Synthesis of 3-(3-formylphenoxy)propyl thioacetate (84)

Propylbromide **83** (4.13 g, 0.017 M) and potassium thioacetate (3.95 g, 0.035 M) were dissolved in 50 ml of dry THF and the mixture refluxed for

16 hrs. The mixture was cooled to ambient temperature, the reaction mixture was filtered to remove precipitates and the solvent of the filtrate was evaporated in vacuo, the dark brown oil was dissolved in 37 ml of diethyl ether and washed twice with 37 ml of brine. The organic layer was dried over CaCl<sub>2</sub>, filtered and solvent evaporated in vacuo. The product was purified by flash chromatography (silica, pentane/diethyl ether 4:1) to yield the thioacetate **84**, 3-(3-formylphenoxy)propyl thioacetate. Yield: 44.4%

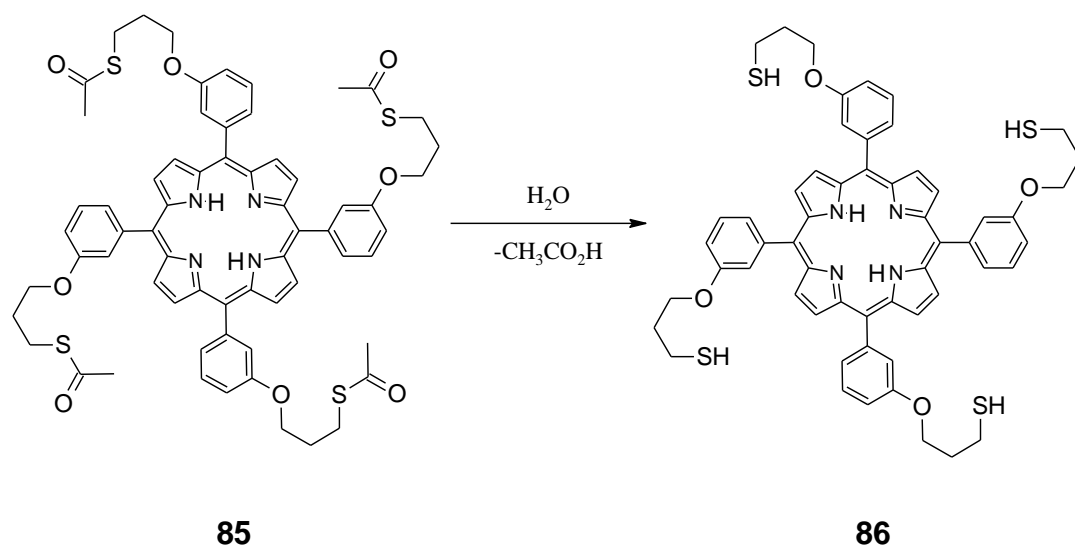


**Scheme 18:** Synthesis of 5,10,15,20-Tetrakis[3-(3-thioacetoxypoxy)phenyl]porphyrin (**85**)

#### 4.12 Synthesis of 3-(3-formylphenoxy)propyl thioacetate (**85**)

Compound **84** (5.15 g, 21.6 mmol) and pyrrole (1.50 ml, 21.6 mmol) were dissolved in 500 ml dichloromethane. Under argon atmosphere a solution of trifluoroacetic acid (1.65 ml, 21.6 mmol) in 10 ml dichloromethane was slowly added. The reaction mixture was stirred 1.5 hrs in the dark under argon, during which time it turned dark purple. *p*-chloranil (3.98 g, 16.2 mmol) was added and the reaction mixture refluxed for 1 hr. The mixture was allowed to cool to ambient temperature, after the mixture was cooled to ambient temperature, triethylamine (3.0 ml, 21.6 mmol) was added to neutralize the solution. The reaction mixture was then filtered and the volume reduced to 50 ml. The product was purified using column

chromatography (silica, CH<sub>2</sub>Cl<sub>2</sub>), to afford Compound **85** (5,10,15,20-tetrakis[3-(3-thioacetoxypropoxy)phenyl]porphyrin). Yield: 30%



**Scheme 19:** Attempted hydrolysis of Compound **85** to Compound **86**

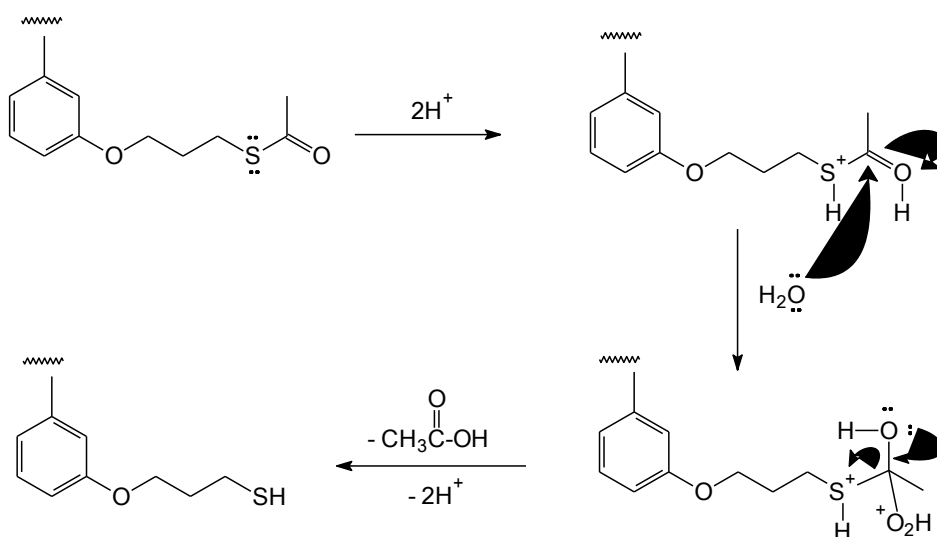
#### 4.13 Attempted hydrolysis of Compound **85** to Compound **86**

A solution of 0.5 mM Compound 4 in *N,N*-dimethylformamide (DMF) was prepared. Hydrolysis of the thioacetoxypropoxy porphyrin 5,10,15,20-Tetrakis[3-(3-thioacetoxypropoxy)phenyl]porphyrin (**85**) to the free base porphyrin 5,10,15,20-tetrakis[3-(3-thiolpropoxy)phenyl]porphyrin (**86**) was attempted both under acidic and basic conditions, by adding a solution of HCl (0.5 M in (v/v) 40% H<sub>2</sub>O) for the acid conditions, or a solution of 60% NaOH (0.5 M) in methanol for the alkaline conditions, to the porphyrin solution (100 ml) at room temperature, however, complete hydrolysis was not achieved under both conditions.

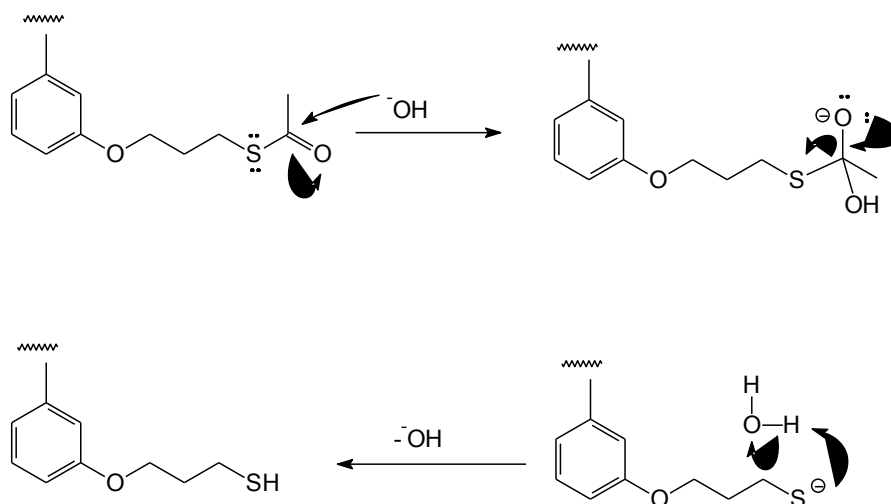
##### 4.13.1 Attempted Acid Hydrolysis

The acid solution (10, 20, 30, 40, 50 ml) was mixed with 50 ml each of porphyrin solution and stirred at room temperature in the dark under inert atmosphere first for 3, then for 5 and 24 hrs. The organic porphyrin phase

was collected, dried over calcium chloride and evaporated in vacuo and the product was characterized by nuclear magnetic resonance (NMR).



Proposed acid catalysed mechanism



Proposed alkaline hydrolysis

**Scheme 20:** Proposed reaction mechanism for the acid and alkaline hydrolysis

#### 4.13.2 Attempted Base Hydrolysis

Sodium hydroxide solution (10, 20, 30, 40, 50 ml) were mixed with 50 ml each of porphyrin solution and stirred at room temperature in the dark under inert atmosphere first for 2, 3, 5 and 24 hrs. The organic porphyrin

phase was collected, dried over calcium chloride and evaporated in vacuo and characterized by nuclear magnetic resonance (NMR).

#### 4.13.3 The mechanism of Hydrolysis of compound 85 to 86

The acid catalysed mechanism is expected to involve protonation of the thioester linkage and the carbonyl carbon of the thioacetate. Nucleophilic attack by a molecule of water should then displace one molecule of acetic acid, and release the acid catalyst. Alkaline hydrolysis on the other hand should proceed smoothly by nucleophilic attack from a hydroxyl group followed by substitution of a thioacetate group.

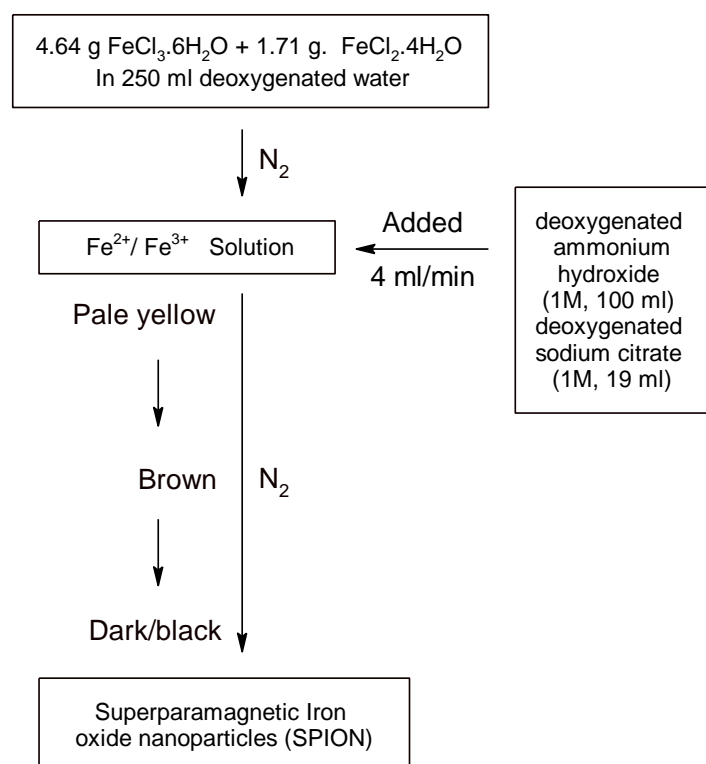


**Figure 28:** Schematic diagram for the formation of SPION



## 4.14 Preparation of Iron Oxide-Gold, Core-Shell nanoparticle

### 4.14.1 Introduction

Co-precipitation is by far the most commonly used method for the preparation of  $\text{Fe}_3\text{O}_4$  nanoparticles for biotechnology, and it mainly involves the addition of a aqueous base to aqueous salt solutions of  $\text{Fe}^{2+}$  and  $\text{Fe}^{3+}$ .<sup>158</sup> The iron oxide nanoparticles were prepared by the co-precipitation of ferric and ferrous chloride in the presence of ammonium hydroxide.

### 4.14.2 Gold coating

Gold was used for coating because it is miscible with iron. The gold shell, apart from serving as an outer surface for the covalent bonding of the porphyrin molecules, is also effective in preventing oxidation of the iron.

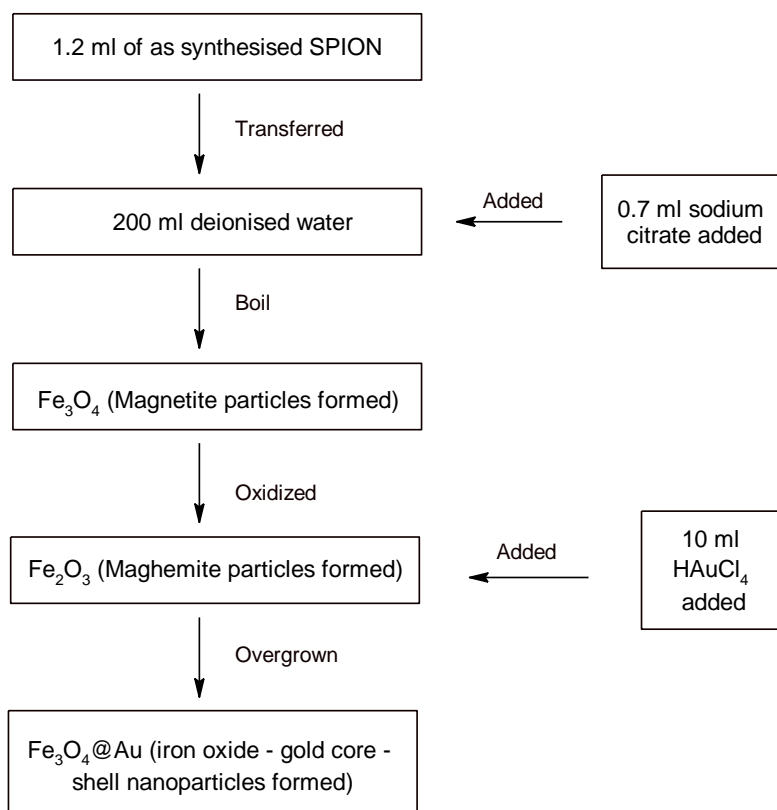


**Figure 29:** Schematic diagram showing the procedures of coating the  $\text{Fe}_3\text{O}_4$  nanoparticles with Au and the formation of magnetic nanoparticles ( $\text{Fe}_3\text{O}_4@Au$  NPs).

#### 4.14.3 Synthesis of the superparamagnetic iron oxide (SPION)<sup>116</sup>

Distilled deionised water and a mixture of ammonium hydroxide and sodium citrate were deoxygenated by bubbling with pure N<sub>2</sub> gas for 1 hour prior to use. Solutions of ferric chloride hexahydrate (4.64g, 17 mmol FeCl<sub>3</sub>.6H<sub>2</sub>O, >99%) and ferrous chloride tetrahydrate (1.71g 8.5 mmol FeCl<sub>2</sub>.4H<sub>2</sub>O, >99%) were prepared as iron species with molar ratio 2:1 under nitrogen atmosphere to stabilize the solution and prevent the oxidation of Fe<sub>3</sub>O<sub>4</sub>. To this vigorously stirred and N<sub>2</sub> atmosphere-protected solution, a mixture of freshly deoxygenated NH<sub>4</sub>OH (1M, 100 ml) and Na<sub>3</sub>C<sub>6</sub>H<sub>5</sub>O<sub>7</sub>.2H<sub>2</sub>O (1M, 19 ml) was added at a rate of 4 ml/min, resulting in a pale yellow color solution changing to brown and finally to dark black. After that, stirring was allowed for an additional 30 minutes, and the solution was then cooled to room temperature. This is illustrated in figure #.

#### 4.14.4 The gold coating process was as follows<sup>116</sup>:

As-synthesized suspension of SPION (1.2ml) was transferred into 200 ml deionized water. After addition of sodium citrate (155.2 mM, 0.7 ml), this mixture was then stirred vigorously and heated to boil (98°C). During this period, magnetite particles would be oxidized partially or completely to maghemite before being coated. Once boiling, HAuCl<sub>4</sub> solution (10 mM, 10 ml) was injected as soon as possible, and the initially pale yellow solution changed color to brown and dark brown, and then to a final deep red characteristic gold colloids. The heating mantle was removed 15 minutes after injection, and the stirring was continued for an additional 15 minutes. This procedure is illustrated schematically in figure 29.

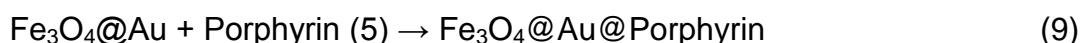
## 4.15 Immobilization of the Porphyrin macromolecule onto the Iron Oxide-Gold, Core-Shell Surface.

### 4.15.1 Introduction

Porphyrins have been covalently bonded to various kinds of surfaces, such as silicon, silica, and polymers and gold and they were also encapsulated in zeolites.<sup>114j</sup> The most intensively studied and successful existing methods are based on the sulphur-gold linkages, and a large number of porphyrin monomers bearing thiols have been prepared. In order to avoid problems associated with disulphide formation the thiol is best handled in a protected form.<sup>105</sup> This report presents for the first time the deposition of thioacetyl derivatised porphyrins iron oxide-gold, core-shell nanoparticles.

### 4.15.2 Procedure

Equal volumes of 0.5 mM solution of 5,10,15,20-tetrakis[3-(3-thioacetoxypoxy)phenyl]porphyrin (**85**) in chloroform and 0.5 mM suspension of the iron oxide-gold, core-shell nanoparticles are shaken together. Upon the phase transfer of the nanoparticles, the bottom layer was collected, dried over calcium chloride and concentrated in vacuo to isolate the porphyrin coated iron oxide-gold, core-shell particles. The porphyrin capped particles were rinsed with chloroform and finally blown dry with a stream of argon gas to ensure that any non-specifically bonded porphyrins are removed from the surface of the nanoparticles. This reaction can be represented as:



## Chapter 5

### 5.1 Introduction

This chapter presents the data collected from 3-hydroxybenzaldehyde (**82**), 3-(3-formylphenoxy)propyl bromide (**83**), 3-(3-formylphenoxy)propyl thioacetate (**84**) 5,10,15,20-tetrakis[3-(3-thioacetoxypoxy)phenyl]porphyrin (**85**) iron oxide nanoparticles, iron oxide – gold, core – shell nanoparticles and iron oxide – gold, core shell nanoparticles functionalized with 5,10,15,20-tetrakis[3-(3-thioacetoxypoxy)phenyl]porphyrin (**85**). The data includes the spectroscopic data collected using NMR, FT-IR and UV-Visible spectroscopy, the microscopy data from TEM, HRTEM and AFM, the X-Ray diffraction data, the magnetization data from SQUID and kinetic data from kinetic studies.

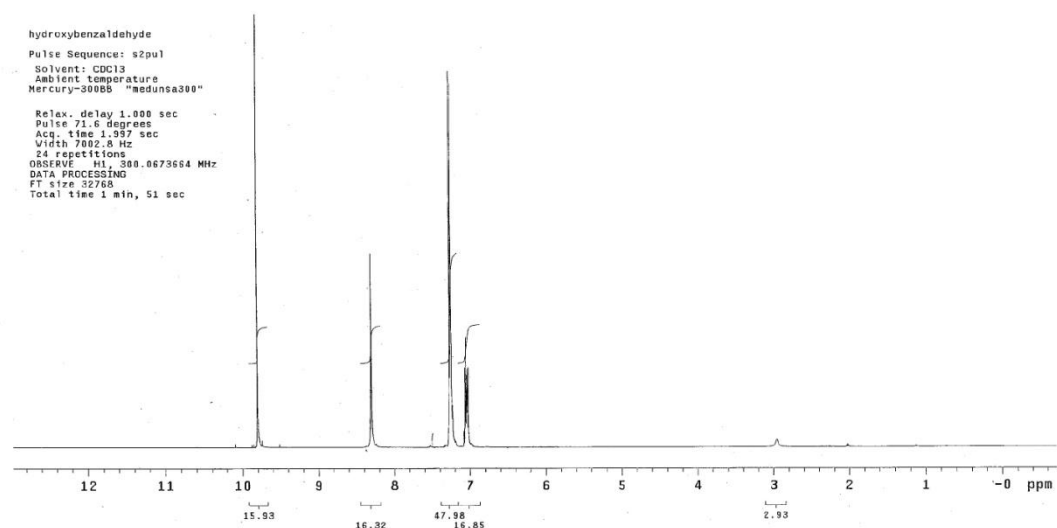


**Figure 30 (a):** Proton nmr of 3-hydroxybenzaldehyde

#### 5.1.1 3-Hydroxybenzaldehyde

<sup>1</sup>H nmr and <sup>13</sup>C nmr spectra were measured on a Varian Mercury (300 MHz and at 75 MHz) in CDCl<sub>3</sub> as solvent. Chemical shifts ( $\delta$  values) are reported in ppm, using the residual solvent peak in CDCl<sub>3</sub> ( $\delta_{\text{H}} = 7.26$  and  $\delta_{\text{C}} = 77.0$ ) as internal standards, coupling constants ( $J$ ) are given in Hz without signs. Flash column chromatography was performed using of 60 Å (35-70 $\mu$ m) silica gel. The following proton NMR were obtained. However the

appearance of 1 H singlet peak at  $\delta = 9.81$  is indicative of the hydrogen atom of the  $-OH$  group which has been deshielded by the oxygen atom thus appearing downfield of the spectra. At  $\delta = 7.039-7.28$  are series of peaks (multiplets of singlet and singlet) representing the aromatic protons of the benzene ring figs. 30 (a) and (b). See Appendix I for more details.

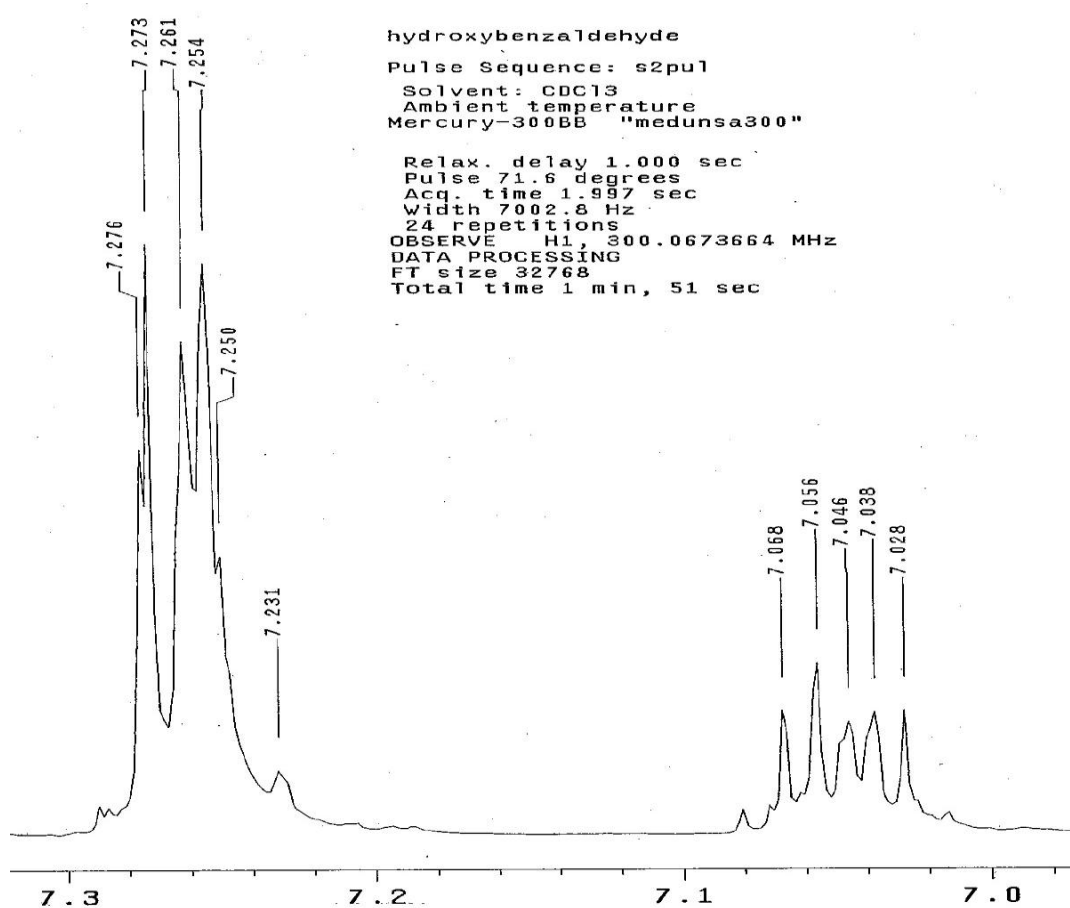


**Figure 30 (b):** Spectra showing the aromatic protons of 3-hydroxybenzaldehyde

### 5.1.2 3-(3-Formylphenoxy)propyl bromide

The following proton nmr results were obtained from the synthesis of 3-(3-formylphenoxy)propyl bromide. Important peaks are found at:  $\delta = 9.95$  (s, 1 H), 7.44-7.25 (m, 3 H), 7.17 (m, 1 H), 4.16 (t, 2 H), 3.61 (t, 2 H) 2.32 (m, 2 H).  $^{13}C$  NMR (75.4 MHz):  $\delta = 192.3, 59.5, 138.02, 130.4, 123.9, 122.1, 113.1, 65.8, 32.4, 30.0$ . The peak at  $\delta = 9.95$  represents the carbonyl proton, the series of peaks at  $\delta = 4.16, 3.61$  and 2.32 was indicative of the

introduction of the alkyl bromide group of atoms (-CH<sub>2</sub>CH<sub>2</sub>CH<sub>2</sub>Br) with the methine group peak next to the oxygen atom directly linked to the phenyl ring showing at 4.16 as 2 H triplet because of the neighbouring -CH<sub>2</sub> group (Fig. 31 b). This assertion was further reinforced with the doublet of triplet peak of the middle -CH<sub>2</sub> at  $\delta$  = 3.61. The influence of the bromo atom on the -CH<sub>2</sub> group next to it caused the appearance of the 2 H multiplet at between 2.18 and 2.32 ppm figs. 31 (a), (b) and (c) . See other attached spectra (Appendix II) for more details.

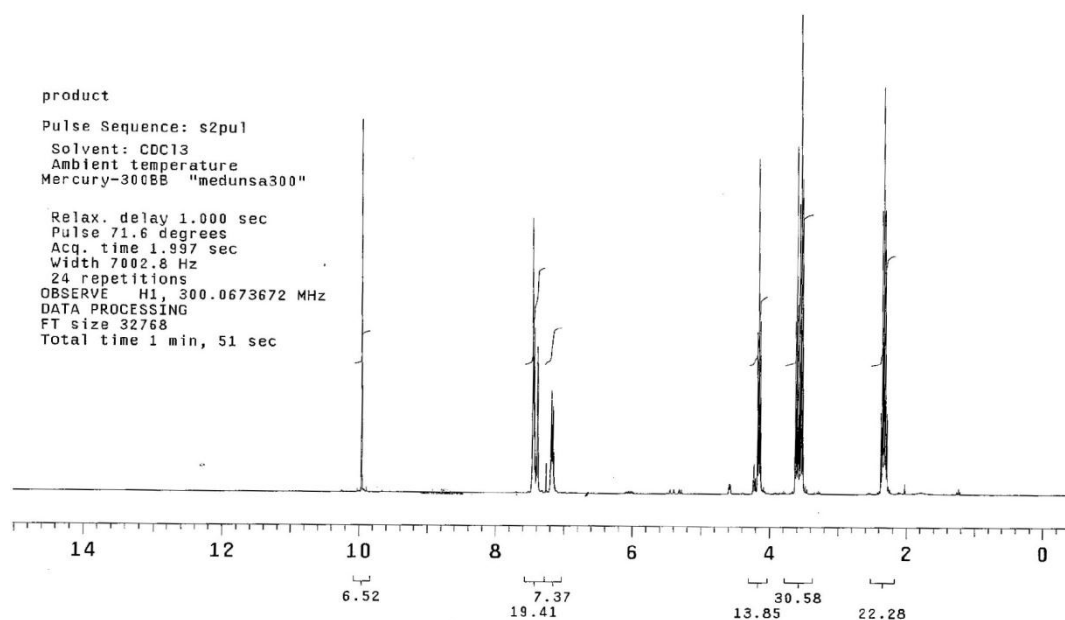


**Figure 31 (a):** Proton 3-(3-Formylphenoxy)propyl bromide

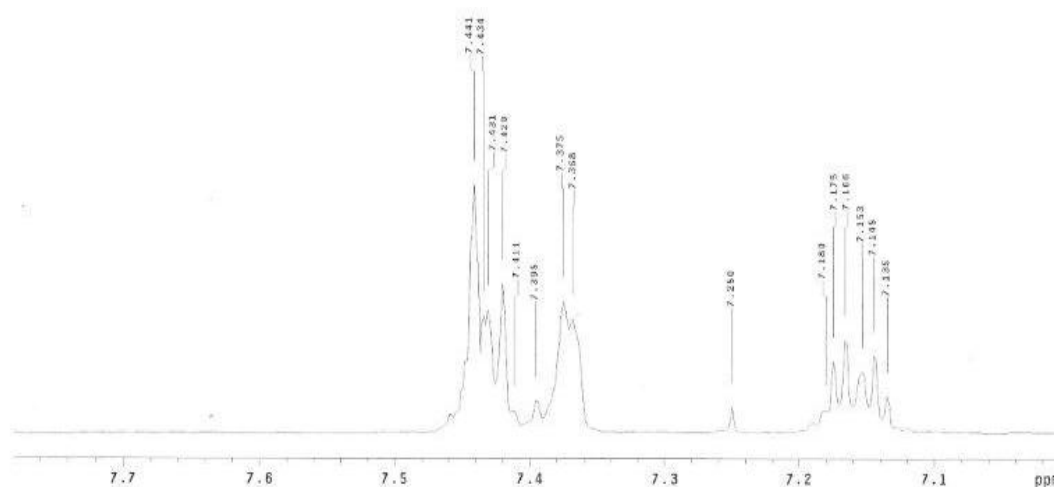


**Figure 31 (b):** Expanded spectrum of fig.31 (a)

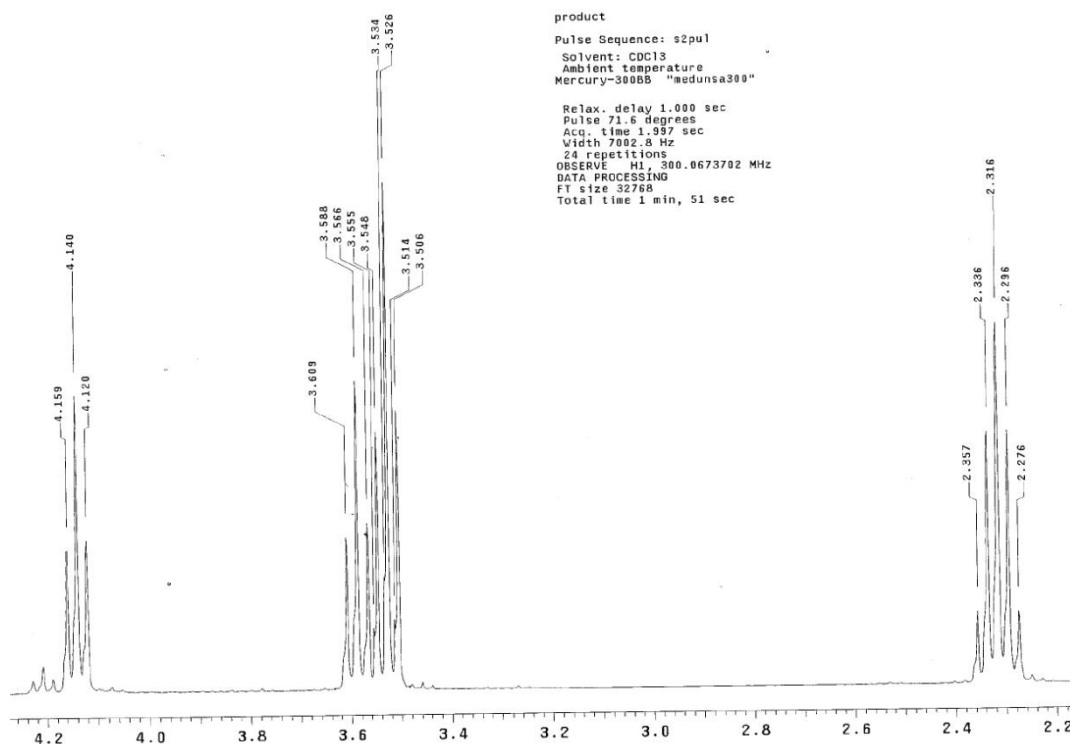


**Figure 31 (c):** Expanded spectrum of fig. 31(a)

### 5.1.3 3-(3-Formylphenoxy)propyl thioacetate

The following proton nmr results were obtained from the synthesis of 3-(3-formylphenoxy)propyl thioacetate through nucleophilic displacement of the bromo atom by the thioacetate group using potassium thioacetate. Important peaks are found at: <sup>1</sup>H NMR (300MHz, CDCl<sub>3</sub>, 22°C): δ = 9.92 (s, 1 H), 7.41-7.40 (m, 2 H), 7.38 (m, 1 H), 7.13 (m, 1 H), 4.04 (t, 2 H), 3.04 (t, 2 H), 2.30 (s, 3 H), 2.07 (m, 2 H). <sup>13</sup>C NMR (75.4 MHz): δ = 195.5, 192.0, 159.2, 137.6, 123.5, 121.8, 112.7, 66.4, 30.5, 29.2, 25.9. The most important peak of note in the spectrum of this compound is the appearance of the 3 H singlet peak from the -CH<sub>3</sub> of the thioacetate group figs. 32 (a). See the attached spectra (Appendix III) for more details.

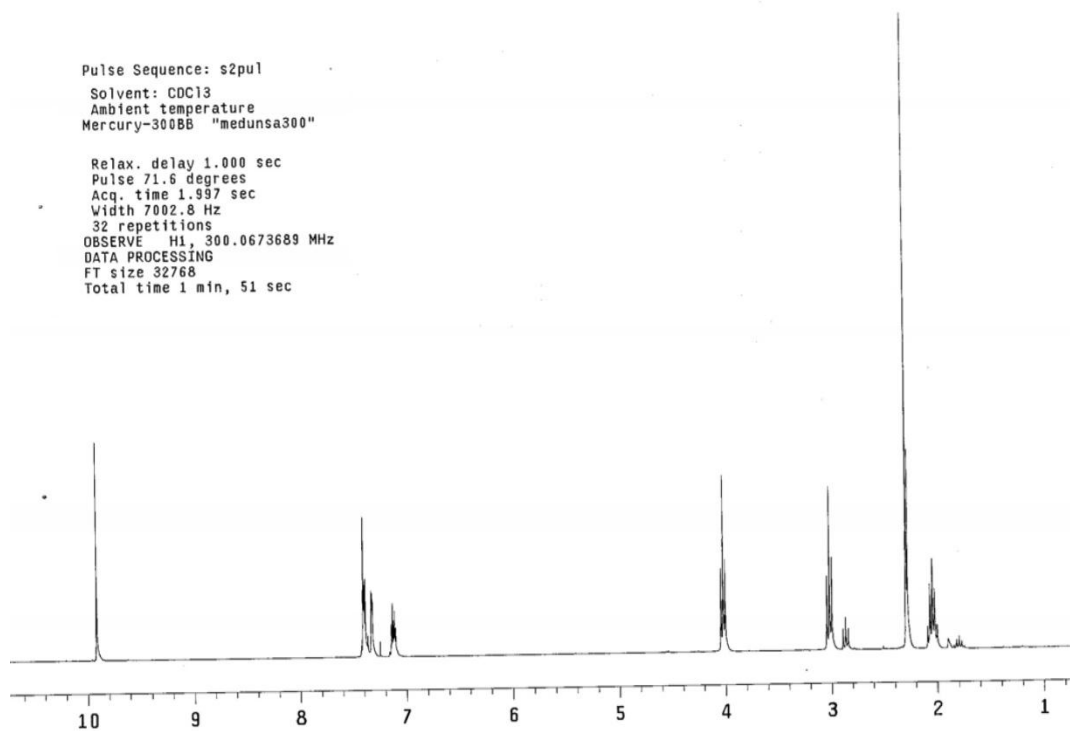


**Figure 32 (a):** Proton nmr of 3-(3-Formylphenoxy)propyl thioacetate

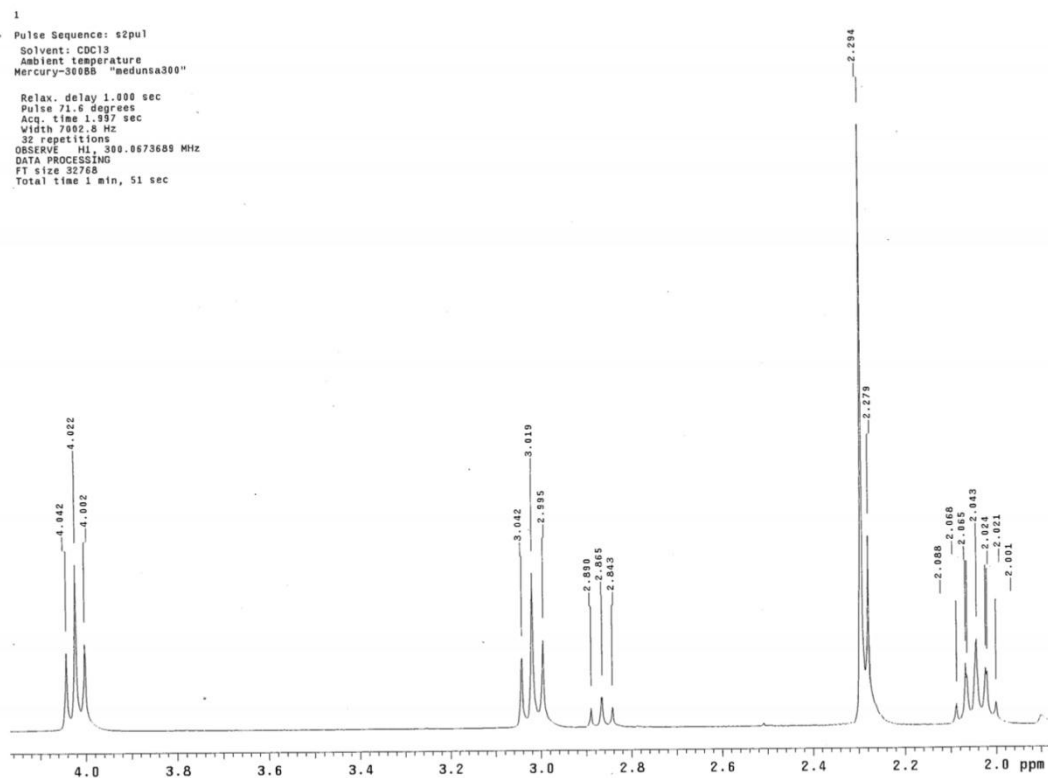


**Figure 32 (b):** Expanded spectrum of fig. 32 (a)



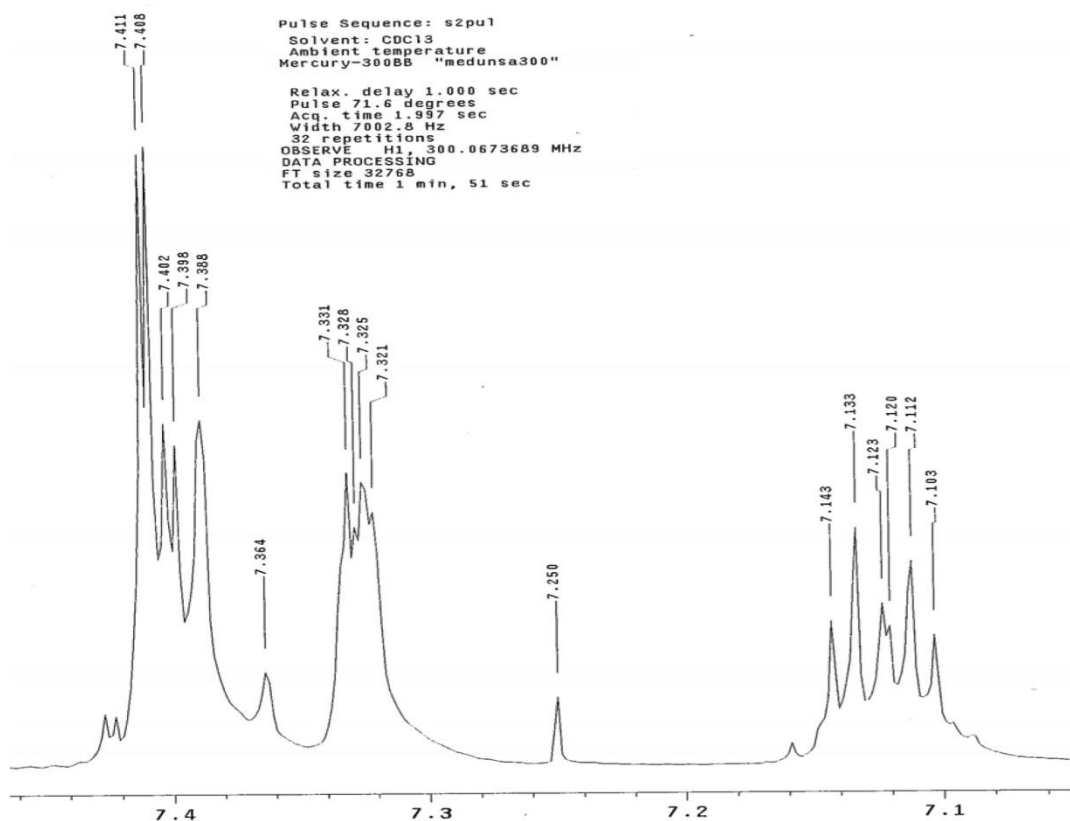


**Figure 32 (c):** Expanded spectrum of fig. 32 (b)

#### 5.1.4 5,10,15,20-Tetrakis[3-(3-thioacetoxypoxy)phenyl]porphyrin

The following proton nmr results were obtained from the synthesis of 5,10,15,20-tetrakis[3-(3-thioacetoxypoxy)phenyl] porphyrin through condensation of Compound **84** with a freshly distilled pyrrole reagent. Important peaks are found at:  $^1\text{H}$  NMR (300MHz,  $\text{CDCl}_3$ ,  $22^\circ\text{C}$ ):  $\delta = -2.82$  (s, 2 H), 1.56 (m, 8 H), 2.14 (m, 8H), 2.30 (s, 12 H), 3.13 (t, 8 H), 4.20 (t, 8 H), 7.33 (d, 4 H), 7.61 (t, 4 H), 7.63 (s, 4 H), 7.7 (d, 4 H), 7.83 (s, 8 H).  $^{13}\text{C}$  NMR (75.4 MHz):  $\delta = 157.1, 143.4, 127.8, 127.7, 127.5, 120.9, 119.8, 114.2, 77.4, 66.4, 30.6, 29.4, 26.0$ . The characteristic feature of porphyrin macrocycle spectrum is the appearance of a peak at  $\delta = -2.82$  with a 2 H singlet peak representing the hindered N-H protons of the porphyrin

molecule fig. 33 (a). The non-appearance of a 1 H singlet peak of the carbonyl carbon at between 9 – 10 ppm in this spectrum is an indication that the condensation reaction of pyrrole with compound **84** 3-(3-formylphenoxy)propyl thioacetate is a success. See other attached spectra (Appendix IV) for more details.

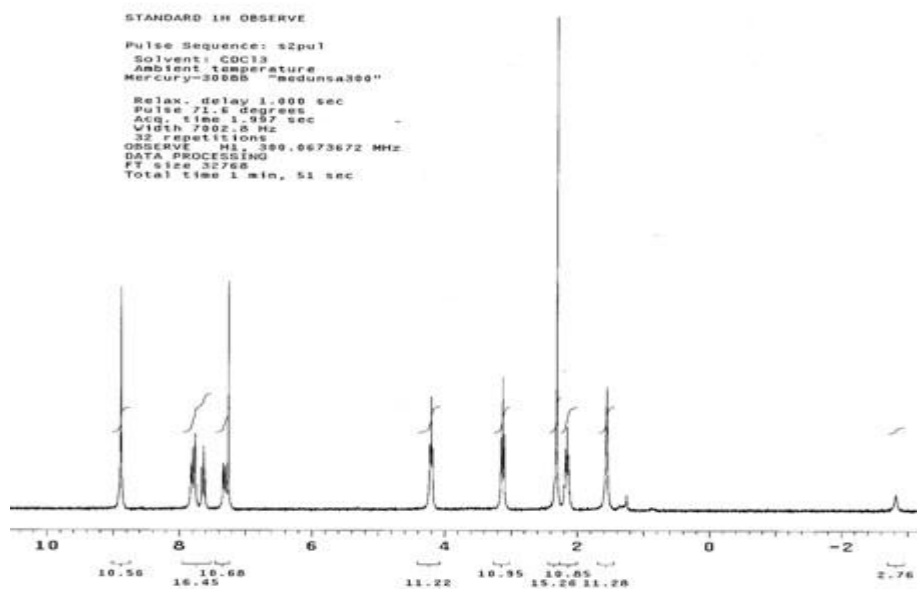


**Figure 33 (a):** Proton nmr of 5,10,15,20-Tetrakis(thioacetoxypoxy)phenylporphyrin

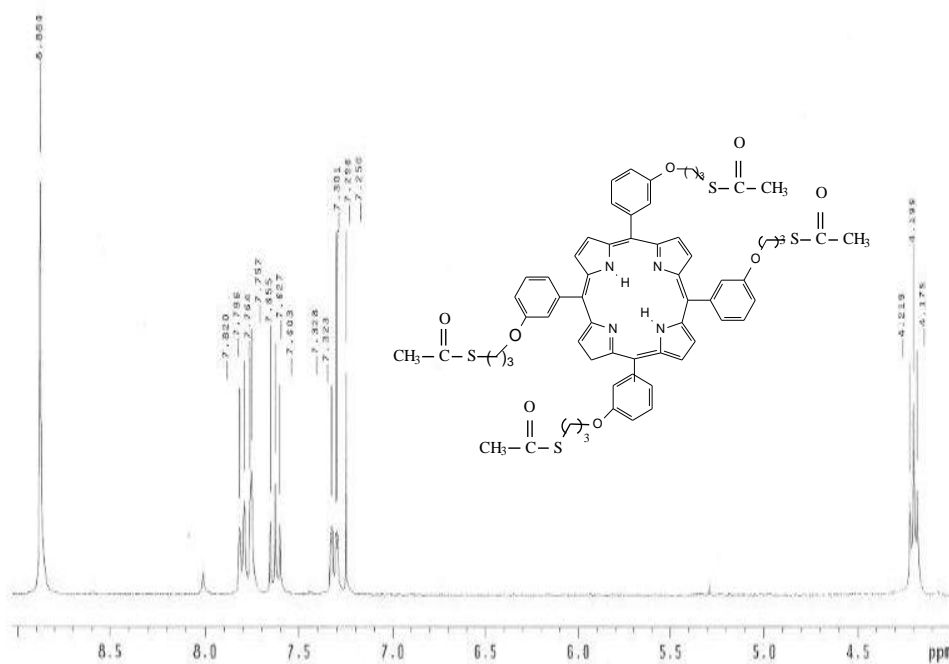


**Figure33 (b):** Expanded spectrum of fig.33 (a)

### 5.1.5 Compound **86** NMR

All attempts to obtain NMR results for Compound **86** which was obtained through acid and alkali hydrolysis of Compound **85** (see Sections **4.13.1** and **4.13.2**) prove difficult and failed to show a proton peak for the displacement of the thioacetate group but the displacement is assumed to take place *in situ* along with the deposition on the gold coated nanoparticles via the Au-S covalent bonding. The mechanism of the hydrolysis reactions (see **Scheme 20** page 138) suggests this is the case and was exemplified by subsequent optical analyses via the UV and IR spectra and characterization through the TEM, HRTEM and magnetic measurements of the functionalized porphyrin.

## 5.2 Kinetic Studies of the Immobilization of Porphyrin onto the Magnetic Seeds Using UV-Visible Spectrophotometer to Monitor the Reaction

### 5.2.1 Kinetic Studies

The rate of the reaction was investigated to determine the rate order or rate law and the relationships between the relative change in concentration of the reactants (porphyrin and iron oxide – gold, core - shell nanoparticles) and the product (porphyrin/nanoparticle). The stoichiometry coefficients for a chemical reaction are determined by comparing the slopes of the plot of the concentration against time for the reactants and products. So for a reaction expressed as:



The rate of a reaction is expressed as

$$R = -d[A]/dt = -d[B]/dt = d[A]/dt \quad (11)$$

Where  $R$  = rate of reaction, defined as the slope of the plot of the concentration against time for any of the species,  $[ ]$  = concentration of reactants or products,  $-d$  = negative indicate decrease in the concentrations of the reactants,  $d$  = change in concentration and/or change in time. So for a first order reaction, the rate of the reaction is directly proportional to the concentration of one of the reactants

$$R = K[A] \quad (12)$$

Where,  $K$  = rate constant and has units of  $\text{sec}^{-1}$

### 5.2.2 Obtaining data for standard curve for nanoparticles.

This was done in order that the concentrations of nanoparticle suspension can be monitored in the nanoparticle/porphyrin mixture. To determine whether there is a decrease in the concentration of the nanoparticle as the reaction proceeds or whether there is no phase transfer. Decrease in the concentration of the nanoparticle would suggest there is a transfer of the particles into the organic porphyrin phase hence the porphyrin molecules attaching themselves onto the nanoparticles. The standard curve data were obtained by preparing various concentrations of the nanoparticle suspension and taking their absorbance on UV-Visible spectrometer at 526 nm which was obtained when the nanoparticle suspension was scanned for wavelength of maximum absorption.

The UV-Visible (Varian Cary 100) absorption spectra of the deionised water used in the procedure of preparation of the nanoparticles showed no absorption peak in a wavelength range of 350-800 nm, but after introducing the suspension of the Au-coated magnetic nanoparticles, an absorption peak located at 526 nm appeared which is ascribed to the surface plasmon of nanosized  $\text{Fe}_3\text{O}_4@Au$  nanoparticles. Porphyrins being highly conjugated aromatic macrocycle show intense absorption in the region of about 400 nm and weaker absorptions at between 650 and 700 nm, the wavelength of maximum absorption measured for the porphyrin solution

was 420 nm while 526 nm was recorded for the  $\text{Fe}_3\text{O}_4@\text{Au}$  as the  $\lambda\text{-max}$  respectively.

**Table 7:** Standard curve data for nanoparticles

#	Abosrbance	Conc. ( $\text{molL}^{-1}$ )
1	0.0029	0.0002
2	0.0058	0.0004
3	0.0082	0.0006
4	0.0113	0.0008
5	0.0136	0.0010
6	0.0166	0.0012
7	0.0205	0.0014
8	0.0219	0.0016
9	0.0252	0.0018
10	0.0272	0.0020

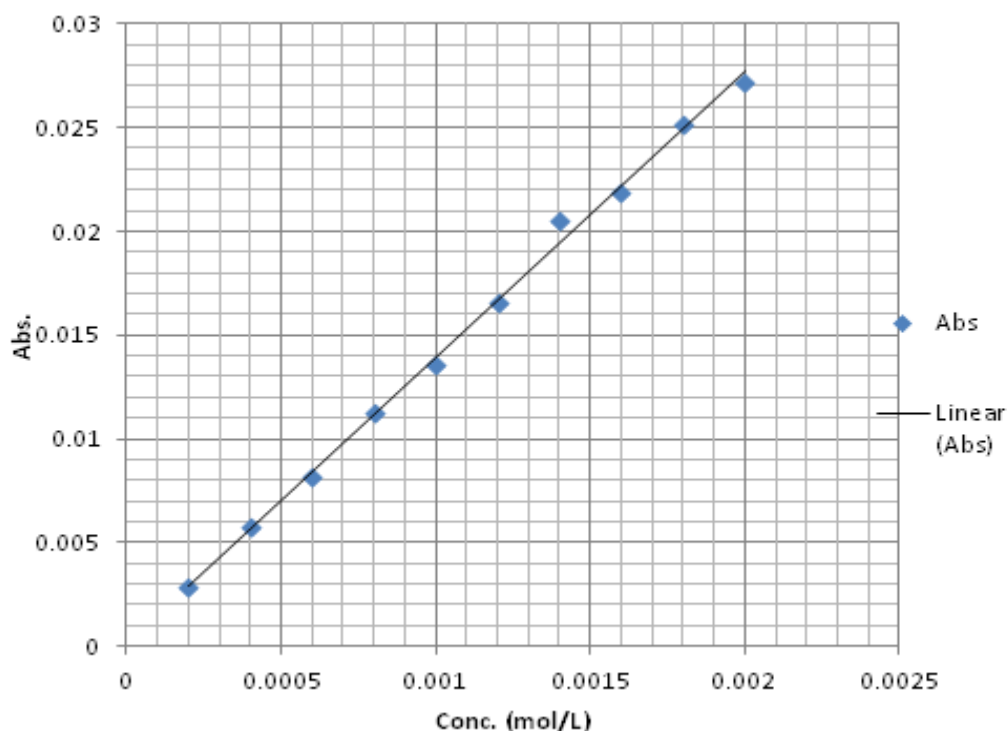


**Figure 34:** Graph of the standard curve for nanoparticles

### 5.2.3 Data for the standard curve for nanoparticles taken at 526nm in the porphyrin/nanoparticle mixture

Equal volumes of 100 mL each of 0.002 mM of porphyrin in chloroform and suspension of the magnetic nanoparticles were transferred into a 250 mL 2-neck separatory funnel mounted on a magnetic stirrer thus having an

organic porphyrin phase below and aqueous nanoparticle phase above. The mixture was stirred vigorously and an aliquot part of each phase was taken at 600 s interval for UV-Visible measurement.

#### 5.2.4 Rate of transfer of nanoparticles from aqueous phase to organic porphyrin phase

The rate of transfer of nanoparticles from aqueous phase to organic phase was determined by the rate of decrease in the absorbance of nanoparticles in the aqueous phase. This is shown in table 8 and figure 35.

**Table 8:** Concentrations calculated from the absorbance of nanoparticles in the aqueous phase.

#	Time (s)	Absorbance	Conc. (molL <sup>-1</sup> )
1	0	0.0258	0.00200
2	600	0.0241	0.00172
3	1200	0.0228	0.00158
4	1800	0.0190	0.00134
5	2400	0.0138	0.00098
6	3000	0.111	0.00077
7	3600	0.0085	0.00067
8	4200	0.0070	0.00049
9	4800	0.0042	0.00032
10	5400	0.0029	0.00025
11	6000	0.0015	0.00013
12	6600	0.0015	0.00013

The concentration of the deposition was also monitored by deducing the concentration of the nanoparticles in the organic porphyrin phase from the absorbance of the nanoparticles in the organic porphyrin phase (Tab.8 and fig. 36). There was a decrease in the concentration of the nanoparticles in the aqueous phase (fig. 35) and corresponding increase in its concentration in the organic phase. When the UV measurement was taken again for the organic phase after the phase transfer a new shift to a longer wavelength of maximum absorption was recorded for the porphyrin solution from the initial 420 nm to 535 nm indicative of a deposition of the porphyrin molecules on the nanoparticles fig 39 b.

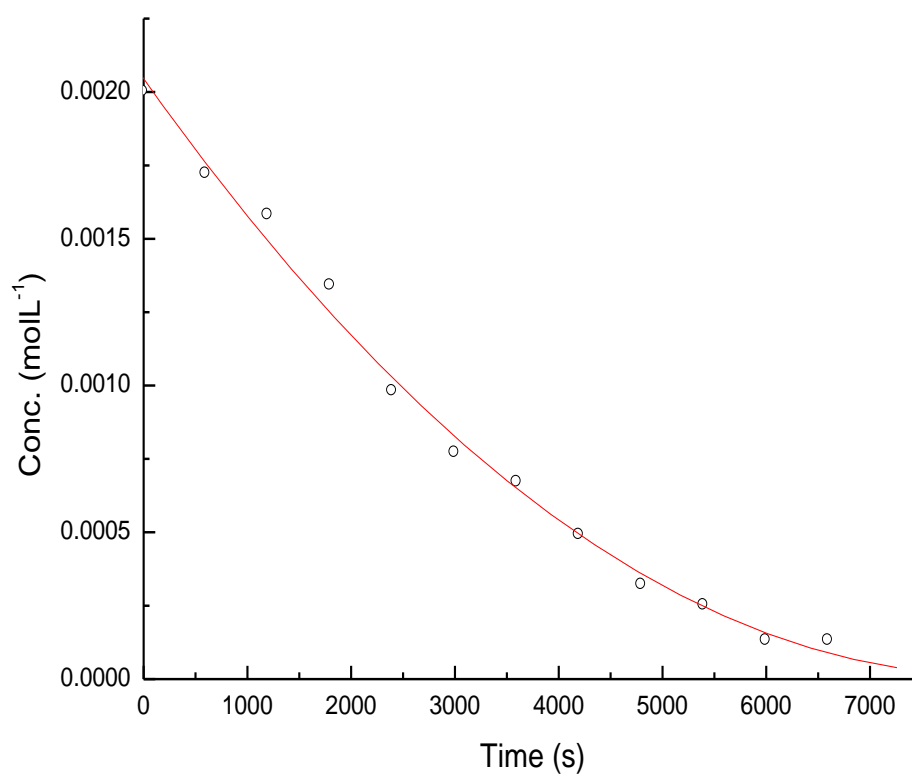


**Figure 35:** Graph showing the decrease in the concentration of nanoparticles in the aqueous phase of the nanoparticle/porphyrin mixture.

**Table 9:** Concentration of nanoparticles calculated from the absorbance of the nanoparticles in the organic phase of the mixture of porphyrin solution and suspension of nanoparticles

#	Time (s)	Conc. (molL <sup>-1</sup> ) <sup>a</sup>
<b>1</b>	0	0.0020
<b>2</b>	600	0.0154
<b>3</b>	1200	0.0186
<b>4</b>	1800	0.0318
<b>5</b>	2400	0.0456
<b>6</b>	3000	0.0642
<b>7</b>	3600	0.0711
<b>8</b>	4200	0.0785
<b>9</b>	4800	0.0798
<b>10</b>	5400	0.0798
<b>11</b>	6000	-
<b>12</b>	6600	-

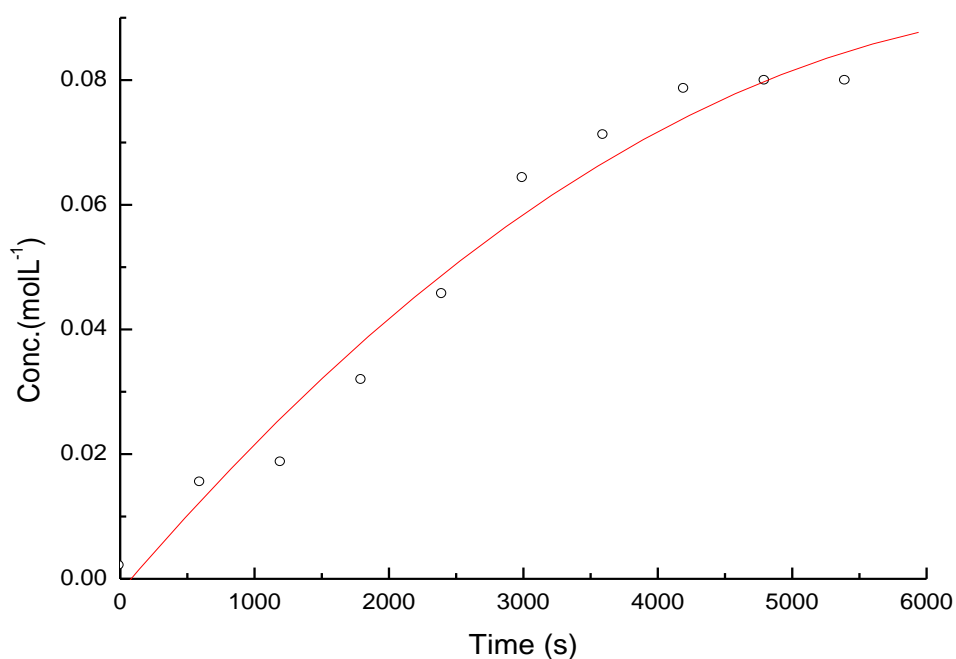


**Figure 36:** Graph showing the increase in concentration of nanoparticles in the organic porphyrin phase.

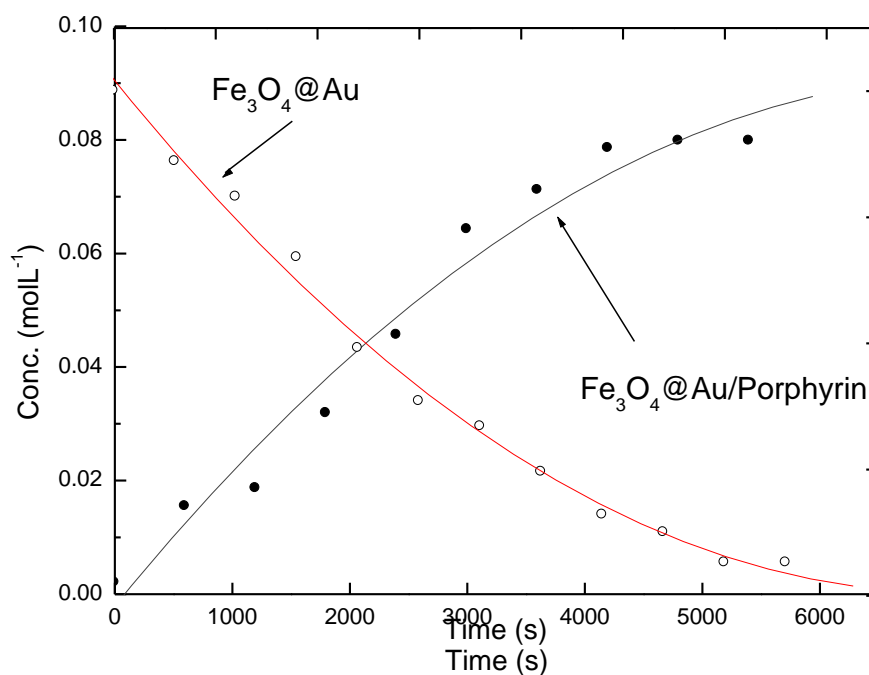


**Figure 37:** Graph of transfer of nanoparticles from aqueous phase and concentrations of nanoparticles in the aqueous and organic porphyrin phase.



### 5.2.5 Rate order of the reaction

The rate of a reaction is expressed as  $R = d[\ ]/dt$ , where  $R$  = rate of reaction,  $d[\ ]$  = change in concentration,  $dt$  = elapsed time (concentration expressed in mol/L and time expressed in seconds). If the reaction is a first order reaction then,  $R/[\ ] = K_1$ , and therefore  $R = K_1[\ ]$ . For a second order reaction,  $R = K_2[\ ]^2$ . It follows therefore that if the reaction is a second order reaction then,  $R/[\ ]^2 = K_2$ , and if it is a third order, then,  $R/[\ ]^3 = K_3$ . Looking at Table 9, it is difficult to establish the order or rate law for this reaction because none of the rate has generated a constant,  $k$ , the nearest data in column 3 would have suggested a first order reaction but then it cannot be taken to be reliably so because of the rise and fall of the data, and fitting the data with various isotherms has equally not produced a clear rate order. This therefore remains a challenge for follow up studies or perhaps the reaction required some other complicated fittings beyond the scope of this present studies.

**Table 10: Data for rate order of the reaction**

Time/s	[ ]	Rate	Rate/[ ]	Rate/[ ] <sup>2</sup>	Rate/[ ] <sup>3</sup>
0	0.002	4.67E-07	2.33E-04	0.11667	58.33333
600	0.00172	2.33E-07	1.36E-04	0.07887	45.8555
1200	0.00158	4.00E-07	2.53E-04	0.16023	101.41186
1800	0.00134	6.00E-07	4.48E-04	0.33415	249.36578
2400	9.80E-04	3.50E-07	3.57E-04	0.36443	371.86886
3000	7.70E-04	1.67E-07	2.16E-04	0.2811	365.07036
3600	6.70E-04	3.00E-07	4.48E-04	0.6683	997.46312
4200	4.90E-04	2.83E-07	5.78E-04	1.18006	2408.2936
4800	3.20E-04	1.17E-07	3.65E-04	1.13932	3560.38411
5400	2.50E-04	2.00E-07	8.00E-04	3.2	12800
6000	1.30E-04	0	0	0	0
6600	1.30E-04	--	--	--	--

However the results of the UV measurements taken during the experiments clearly demonstrates that the rate law of the reaction is characteristic of a surface reaction on a large surface area with the decreasing concentration in the nanoparticle suspension phase and increase in the concentration of the nanoparticles in the nanoparticles/prophyrin phase (Figures 35-37).

## 5.3 Optical Analyses

### 5.3.1 UV-Visible

Deionised water used in the procedure of preparation of the nanoparticles showed no absorption peak in a wavelength range of 350-800 nm, but after introducing the suspension of the Au-coated magnetic nanoparticles, an absorption peak located at 526 nm appeared which is ascribed to the surface plasmon of nanosized  $\text{Fe}_3\text{O}_4@Au$  nanoparticles. Porphyrins being highly conjugated aromatic macrocycle show intense absorption in the region of about 420 nm and weaker absorptions at between 650 and 700 nm, the wavelength of maximum absorption measured for the porphyrin solution was 420 nm (figs 38 and 39).

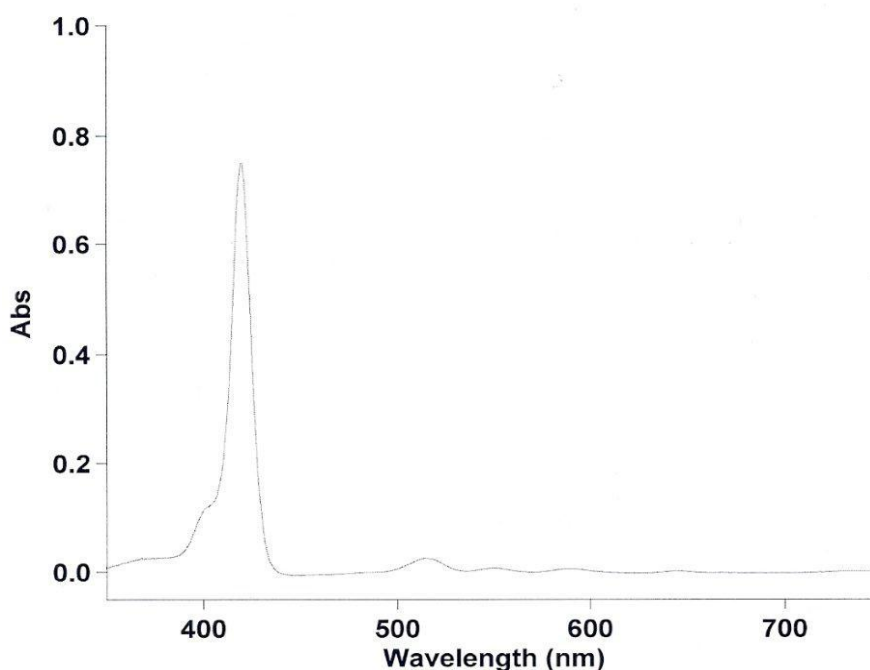


**Figure 38:** UV spectrum of porphyrin solution

The results further show decrease in concentration of nanoparticle in a two-phase mixture of nanoparticle suspension and porphyrin solution and an increase in concentration of the nanoparticle/porphyrin deposition (Table. 8). This surface reaction depicts the porphyrin as being covalently bonded

to the gold surface through a thiol linker which is similar to the formation of self-assembled monolayers (SAM) of alkene thiols on gold surface.<sup>246</sup> When the UV of the functionalized sample was taken, a shift in the wavelength of maximum absorption, 535 nm was recorded (fig. 40).

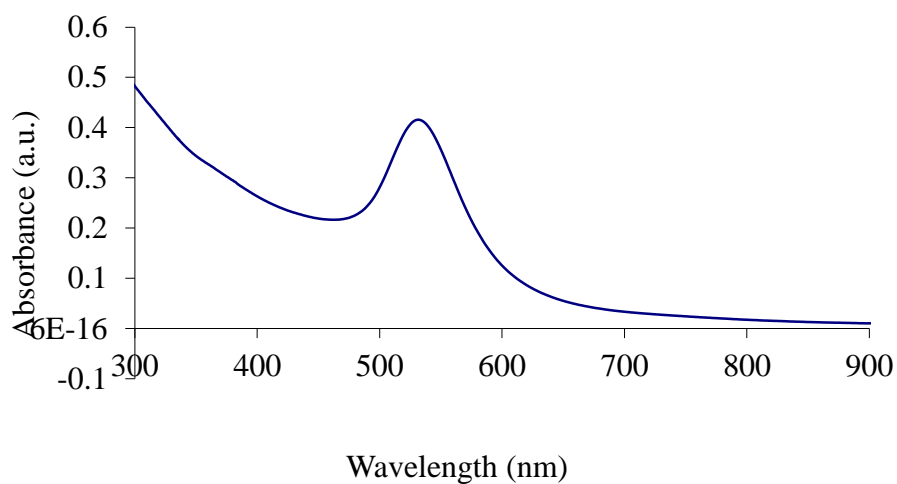


**Figure 39 :** UV spectrum of gold coated SPION

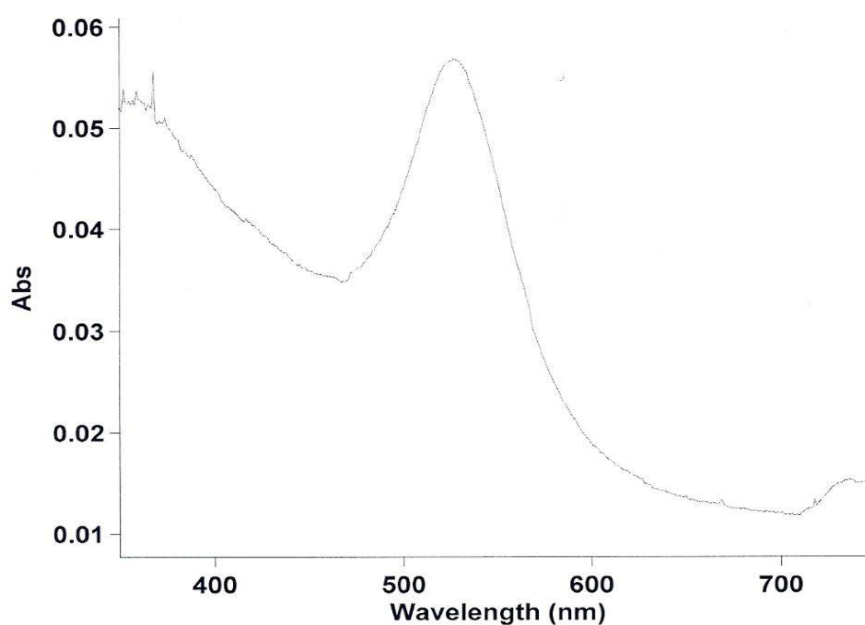


**Figure 40:** UV spectrum of functionalized sample

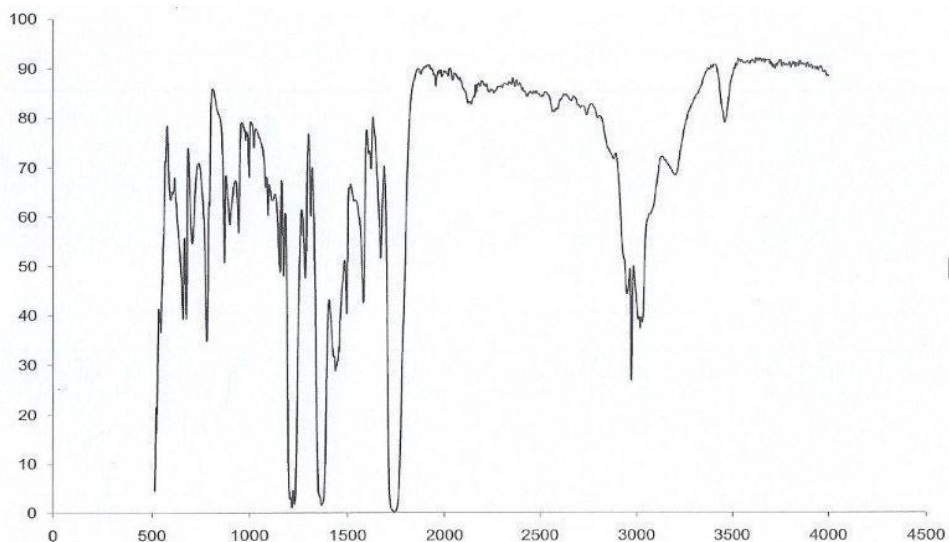
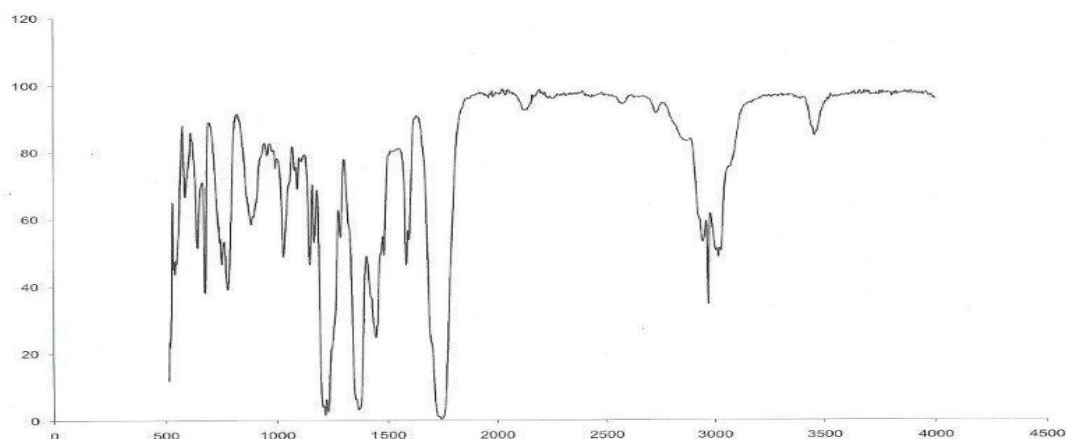


**Figure 41:** FT-IR Spectrum Of Compound **82**

### 5.3.2 Infra-red Analysis

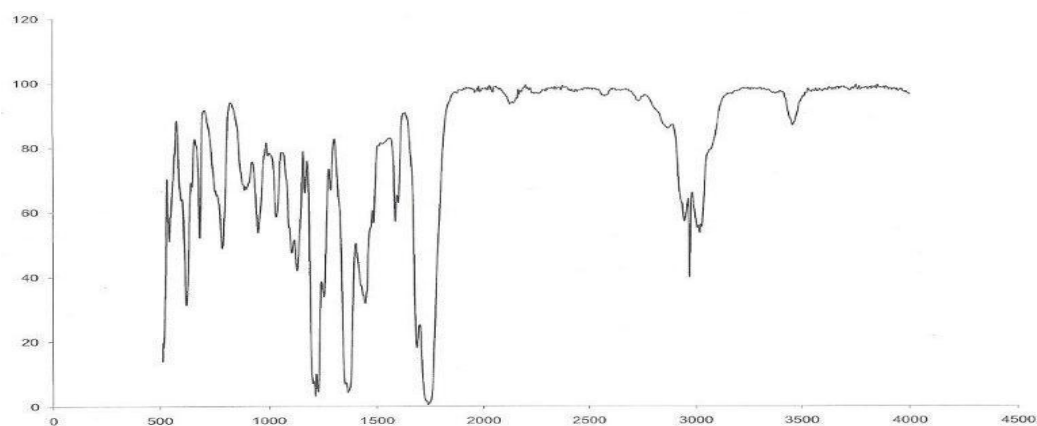
Perkin Elmer spectrum 100, FT-IR spectrometer was used to obtain the IR spectra of the functional groups of the synthesized compounds. The absorption peaks observed at between 3000 to 2800  $\text{cm}^{-1}$  are indicative of the presence of an hydroxyl group (OH) as it appeared on the starting material, 3-hydroxybenzaldehyde (fig. 41). One of the most characteristic absorption bands in an IR spectrum of carbonyl compounds is the one due to the presence of carbonyl group.

This strong band is usually found at wave numbers from 1780 to 1650  $\text{cm}^{-1}$ , hence the strong absorption band at 1683 and 1681  $\text{cm}^{-1}$  is ascribed to the carbonyl group (C=O) on all the synthesized benzaldehydes which is due to the stretching of the C=O bond (figs. 40-44), while the absorption band due to the C-O bond stretching is found at 1254  $\text{cm}^{-1}$ . There is a hydrogen bonded to the carbon of the carbonyl group of aldehydes, the presence of this C-H bond gives rise to absorptions at 2820 and 2734  $\text{cm}^{-1}$ .



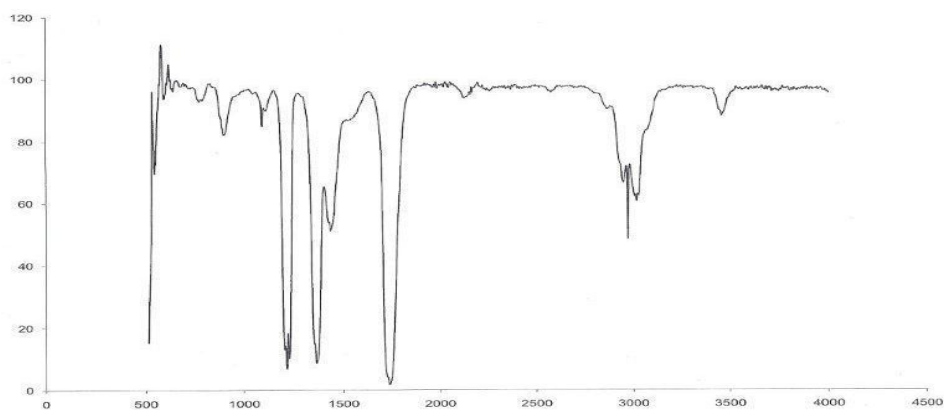
**Figure 42:** IR spectrum of Compound **83**

A series of absorption bands between  $1400 - 900 \text{ cm}^{-1}$  (the finger print region) could be ascribed to the methylene group while the peak between  $600 - 500 \text{ cm}^{-1}$  was assigned to C-Br stretching absorption (fig. 42).



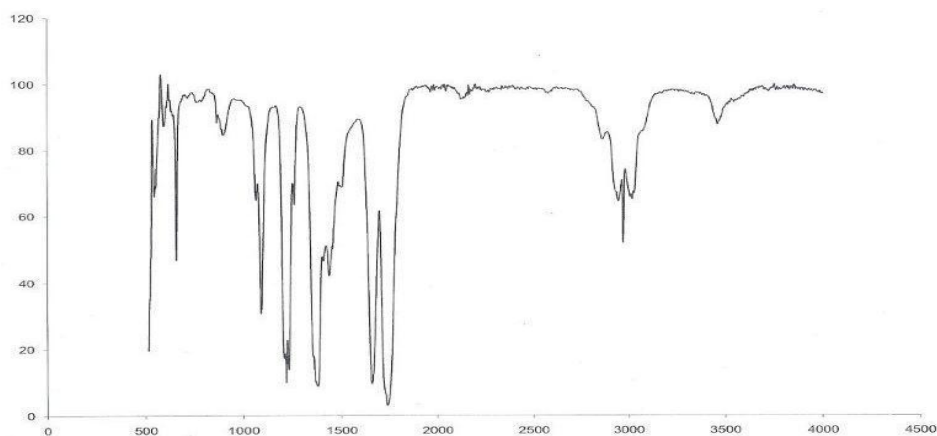
**Figure 43:** IR spectrum of Compound **84**

Figure 43 shows the low intensity absorption band at  $2950 \text{ cm}^{-1}$  which was ascribed to the S-H group of the porphyrin macrocycle. The complex series of absorption bands found at the fingerprint region serve as the spectroscopic fingerprints between  $1400$  to  $680 \text{ cm}^{-1}$  for all the compounds are indicative of the methylene group on all the synthesized compounds. The strong band at  $1600 \text{ cm}^{-1}$  is consistent with the skeletal vibrations of an aromatic system while the prominent absorption at  $1760 \text{ cm}^{-1}$  indicates C=O stretching vibration of the aldehyde group.



**Figure 44:** IR spectrum of Compound **85**

In fig.44 the band at around  $2970\text{ cm}^{-1}$  is due to asymmetric C-H stretching vibration of the methyl group and a corresponding bending vibration occurs at around  $1420\text{ cm}^{-1}$ . The strong absorptions at between  $1250\text{-}1175\text{ cm}^{-1}$  exhibit asymmetric stretching vibrations of an asymmetric ether C-O-C while the hindered N-H band appearing at around  $1600\text{-}1500\text{ cm}^{-1}$  is indicative of the cyclic porphyrin ring.



**Figure 45 (a):** IR spectrum of Compound **86**

Figure 45 (a) depicts the S-H stretching vibration in most compounds containing thiol group which absorbs as a weak band in the region between  $2890\text{-}2800\text{ cm}^{-1}$  hence the absorption band at around that same region is indicative of the presence of the S-H group replacing the thioacetal group of atoms in compound **85**.

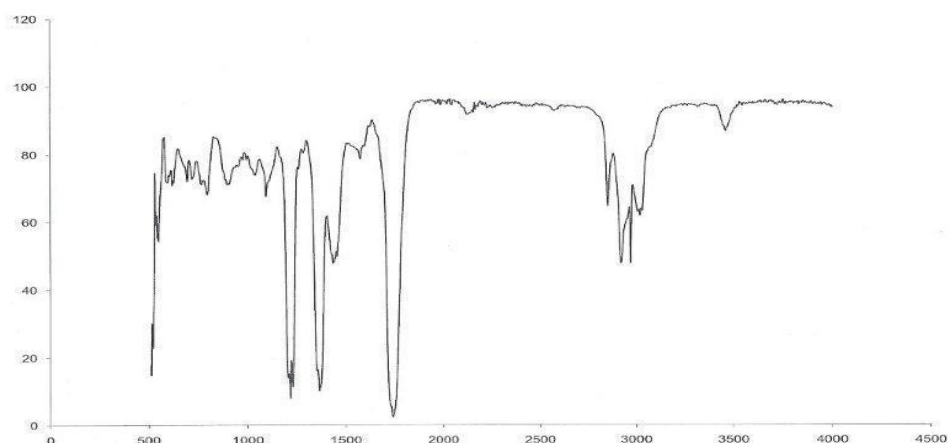


**Figure 45 (b):** IR spectrum of functionalized gold coated sample

The spectrum of the functionalized sample (fig.45b) shows distinctive features from the spectrum of thiolated porphyrin in fig. 45a. The new peaks arising from the region of 2950-3200  $\text{cm}^{-1}$  are ascribed to the sitting position of the thiol group on the gold surface.

<b>Table 11: Band positions and assignments of functional groups</b>		
<b>3-Hydroxhbenzaldehyde (Compound 82)</b>		
Wave number $\text{cm}^{-1}$	Functional group possible assignment	Comments
3000-2800	O-H	Indicative of the presence of O-H group
2820-2734	C-H	
1780-1650	C=O	Strong absorption due to stretching of the C=O band
1254	C-O	Due to C-O bond stretching
<b>3-(3-formylphenoxy)propyl bromide (Compound 83)</b>		
1400-900	-CH <sub>2</sub> -	Finger print region assigned to the methylene group
600-500	C-Br	C-Br stretching
<b>3-(3-formylphenoxy)propyl thioacetate (Compound 84)</b>		
2950	S-H	Low intensity absorption
1760	C=O	Stretching vibration of the carbonyl group
1600		Skeletal vibration of an aromatic system
1400-680	-CH <sub>2</sub> -	
<b>5,10,15,20-Tetrakis[3-(3-thioacetoxypoxy)phenyl]porphyrin (85)</b>		
2970, 1420	C-H	Stretching vibration of the methyl group and the corresponding vibration at 1420
1600-1500	N-H	Indicative of the hindered N-H of the cyclic porphyrin ring
1250-1175	C-O-C	Asymmetric stretching vibrations of an ether
<b>5,10,15,20-Tetrakis[3-(3-thioacetoxypoxy)phenyl]porphyrin (85) adsorbed on nanoparticles</b>		
2890-2800	S-H	Weak absorption of stretching vibration

## 5.4 TEM and HRTEM Micrographs

A typical transmission electron microscope (TEM) image of the as-synthesized iron oxide nanoparticles formed is presented in Figure 46 A. In general, the particles are spherical in shape and nearly monodispersed. The aggregation by some of the particles might be attributed to high surface energy of the bare iron oxide nanoparticles, which enhance adhesion between the nanoparticles of different sizes. According to Oluwafemi and Wang *et al.*, adhesion tend to occur between nanoparticles as a result of dipole-dipole interactions between the highly charge surfaces of the nanocrystals.<sup>260,,261</sup> This adhesion between nanocrystals can induce a significant change on their morphology and hence, cause a transition from dot to elongated particles as a result of oriented attachment (self – assembly).<sup>262</sup> Figure 46 shows the fusion between four dots particles (marked as I, II & III), which could lead to the formation of elongated particles. The gap between the dot particles is due to incomplete adhesion between the nanoparticles “adhesives”. Figure 46 B presents a histogram of the particle size distribution. The particle sizes are in the range 34 – 58 nm with the mean particle diameter of 42.41 nm  $\pm$  12.03 nm and standard deviation of ( $\sigma$ ) 0.27 nm indicating broad size distribution.

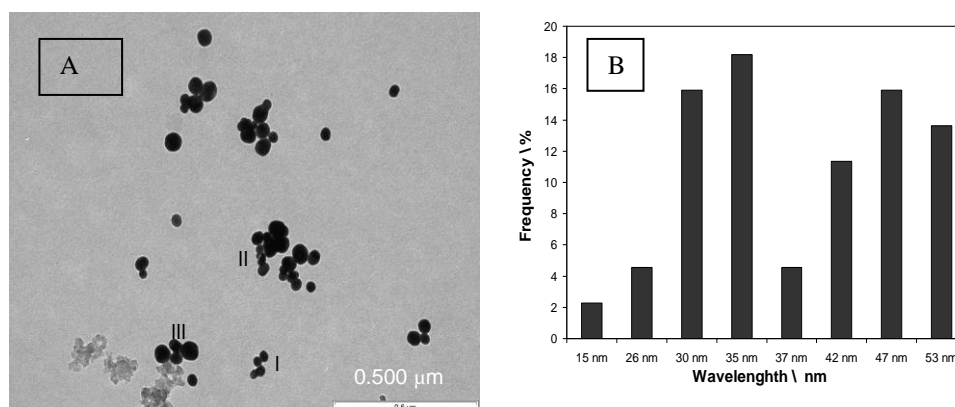


**Figure 46:** (a) TEM images and (b) Particle size distribution of super-paramagnetic Iron oxide nanoparticles (SPION).

Figure 47 shows the TEM image and particle size distribution of the gold coated super paramagnetic iron oxide nanoparticles. The particles are spherical in shape, nearly mono-dispersed and bigger in size compared to



the uncoated iron oxide nanoparticles. The particle diameters are in the range 34-54 nm. The average particle size as determined from the TEM image for the selected fraction is  $44.26 \text{ nm} \pm 6.93 \text{ nm}$ . The relative standard deviation of the sizes of the nanoparticles (0.16 nm) indicates that, the size distribution is very broad. The increase in particle size compared to the uncoated iron oxide nanoparticles is attributed to the coating of the nanoparticles surface by the gold shell. This also reduces the surface energy of the nanoparticles and hence the degree of aggregation. The presence of the aggregated nanoparticles in the TEM image after the coating has been attributed to the insufficient passivation of the nanoparticles surface by the gold shell.

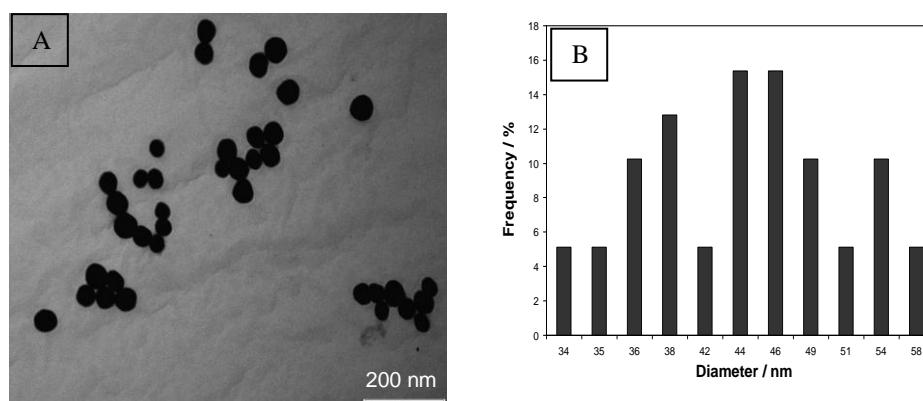


**Figure 47:** (a) TEM images and (b) Particle size distribution of gold coated super paramagnetic Iron oxide nanoparticles.

The electron microscope images of the functionalised gold coated iron oxide nanoparticles are presented in figure 48. The TEM image (Figure 48 A) shows that the as-synthesised materials are monodispersed and appear in spherical, cubic, irregular hexagon and oblong shapes with an average diameter of 44.65 nm. The HRTEM image (Fig. 48 B), shows the existence of lattice planes which confirms the crystallinity of the material. The spacing between adjacent lattice planes is about 0.23 nm which corresponds to the (311) interplanar distance of  $\text{Fe}_3\text{O}_4$  nanocrystals.<sup>263</sup>

Figure 48 B inlet is the selected area electron diffraction (SAED) patterns recorded on a single nanoparticle in Fig. 48 A. The SAED patterns composed of many separated bright spots instead of rings, which imply the

single crystal-like diffraction of the functionalised nanoparticles. The set of brighter spots in the SAED represents that most of nanoparticles have the same orientation. Some disordered spot coexist with those ordered bright spots. This phenomenon had been probably attributed to misarranged nanoparticles.<sup>264</sup> The HRTEM and SAED results indicate that most of nanoparticles self-assembled along the same crystal orientation. According to Cheng *et al.*,<sup>264</sup> this phenomenon, namely oriented aggregation, is induced by the spontaneous tendency of nanoparticles to minimize their high surface energy.

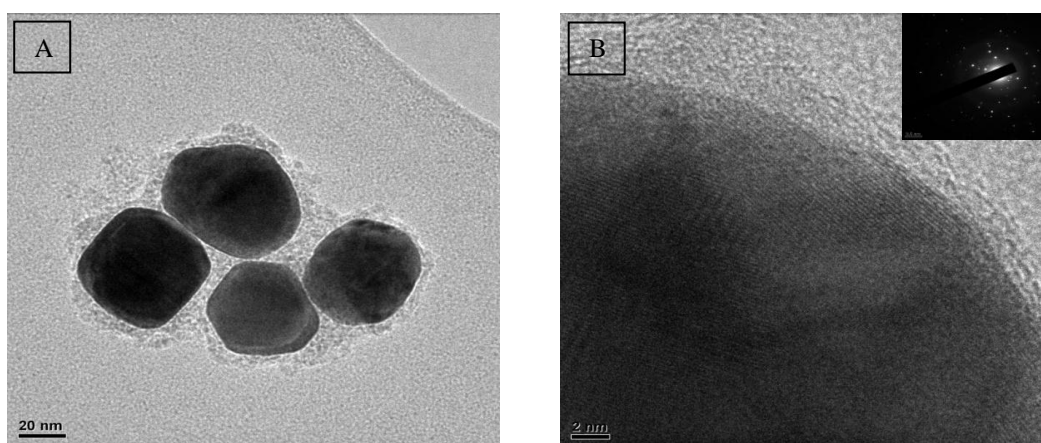


**Figure 48:** (a) TEM and (b) HRTEM images with SAED (inlet) of functionalised gold coated super paramagnetic Iron oxide nanoparticles.

### **5.5 Atomic force microscopy (ATM), X-ray microscopy (XRD) and SQUID magnetometry**

Atomic force microscopy (ATM) analysis was used to confirm the transmission electron microscopy (TEM) and HRTEM findings and it further revealed the surface characteristics of the nanoparticles, while x-ray diffraction studies also suggest the presence of a gold based shell. SQUID magnetometry was employed to study the magnetization of the nanoparticles and the functionalized nanoparticles.

### 5.5.1 Atomic force microscopy

The gold coated SPION were analysed with AFM. All the AFM investigations conducted on the sample showed well dispersed nanoparticles on the scanning surface. The tapping mode was used and both the height and phase images were captured, using the RTESPW tip at a scan rate of 0.803 Hz. The samples were also scanned with a Platinum Coated tip, SCM-PIT at a scan rate of 1.00 Hz. Typical AFM images using the RTESPW tip and a scan rate of 0.803 Hz, and the platinum coated tip, SCM-PIT at a scan rate of 1.00 Hz are shown in figure 49.

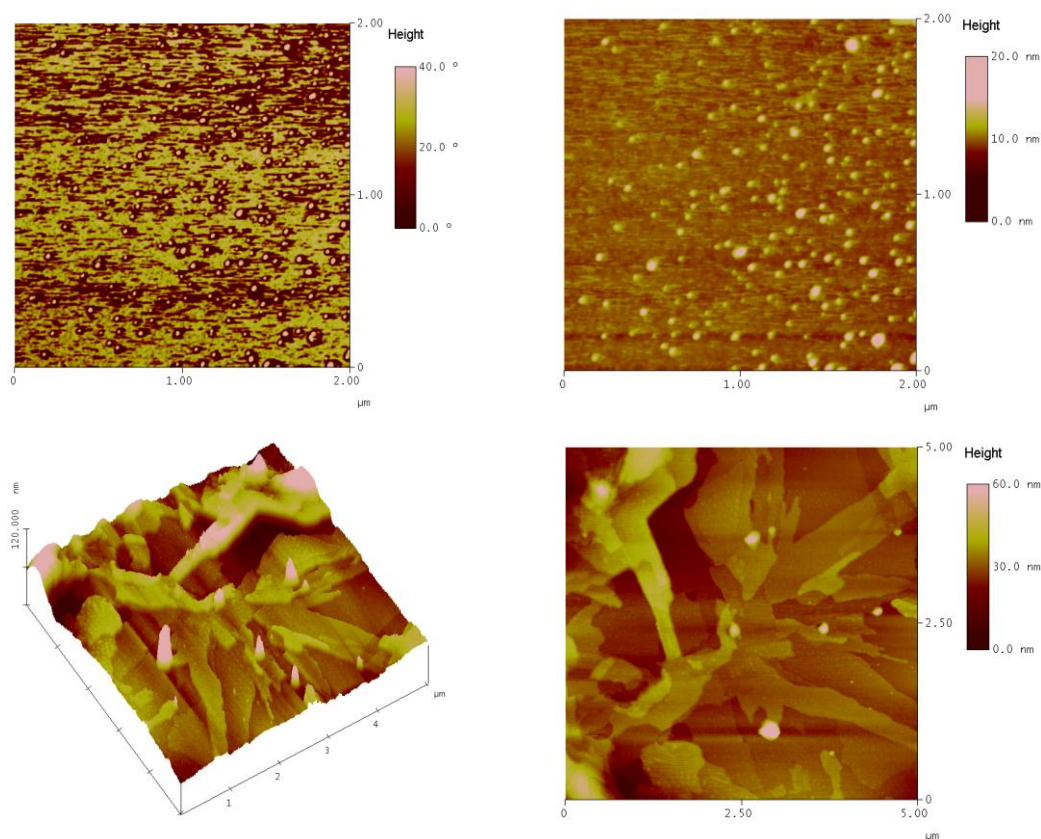


**Figure 49:** Atomic force microscopy using the RTESPW tip and a scan rate of 0.803 Hz, and the platinum coated tip, SCM-PIT at a scan rate of 1.00 Hz.

### 5.5.2 X-Ray diffraction measurements

A representative XRD pattern of the gold coated SPION is shown in Fig. 50. All the peaks correspond to the metallic gold diffraction. The pattern of

$\alpha$ -Fe is hidden under the pattern of Au due to the overlapping of their diffraction peaks at  $2\theta = 44.8^\circ$ ,  $65.3^\circ$ , and  $82.5^\circ$ .

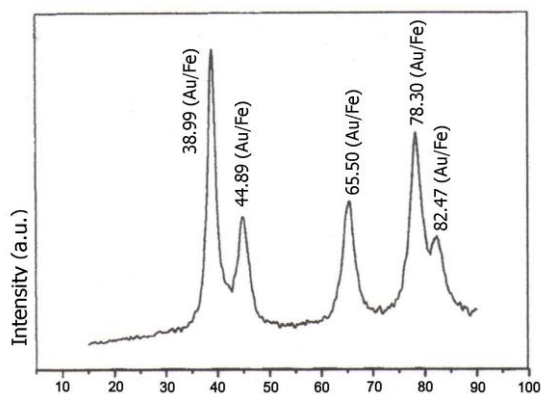


**Figure 50:** XRD pattern of the gold coated SPION

### 5.5.3 Magnetic measurements of the gold coated & functionalised nanoparticles (SQUID magnetometer)

The magnetic properties of functionalised sample (sample 2 = functionalised SPION) and the gold coated sample (sample F = gold coated SPION) were studied as function of temperature between 2.0 K and 300 K using a fixed field, as well as two fixed temperatures, viz 2.0 K and 300 K as function of field. For the temperature-dependence studies, both field-cooled (cooling in a small magnetic field to 2.0 K, then measuring in the magnetic field upon warming to 300 K) and zero-field cooled mode (cooling the sample in zero applied field to 2.0 K, then applying the field and measure in field while warming up back to 300 K) was used.

Care was taken to use very small magnetic fields during temperature scans in order to avoid induced or non-spontaneous magnetic effects in the sample. For sample containment, a compressed specimen was held fixed inside a synthetic, magnetically transparent sample holder which has the advantage of being able to avoid spurious signals originating from glue used as fixing agents.

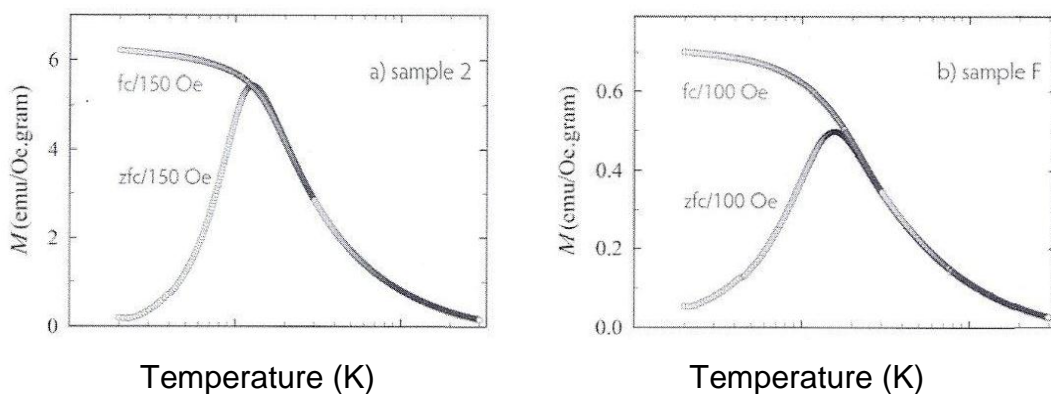


**Figure 51:** Temperature-dependent magnetic moment of (a) functionalised SPION and (b) gold coated SPION taken in field-cooling (blue) and zero-field cooling (zfc) modes respectively.

Figure 51 (a) shows a field-cooled/zero-field cooled (fc/zfc) temperature for functionalised SPION and figure 51 (b) that of gold coated SPION. The magnetic response of both samples bifurcates between 10 K and 20 K. This correspondence between the two samples clearly points towards an identical magnetic species responsible for the observed temperature-dependent effects.

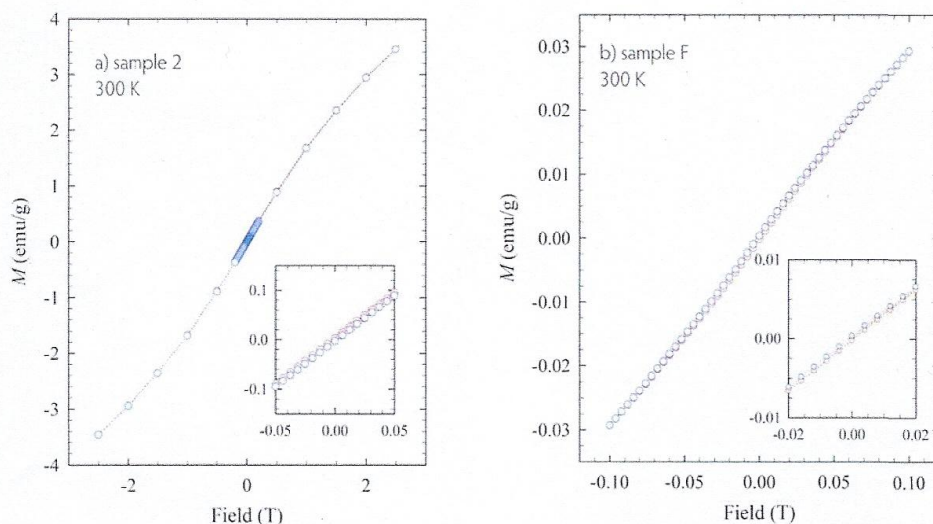


**Figure 52:** Room-temperature field-dependent measurements of the magnetic moment in (a) sample “2” and (b) sample “F”. The insets show data near to  $B=0$  in order to emphasize the negligible hysteresis associated with the two samples at room temperature (cf. Fig. 46 at low temperature).

The implementation of very small fields (between 100 Oe and 150 Oe) for these measurements lends confidence in determining the spontaneous blocking temperature  $T_B = 15.7 \pm 0.1$  k and  $T_B = 12.8 \pm 0.1$  K. As is typical

of short range ordering effects in magnetic materials, ZFC data reflect the unperturbed magnetic response of the magnetic species and a melting effect of spin correlations upon warming through  $T_B$ . During cooling of the samples inside a finite field on the other hand, the freezing effect (large decrease in the measured magnetic moment) is no longer witnessed as a result of the applied field that prevents magnetic order from taking place in an entirely spontaneous manner below  $T_B$ .

Next, the measurement was focused on field scans at constant temperature. Figure 52 (a) displays the magnetic response versus field at 300 K for functionalised SPION, while the results for gold coated SPION are plotted in figure 52 (b). The data collected for increasing magnetic fields (red symbols) were distinguished from that of decreasing fields (blue symbols). There are three notable observations made from the results in figure 52:

- (i) The magnetic hysteresis is negligible in both cases, as can be seen especially on the magnified scales in the inset of each figure,
- (ii) Neither of the two samples could be saturated magnetically, even in applied fields up to 25,000 Oe, and
- (iii) Functionalised SPION sample reaches a magnetic response of 6.5 times greater than that of gold coated sample at a comparable field of 1,000 Oe. At temperatures well below the blocking temperature  $T_B$ , a number of observables distinguish the  $T = 2 \text{ K} < T_B$  behaviour from that of the high-temperature region. A clear magnetic hysteresis is evident at low temperature, as shown in Figure 53. In figure 53 (a), a total hysteresis width of 2,600 Oe is found in functionalised sample and similarly 2,400 Oe in the case of gold coated sample shown in figure 46 (b). There is no detectable exchange bias in either of the two materials. Furthermore, both materials show tendencies to saturation at high field. Comparing the magnetic specimens directly with each other, one notes that at 2 K the high-field (20,000 Oe) response of functionalised SPION sample is now 11.4 times greater than that of gold coated SPION.

Conclusively therefore, a clear magnetic behaviour has been established from the two different samples (coated and functionalised samples). No long-range cooperative behaviour is evident anywhere from room temperature down to 2 K, which attests to a characteristic length scale of the Fe-magnetic agglomerations on the nano-scale. Being especially prone to intrinsic ferromagnetic ordering, any impurity form of Fe or macro-scale Fe aggregates would impart a very large and easily identifiable magnetic signal. Such a response was completely absent from these studies and hence testifies to the homogeneity quality of the materials under investigation.

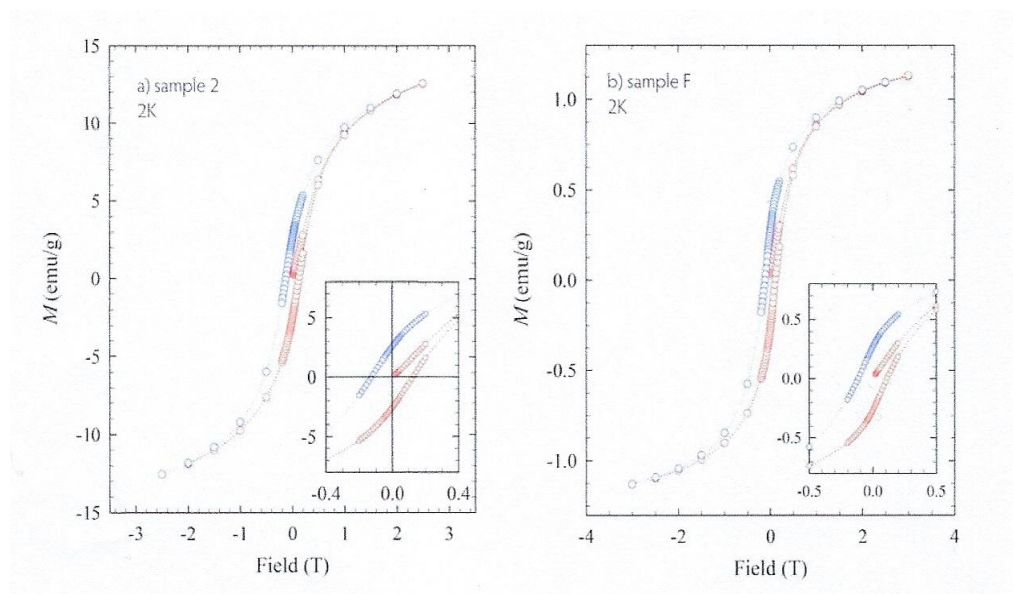


**Figure 53:** Low-temperature (2 K) field-dependent measurements of the magnetic moment in (a) functionalised SPION and (b) gold coated SPION. The insets show data near to  $B=0$ . A sizeable magnetic hysteresis is evident in both samples and may be attributed to a magnetic field-induced spin alignment within the spin-glass state. Such a spin alignment tends to randomize entirely in the paramagnetic state (cf. Fig.52, at room temperature) due to the thermal energy available to the spin system at room temperature.

The paramagnetic state has been shown to be retained over a large range temperature interval in the samples. At room temperature the materials exhibits completely reversible magnetic behaviour with no indication of magnetic remanence or field-induced effects. The materials could be cycled magnetically with what appears to be complete and full retention of the magnetic of the magnetic properties over the range of fields implemented in this study. The effects of short-range correlations become

evident at low temperatures in both samples through a freezing temperature,  $T_B$ , of approximately 15 K. This form of cooperative behaviour is clearly a phenomenon that occurs within the length scale of the particles themselves, and the ordering thus formed below  $T_B$  is fully dissolved again upon subsequent warming the material above  $T_B$ .



## CHAPTER 6

### 6.1 Discussion and Conclusion

### 6.2 NMR Results

The NMR results show that the 3-hydroxybenzaldehyde (**82**, See Appendix 1) was successfully converted to 3-(3-Formylphenoxy)propyl bromide (**83**) by the appearance of the carbon and protons of the propyl group on both the  $^{13}\text{C}$  and  $^1\text{H}$  spectra of (**83**, See Appendix 2) while the spectra of 3-(3-thioacetoxypoxy)benzaldehyde (**84**) showed sufficient nucleophilic replacement of the bromo atom by the thioacetate group. The appearance of a peak at  $\delta$  -2.82 on the proton NMR spectrum of 5,10,15,20-tetrakis[3-(3-thioacetoxypoxy)phenyl]porphyrin (**85**), See Appendix 3) shows the characteristic formation of porphyrin derivative of compound (**3**). Acid hydrolysis and alkaline hydrolysis of compound (**85**) produces 5,10,15,20-tetrakis[3-(3-thiopropoxy)phenyl]porphyrin **compound** (**86**). Summarily, the characterization of all synthesized compounds were confirmed using NMR spectroscopy by assigning appropriate peaks on the spectra obtained to corresponding protons on the structure of the various compounds.

### 6.3 Optical Analyses

#### 6.3.1 UV-Visible

Characterization of the porphyrin was further confirmed with both the Visible spectrum which shows a  $\lambda$ -max of 420 nm (characteristic of porphyrins) and 526 nm for the iron oxide-gold nanoparticles. The kinetic studies data of the deposition of the nanoparticle on the porphyrin with thiol derivatised side chains which was monitored using the UV-Vis spectrophotometry clearly depicts the immobilization of the nanoparticle on the porphyrin molecule by the continued decrease in the concentration of the nanoparticle suspension and increase in the concentration of the nanoparticle@porphyrin ( $\text{Fe}_3\text{O}_4@Au@Porphyrin$ ) structure and the new

absorption band of 535 nm for the nanoparticle/porphyrin mixture was also indicative of the functionalized sample. This suggests that the porphyrin molecules were able to attach to the gold surface through a thiol linker with the gold coated nanoparticles.

### 6.3.2 Infrared Analysis

The infra-red spectra display characteristic absorption bands expected of the various functional groups on the starting material, the intermediate products, the porphyrin structure as well as that of the nanoparticles with immobilized macrocycle (functionalized sample). Characteristic O-H absorption band for the starting (3-hydroxybenzaldehyde **82**) material was located at between 3000 to 2800  $\text{cm}^{-1}$  while one of the most characteristic strong absorption bands in an IR spectrum of carbonyl compounds was located at wave numbers from 1780 to 1650  $\text{cm}^{-1}$  for compounds **82** to **85**. At 1600 to 1500  $\text{cm}^{-1}$ , N-H absorption band was observed for compounds **85** and **86** which is indicative of the hindered N-H group of the cyclic porphyrin ring. A weak absorption of stretching vibration was also ascribed to the S-H group of compound **86** at 2890 to 2800  $\text{cm}^{-1}$ .

## 6.4 Kinetic Studies

### 6.4.1 Discussion on Kinetic Studies

While a particular order of reaction was not established for the deposition of the porphyrin on the synthesized nanoparticles, the kinetic studies showed that the surface reaction of the porphyrin with nanoparticles did take place through a thiol-linker on the inert outer gold layer of the nanoparticles and various experiments with different concentrations of the nanoparticles suspension with the porphyrin drug were conducted to show that the porphyrin drug is not stripped by merely dissolving the nanoparticles in organic solvents. Figure 37 in particular shows that there is a phase transfer reaction in which nanoparticles move from the aqueous to the organic phase.

## 6.5 Characterization

### 6.5.1 TEM and HRTEM

According to the TEM image (Fig. 46), the particle size for the SPION are in the range 34 – 58 nm with the mean particle diameter of  $42.41 \text{ nm} \pm 12.03 \text{ nm}$  and standard deviation of ( $\sigma$ ) 0.27 nm indicating broad size distribution and the  $\text{Fe}_3\text{O}_4@Au$  nanoparticles were well dispersed, small and were spherical in shape. For the gold coated SPION the particle diameters are in the range 34-54 nm. The average particle size as determined from the TEM image for the selected fraction is  $44.26 \text{ nm} \pm 6.93 \text{ nm}$ . The relative standard deviation of the sizes of the nanoparticles (0.16 nm) indicates that, the size distribution is very broad.

The increase in particle size compared to the uncoated iron oxide nanoparticles is attributed to the coating of the nanoparticles surface by the gold shell. This also reduces the surface energy of the nanoparticles and hence the degree of aggregation. The presence of the aggregated nanoparticles in the TEM image after the coating has been attributed to the insufficient passivation of the nanoparticles surface by the gold shell (fig.47). The HRTEM image (Fig. 48 B), shows the existence of lattice planes which confirms the crystallinity of the material. The spacing between adjacent lattice planes is about 0.23 nm which corresponds to the (311) interplanar distance of  $\text{Fe}_3\text{O}_4$  nanocrystals.<sup>263</sup>

Figure 48 B inlet is the selected area electron diffraction (SAED) patterns recorded on a single nanoparticle in Fig. 48 A. The SAED patterns composed of many separated bright spots instead of rings, which imply the single crystal-like diffraction of the functionalised nanoparticles. The set of brighter spots in the SAED represents that most of nanoparticles have the same orientation. Some disordered spot coexist with those of ordered bright spots. This phenomenon was attributed to misarranged nanoparticles.<sup>264</sup> The HRTEM and SAED results indicate that most of

nanoparticles self-assembled along the same crystal orientation. According to Cheng *et al.*,<sup>264</sup> this phenomenon, namely oriented aggregation, is induced by the spontaneous tendency of nanoparticles to minimize their high surface energy. The TEM and HRTEM measurement on the adlayer shows that the porphyrin molecules were well deposited on the gold coated SPION as indicated by the TEM and HRTEM micrographs.

### **6.5.2 Magnetic measurements of the gold coated & functionalised nanoparticles**

Atomic force microscopy (AFM) analysis was used to confirm the transmission electron microscopy (TEM) and HRTEM findings and it further revealed the surface characteristics of the nanoparticles while X-ray diffraction studies also suggest the presence of a gold based shell.

SQUID magnetometry was employed to study the magnetization of the nanoparticles and the functionalized nanoparticles. Conclusively, a clear magnetic behaviour has been established from the two different samples (coated and functionalised samples). No long-range cooperative behaviour is evident anywhere from room temperature down to 2 K, which attests to a characteristic length scale of the Fe-magnetic agglomerations on the nano-scale.

Being especially prone to intrinsic ferromagnetic ordering, any impurity form of Fe or macro-scale Fe aggregates would impart a very large and easily identifiable magnetic signal. Such a response was completely absent from these studies and hence testifies to the homogeneity quality of the materials under investigation.

### **6.5.3 Conclusion**

The study has shown the successful synthesis of a photosensitizer and its immobilization on a gold coated superparamagnetic iron oxide – gold, core-shell nanoparticles supported with analytical instrumental analysis such as

NMR, UV-Visible and IR spectrometers, transmission electron microscopy (TEM), high resolution transmission electron microscope (HRTEM), atomic force spectroscopy (AFM), X-ray diffraction spectroscopy (XRD) and magnetization studies using superconducting quantum interference device (SQUID).

The kinetic studies and the HRTEM images confirmed the deposition of the porphyrin macromolecules as a coat on the magnetites particles. Aliquot samples of the aqueous phase of the suspension of 0.002 mM Fe<sub>3</sub>O<sub>4</sub>@Au taken for absorbance measurement at every 600 s showed a decrease in the concentration of the suspension while a noticeable and appreciable increase was also noted in the concentration of the porphyrin functionalized nanoparticles measured at a  $\lambda$  max of 535 nm representing the functionalized sample.

#### **6.5.4 Recommendations**

There are some challenges that still required to be investigated further in this studies. The inability to obtain an NMR data for compound **86** need to be looked into because all available informations via the UV, IR analyses and the kinetic studies shows that there was a nucleophilic replacement of the acetal group. The potency of the photosensitizer itself for use as possible PDT agent need to be evaluated and its hydrophilicity and hydrophobicity required to be investigated.

## Chapter 7

### REFERENCES

1. Bines J, Oleske D. M and Cobleigh M. A. *Journal of Clinical Oncology*. 1996 **14**: 1718
2. Harrison L. B, Chadha M, Hill R. J, Hu K and Shasha D. *Oncologist*., 2002. **7**: 492.
3. Bomford C. K, Kunkler I. H, and Walter J. 2003. "Textbook of Radiotherapy", 6<sup>th</sup> Ed. Walter & Miller's. p 311.
4. Niederhuber J. E. "Abeloff's Clinical Oncology". 4<sup>th</sup> Ed. 2008.
5. Oleynikov D. *Surgical Clinics of North America*. 2008. **88**, 1121.
6. [www.cancercompass.com](http://www.cancercompass.com) >...> Conventional treatments
7. Meyer-Betz F. *Dtsch. Arch. Klin. Med.*, 1913. **112**, 476.
8. Moan J and Peng Q. *Journal of Photochemistry and Photobiology*., 2003. **2**, 1.
9. Dolmans D. E. J. G. J, Fukumara D, and Jain R. K. *Nature Reviews Cancer*., 2003. **3**, 380
10. Wilson B. C. *Canadian Journal of Gastroenterology*., 2002. **16**, 393.
11. Vroueraets M. B, Visser G. M. W, Snow G. B and van Dongen G. A. M. S., *Anticancer Research*., 2003. **23**, 505.
12. Bown S. G. *Journal of Photochemistry and Photobiology*., B: Biol., 1990. **6**, 1.
13. (a) Barr H, Krasner N, Boulos P. B, and Bown P. G. *Br. J. Surg.*, 1990. **77**, 93. (b) Dougherty J, Gomer C. J and Henderson B. W. *Journal of the National Cancer Insititute*., 1998. **90**, 889.
14. U. S. Food and Drug Administration, *Approved claims for palliative line therapy*., December 2003. Retrieved from [www.accessdata.fda.gov/scipts/cder/onctools/linelist.cfm](http://www.accessdata.fda.gov/scipts/cder/onctools/linelist.cfm)
15. U. S. Food and Drug, *FDA approves photofrin for treatment of pre-cancerous lesions in Barrett's esophagus*., August 2003. Retrieved from [www.fda.gov/bbs/topics/ANSWERS/20003/ANS01246.html](http://www.fda.gov/bbs/topics/ANSWERS/20003/ANS01246.html)
16. Bonnett R and Berenbaum M. Tumor Photochemotherapy. *Spectrum*. 1989. **218**: 8

17. B. W. Henderson and T. J. Dougherty, *Photochem. Photobiol.*, 1992. **55**, 145.
18. Neely W. C, Martin J. M. and Baker S. A. *Photochem. Photobiol.* 1988. **48**, 423.
19. Brown S. *Photodynamics New*.1999. Special Issue for Clinicians. 1.
20. Brown S. *International Photodynamics*. 1996. **1**: 5.
21. Kessel D. *International Photodynamics*. 1995. **1**: 2.
22. Dougherty T. J, Gomer C. J and Henderson B. W. *Journal of the National Cancer Institute.*, 1998. **90**, 889.
23. Dickson E. F. G, Goyan R. L and Pottier R. H. *Cellular and Molecular Biology*. 2003. **48**, 939.
24. Capella M. A. M and Capella L. S. *Journal of Biomedical Science.*, 2003. **10**, 361.
25. Jori G. *Journal of Photochemistry and photobiology B: Biology* ., 1996. **36**, 87.
26. Pandy R. K, Shiau F. Y, Sumlin A. B, Dougherty T. J and Smith K. M. *Bioorganic and Medicinal Chemistry Letters.*, 1994. **4**, 1263.
27. Kozyrev A. N, Zheng G, Zheng C, Dougherty T. J, Smith K. M and Pandy R. K. *Tetrahedron Letters.*, 1996. **37**, 6431.
28. Pandy R. K, Jagerovic N, Ryan J. M, Dougherty T. J and Smith K. M. *Tetrahedron Letters.*, 1996. **52**, 5349.
29. R. Bonnett, *New Scientist*, 1989, **42**, 55.
30. B. W. Henderson and T. J. Dougherty, *Photochem. Photobiol.*, 1992. **55**, 145.
31. Silver H. *Arch Dermatol Syphilol*, 1937. **36**, 1118.
32. Dougherty T. J, Kaufman J. E, Goldfarb A, Weishaupt K. R, Boyle D, and Mittleman A. *Cancer Res.*, 1977. **38**, 2628.
33. Elumalai, P., Atkins, P., de Paula, J. *Atkins' Physical Chemistry*, Oxford University Press, 2002. [ISBN 0-19-879285-9](#)
34. Dahlman A, Wile A. G, Burns R. G, Johnson F, and Berns M. W, *Cancer Res.*, 1982. **43**, 430.
35. Dougherty T. J. *J. Invest Dermatol*, 1981. **77**, 122.
36. Diezel W, Meffert H and Sonnichsen N. *Dermatol Monatsschr.*, 1980. **166**, 599.

37. (a) Rothemund P. *J. Am. Chem. Soc.*, 1936. **58**: 625. (b) Adler A. D, Longo F. R, Finarelli J. D, Goldmacher J, Assour J and Korsakoff L. *J. Org. Chem.* 1967. **32** (2): 476. (c) Rothemund P. *J. Am. Chem. Soc.*, 1935. **57**: 2010. (d) Bonnet R, Joannou S, White R. D, Wienfield U and Berenbaum M. C. *Photobiochemistry and Photobiophysics, Suppl.*, 1987. 45 (e) Falvo R. E, Mink L. M and Marsh D. F. *J. Chem. Educ.* 1999. **76**: 237.
38. Ferraudi G, Arguello G. A, Ali H, van Lier J. E. *Journal of Photochemistry and Photobiology.* 1988. **47**, 657.
39. (a) Firey P. A, Jones T. W, Jori G and Rodgers M. A. *Journal of Photochemistry and Photobiology.*, 1988. **48**, 357. (b) Balivada S, Rachakatla R. S, Wang H, Samarakoon T. N, Dani R. K, Pyle M, Kroh F. O, Walker B, Leaym X, Koper O. B, Tamura M, Chikan V, Bossmann S. H and Troyer D. L. *BMC Cancer.* 2010. **10**, 119.
40. (a) Dougherty T. J and Kessel D. *J. International Photodynamics.*, 1995. **1**, 2. (b) Henderson B, Dougherty T. *Photochem Photobiol.* 1992; **55**: 145 (c) Wilson B. *Photodynamic News.* 1998; **1**: 6.
41. Bonnet R and Djelal B. *m-TPHC, Phtodynamics*, 1993. **6**, 2.
42. (a) Adams A. *Science.* 1998. **279**, 1307b (b) Magda D. J, Wang Z, Gerasimchuk N, Wei W, Anzenbacher P. Jr. and Sessler J. L. *Pure Appl. Chem.*, 2004. **76**: 365. (c) Roberts W. G. *et al, J. Natl. Cancer Inst.*, 1991. **83**, 18.
43. Brown S, van den Bergh H, Sickenberg M and Ballini J. P. *Photodynamics news*, 1998. **1**, 2.
44. Songca S. P, Bonnet R and Maes C. M. S. *Afr. J. Chem*, 1997. **50**, 40.
45. Brown S, van den Bergh H and Dougherty T. J. *International Photodynamics*, 1996. **1**, 6.
46. Sessler J. L, Murai T, Lynch V and Cyr M. *J. Am. Chem. Soc.*, 1998. **110**, 5586.
47. (a) Sessler J. L, Hemmi G. W, Mody T. D, Murai T, Burrell A and Young S. W. *Acc, Chem. Res.*, 1994. **27**, 43. (b) Sessler J. L, Miller R. A. *Biochem Pharmacol.* 2000; **59**: 733
48. Sessler J. L, Mody T. D, Hemmi G. W and Lynch V. *Inorg. Chem.*, 1993. **32**, 3175.



49. Henderson B. W, Bellnier D. A, Greco W. R, Sharma A, Pandey R. K, Vaughan L. A, Weishaup K. R and Dougherty T. J. *Cancer Res.*, 1997. **57**, 4000.
50. Woodburn K. W, Fan Q, Kessel D and Young S. W. *Proc. SPIE.*, 1997. **2970**, 44.
51. Woodburn K. W, Fan Q, Kessel D, Miles D. R, Luo Y and Young S. W. *Photochem. Photobiol.*, 1997. **65**, 410.
52. Sessler J. L, Mody T. D, Hemmi G. W, Lynch V, Young S. W and Miller R. A. *J. Am. Soc.*, 1993. **115**, 10368.
53. (a) Young S. W, Sidhu M. K, Qing F, Muller H. H, Neuder M, Zanassi G, Mody T. D, Hemmi G, Dow W. C, Mutch J. D, Sessler J. L and Miller R. A. *Invest. Radiol.*, 1994. **29**, 39. (b) Fruehauf J. P and Meyskens F. L. Jr., *Clin Cancer Res.*, 2007. **13**: 789. (c) Evans J. P, Xu F, Sirisawad M, Miller R, Naumovski L and Ortiz de Montellano P. R. *Mol Pharmacol.* 2007. **7**, 193.
54. Young S. W, Qing F, Harriman A, Sessler J. L, Mody T. D, Hemmi G. W, Hao Y and Miller R. A. *Proc. Natl. Acad. Sci. U.S.A.*, 1996. **93**, 6610.
55. (a) Woodburn K. W, Fan Q, Kessel D, Luo Y, Young S. W. *J. Inv. Dermatology*, 1998. **110**, 746. (b) Blumenkranz M. S, Woodburn K. W, Qing F, Verdooner S, Kessel D and Miller R. 2000. *Am J Ophthalmol.* **129**, 353.
56. Theimann P and Woodburn K. W. *Proc. SPIE.*, 1998. **3247**, 56.
57. Mody T. D, Wright M, Linqvist V, Young S. W, Sessler J. L, Berns M, Dow W. C and Miller R. A. *Photochem. Photobiol.*, 1994. **59**, 375.
58. Young S. W, Wright M, Mody T. D, Sessler J. L, Woodburn K. W, Dow W. C and Miller R. A. *Photochem. Photobiol.* 1996. **63**, 892.
59. Woodburn K. W, Fan Q, Miles D. R, Kessel D, Luo Y and Young S. W. *Photochem. Photobiol.*, 1997. **65**, 410.
60. (a) Summer W , Pichlmeier U , Meinel T , Wiestler O. D , Zanella F and Reulen H. J. *Lancet Oncol.* 2006. **7**: 392. (b) Sessler J. L, Dow W. C, O'Comnor D, Harriman A, Hemmi G, Mody T. D, Miller R. A, Qing F, Springs S, Woodburn K. W and Young S. W. *J. Alloys and Compounds.*, 1997. **146**, 249.

61. Young S. W, Wright M, Mody T. D, Sessler J. L, Woodburn K. W, Dow W. C and Miller R. A. *Photochem. Photobiol.*, 1995. **61**, 815.
62. Young S. W, Wright M, Mody T. D, Sessler J. L, Woodburn K. W, Dow W. C and Miller R. A. *Photochem. Photobiol.*, 1996. **63**, 892.
63. Marcus S. L. *J International Photodynamics.*, 1996. **1**, 2.
64. Brown S. B, Pottier R and Kennedy J. *International Photodynamics.*, 1997. **1**, 4.
65. Peng Q, Berg K, Moan J, Kongshaug M and Nesland J. M. *Photochem. Photobiol.*, 1997. **65**, 235.
66. Peng Q, Warloe T, Berg K, Moan J and Kongshu M. *Cancer*, 1997. **79**, 2282.
67. Brown S, van den Bergh H, Lange N and Jichlinski P. *Photodynamics News*, 1992. **2**, 4.
68. (a) Stryer L. Biochemistry, 1981. Second Edition, W. H Freeman & Company. p 505. (b) Morris G. M, Micca P. L and Coderre J. A. *Applied Radiation and Isotopes*. 2004. **61**, 917. (c) Hill J. S, Kahl S. B, Kaye A. H, Styli S. S, Koo M. S, Gonzales M. F, Vardaxis N. J and Johnson C. I. *Proc Natl Acad Sci*. 1992. **89**: 1785.
69. Singh R. J, Felix J. B, and Kalyanaraman B. *Photochem Photobiol.* 1992.**55**, 483.
70. Richter M, Sternberg E, Waterfield E, Dolphin D and Levy J. G. *Proc. SPIE*. 1988. **997**, 132.
71. Hill J. S, Kahl S. B, Kaye A. H, Styli S. S, Koo M. S, Gonzales M. F, Vardaxis . J and Johnson C. I. *Proc. Acad. Sci., U.S.A*, 1992. **89**, 1785.
72. Hill J. S, Kahl S. B, Styli S. S, Nakamura Y, Koo M and Kaye A. H. *Proc. Natl. Acad. Sci. USA*, 1995. **92**, 12126.
73. Barth R. F, Solloway A. H and Fairchild R. G. *Cancer Res.*, 1990. **50**, 1061.
74. Locher G. L and Roentgenol A. G. *Radium Ther.*, 1936. **36**, 1.
75. (a) Barth R. F, Solloway A. H and Fairchild R. G. *Sci. Am.* 1990. 100. (b) Yannuzzi L. A, Slakter J. S, Gross N. E, Spaide R. F, Costa D, Huang D, Klanchnik J and Aizman A. *Retina*. 2003. **23**: 288. (c) Augustin A. J and Schmidt-Erfurth U. *Eur J Ophthalmol.*, 2006. **16**: 824. (d) Cruess A. F, Zlateva G, Pleil A. M and Wirostko B. *Acta Ophthalmol.* 2009. **87**: 118.

- (e) Lai T. Y, Chan W. M, Li H, Liu D. T and Lam D. S. 2006. **90**: 869. (f) Brown D. M, Michels M and Kaiser P. K. *Ophthalmology*. 2009. **116**: 57. (g) Shah G. K, Sang D. N and Hughes M. S. *Retina*. 2009. **29**: 133. (h) Kaiser P. K. *Curr Med Res Opin*. 2007. **23**: 477. (i) Ober M. D, Yannuzzi L. A, Do D. V, Spaide R. F, Bressler N. M, Jampol L. M, Angelilli A, Eandi C. M and Lyon A. T. *Ophthalmology*. 2005. **112**: 288. (j) Spaide R. F, Sorenson J and Maranan L. 2005. **112**: 301.
76. United States Securities and Exchange Commission, Washington, DC 20549 [X] Annual Report Pursuant To Section 13 or 15(d) of the securities exchange act of 1934. Commission File Number: 000-26658. Pharmacyclics, INC.
77. (a) Yeung A. C. Stanford University School of Medicine Summit. Regional Photodynamic Therapy for Vulnerable Plaque Stabilization: Antrin. P 1-32. (b) Seshiah PN, Kereiakes DJ, Vasudevan SS, . *Circulation*. 2002; **105**: 174.
78. (a) Dragicevic-Curic N, Grafe S, Albrecht V and Fahr A., *J. Photochem Photobiol B*. 2008. **91**: 41. (b) Lorenz K. J and Maier H. *HNO*. 2008. **56**: 402. (c) O'Connor A. E, Gallagher W. M and Byrne A. T. *Photochemistry and Photobiology*. 2009. **85**: 1053. (d) Lorenz K. J and Maier H. *Eur Arch Otorhinolaryngol*. 2009. **266**, 1937. (e) Tan I, Dolivet G, Ceruse P, Vander Poorten V, Mahy P, Roest G and Rauschnig W. *J. Clin Oncol* (Meeting Abstracts) 2008. **26**, 17001. (f) Holloway H, Hatanaka H and Davis M. A. *J. Med. Chem.*, 1967. **10**, 714. (g) Lang K, Schulte K. W, Ruzicka T and Fritsch C. *Skin Therapy Letter*. 2001. **6**: 1.
79. (a) Barth R. F, Coderre J. A, Vicente M. G. H and Blue T. E. *Clinical Cancer Research*. 2005. **11**, 3987 (b) Kahl S. B and Koo M. S. *J. Chem. Soc. Commun*. 1990. 1769.
80. Kahl S. B, Joel D. D, Nawrocky M. M, Micca P. L, Tran K. P, Finkel G. C and Slatkin D. N. *Proc. Natl. Acad. Sci. USA*, 1990. **87**, 7265.
81. (a) Kaye J. S, Sawyer A. S, Morstyn W. H, Megison G, and Stylli P. D. *Neurosurgery*, 1990. **26**, 248. (b) Global Cancer Facts and Figures. [www.cancer.org/cancerfactsfigures/globalcancerfactsfigures2007](http://www.cancer.org/cancerfactsfigures/globalcancerfactsfigures2007).
82. (a) Losev O. V. (Reproduced in English) *Physics of the Solid State*. 2004. **46**, 1. (b) O.V. Lossev O. V. *Philosophical Magazine* 1928. **5**: 1024.

83. Knyukshto V. N, Shul'ga A. M, Sagun E. I and Zen'kevich E. I. *Optics & Spectroscopy*. 2006. 101. **6**, 895.
84. (a) Wingo P. A, Landis S, Parker S and Bolden S. *J. Reg. Management*, 1998. **25**, 43. (b) Wingo P. A, Landis S and Ries L. A. *CA Cancer J. Clin*, 1997. **47**, 239.
85. Wingo P. A, Ries L. A and Rosenberg H. M., *Cancer.*, 1998, **82**, 1197.
86. Landis S. H, Murray T, Bolden S and Wingo P. A., *CA Cancer J. Clin.*, 1999. **49**, 8.
87. Rothmund P. *J. Am. Chem. Soc.*, 1936. **58**, 625.
88. Rothmund P, *J. Am. Chem. Soc.*, 1935. **57**, 2010.
89. Adler A. D, Longo F. R, Finarelli J. D, Goldmacher J, Assour J and Korsakoff L. *J. Org. Chem.*, 1967. **32**, 476.
90. <http://www.lasalle.edu/~prushan/Abs/and> Fluor
91. (a) Milgrom L. R. 1997. Oxford. *The Porphyrins*, ed. D. Dolphin, Academic Press, New York, 1978. (b) D. F. Marsh and L. M. Mink, 1996. *J. Chem. Ed.*, **73**, 1181.
92. Patrice T. *Photodynamic News*. 1999. **2**: 1.
93. Henderson B. W, Belnier D. A, Greco W. R, Sharma A, Pandey R. K and Vaughn L. A. *Cancer Res.*, 1997. **57**, 4000.
94. Ottaway J. H and Apps D. K, *Biochemistry* 4<sup>th</sup> Edition, 1984. London, Bailliere Trindall
95. Alan D. *Academy of Sciences*, 1975. 267.
96. Williams D. H and Fleming I. A, *Spectroscopic Methods in Organic Chemistry*, 5<sup>th</sup> Edition. 1987. McGraw-Hill, New York. 15.
97. Okuno Y, Kamikado T, Yokoyama S and Mashiko M. *Journal Molecular Structure (Theochem)*. 2003. **631**, 13-20.
98. Cammidge A.N and Ozturk O. *J. Org. Chem*. 2002. **67**: 7457.
99. Shinmori H, Kajiwara O and Osuka S. *Tetrahedron Letters*. 2001. **42**, 3617. 91.
100. Songca S.P and Mbatha B. *S.Afr. j. Chem*. 2000. **53**: 1.
101. Songca S.P and Mbatha B. *J. Pharm. Pharmacol*. 2000. **52**, 1.
102. Dazhong F, Taniguchi M, Yao Z, Dhanalekshmi S and Lindsey J. L. *Tetrahedron*. 2005. **61**, 10291.

103. Littler B. J, Miller M. A, Hung C. H, Wagner R. W, O'Shea D. F, Boyle P. D and Lindsey J. S. *J. Org. Chem.* 1999. **64**, 1391.
104. Rao P. D, Dhanalekshmi S, Littler B. J and Lindsey J. S. *J. Org. Chem.* 2000. **65**, 7323.
105. Geier G. R and Lindsey J. S. *Tetrahedron.* 2004. **60**, 11435.
106. Zusuki A. *Pure and Appl. Chem.* 1994. **66**: 213.
107. Lindsey J. S and Wagner R. W. *J. Org. Chem.* 1989. **54**: 836.
108. Nagarkatti J. P and Ashley K. R. *Synthesis.* 1974. 186.
109. Casiraghi G, Cornia M, Rassu G, Del Sante C and Spanu P. *Tetrahedron.* 1992. **48**, 5619.
110. Vigmond S. J, Shang M. C, Kallury K. M. R and Thompson M. *Tetrahedron Lett.* 1994. **35**, 2455.
111. (a) Mizutani T, Ema T, Tomita T, Kuroda Y and Ogoshi H. *J. Chem. Soc., Chem. Commun.* 1993. 520. (b) Mizutani T, Ema T, Tomita T, Kuroda Y and Ogoshi H. *J. Am. Chem. Soc.* 1994. **116**, 4240-4250.
112. Hombrecher H. K and Horter G. *Liebigs Ann. Chem.* 1991. 219.
113. Yu L and Lindsey J. S. *Tetrahedron* 2001. **57**, 9286.
114. (a) Lee C. H and Lindsey J. S. *Tetrahedron.* 1994. **50**: 11427. (b) Schweizer E. E, Berninger C. J, Crouse D. M, Davis R. A and Logothetis R. S. *The Journal of organic Chemistry.* 1969. **34**: 207. (c) Gryko D. T, Clausen C and Lindsey J. S. *J. Org. Chem.* 1999. **64**, 8635. (d) Sheldon R. A (Ed.), 1994. *Metalloporphyrins in catalytic Oxidation.* Marcel Dekker, New York. (e) Pavlovic E, Quist A. P, Gelius U, Nyholm L and Oscarsson L. *Langmuir.* 2003. **19**, 4217. (f) Battioni P, Bartoli J. F, Mansuy D, Byun Y. S and Traylor T. G. *J. Chem. Soc. Commun.* 1991. 1051. (g) Ji Balkus K. J, Khanmamedova K. A, Dixon K. M and Bedioui F. *Appl. Catal. A: General.* 1996. **143**, 159. (h) Zhan B.-Z and Li X.-Y. *Chem. Commun.* 1998. 349. (i) Woltinger J, Backrall J.-E and Zsigmond A. *Chem. Eur. J.* 1999. **5**, 1460.
115. Schwertmann T. and Cornell R.M. (1991). *Iron oxides in the laboratory: Preparation and characterization*, VCH, Weinheim, Cambridge, 137: 11.
116. Berry C.C. and Curtis A.S.G. *Journal of Physics D: Applied Physics*, 2003. **36**: 198.

117. Carpenter E. E, Kumbhar A, Wiemam J. A, Srikanth H, Wiggins J, Zhou W and O'Connor C. J. *Materials Science and Engineering*. 2000. **286**, 81.
118. Tarjaj P. and Serna C. *J. Am. Chem. Soc.* 2003. **125**, 15754.
119. Tarjaj P., Morales M.P., Verdaguer S., Carreno T. and Serna C.J. *Journal of Physics D: Applied Physics*. 2003. **36**, 182.
120. Seino S., Kinoshita T., Otome Y., Nakagawa T., Okitsu K., Mizukoshi Y., Nakayama T., Sekino T., Niihara K. and Yamamoto T.A. *Journal of Magnetism and Magnetic Materials*. 2005. **293**, 144.
121. Pankhurst Q.A., Conolly J., Jones S.K. and Dobson J. (2003). *Journal of Physics D: Applied Physics*, **36**: R167.
122. Zhang Y., Zeng G.M., Tang L., Huang D.L., Jiang X.Y. and Chen Y.N. *Biosensors and Bioelectronics*. 2007. **22**, 2121.
123. Park J.I. and Cheon J. *J. Am Chem. Soc.* 2001. **123**: 5743.
124. A. S. Waniewska, M. Gutowski and H. K. Lachowicz. *Physical Review*. **46**: 14594.
125. Kinoshita T., Seino S., Mizukoshi Y., Nakagawa T. and Yamamoto T.A. *Journal of Magnetism and Magnetic Materials*. 2007. **311**, 255.
126. Yonglan L. *Materials Letters*. 2207. **61**, 1039.
127. Lu Q.H., Yao K.L., Xi D., Liu Z.L., Luo X.P. and Ning Q. *Journal of Magnetism and Magnetic Materials*. 2006. **301**: 44.
128. Davis R. *Powder Technology*, 2001. **119**, 45.
129. Carpenter E.E., Sangergorio C. and O'Connor C. J Institute of Electrical and Electronics Engineers for Transmission Magnetism, 1999. **35**, 3496.
130. Yamamoto T., Shull R.D., Bandaru P.R., Cosandey F. and Hahn H.W. *Japanese Journal of Applied Physics*, 1994. **33**, 1301.
131. Yamamoto T.A., Nishimaki K., Harabe T., Shiomi K., Nakagawa T. and Katsura M. *Nano Structured Materials*, 1999. **12**, 523.
132. Tanaka M., Misaka Y., Shiomi K., Yamamoto T.A., Nakagawa T., Katsura M., Numazawa T., Nakayama T. and Niihara K. *Scripture Material*. 2001. **44**, 2141.
133. Yamamoto T.A., Tanaka M., Misaka Y., Nakagawa T., Nakayama T., Niihara K. and Numazawa T. *Scripture Materials*. 2002. **46**, 89.
134. Yamamoto T., Croft M.C., Shull R.D. and Hahn H.W. *Nano Structured Materials*. 1995. **6**, 965.

135. Nishimaki K., Yamamoto T.A., Nakagawa T. and Katsura M. *Japanese Journal of Applied Physics*. 2000. **39**, 1225.
136. Liu Z.L., Ding Z.H., Yao K.L., Tao J., Du G.H., Lu Q.H., Wang X., Gong F.L. and Chen X. *Journal of Magnetism and Magnetic Materials*. 2003. **265**, 98.
137. Liu Z., Liu Y., Yang Y., Shen G. and Yu R. *Analytica Chimica Acta*. 2005. **533**, 3.
138. Gong J.L., Huang Y., Chen J.W., Jiang J.H., Shen J.L. and Yu R.Q. *Biosensors and Bioelectronics*. 2007. **22**, 1501.
139. Ashtari P., He X., Wang K. and Gong P. *Talanta*. 2005. **67**, 548.
140. Gao Y., Chen B., Li H. and Ma Y. *Materials Chemistry and Physics*, 2003. **80**, 348.
141. Aurich K., Schwalbe M., Clement J.H., Weitschies W., and Buske N. *Journal of Magnetism and Magnetic Materials*. 2007. **311**, 1.
142. Liu Z.M., Yang H.F., Li Y.F., Liu Y.L., Shen G.L. and Yu R.Q. *Sensors and Actuators B. Chemical*. 2006. **113**, 956.
143. Wagner J., Autenrieth T. and Hempelmann R. *Journal of Magnetism and Magnetic Materials*. 2002. **252**, 4.
144. Zhang S., Dong D., Sui Y., Liu Z., Wang H., Qian Z. and Su W. *Journal of Alloys and Compounds*. 2006. **415**, 257.
145. Tie S.L., Lee H.C., Bae Y.S., Kim M.B., Lee K. and Lee C.H. *Physicochemical and Engineering Aspects*. 2007. **293**, 278.
146. Wu X., Jin G., Guan L., Cao H. and Guo X.Y. *Materials Science and Engineering*. 2006. **433**, 190.
147. Wang Y. and Lee J.K. *Journal of Molecular Catalysis A: Chemical*. 2007. **263**, 163.
148. Seto T., Koga k., Takano F., Akinaga H., Ori T., Hirasawa M. and Murayama M. *Journal Photochemistry and Photobiology*. 2006. **182**, 342.
149. Zhang X.F., Dong X.L., Huang H., Lv B., Zhu X.G., Lei J.P., Ma S., Liu W. and Zhang Z.D. *Materials Science and Engineering*. 2007. **454**, 211.
150. Lim J., Tilton R.D., Eggeman A. and Majetich S.A. *Journal of Magnetism and Magnetic Materials*. 2007. **311**, 78.
151. Carpenter E.E. *Journal of Magnetism and Magnetic Materials*. 2001. **225**, 17.

152. Zaitsev V., Filimonov D.S., Preshyakov I.A., Gambino R.J. and Chu B. *Journal of Colloid and Interface Science*. 1999. **212**, 49.
153. Gupta A.K. and Gupta M. *Biomaterials*. 2005. **26**, 3995.
154. Maity D. and Agrawal D.C. *Journal of Magnetism and Magnetic Materials*. 2007. **308**, 46.
155. Sugimoto T. and Matijevi E. *Journal of Colloid Interface Sciences*. 1980. **74**, 227.
156. Winnik F.M., Morneau A., Ziolo R.F., Stover H.D.H. and Li W.H *Langmuir*. 1995. **11**, 3660.
157. Yaacob I.I., Nunens A.C., Bose A. and Shah D.O. *Journal of Colloid Interface Sciences*. 1994. **168**, 289.
158. Khalafalla S.E. and Reimers G.W. Institute of Electrical and Electronics Engineers for Transmission Magnetism, 1980. **16**, 178.
159. Qiu X. *Chinese Journal of Chemistry*. 2000. **18**, 834.
160. Vayssieres L., Chanei C., Tronc E. and Jolivet J.P. *Journal of Interface Science*. 1998. **205**, 205.
161. Liu X., Guan Y., Ma Z. and Liu H. *Langmuir*. 2004. **20**, 10278.
162. Lopez-Quintela M.A. and Rivas J. *Journal of Colloid Interface Sciences*. 1993. **158**, 446.
163. Gupta A.K. and Wells S. *Nanobiosciences*. 2004. **3**, 66.
164. Lee Y., Lee J., Bae C.J., Park J.G., Noh. and Park J.H. *Advanced Functional Materials*. 2005. **15**, 503.
165. Rockenberger J., Scher E.C. and Alivisators A.P. (1999). *J. Am. Chem. Soc.* 1999. **121**, 11595.
166. Sun S. and Zeng H. *J. Am. Chem Soc.* 2002. **124**, 8204.
167. LaConte L., Nitin N. and Bao G. *Nanotoday*. 2005. **32**, 32.
168. Nitin N., LaConte L.E.W., Zurkiya O., Hu X. and Bao G. *Journal of Biological Inorganic Chemistry*. 2004. **9**, 706.
169. Reimers G.W. and Khalafalla S.E. (1972). Preparing magnetic fluids by a peptizing method. US Bureau Mines Technical Representative: 1972. 59.
170. Sjogren C.E., Briley-Saebo K., Hanson M. and Johansson C. *Magnetic Resonance in Medicine*. 1994. **31**, 268.
171. Gupta A.K. and Curtis A.S.G. *Biomaterials*. 2004. **25**, 3029.



172. Kim D.K., Zhang Y., Voit W., Rao K.V. and Muhammed M. *Journal of Magnetism and Magnetic Materials*. 2001. **225**, 30.
173. Bailey R.L *Journal of Magnetism and Magnetic Materials*. 1983. **39**, 178.
174. Charles S.W. and Popplewell J. Progress in the development of ferromagnetic liquids. Institute of Electrical and Electronics Engineers for Transmission Magnetism, 1980, **16**, 172.
175. Guzmán M.G., Dille J. and Godet S. Synthesis of silver nanoparticles by chemical reduction method and their antibacterial activity. Proceedings of World Academy of Science, Engineering and Technology, 2008. **33**, 2070.
176. Tepper T., Ilievski F., Ross C.A., Zaman T.R., Ram R.J., Sung S.Y. and Stadler B.J.H. *Journal of Applied Physics*. 2003. **93**, 6948.
177. Mendenhall G.D., Geng Y. and Hwang J. *Journal of Colloid and Interface Science*. 1996. **184**, 519.
178. Yee C., Kataby G., Ulman A., Prozorov T., White H., King A., Rafailovich M., Sokolov J. and Gedanken A. *Langmuir*. 1999. **15**, 7111.
179. Sahoo Y., Pizem H., Fried T., Golodnitsky D., Burstein L., Sukenik C.N. and Markovich G. *Langmuir*. 2001. **17**, 7907.
180. Tadmor R., Rosensweig R.E., Frey J. and Klein J *Langmuir*. 1997. **16**, 9117.
181. Berry C.C., Wells S., Charles S. and Curtis A.S.G. *Biomaterials*. 2003. **24**, 4551.
182. Gupta P.K. and Hung C.T. *Life Sciences*. 1989. **44**, 175.
183. Ugelstad J., Stenstad P., Kilaas L., Prestvik W.S., Herje R., Bererge A. and Hornes E. *Blood Purification*. 1993. **11**, 349.
184. Lee J., Isobe T. and Senna M. *Journal of Colloid and Interface Science*. 1996. **177**, 490.
185. Ng V., Lee Y.V., Chen B.T. and Adeyeye A.O. *Nanotechnology*. 2002. **13**, 554.
186. Chen M., Yamamuro S., Farrell D. and Majetich S.A *J. Appl. Phys.* 2003. **93**, 7551.
187. Lin J., Zhou W., Kumbhar A., Fang J., Carpenter E.E. and O'Connor C.J. *Journal of Solid State Chemistry*. 2001. **159**, 26.
188. Ulman A. *Chemical Reviews*. 1996. **96**, 1533.

189. Mulvaney P., Liz-Marzán L.M., Giersig M. and Ung T. *J. Mat. Chem.* 2000. **10**, 1259.
190. Tartaj P., González-Carreño T. and Serna C.J. *Advanced Materials.* 2001. **13**, 1620.
191. Tartaj P., González-Carreño T. and Serna C.J. *Langmuir.* 2002. **18**, 4556.
192. Santra S., Tapeç R., Theodoropoulou N., Dobson J., Hebard A. and Tan W. *Langmuir.* 2001. **17**, 2900.
193. Roberts M.J., Bentley M.D. and Harris J.M. *Advanced Drug Delivery Reviews.* 2002. **54**, 459.
194. Sato T., Iijima T., Sekin M. and Inagaki N. *Journal of Magnetism and Magnetic Materials.* 1987. **65**, 252.
195. Lefebure S., Dubois V., Cabuil V., Neveu D and Massart S. *Journal of Materials Research.* 1998. **10**, 2975.
196. Bean C.P. and Livingstone J.D. *Journal of Applied Physics.* 1959. **30**, 120S.
197. Chatterjee J., Haik Y. and Chen C.J. *Journal of Magnetism and Magnetic Materials.* 2003. **257**, 113.
198. Li Y., Xiong P., Molnár S.V., Wirth S., Ohno Y. and Ohno H *Applied Physics Letters*, 2002. **80**, 4644.
199. Han D.H., Wang J.P. and Luo H.L. *Journal of Magnetism and Magnetic Materials.* 1994. **136**, 176.
200. Tourinho F., Franck R., Massart R. and Perzynski R. *Progress in Colloid and Polymer Science*, 1989. **79**, 128.
201. Gomez-Lopera S.A., Plaza R.C. and Delgado A.V. *Journal of Colloid and Interface Science.* 2001. **240**, 40.
202. Voit W., Kim D.K., Zapka W., Muhammed M. and Rao K.V. *Materials Research Society.* 2001. **676**: 8. 1.
203. Gupta A.K. and Curtis A.S.G. *Proceedings of the 30<sup>th</sup> Annual Symposium of Controlled Release of Bioactive Materials*, 2003. **30**, 788.
204. Bradbury A., Menear S., O'Grady K. and Chantrell R.W. *Institute of Electrical and Electronics Engineers Transactions on Magnetics*, 1984. **20**, 1846.
205. Olsvik O., Popovic T., Skjerve E., Cudjoe K.S., Hornes E., Ugelstad J. and Ulhen M. *Clinical Microbiology Reviews.* 1994. **7**, 43.

206. Yeh T.C., Zhang W., Ldstad S.T. and Ho C. *Magnetic Resonance in Medicine*. 1993. **30**, 617.
207. Handgretinger R., Lang P., Schumm M., Taylor G., Neu S., Koscielnak E., Niethammer D. and Klingebiel T. *Bone Marrow Transplant*. 1998. **21**, 987.
208. Schoepf U., Marecos E., Jain R. and Weissleder R. *Bio Techniques*. 1998. **24**, 642.
209. Weissleder R., Cheng H.C., Bogdanova A. and Bogdanov A. *Journal of Magnetic Resonance Imaging*. 1997. **7**, 258.
210. Gupta A.K., Berry C., Gupta M. and Curtis A. Institute of Electrical and Electronics Engineers for Transmission Nanobiosciences, 2003. **2**, 256.
211. Lobel B., Eyal O., Kariv N. and Katzir A. *Lasers in Surgery and Medicine*. 2000. **26**, 4.
212. Xu H.H., Smith D.T. and Simon C.G. *Biomaterials*. 2004. **25**, 4615.
213. Sokolov K., Follen M., Aaron J., Pavlova I., Malpica A., Lotan R. and Richards-Kortum R. *Cancer Research*. 1999. **63**, 1999.
214. Bulte J.W., Douglas T. and Witwer B. *Nature Biotechnology*. 2001. **19**, 1141.
215. Hooper C. National Institutes of Health Catalyst, 2000. **8**, 15256.
216. Kubo T., Sugita T., Shimose S., Nitta Y., Ikuta Y. and Murakami T. *International Journal of Oncology*. 2000. **17**, 309.
217. Kubo T., Sugita T., Shimose S., Nitta Y., Ikuta Y. and Murakami T. *International Journal of Oncology*. 2001. **18**, 121.
218. Tomalia D.A. *Progress in Polymer Science*, 2005. **30**, 294.
219. Boyd B.J. Technology overviews. Colloidal Drug Delivery, drug delivery report autumn/winter, PharmaVentures Ltd, Oxford, UK: 2005. P 63.
220. Johnson G.A. *Magnetic Resonance*. 1993. **9**: 1.
221. Moghimi S.M., Hunter A.C.H. and Murray J.C. *Pharmacological Reviews*. 2001. **53**, 283.
222. Vlamidir S., Zaitsev V., Dmitry S., Filimonov I., Gambino R.J., Chu B. and Presnyakov A. *Journal of Colloid and Interface Science*. 1999. **212**, 49.
223. Arbab A.S., Bashaw L.A., Miller B.R., Jordan E.K., Lewis B.K., Kalish H. and Frank J.A. *Radiology*. 2003. **229**, 838.
224. Reimers P. and Weissleder R. *Radiology*. 1996. **36**, 153.

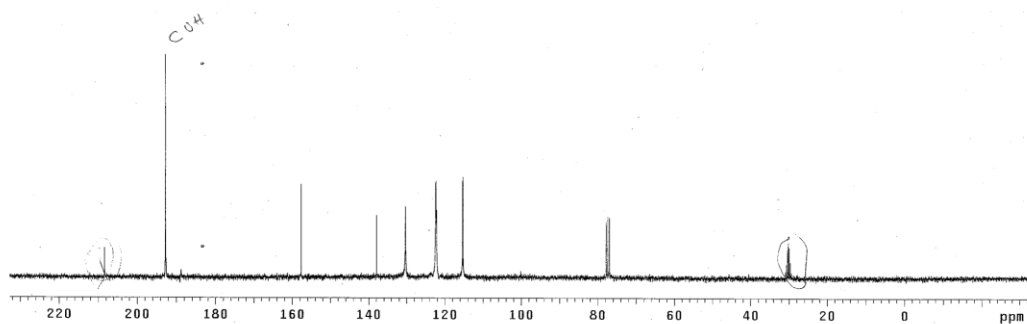
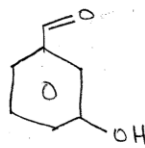
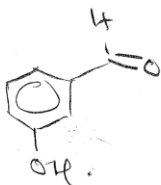
225. Tillotson T.M., Gash A.E., Simpson R.L., Hrubesh L.W. and Satcher J.H. *Journal of Non-Crystalline Solids*. 2001. **285**, 335.
226. Torchilin V.P. and Trubetsky V.S. *Advanced Drug Delivery Reviews*. 1995. **16**, 141.
227. Goya G.f., Berquo T.S. and Fonseca F.C *Journal of Applied Physics*. 2003. **94**, 3520.
228. Weissleder R., Bogdanov A., Neuwelt E.A. and Papisov M. *Advanced Drug Delivery Reviews*. 1995. **16**, 321.
229. [http://garden of praise.com/ibdhipp.htm](http://garden.of.praise.com/ibdhipp.htm)
230. Jankowski C. Hippocrates: Making the way for medicine. 5301 Oceanus Drive. Huntington Beach, CA 92649. <http://www.tcmpub.com>
231. Nielsen O.S., Horsman M. and Overgaard J. *European Journal of Cancer*, 2001. **37**, 1587.
232. Gordon R.T., Hines J.R. and Gordon D. *Medical Hypothesis*. 1979. **5**, 83.
233. Luderer A.A., Borreli N.F., Panzarino J.N., Mansfield G.R., Hess D.M., Brown J.L. and Barnett E.H. *Radiation Resolution*. 1983. **94**, 190.
234. Chan D.C.F., Kirpotin D.B. and Bunn Jr P.A. *Journal of Magnetism and Magnetic Materials*.1993. **122**, 374.
235. Scherer F., Anton M., Schilinger U., Henke J., Bergemann C., Kruger A., Gansbacher B. and Plank C. *Gene Therapy*. 2002. **9**, 102.
236. Krotz F., Wit C., Sohn H.Y., Zahler S., Gloe T., Pohl U. and Plank C. *Molecular Therapy*. 2003. **7**, 700.
237. Bulte J.W.M. and Kraitchman D.L. (2004). *Nuclear Magnetic Resonance Biomedical*. 2004. **17**, 484.
238. Ferrari M. *Nature Reviews Cancer*. 2005. **5**, 161.
239. Cunningham C.H., Arai T., Yang P.C., McConell M.V., Pauly J.M. and Conolly S.M. *Magnetic Resonance in Medicine*. 2005. **53**, 999.
240. Johannsen M., Gneveckow U., Eckelt L., Feussner A., Scholz R., Deger S., Wust P., Loening S.A. and Jordan A. *International Journal of Hyperthermia*. 2005. 21637.
241. Jurgons R., Seliger C., Hilpert A., Trahms I., Odenbach S. and Alexiou C. *Journal of Physics: Condensed Matter*. 2006. **81**, S2893.
242. Jemal A., Siegel R., Ward E., Murray T., Xu J. and Thun M.J. *A Cancer Journal for Clinicians*. 2007. **57**, 43.

243. Ambrose D.L. and Fritz J.S. *Journal of Chromatography B: Biomedical Sciences and Applications*. 1998. **709**, 89.
244. Sunderland C.J., Steiert M., Talmadge J.E., Derfus A.M. and Barry S.E. *Drug Development Research*. 2006. **67**, 70.
245. Neuberger T., Schöpf B., Hoffman H., Hoffmann M. and Rechenberg B.V. *Journal of Magnetism and Magnetic Materials*. 2005. **293**, 483.
246. Häfeli U.O. *International Journal of Pharmaceutics*. 2004. **277**, 19
247. Widder K.J., Morris R.M., Poore G., Howard D.P.Jr. and Senyei A.E. *Proceedings of the National Academic of Sciences*. 1981. **78**, 579.
248. Rotariu O. and Strachani N.J.C. *Journal of Magnetism and Magnetic Materials*. 2005. **293**, 639.
249. Iacob G.H., Rotariu O., Strachan N.J.C. and Häfeli U.O. *Biorheology*. 2004. **41**, 599.
250. Yellen B.B., Forbes Z.G., Halverson D.S., Fridman G., Barbee K.A., Chorny M. and Levy R. *Journal of Magnetism and Magnetic Materials*. 2005. **293**, 647.
251. Pankhurst Q.A., Conolly J., Jones S.K. and Dobson J. *Journal of Physics D: Applied Physics*. 2003. **36**, R167.
252. Fréchet J.M.J. (2005). *Progress in Polymer Science*. 2005. **30**, 844.
253. Lübbe A.S., Alexiou C. and Bergemann C. *Journal of Surgical Research*. 2001. **95**, 200.
254. Lübbe A.S., Bergemann C., Brock J. and McClure D.G. *Journal of Magnetism and Magnetic Materials*. 1999. **194**, 149.
255. Gelperina S, Kisich K, Iseman M. D and Heifets L. *Am. J. Respiratory and Critical Care Medicine*. 2005. **172**, 1487.
256. Macaroff P.P., Simioni A.R., Lacava Z.G.M., Lima E.C.D., Morais P.C. and Tedesco A.C. *Journal of Applied Physics*. 2006. **99**, 08: S102.
257. Park S.I., Lim J.H., Kim J.H., Yun H.I. and Kim C.O. *Journal of Magnetism and Magnetic Materials*. 2006. **304**, e406.
258. Duncan R. and Izzo L. *Advanced Drug Delivery Reviews*. 2005. **57**, 2215.
259. Yin H, Too H. P. and Chow G. M. *Biomaterials*. 2005. **26**, 5818.
260. Yang Q, Tang K, Wang C, Qian Y and SZhang S, *J. Phys. Chem. B*, 2002. **106**, 9227.
261. Oluwafemi O. S, *J. Colloids and Surf. B*, 2009. **73**, 382.

262. Wang Q, Pan D, Jiang S, Ji X, An L and Jiang B. *J. Cryst. Growth*, 2006. **286**, 83.
263. Amendola V, Meneghetti M, Granozzi G, Agnoli S, Polizzi S, Riello P, Boscaini A, Anselmi C, Fracasso G, Colombatti M, Innocenti C, Gatteschi D and Sangregorio D. *J. Mater. Chem.*, 2011. **21**, 3803.
264. Cheng C, Xu F and Gu H, *New J. Chem.*, 2011: **35**, 1072.

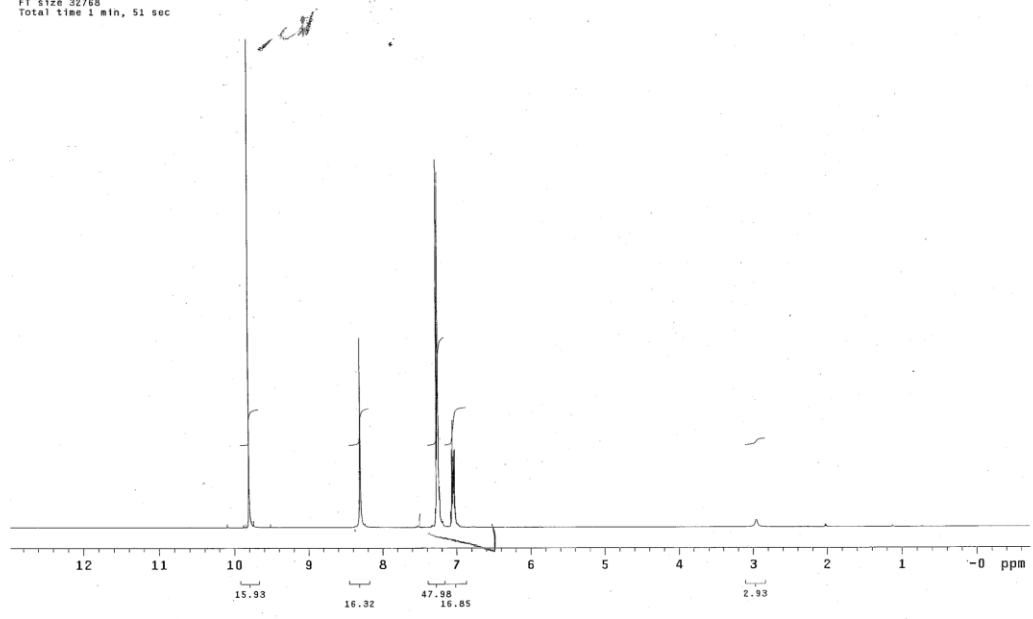
# APPENDIX I

hydroxybenzaldehyde  
Pulse Sequence: s2pu1  
Solvent: CDCl3  
Ambient temperature  
Mercury-300BB "medusa300"  
Pulse 82.1 degrees  
Acq. time 1.815 sec  
Vidch 28900.0 Hz  
1312 repetitions  
OBSERVE C13, 75.4519815 MHz  
DECOUPLE H1, 300.0688577 MHz  
Power 41 dB  
continuously on  
WALTZ-16 modulated  
DATA PROCESSING  
Line broadening 1.0 Hz  
FT size 131072  
Total time 1 hr, 21 min, 53 sec



hydroxybenzaldehyde  
Pulse Sequence: s2pu1  
Solvent: CDCl3  
Ambient temperature  
Mercury-300BS "medunsa300"

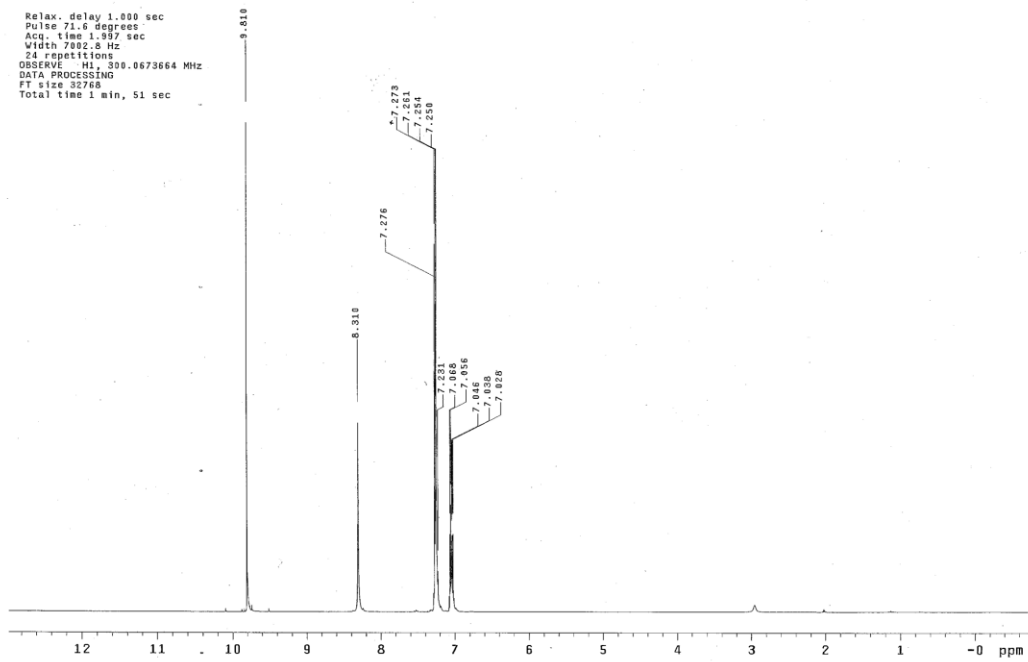
Relax. delay 1.000 sec  
Pulse 71.6 degrees  
Acq. time 1.997 sec  
Vidsh 7002.5 Hz  
24 repetitions  
OBSERVE H1 300.0673664 MHz  
DATA PROCESSING  
FT size 32768  
Total time 1 min, 51 sec





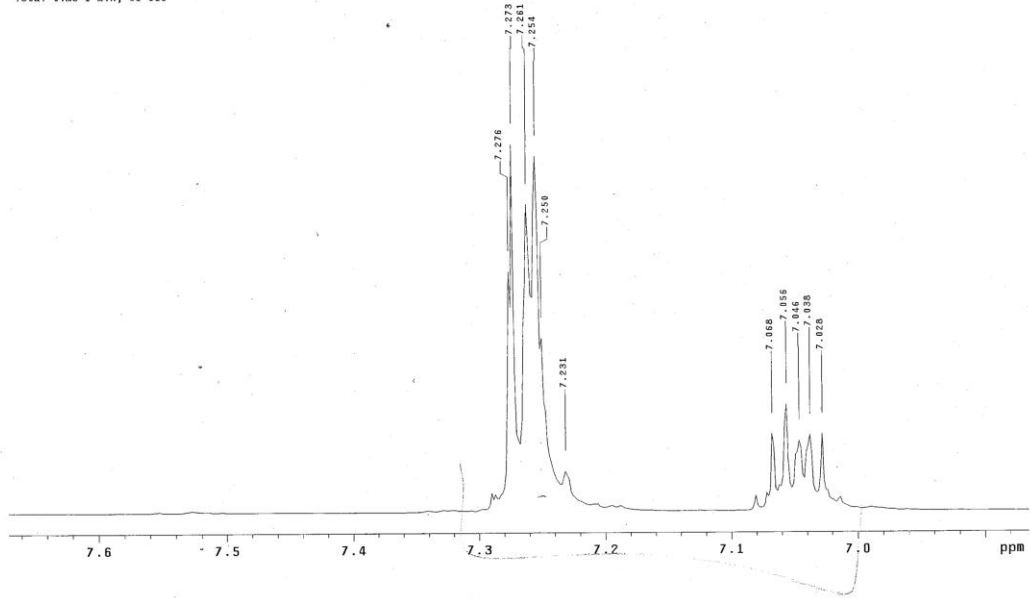
hydroxybenzaldehyde  
Pulse Sequence: s2pu1  
Solvent: CDCl3  
Ambient temperature  
Mercury-300SS "msdusa300"

Relax. delay 1.000 sec  
Pulse 71.6 degrees  
Acq. time 1.997 sec  
Width 7002.6 Hz  
24 repetitions  
OBSERVE H1, 300.0673664 MHz  
DATA PROCESSING  
FT size 32768  
Total time 1 min, 51 sec



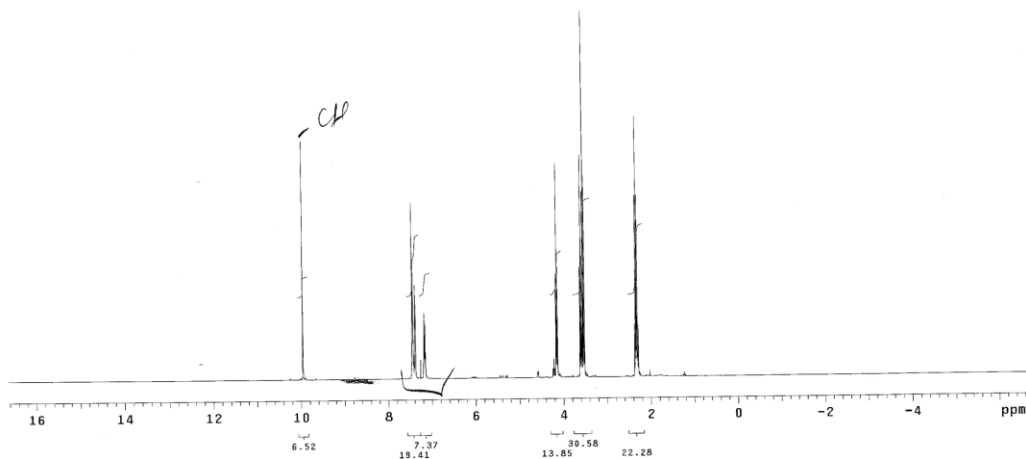
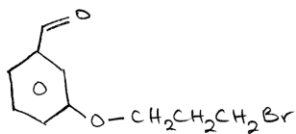
hydroxybenzaldehyde  
Pulse Sequence: s2pu1  
Solvent: CDCl3  
Ambient temperature  
Mercury-300BB "medunsa300"

Relax. delay 1.000 sec  
Pulse 71.8 degrees  
Acq. time 1.997 sec  
Vfwh 7002.8 Hz  
24 repetitions  
OBSERVE H1, 300.0673664 MHz  
DATA PROCESSING  
F1 size 32768  
Total time 1 min, 51 sec



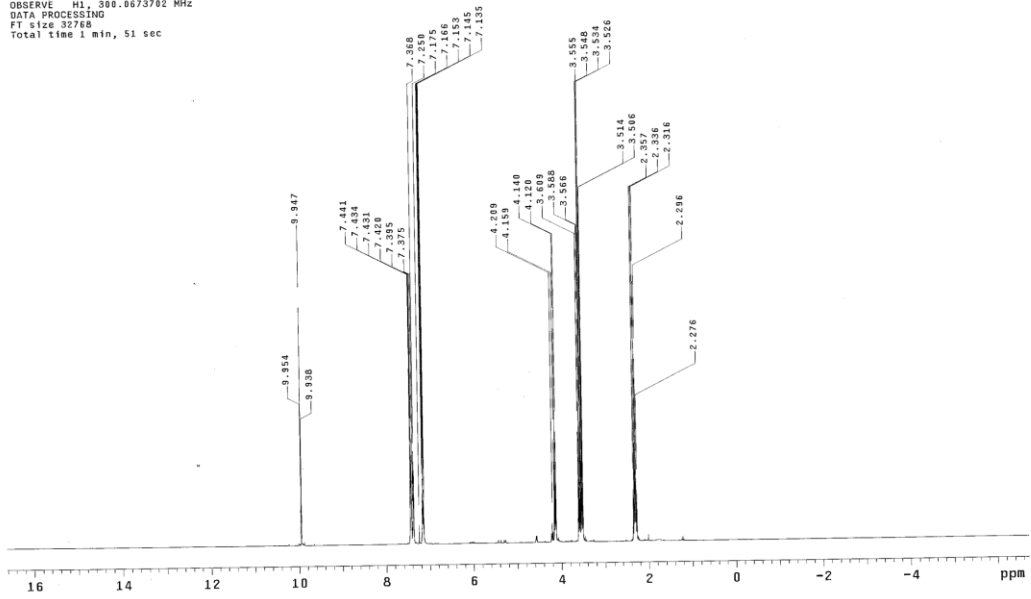
# APPENDIX II

product  
Pulse Sequence: s2pu1  
Solvent: CDCl3  
Ambient temperature  
Mercury-300BB "medunsa300"  
Relax. delay 1.000 sec  
Pulse 71.6 degree  
Acq. time 1.997 sec  
Width 7002.8 Hz  
24 repetitions  
OBSERVE M1, 300.0673672 MHz  
DATA PROCESSING  
FT size 32768  
Total time 1 min, 51 sec



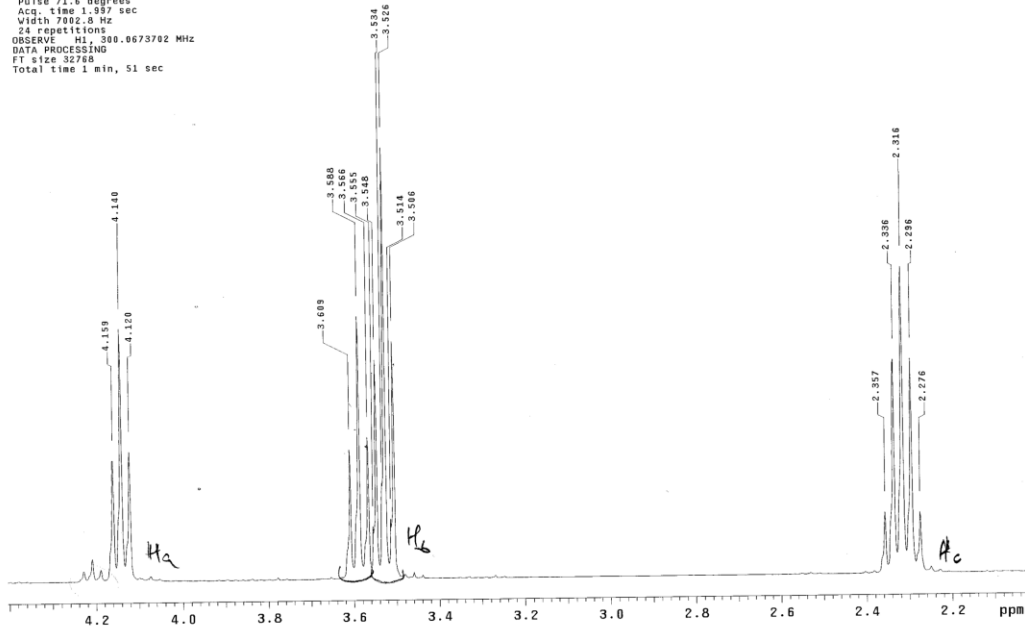
product  
Pulse Sequence: s2pul  
Solvent: CDCl3  
Ambient temperature  
Mercury-3000B "medunsa300"

Relax. delay 1.000 sec  
Pulse 71.6 degrees  
Acq. time 1.937 sec  
Width 7002.8 Hz  
24 repetitions  
OBSERVE H1, 300.0673702 MHz  
DATA PROCESSING  
F1 size 32768  
Total time 1 min, 51 sec



product  
pulse Sequence: s2pul  
Solvent: CDCl3  
Ambient temperature  
Mercury-300BB "medunsa300"

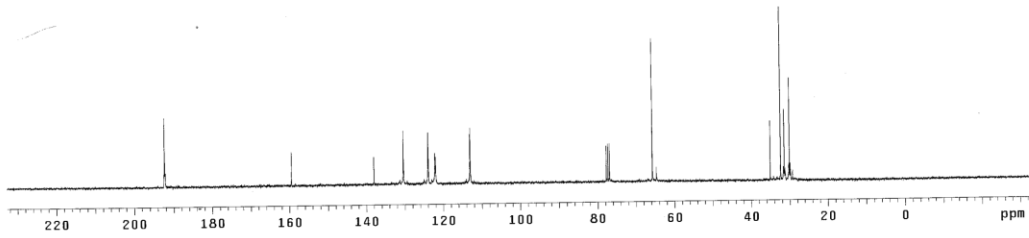
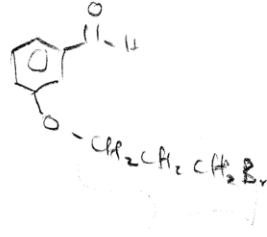
Relax. delay 1.000 sec  
Pulse 71.6 degrees  
Acq. time 1.387 sec  
Width 7002.8 Hz  
24 repetitions  
OBSERVE H1, 300.0673702 MHz  
DATA PROCESSING  
FT size 32768  
Total time 1 min, 51 sec



13C OBSERVE

Pulse Sequence: s2pu1  
Solvent: CDCl3  
Ambient temperature  
Mercury-30000 "medusa300"

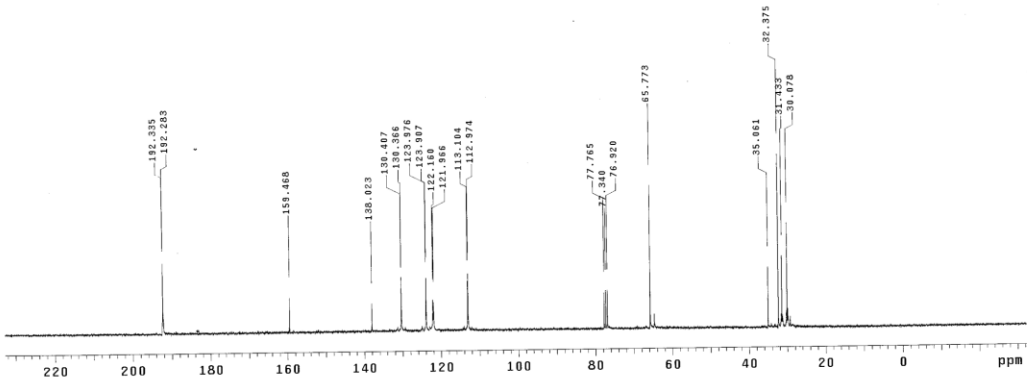
Pulse 82.1 degrees  
Acq. time 1.815 sec  
Width 20000.0 Hz  
2048 repetitions  
OBSERVE c13, 75.4519815 MHz  
DECOUPLE H1, 300.6688577 MHz  
Power 41 dB  
continuously on  
WALTZ-16 modulated  
DATA PROCESSING  
Line broadening 1.0 Hz  
F1 size 131872  
Total time 1 hr, 21 min, 53 sec



13C OBSERVE

Pulse Sequence: s2pul  
Solvent: CDCl3  
Ambient temperature  
Mercury-300B5 "medunsa300"

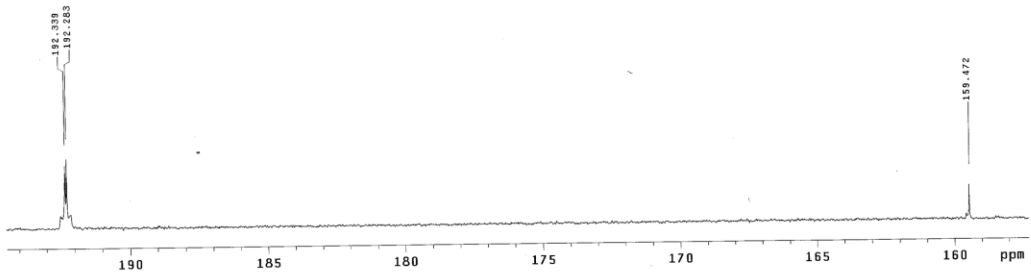
Pulse 82.1 degrees  
Acq. time 1.415 sec  
Width 20000.0 Hz  
2040 repetitions  
OBSERVE C13, 75.4519815 MHz  
DECOUPLE H1, 390.8688577 MHz  
Power 41 dB  
continuously on  
WALTZ-16 modulated  
DATA PROCESSING  
Line broadening 1.0 Hz  
FT size 131072  
Total time 1 hr, 21 min, 53 sec



13C OBSERVE

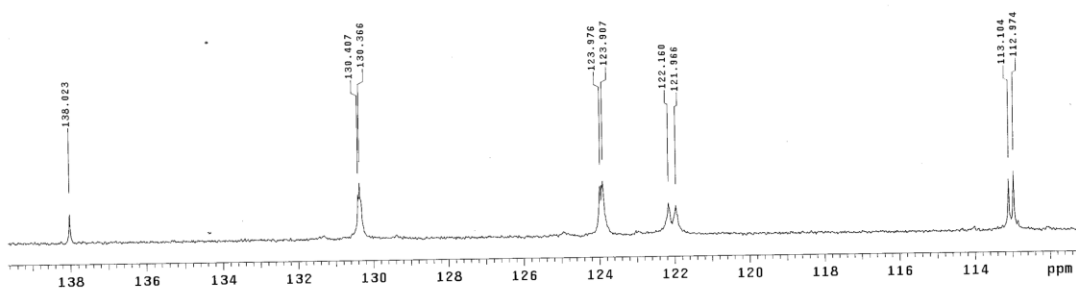
Pulse Sequence: s2pul  
Solvent: CDCl3  
Ambient temperature  
Mercury-300B "redunsa300"

Pulse 82.1 degree  
Acq. time 1.515 sec  
Width 20000.0 Hz  
2043 repetitions  
OBSERVE C13, 75.4519815 MHz  
DECOUPLE H1, 300.8688577 MHz  
Power 41 dB  
continuously on  
VALTZ-16 modulated  
DATA PROCESSING  
Line broadening 1.0 Hz  
FT Size 131072  
Total time 1 hr, 21 min, 53 sec



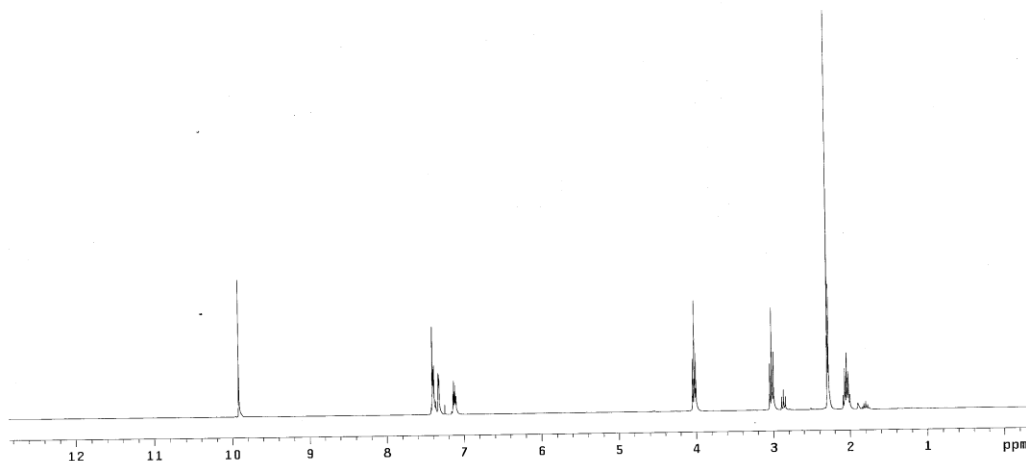
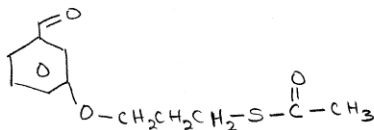


Pulse Sequence: s2pu1  
Solvent: CDCl3  
Ambient temperature  
Mercury-30000 "medunsa300"  
  
Pulse 82.1 degrees  
Acq. time 1.615 sec  
Width 2000.0 Hz  
2040 repetitions  
OBSERVE C13, 75.4519815 MHz  
DECOUPLE H1, 300.0688577 MHz  
Power 41 dB  
continuously on  
WALTZ-16 modulated  
DATA PROCESSING  
Line broadening 1.0 Hz  
FT size 131072  
Total time 1 hr, 21 min, 53 sec

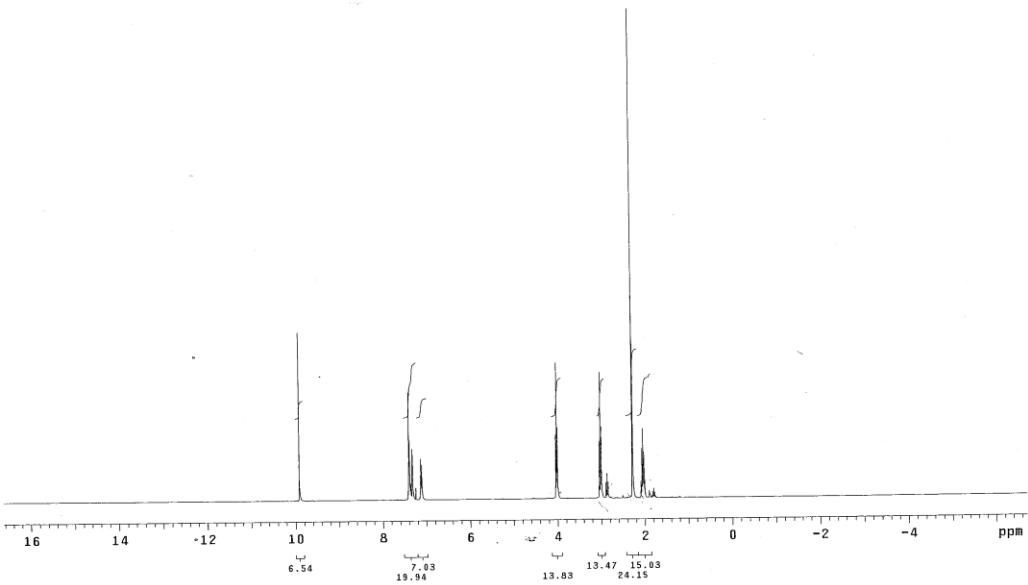


# APPENDIX III

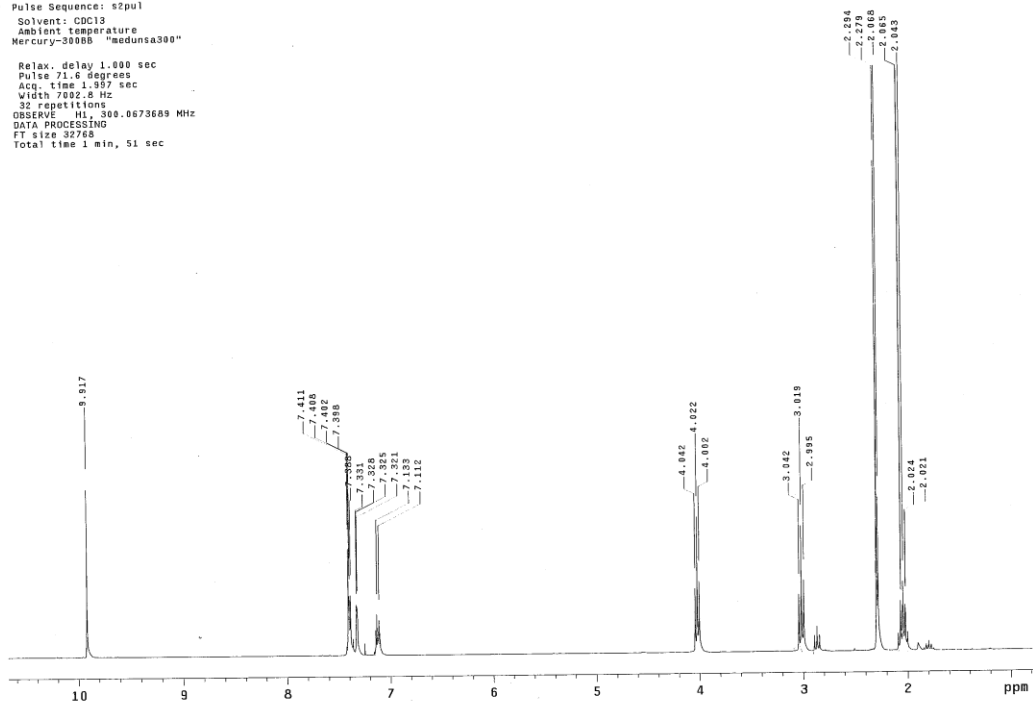
1  
Pulse Sequence: s2pul  
Solvent: CDCl3  
Ambient temperature  
Mercury=300BB "medunsa300"  
Relax. delay 1.000 sec  
Pulse 71.5 degree  
Acq. time 1.957 sec  
Width 7092.5 Hz  
32 repetitions  
OBSERVE: H1, 300.0673689 MHz  
DATA PROCESSING  
F1 size 32768  
Total time 1 min, 51 sec



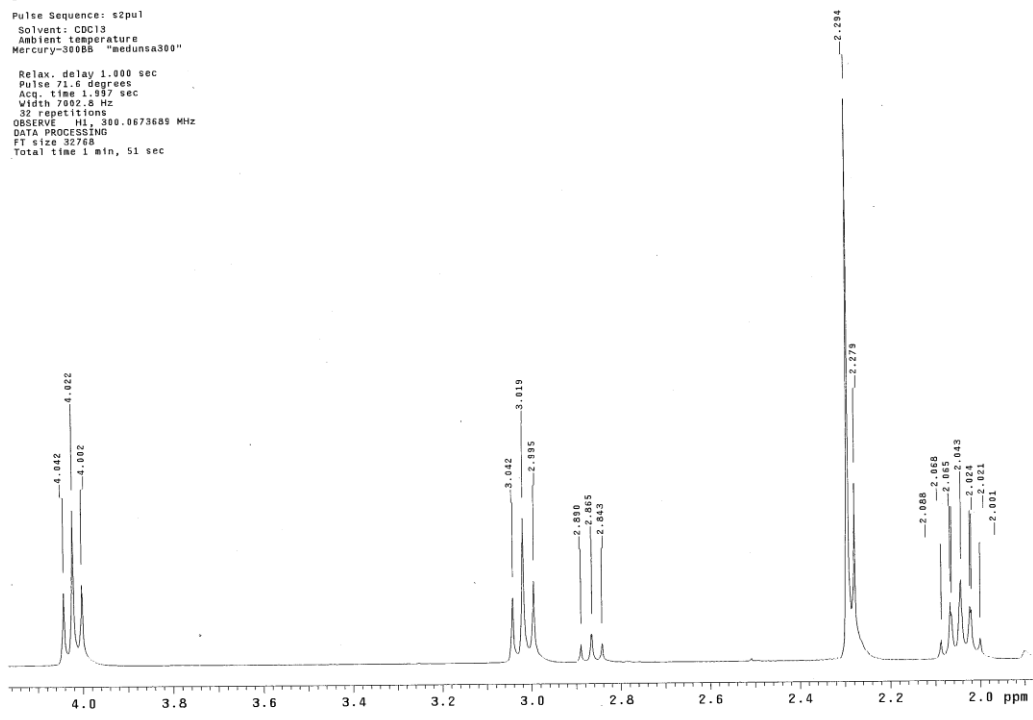
1  
Pulse Sequence: s2pu1  
Solvent: CDCl3  
Ambient temperature  
Mercury-300ES "medusa300"  
Relax. delay 1.000 sec  
Pulse 71.0 degrees  
Acq. time 1.997 sec  
Width 7002.6 Hz  
32 partitions  
OBSERVE H1: 300.0673689 MHz  
DATA PROCESSING  
F1 size 32768  
Total time 1 min, 51 sec



1  
Pulse Sequence: s2pul  
Solvent: CDCl3  
Ambient temperature  
Mercury-30005 "msdunsa300"  
Relax. delay 1.000 sec  
Pulse 71.0 degrees  
Acq. time 1.997 sec  
Width 7002.8 Hz  
32 repetitions  
OBSERVE H1, 300.0673689 MHz  
DATA PROCESSING  
FT size 32768  
Total time 1 min, 51 sec



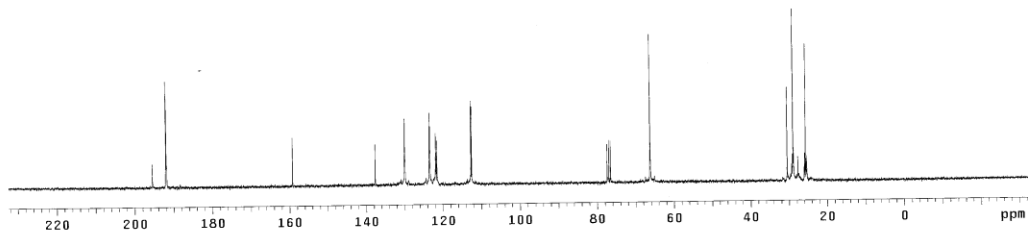
1  
Pulse Sequence: s2pu1  
Solvent: CDCl3  
Ambient temperature  
Mercury-300S "medunsa300"  
Relax. delay 1.000 sec  
Pulse 71.5 degrees  
Acq. time 1.957 sec  
Width 7052.5 Hz  
32 repetitions  
OBSERVE H1: 300.0673689 MHz  
DATA PROCESSING  
FT size 32768  
Total time 1 min, 51 sec



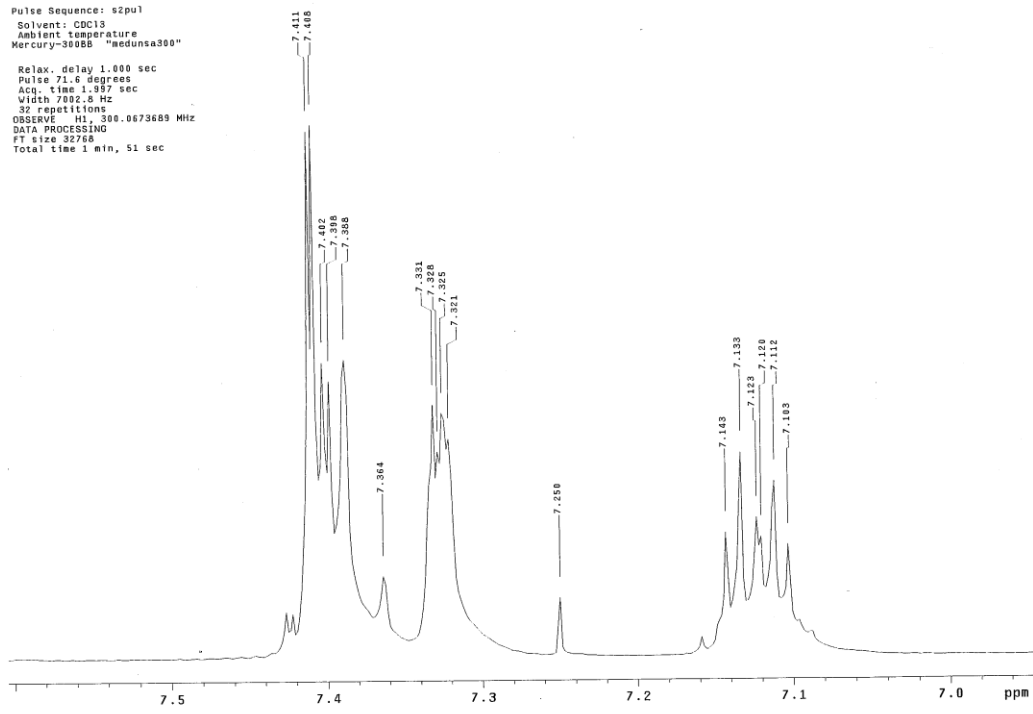
1

Pulse Sequence: s2pul  
Solvent: CDCl3  
Ambient temperature  
Mercury-300BS "medunsa300"

Pulse 82.1 degrees  
Acq. time 1.815 sec  
Width 20000.0 Hz  
2012 repetitions  
OBSERVE CH, 75.4520078 MHz  
DECOUPLE H1, 300.8688577 MHz  
Power 41 dB  
continuously on  
WALTZ-16 modulated  
DATA PROCESSING  
Line broadening 1.0 Hz  
FT size 131072  
Total time 1 hr, 11 min, 20 sec



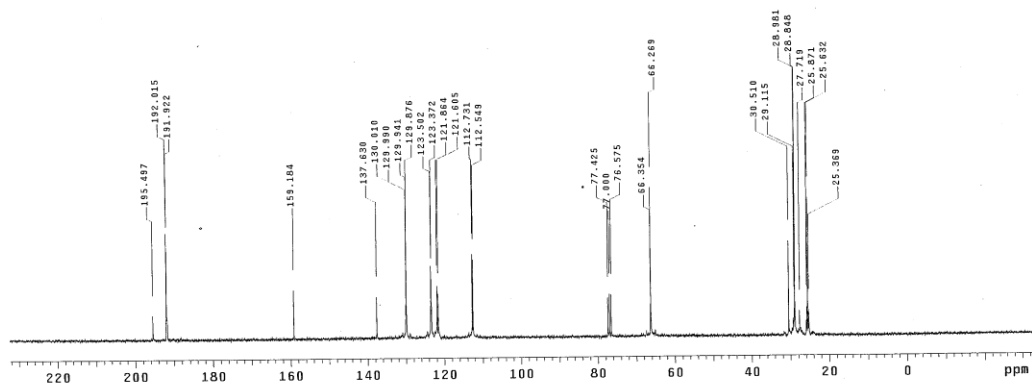
1  
Pulse Sequence: s2pu1  
Solvent: CDCl3  
Ambient temperature  
Mercury-300BS "mcdnsa300"  
Relax. delay 1.000 sec  
Pulse 71.0 degrees  
Acq. time 1.997 sec  
Width 7002.0 Hz  
32 repetitions  
OBSERVE H1: 300.0673689 MHz  
DATA PROCESSING  
F1 size 32768  
Total time 1 min, 51 sec



1

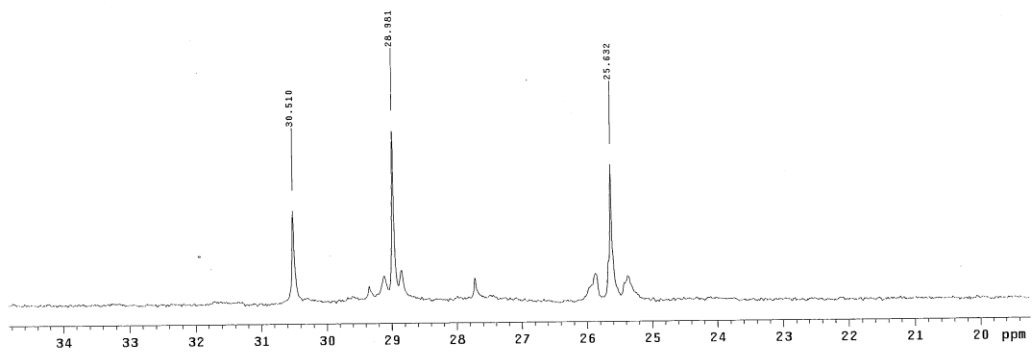
Pulse Sequence: s2pul  
Solvent: CDCl3  
Ambient temperature  
Mercury-300B5 "moduna300"

Pulse 82.1 degrees  
Acq. time 1.815 sec  
Width 22000.0 Hz  
2012 repetitions  
OBSERVE C13, 75.4520078 MHz  
DECOUPLE H1, 300.0688577 MHz  
Power 41 dB  
continuously on  
WALTZ-16 modulated  
DATA PROCESSING  
Line broadening 1.0 Hz  
F1 size 131172  
Total time 1 hr, 11 min, 20 sec

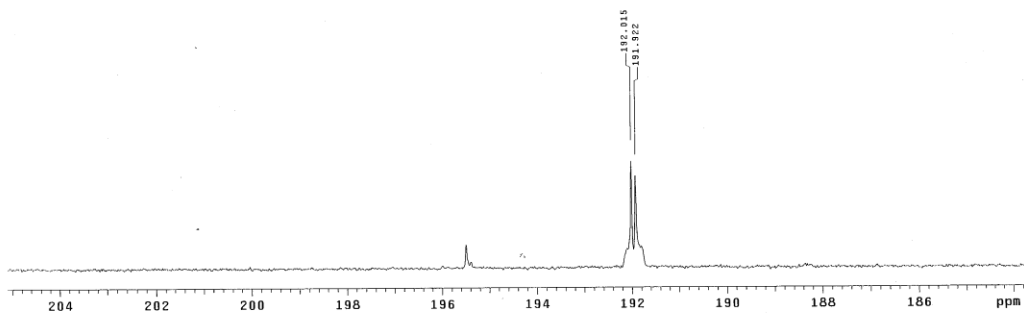




1  
Pulse Sequence: s2pu1  
Solvent: CDCl3  
Ambient temperature  
Mercury-30005 "medusa300"  
Pulse 82.1 degrees  
Acq. time 1.815 sec  
Width 20000.0 Hz  
2012 repetitions  
OBSERVE C13, 75.4520078 MHz  
DECOUPLE H1, 399.0688577 MHz  
Power 41 dB  
continuously on  
WALTZ-16 modulated  
DATA PROCESSING  
Line broadening 1.0 Hz  
FT size 131372  
Total time 1 hr, 11 min, 29 sec



1  
Pulse Sequence: s2pu1  
Solvent: CDCl3  
Ambient temperature  
Mercury-300BB "medusa300"  
  
Pulse 82.1 degrees  
Acq. time 1.815 sec  
Width 20000.0 Hz  
2012 repetitions  
OBSERVE C13, 75.4520078 MHz  
DECOUPLE H1, 300.0688577 MHz  
Power 41 dB  
continuously on  
WALTZ-16 modulated  
DATA PROCESSING  
Line broadening 1.0 Hz  
FT size 131872  
Total time 1 hr, 11 min, 20 sec

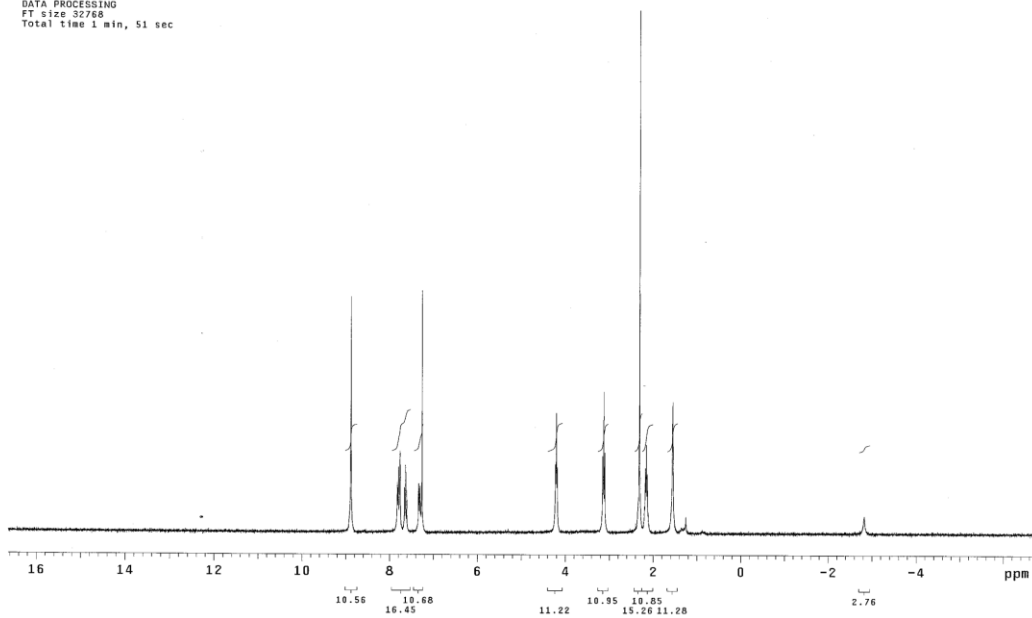


# APPENDIX IV

STANDARD 1H OBSERVE

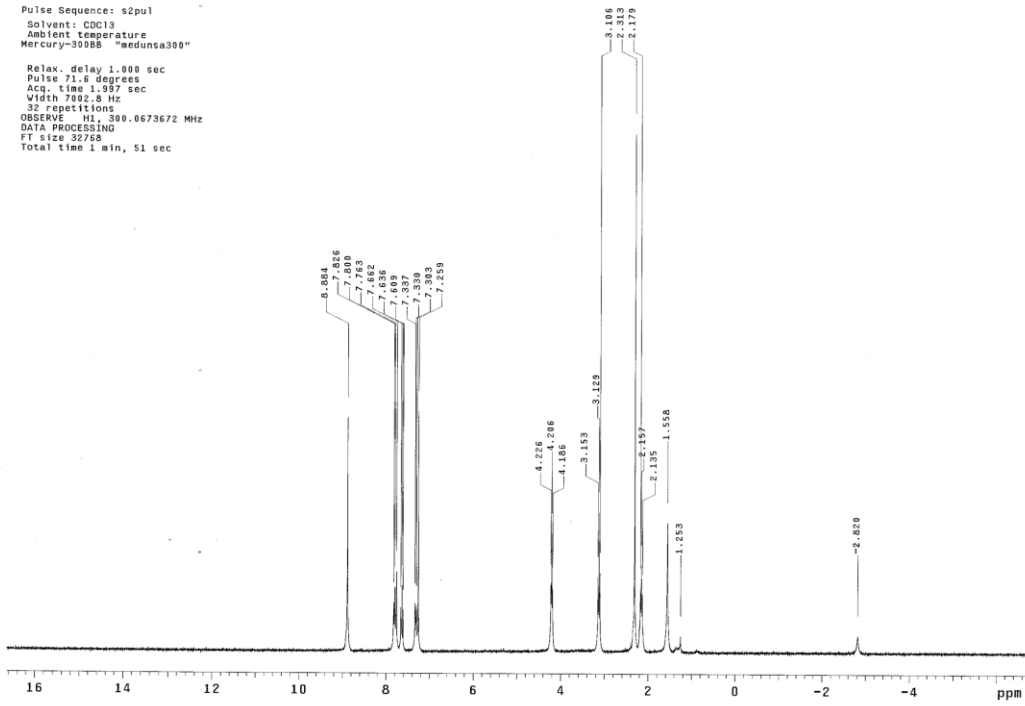
Pulse Sequence: s2pu1  
Solvent: CDCl3  
Ambient temperature  
Mercury-30088 "medusa300"

Relax. delay 1.000 sec  
Pulse 71.6 degrees  
Acq. time 1.997 sec  
Width 7002.8 Hz  
32 repetitions  
OBSERVE H1, 300.0673672 MHz  
DATA PROCESSING  
FT size 32768  
Total time 1 min, 51 sec



STANDARD 1H OBSERVE

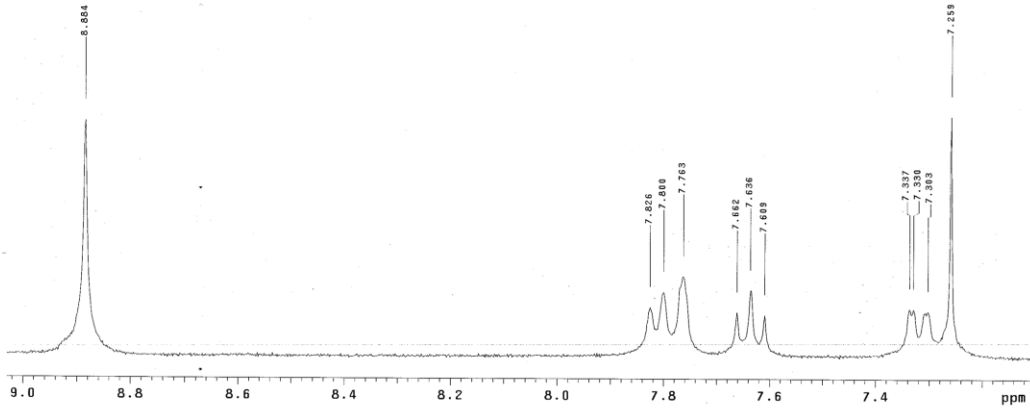
Pulse Sequence: s2pu1  
Solvent: CDCl3  
Ambient Temperature  
Mercury-300BB "meduna300"  
Relax. delay 1.000 sec  
Pulse 71.6 degree  
Acq. time 1.997 sec  
Width 7892.8 Hz  
32 repetitions  
OBSERVE H1, 300.0673672 MHz  
DATA PROCESSING  
FT size 32768  
Total time 1 min, 51 sec



STANDARD 1H OBSERVE

Pulse Sequence: s2pu1  
Solvent: CDCl3  
Ambient temperature  
Mercury-300SS "medusa300"

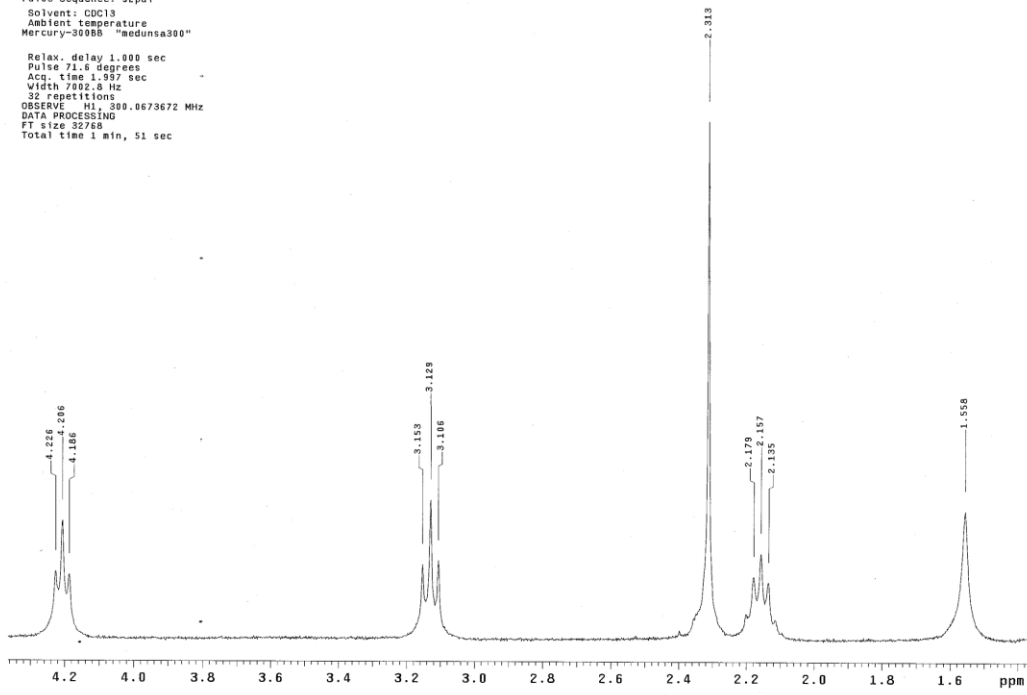
Relax. delay 1.000 sec  
Pulse 71.6 degrees  
Acq. time 1.597 sec  
Width 7002.8 Hz  
32 repetitions  
OBSERVE H1, 300.0673672 MHz  
DATA PROCESSING  
FT size 32768  
Total time 1 min, 51 sec



STANDARD 1H OBSERVE

Pulse Sequence: s2pu1  
Solvent: CDCl3  
Ambient temperature  
Mercury-3000S "medusa300"

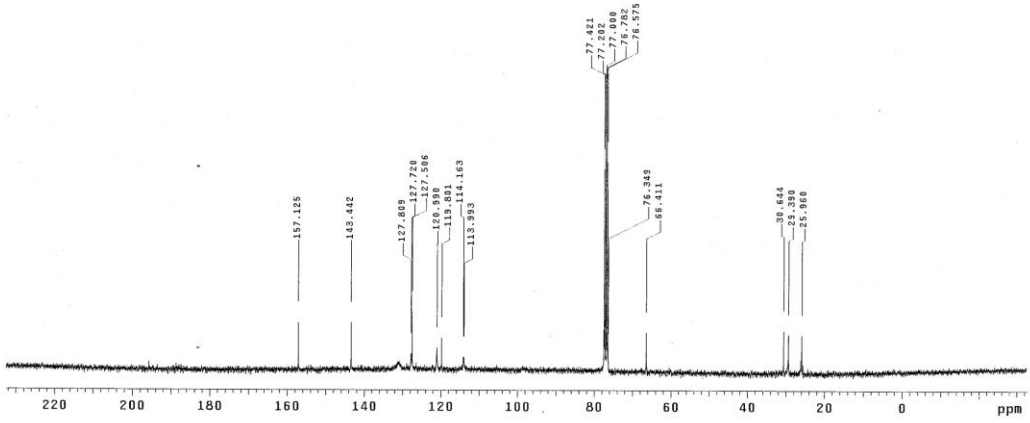
Relax. delay 1.000 sec  
Pulse 71.4 degrees  
Acq. time 1.997 sec  
Width 7802.8 Hz  
32 repetitions  
OBSERVE H1, 300.0673672 MHz  
DATA PROCESSING  
FT size 32768  
Total time 1 min, 51 sec



13C OBSERVE

Pulse Sequence: s2pul  
Solvent: CDCl3  
Ambient temperature  
Mercury-30085 "hedunsa300"

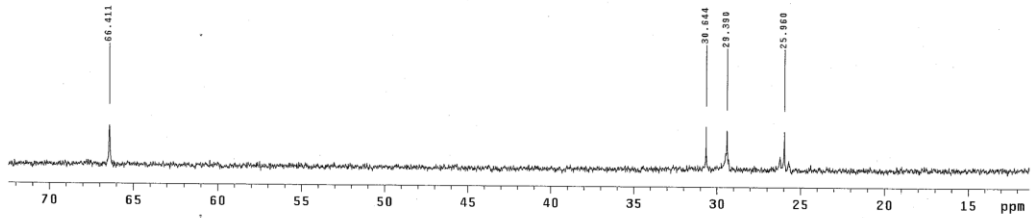
Pulse 82.1 degrees  
Acq. time 1.615 sec  
Width 20000.0 Hz  
35000 repetitions  
OBSERVE C13, 75.4520002 MHz  
DECOUPLE H1, 300.0680577 MHz  
Power 41 dB  
continuously on  
WALTZ-16 modulated  
DATA PROCESSING  
Line broadening 1.0 Hz  
FT size 131072  
Total time 14 hr, 46 min, 19 sec



13C OBSERVE

Pulse Sequence: s2pu1  
Solvent: CDCl3  
Ambient temperature  
Mercury-300BB "medunsa300"

Pulse 92.1 degrees  
Acq. time 1.615 sec  
Width 20000.0 Hz  
25000 repetitions  
OBSERVE C13, 75.4520002 MHz  
DECUPLE H1, 300.6688577 MHz  
Power 41 dB  
continuously on  
WALTZ-16 modulated  
DATA PROCESSING  
Line broadening 1.0 Hz  
FT size 1331972  
Total time 14 hr, 46 min, 19 sec

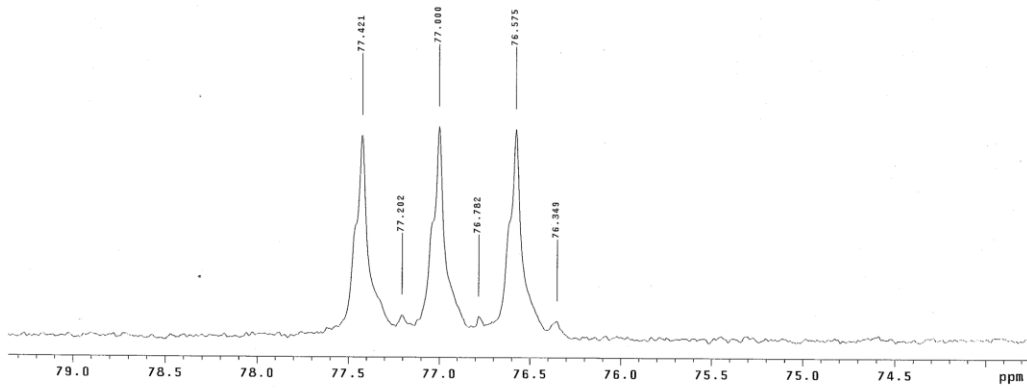




13C OBSERVE

Pulse Sequence: s2pu1  
Solvent: CDCl3  
Ambient temperature  
Mercury-300BB "medunsa300"

Pulse 32.1 degrees  
Acq. time 1.515 sec  
Width 20000.0 Hz  
25000 repetitions  
OBSERVE C13, 75.4520002 MHz  
DECUPLE H1, 300.0688577 MHz  
Power 41 dB  
continuously on  
VALTZ-16 modulated  
DATA PROCESSING  
Line broadening 1.0 Hz  
FT size 133972  
Total time 14 hr, 46 min, 19 sec



13C OBSERVE

Pulse Sequence: s2pu1  
Solvent: CDCl3  
Ambient temperature  
Mercury-300BB "medunsa300"

Pulse 82.1 degrees  
Acq. time 1.515 sec  
Width 20000.0 Hz  
2500 repetitions  
OBSERVE C13, 75.4520002 MHz  
DECOUPLE H1, 300.0688577 MHz  
Power 41 dB  
continuously on  
WALTZ-16 modulated  
DATA PROCESSING  
Line broadening 1.0 Hz  
FT size 133072  
Total time 14 hr, 46 min, 19 sec

